July 2016

# Electromagnetic Scattering Models for InSAR Correlation Measurements of Vegetation and Snow

Yang Lei

# ELECTROMAGNETIC SCATTERING MODELS FOR INSAR CORRELATION MEASUREMENTS OF VEGETATION AND SNOW

A Dissertation Presented

by

YANG LEI

Submitted to the Graduate School of the
University of Massachusetts Amherst in partial fulfillment
of the requirements for the degree of

DOCTOR OF PHILOSOPHY

May 2016

Electrical and Computer Engineering

# ELECTROMAGNETIC SCATTERING MODELS FOR INSAR CORRELATION MEASUREMENTS OF VEGETATION AND SNOW

A Dissertation Presented

by

YANG LEI

Approved as to style and content by:

Paul R. Siqueira, Chair

Stephen J. Frasier, Member

Ramakrishna Janaswamy, Member

Robert N. Treuhaft, Member

C. V. Hollot, Department Chair
Electrical and Computer Engineering

*To my wife, our parents and grandparents.*

*I do not know what I may appear to the world, but to myself I seem to have been only like a boy playing on the sea-shore, and diverting myself in now and then finding a smoother pebble or a prettier shell than ordinary, whilst the great ocean of truth lay all undiscovered before me.*

Isaac Newton

*If I have seen further it is by standing on the shoulders of giants.*

Isaac Newton

*You never fail until you stop trying.*

Albert Einstein

*The value of a man should be seen in what he gives and not in what he is able to receive.*

Albert Einstein

# ACKNOWLEDGMENTS

While I am writing this chapter, it is almost the end to wrap up my graduate study, which indeed reminds me of so many precious and exciting moments during the past seven years at UMass Amherst (with the first two years of master study on Computer Engineering and the following five years of PhD study on Electrical Engineering). First of all, I would like to express my most sincere gratitude to Prof. Paul Siqueira, who has been a great advisor, a patient teacher and a genuine friend not only on supporting and building up my academic career but also on guiding and shaping my working ethics. Without his intelligent and creative insights and generous help, neither would I find so many interesting and significant research topics that are presented in this dissertation, nor be awarded the NASA graduate fellowship. He is that kind of advisor who always designs research topics that fully exploit the student's expertise and also always put himself in the student's shoes. So many times when I drop by his office and ask him a question, no matter how simple the question is, Prof. Siqueira always put his work on hold, invites me for a discussion, and endeavors to fix the problem diligently and patiently. Moreover, he even takes any chance to create an opportunity for his students. Without his introduction at each conference, I would never know that many peers in the community of remote sensing. Without his recommendation and efforts, I would never make the short visit to NASA/JPL and then know Dr. Robert Treuhaft personally, which in turn opens two potential job opportunities for me. Without his concern and generous help, I would never have the intern opportunity at Applied GeoSolutions for the final semester, which improves and advances my research work in the perspective of real business. In short, without his encouragements and support, I would never be who I am in the academic

career. In each culture, one is considered fortunate to find a great advisor or mentor. Especially, in Chinese culture, there is a phrase called "Once teacher, always father". I am determined to continue applying what I learned from Prof. Siqueira and cherish this advisorship and friendship in my future career.

Also, I would like to thank Dr. Robert Treuhaft from NASA/JPL, who will serve as my postdoc mentor after I graduate. As a world-renowned physicist, Robert is also very easygoing and always helpful to young scholars. Without his great efforts, I cannot be awarded the NASA postdoc fellowship for the next two years. Through many direct discussions with Robert, which help me refine or even reformulate some of the essential models in this dissertation, I learned a lot from his physical insights and the enthusiasm in understanding and discovering each unknown topic. Although I have directly worked with him only for a month, his mature and responsible attitude towards scientific research has already set up an excellent example for me.

Then, my thanks go to Prof. Stephen Frasier and Prof. Ramakrishna Janaswamy, who take time to be my committee members and read through my dissertation. I really appreciate their insightful comments for the proposal of the dissertation and the final defense.

The work presented in this dissertation involves a lot of contribution from my colleagues in the Microwave Remote Sensing Laboratory (MIRSL) at UMass Amherst. Caitlin Dickinson processed the National Land Cover Database 2006 (NLCD2006) creating a mask of waterbodies in Maine, US, and also generated a forest height map from the clustered ICESAT data over ILCP, Queensland, Australia. Tracy Whelen nicely converted my MATLAB code for forest height estimation and mosaic map generation to a python-based software package, and has been working hard to update it through a lot of test runs. Gerard Carregal was working with us to process ROI_PAC products and then to input the results to the python-based software package. The

presented work also benefits from many personal discussions with Kan Fu, Xingjian Chen, Dustin Lagoy and etc.

I would also like to acknowledge several external colleagues. Richard Lucas, from Aberystwyth University, provided the airborne lidar data and the clustered ICESAT data over ILCP, Australia. I feel so grateful to the private company Applied GeoSolutions, especially William Salas and Nathan Torbick for identifying the forest height mosaic generation as a potential useful product, providing me the intern opportunity in my final semester and pushing this project ahead by extensively validating the approach and the software over various test areas, as well as Diya Chowdhury for working with me directly to test the python package and also to process a lot of ALOS/PALSAR data using ROI_PAC.

I want to thank my previous advisors and mentors whose guidance and encouragements have a big impact on me. These include Prof. Xiao-jian Xu and Prof. Shi-xiang Qian from Beihang University, and Prof. Ramgopal Mettu from Tulane University. Also, I want to show gratitude to my Chinese friends for their long-term support, such as Tao Chu (who introduced me to the field of remote sensing and to know Prof. Siqueira), Xiang-long Liu, Ji-mo Zhang, Shen Shen, Zi-xuan Wang, Qiang Liu, Yin-xiao Li, to name a few. My special thanks goes to Gladys Wang who is the wife of Prof. Siquiera and has been constantly helping and concerning my wife and me along with other Chinese students in a manner such as our host family, which indeed warms the hearts of the international students.

Finally, I owe my most sincere thanks to my wife Xiao-fei (Shirley) Yue who has been understanding, supporting and taking care of me so well during the most stressful time when I was waiting for the job opportunities, writing papers and preparing for the dissertation. I always think that half of the value in this dissertation is attributed to my wife, since her endless love and encouragements are the most excellent motivation for me to devote myself into scientific research. Also, I owe a lot of thanks to my

wife's family who have been supporting and encouraging me a lot. Last but not least, I feel so grateful to my family for their life-long education and support. To me, they are the best parents and grandparents in this world, without whom I would not be who I am.

The work as presented in this dissertation was supported by NASA Headquarters under the NASA Earth and Space Science Fellowship (NESSF) Program during the past three years (2012–2015).

# ABSTRACT

## ELECTROMAGNETIC SCATTERING MODELS FOR INSAR CORRELATION MEASUREMENTS OF VEGETATION AND SNOW

MAY 2016

YANG LEI

B.Sc., BEIHANG UNIVERSITY

M.Sc., UNIVERSITY OF MASSACHUSETTS AMHERST

Ph.D., UNIVERSITY OF MASSACHUSETTS AMHERST

Directed by: Professor Paul R. Siqueira

Interferometric Synthetic Aperture Radar (InSAR) has proved successful and efficient in measuring the vertical structure of the distributed targets such as vegetation and snow, which are dominated by volume scattering. In particular, the InSAR correlation measurement has been utilized to retrieve the target vertical structural information. One existing and well-known electromagnetic scattering model of the InSAR correlation was first brought forward focusing on the single-pass InSAR observation of a sparse random medium like vegetation. However, the lack of the adaption of this InSAR scattering model for repeat-pass InSAR observation of vegetation as well as for single-pass InSAR observation of snow by considering its dense medium characteristics, essentially constrain fully exploiting InSAR's capability of measuring sparse and dense medium characteristics.

In this work, the well-known InSAR scattering model will be adapted to accommodate the two scenarios: 1) repeat-pass InSAR observation of vegetation and 2) single-pass InSAR observation of snow and considering its dense medium characteristics. Theoretical model derivations as well as parameter retrieval approaches are demonstrated for both of the applications, respectively. Both of the simulated and ground validation results are also presented. The InSAR scattering models along with the parameter retrieval analysis described in this work will expand InSAR's capability as well as the range of vegetation and snow characteristics that can be retrieved by single-pass and/or repeat-pass InSAR systems.

# TABLE OF CONTENTS

# LIST OF TABLES

**Table** **Page**

# LIST OF FIGURES

**Figure** **Page**

# CHAPTER 1

# INTRODUCTION

Synthetic Aperture Radar (SAR) has the capability of mapping the terrestrial land cover as well as monitoring the land cover (and thus climate) change on a large scale. For distributed targets (such as vegetation and snow) that are dominated by volume scattering, an Interferometric SAR (InSAR) has proved successful and efficient in measuring the vertical structure of the targets. As illustrated in Figure 1.1, an InSAR observing configuration collects a pair of SAR observations from the distributed targets at two slightly different incidence angles, either using 1) two different antennas deployed on the same platform (single-pass), or using 2) the same antenna onboard a platform that revisits the ground area periodically (repeat-pass). In either case, the complex InSAR correlation coefficient between the two observations is the important InSAR metric that is usually utilized to retrieve the target vertical structure, and can be defined as [64]

$$\gamma = \frac{\langle E_1 E_2^* \rangle}{\sqrt{\langle |E_1|^2 \rangle \langle |E_2|^2 \rangle}} \tag{1.1}$$

where $E_1$ and $E_2$ are the received electric fields at two antennas (or from two passes of the same antenna) that are separated by some distance (terms as the *interferometric baseline*, and denoted as $B$). Here the angular brackets represent ensemble averaging, which can be replaced by spatial averaging [79].

One existing and well-known electromagnetic scattering model of the InSAR correlation was first brought forward by Treuhaft *et al.*, [80, 81], focusing on the single-pass

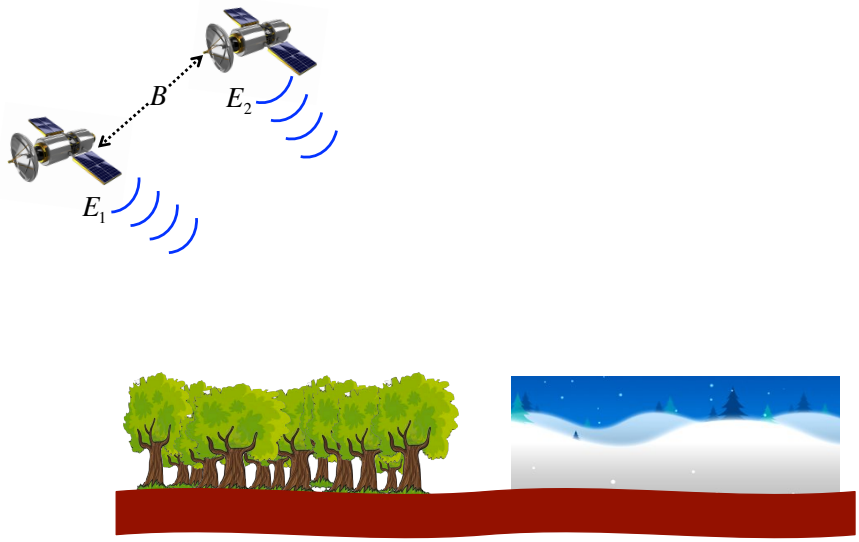


Figure 1.1: Illustration of the observing geometry of SAR interferometry (InSAR) over land covers such as vegetation and snow. $E_1$ and $E_2$ are the received electric fields at two antennas (or from two passes of the same antenna) that are separated by the interferometric baseline, $B$. The InSAR complex correlation coefficient between $E_1$ and $E_2$ is thus defined as $\gamma = \frac{\langle E_1 E_2^* \rangle}{\sqrt{\langle |E_1|^2 \rangle \langle |E_2|^2 \rangle}}$.

InSAR observation of a sparse random medium such as vegetation. However, the lack of the adaption of this InSAR scattering model for repeat-pass InSAR observation of vegetation essentially constrains the utility and explanations of the accumulated data volume from spaceborne repeat-pass InSAR missions, such as Japan Aerospace eXploration Agency (JAXA)'s Advanced Land Observing Satellite (ALOS)-1 and -2 [66, 28], and National Aeronautics and Space Administration (NASA)'s NASA-ISRO SAR (NISAR) [3]. Furthermore, the same InSAR scattering model has also been directly used to retrieve the snow characteristics at the lower end of the microwave spectrum by considering snow as equivalent to a sparse random medium [49, 89]. Therefore, the lack of the adaption of this InSAR scattering model for the single-pass InSAR observation of snow by considering its dense medium characteristics, also constrains fully exploiting InSAR's capability of measuring dense medium characteristics.

Therefore, the original contributions of this dissertation are on adapting the well-known InSAR scattering model so as to accommodate these two scenarios: 1) repeat-pass InSAR observation of vegetation and 2) single-pass InSAR observation of snow and considering its dense medium characteristics. In this chapter, the scientific motivation, the relevant previous work and the merits of this work on the aspect of SAR/InSAR scattering models for the retrieval of snow characteristics, as well as single-/repeat-pass InSAR scattering models for the retrieval of vegetation characteristics, are discussed.

## 1.1 SAR/InSAR scattering models for the retrieval of snow characteristics

Snow characteristics, such as Snow Water Equivalent (SWE) and snow grain size, are important in the monitoring of the hydrological cycle and as indicators of climate change in snow-dominated regions [6]. As illustrated in Figure 1.2, a dry snow sample is comprised with ice particles and air bubbles. Dealing with wet snow is beyond the scope of this work since a high water content will be incorporated making the modeling more complicated. Therefore, when "snow" is mentioned in this work, it refers to the dry snow only.

Three independent quantities are usually used to characterize a snow sample: grain size, volume fraction and layer depth. However, for the hydrological purpose, it is also desired to know how much equivalent water content there is in the snowpack. Given a unit area (e.g. 1 $m^2$), SWE is defined as the depth of the water content after melting the snowpack, and can be expressed as

$$\text{SWE} = \text{volume fraction} \times \text{layer depth} \times 0.917, \tag{1.2}$$

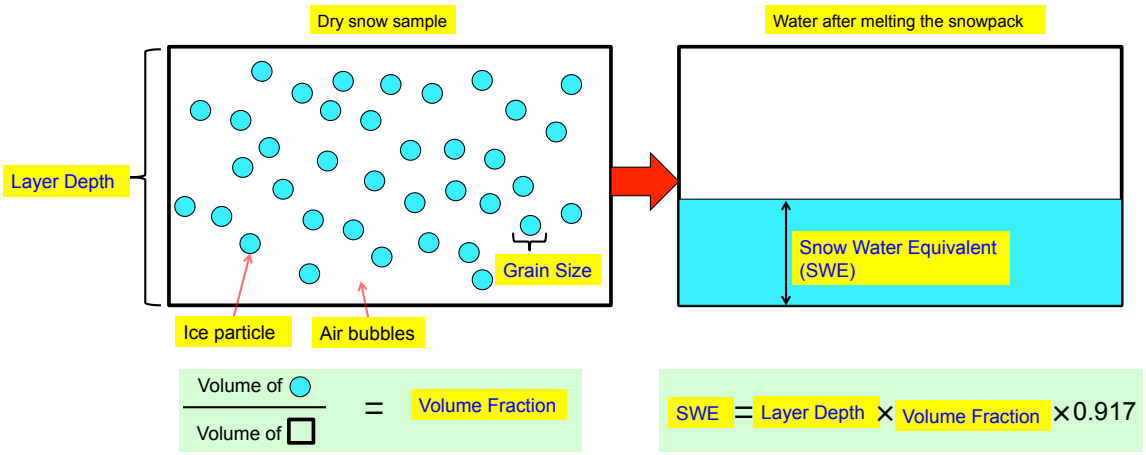


Figure 1.2: Illustration of the dry snow (comprised with ice particles and air bubbles) characteristics (*i.e.*, grain size, volume fraction, layer depth) and the Snow Water Equivalent (SWE) measure. By definition, SWE = volume fraction × layer depth × 0.917.

where volume fraction and layer depth are both illustratively defined in Figure 1.2 and the constant 0.917 relates to the density of ice.

The utility of a microwave-frequency SAR instrument onboard an aircraft or a satellite has the potential of measuring the snow characteristics for a large region at fine resolutions. In order to provide a theoretical basis for characterizing the microwave remote sensing for a dense medium like snow, a number of electromagnetic scattering models have been developed over time. Fundamentally, these models can be divided into two groups. One is to model snow as a continuous random medium with small perturbations occurring spatially against a uniform background permittivity [82]. In this approach, a correlation function is used to characterize the spatially-varying behavior of the permittivity fluctuations [88]. In one such analysis, Ding *et al.*, [13] introduced a bi-continuous model to capture microstructures within the snow scattering layer and to numerically solve for the snow scattering properties through the incorporation of dense medium radiative transfer (DMRT) theory [95, 92].

A second approach is to model a dense medium like snow as a random collection of discrete scatterers, or particles. In such a model, the conditional probability of finding

one particle given the location of another is used to characterize the pair-wise correlation between particle locations and is termed the *pair distribution function* [82]. This physically-based distribution function is combined with the Quasi-Crystalline Approximation (QCA) and DMRT to solve for the scattering properties analytically [86]. In such analyses, multi-layer scattering and multiple-sized particle distribution effects can be incorporated in the model [51, 14, 94].

Existing snow-characteristic retrieval algorithms are primarily based on measurements of SAR backscatter power, where the volume scattering component is characterized by the radiative transfer theory, and the surface scattering part is described by the Integral Equation Model (IEM) or the Advanced Integral Equation Model (AIEM) [70, 71, 72, 67, 58]. In the above algorithms, the discrete random medium representation is used to characterize the snow volume. Since the bi-continuous model [13] was brought forward, efforts have also been made to combine it with existing snow retrieval methods that use SAR backscatter power [93].

By contrast, Interferometric SAR (InSAR) measurements have used the complex correlation to estimate the vertical structure from volume-scattering targets, and in particular, for vegetation remote sensing using C- and L-band interferometry [80, 81, 57]. The retrieval of snow layer depth for dry snow has also been studied using C-band and X-band InSAR correlation [49, 89], where the wavelength is much larger than the snow grain size, and thus the extinction due to multiple-scattering is not expected to dominate the scattering interaction.

Alternative methods exist as well for measuring snow depth. One example uses an S-band altimeter whose signal sees both the top and the bottom of the snow layer (e.g. [41]). Another is a two-frequency system where a combination of low and high frequency are used to estimate the bottom and top of the snow layer (e.g. see [50] for one example that used lidar).

To date, most retrieval algorithms for snow characteristics rely on SAR backscatter power measurements while only a few are based on InSAR correlation measurements. For the approaches that use the InSAR correlation, there is lack of a physical scattering model that takes into account the dense medium characteristics of snow. This work addresses that issue by deriving a physical scattering model that connects InSAR correlation measurements to the physical dense-medium characteristics of grain size, volume fraction and layer depth.

In this work, the discrete random medium representation is used with the *Foldy-Lax* multiple scattering equations for modeling a dense medium [82, 26, 16, 35, 36]. In particular, the Foldy-Lax multiple scattering equations are solved using QCA and the pair distribution function [82] and connecting that to an analytical expression for the InSAR correlation, as done by [80] for a sparse vegetation medium. It is shown for the InSAR model derived here, that the InSAR correlation is sensitive to the snow layer depth (as in [89, 49]) at Ku- to L-band, and to the snow grain size and volume fraction at Ka-band.

## 1.2 Single-/repeat-pass InSAR scattering models for the retrieval of vegetation characteristics

Since forest structure and aboveground biomass are of great value to terrestrial ecology, habitat biodiversity, and global carbon storage assessments, it is desired to monitor and quantify the state of, and change in aboveground biomass and forest height. Through the sensing of vegetation vertical structure, worldwide, a spaceborne satellite mission such as the once-planned Deformation, Ecosystem Structure and Dynamics of Ice (DESDynI) mission (with both radar and lidar deployed) from NASA would have the capability of mapping the global vegetation structural information at fine resolutions, which is important to understand and monitor the global carbon budget and climate change. Since the lidar portion of the mission has been

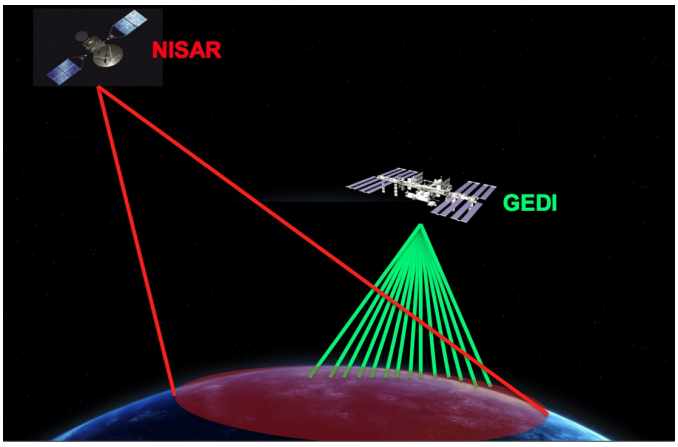


Figure 1.3: Illustration of the observing geometry of two future spaceborne InSAR and lidar missions: NISAR (to be launched in 2020) and GEDI (to be launched in 2019). NISAR has a repeat-pass L-band InSAR deployed revisiting the same ground area every 12 days with a swath width of 250 km (indicated by the "red" shade area in the figure). The GEDI lidar is a multi-beam waveform lidar deployed on the International Space Station with 14 beams that are separated 500 m apart from each other (illustrated as "green" lines in the figure). Note this figure is a notional illustration, which does not reflect the exact scale of the spatial dimensions.

cancelled [21], a separate spaceborne lidar mission (Global Ecosystem Dynamics Investigation or GEDI) was recently selected [15], with a separate radar mission formulated known as NISAR [3]. An illustrative overview of two future missions (NISAR [3] and GEDI [15]) is shown in Figure 1.3. NISAR (or repear-pass InSAR) has complete spatial coverage while the data interpretation is more difficult leading to a moderate accuracy in measuring the vertical structure; in comparison, GEDI (or lidar) has a sparse spatial coverage while the lidar data interpretation is much easier than radar resulting in a much better vertical confidence. Therefore, it is desired to 1) fully exploit the capability of repeat-pass InSAR data in measuring the vegetation vertical structure, and 2) combine the complete spatial coverage of repeat-pass InSAR and precise vertical measurements of lidar so as to generate large-scale (potentially global-scale) forest structure and disturbance maps.

Multi-baseline, single-pass InSAR and/or Polarimetric InSAR (PolInSAR) correlation observations have been shown to be sensitive to vegetation vertical structure

and forest height through the use of a physical scattering model [81, 57], often termed as the Random Volume over Ground (RVoG) model that relates complex correlations to the vegetation structure and/or height. In repeat-pass SAR interferometry however, the correlation measurements are additionally effected by changes in the scene between passes. This causes a *temporal decorrelation* contribution to the InSAR cross-correlation [2, 76]. The degree of temporal decorrelation is primarily dependent on the changes in environmental conditions (e.g. moisture [40, 39], wind [5, 33], tree regrowth [4], freezing [77]) during the repeat period (referred to as *temporal baseline*). The longer the temporal baseline, the more likely the environmental conditions will have changed. In this work, we will use the term "temporal baseline" to characterize the possibility of weather changes.

Generally speaking, in repeat-pass InSAR applications, the RVoG model has also been successfully used to provide estimates of forest heights with airborne temporal baselines of 40 minutes at both L- and P-band [24]. For moderate temporal baselines (*i.e.* less than 15 days), modified versions of the RVoG model have been demonstrated to account for the effect of ground dielectric change and random motion of the volume scatterers [40, 56]. Askne et al. [5] and Lavalle et al. [33, 34] have introduced a coordinate-dependence of the vertical motion profile, which can be incorporated into the RVoG model characterizing the wind-induced temporal decorrelation.

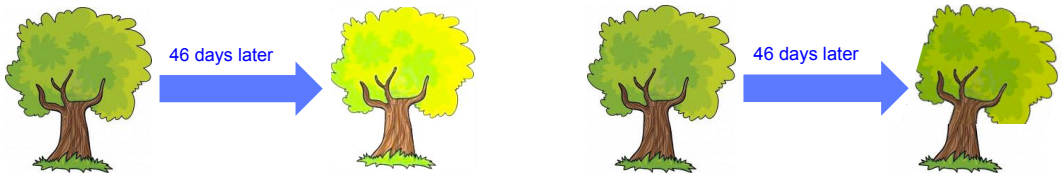


(**a**) Dielectric Fluctuation (**b**) Random Motion

Figure 1.4: The temporal decorrelation effects due to dielectric change and random motion of the volume scatterers within a repeat period of 46 days.

For spaceborne repeat-pass InSAR systems with large temporal baselines (on the order of months; at least 46 days for ALOS), the effects of temporal decorrelation (both dielectric change and random motion; Figure 1.4) often dominate the correlation observations even under the condition of small $\kappa_z$ (the interferometric vertical wavenumber) so that the observed correlation magnitudes are relatively low. Without a physical scattering model (*i.e.* a proper modification of the RVoG model), the interpretation and utility of the spaceborne repeat-pass InSAR correlation data, where large temporal baselines are common, is constrained.

In this work, we use the discrete random medium representation by considering the forest as a sparse random medium that is comprised with a collection of small discrete scatterers [80, 81]. The effect of multiple scattering is taken into account using the *Foldy-Lax* multiple scattering equations [82, 26, 16, 35, 36]. We make a note here, although this assumption might not be valid for large dominant scatterers like tree trunks, it is assumed as such in this work for the sake of simplicity. Moreover, as will be demonstrated by the simulated and ground validation results that, the InSAR scattering model derived from this simplified scenario is indeed capable of characterizing the variation of InSAR correlation measurements with respect to the medium characteristics of vegetation.

During the repeat period of the SAR platform between passes, the vegetation components (e.g. leaf, branch, trunk) are expected to move due to wind-induced displacement. At the same time, the scatterers' dielectric properties (and thus scattering properties) will fluctuate due to moisture-induced dielectric change. In order to investigate the temporal decorrelation effects due to dielectric fluctuation and random motion of the volume scatterers, both the scattering amplitude (as a function of the dielectric constant) and the spatial position of each scattering element are allowed to change during the repeat period of the satellite. By following [80] to derive the single-pass InSAR correlation model, a similar derivation can be performed for the

repeat-pass InSAR correlation model. This derived repeat-pass InSAR correlation model can be represented as a physical augmentation of the random motion model developed by Askne et al. [5] and Lavalle et al. [33, 34] through the incorporation of a dielectric fluctuation profile. Since the parameters in the dielectric fluctuation profile are physically defined, this formulation is useful in that it highlights the physical mechanism for the decorrelation due to dielectric fluctuations in a volume scattering target and enables a detailed examination of this phenomenon. Once constructed, the mathematical formulation of this scattering model is cast into a modified version of the RVoG model such that it can separately take into account dielectric fluctuations in the ground and volume components.

Using this modified RVoG model, a semi-empirical forest height inversion approach is then developed. In particular, by assuming (1) the temporal change parameters and forest backscatter profile/extinction coefficient follow some mean behavior across each interferogram; (2) the ground scattering contribution is minimal for cross-polarization; and (3) the interferometric vertical wavenumber is small, a simplified inversion approach is developed to link the observed cross-polarized InSAR correlation magnitude to forest height with the model parameters characterizing the temporal change effects (both dielectric change and random motion). These model parameters are thus determined by fitting the InSAR-inverted forest height with ground validation (such as lidar) height data. The temporal change parameters derived from this supervised regression are used as the basis for propagating the height estimates to available interferometric pairs (through the overlaps between adjacent pairs) for a much larger area, thus creating a large-scale mosaic map of forest height. Further, an automatic mosaicking algorithm is developed to efficiently perform the mosaicking task by constructing a matrix formulation of the nonlinear least squares fitting problem. Also, since repeat-pass InSAR data have a good sensitivity to forest disturbance (such as selective logging and/or forest degradation), the forest height inversion ap-

proach developed in this work is also shown to be capable of detecting such forest disturbance events.

## 1.3 Organization of this dissertation

This dissertation begins by the introduction (Chapter 1) of the scientific motivation, relevant previous swork and the significance of this work. In Chapter 2, adaptions of the well-known InSAR scattering model by [80, 81] are made so as to accommodate the following two scenarios envisioned in the abstract and Chapter 1: 1) repeat-pass InSAR observation of vegetation and 2) single-pass InSAR observation of snow and considering its dense medium characteristics, where the theoretical derivations are demonstrated based on the Foldy-Lax multiple scattering equations and the Distorted Born Approximation. In Chapter 3, the parameter retrieval approaches are investigated for inverting snow and vegetation characteristics, respectively. This is followed by Chapter 4 showing the simulated validation results of the InSAR scattering models along with the parameter retrieval approaches. A large amount of ground validation results are demonstrated in Chapter 5 for the retrieval of vegetation characteristics using spaceborne repeat-pass InSAR data. Since the theoretical electromagnetic modeling involves intensive mathematical derivations, which are not necessary to understand the major theme of this dissertation, all of the involved derivations will be demonstrated in Chapter 6. This dissertation will conclude with Chapter 7 along with four appendices. These appendices are used to provide qualitative and/or quantitative proofs for some of the key components of this work, but are not considered critical in their overall understanding.

# CHAPTER 2

# ELECTROMAGNETIC SCATTERING MODELS FOR INSAR CORRELATION MEASUREMENTS

In this chapter, the InSAR scattering models for random media are derived in a rigorous and physical manner. First, Section 2.1 introduces a discrete representation of random media, solves the coherent field and then derives the single-scatterer SAR backscattered field based on the Foldy-Lax multiple scattering equations and the Distorted Born Approximation, which establish the foundation of the electromagnetic scattering in a random volume of discrete scatterers. Next, the derived single-scatterer SAR backscattered field is applied to the single-pass InSAR observation of snow (Section 2.2) as well as the repeat-pass InSAR observation of vegetation (Section 2.3), which are the two original contributions of this dissertation. Although the derivation in Section 2.1 is partially adapted from the well-known model developed by Treuhaft *et al.* for the single-pass InSAR observation of vegetation [80, 81], a different set of notation and formulation have been accepted in this work so as to create convenient and consistent derivation, which also conforms with previous work [82, 26, 16, 35, 36]. Another original contribution in the derivation of Section 2.1 is to incorporate the pair distribution function for characterizing the pairwise interaction between particles, which is essentially important in a dense medium.

## 2.1 A discrete representation of random media

Considering a random medium that is comprised with a collection of discrete scatterers, the Foldy-Lax multiple scattering equations introduce a pair of equations that

express the total electric field at any point within the medium in terms of the effective field (or called exciting field) incident on each scatterer. In particular, the concept of configuration averaging (*i.e.* an averaging over both of the scatterer position and its scattering amplitude) is applied in order to solve the Foldy-Lax multiple scattering equations. The averaged total field within the random medium is known as the coherent field. Only the scattering of the coherent field by the individual discrete scatterers is considered in this work, which is equivalent to the Distorted Born Approximation. Therefore, the backscattered field due to each scatterer at each frequency can be obtained. Moreover, by utilizing the SAR point target response, one can thus derive the single-scatterer SAR backscattered field, which is the essential component that is utilized in Section 2.2 and Section 2.3 for further developing the snow and vegetation InSAR scattering models.

### 2.1.1 Foldy-Lax multiple scattering formulation

For the sake of simplicity, a half-space random medium scenario is first considered. In this section, the coherent wave propagation through this half-space medium is studied. This is equivalent to a refracted wave propagation with an effective propagation constant that is dependent on the medium characteristics. Then, in the following section, the backscattering of the coherent field due to a finite extent of discrete scatterers will be treated.

Given an incident wave $E_{inc}(\overline{R},\omega)$ impinging on the discrete random medium with $N$ independent scatterers, for each frequency $\omega$, the total electric field at any point $\overline{R}$ in the medium can be written as

$$E(\overline{R},\omega) \;=\; E_{inc}(\overline{R},\omega)+\sum_{j=1}^{N} E^{ex}(\overline{R_j},\omega)\frac{e^{jk|\overline{R}-\overline{R_j}|}}{|\overline{R}-\overline{R_j}|}f_j(\widehat{R_1R_j},\widehat{R_jR}) \qquad (2.1)$$

where $k$ is the free-space wavenumber at frequency $\omega$, $E(\overline{R},\omega)$ is the total electric field at an arbitrary point in the random medium, $E^{ex}(\overline{R_j},\omega)$ is the effective field

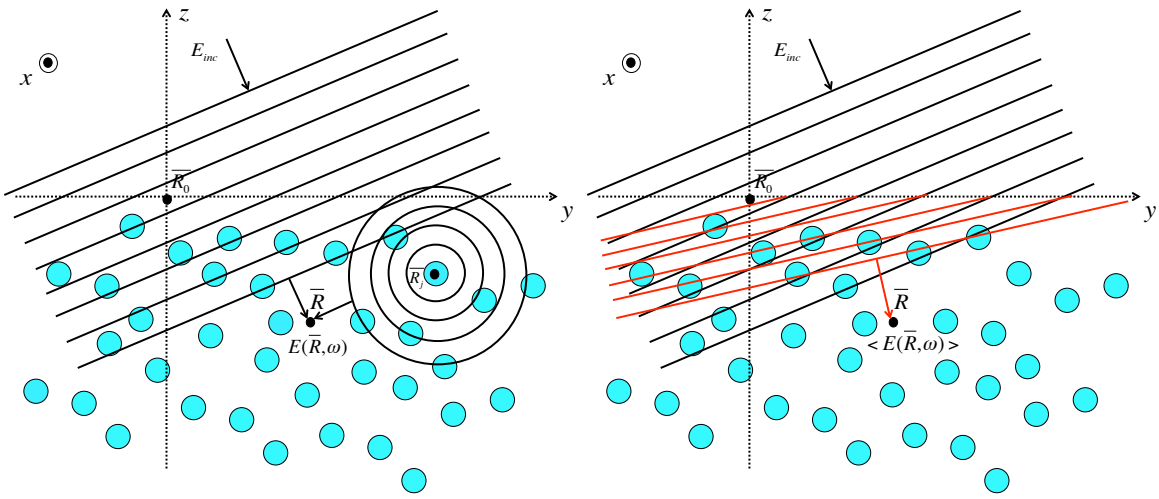


(**a**) (**b**)

Figure 2.1: Illustration of the multiple scattering effect in the random medium. The total field inside the random medium is shown (**a**) without configuration averaging and (**b**) with configuration averaging (colored in "red"; termed as the coherent field). The local Cartesian coordinate system $(x, y, z)$ has its origin referenced to the center of the resolution cell, $\overline{R_0}$, which is located on the "air-medium" interface ($x$-$y$ plane).

(or exciting field) that is applied to the $j^{th}$ scatterer, $f_j(\widehat{R_1R_j}, \widehat{R_jR})$ is the scattering amplitude of the $j^{th}$ scatterer with the incoming direction $\widehat{R_1R_j}$, a unit vector from the antenna position $\overline{R_1}$ to the scatterer position $\overline{R_j}$ (when the medium-to-air contrast is large, the propagation direction of the refracted wave should be considered instead), and the outgoing direction $\widehat{R_jR}$, a unit vector from the scatterer position $\overline{R_j}$ to $\overline{R}$.

Further, the effective field at scatterer $j$ can be attributed to the scattered waves from all of the other scatterers along with the transmitted wave $E_{inc}(\overline{R_j}, \omega)$, *i.e.*

$$E^{ex}(\overline{R_j}, \omega) \quad = \quad E_{inc}(\overline{R_j}, \omega) + \sum_{\substack{s=1 \\ s \neq j}}^{N} E^{ex}(\overline{R_s}, \omega) \frac{e^{jk|\overline{R_s} - \overline{R_j}|}}{|\overline{R_s} - \overline{R_j}|} f_s(\widehat{R_1R_s}, \widehat{R_sR_j}), \quad (2.2)$$

is a functional equation determining $E^{ex}(\overline{R_j}, \omega)$. Note (2.1) and (2.2) are called the point target Foldy-Lax multiple scattering equations [82, 26, 16, 35, 36], which serve as the basis for the following derivation. This configuration is illustrated in Figure 2.1a.

Note although we refer to the point target Foldy-Lax multiple scattering equations in this work, a similar derivation can be made by assuming the medium is comprised with spherical particles with the use of the *T-matrix* formulation [82]. However, the InSAR correlation model for this scenario of spherical particles can be shown to conform with the results derived in this work. It should be noted that we indeed consider a dense medium consisting of spherical particles while generating the simulation results in Section 4.1. For the sake of convenience and simplicity in the model derivation, however, we thus consider the point target Foldy-Lax multiple scattering equations, which is similar to [80, 81]. Another note is, even though some finite-shape (such as spherical) particles are considered here, they are still considered as electrically small scatterers. In other words, if the scatterers are electrically huge (on the order of several wavelengths), the electric field at the surface of individual scatterers will vary from point to point, such that the simple version of Foldy-Lax multiple scattering equations that are shown here as well as the following effective-medium assumption will probably be invalid.

### 2.1.2 Configuration-averaged effective field and coherent field

While solving the Foldy-Lax equations, (2.1) and (2.2), directly is computationally impossible when the number of scatterers is large, the concept of configuration averaging is introduced. Configuration averaging is averaging over each scatterer's position and scattering amplitude. As shown later, the Foldy-Lax equations can be solved in the sense of configuration averaging. Through taking the configuration average with respect to the $j^{th}$ scatterer, the Foldy-Lax multiple scattering equations are rewritten as [82, 26, 16, 35, 36]

$$\begin{aligned} \langle E(\overline{R},\omega)\rangle &= E_{inc}(\overline{R},\omega) + \sum_{j=1}^{N} \iint \langle E^{ex}(\overline{R_j},\omega)\rangle_j \frac{e^{jk|\overline{R}-\overline{R_j}|}}{|\overline{R}-\overline{R_j}|} f_j \\ &\quad P(\overline{R_j})P(f_j)d\overline{R_j}df_j \end{aligned} \tag{2.3}$$

and

$$\langle E^{ex}(\overline{R_j},\omega)\rangle_j = E_{inc}(\overline{R_j},\omega) + \sum_{\substack{s=1\\ s\neq j}}^{N} \iint \langle E^{ex}(\overline{R_s},\omega)\rangle_{sj} \frac{e^{jk|\overline{R_s}-\overline{R_j}|}}{|\overline{R_s}-\overline{R_j}|} f_s$$
$$P(\overline{R_s}|\overline{R_j}) P(f_s|f_j) d\overline{R_s} df_s, \tag{2.4}$$

where the scattering amplitudes are assumed independent of the scatterer positions and the unit-vector arguments in $f_j$ and $f_s$ are omitted here for conciseness of notation. Here, "$\langle\ \rangle_j$" is called the conditional configuration average given scatterer $j$ is fixed (*i.e.* the configuration averaging is taken over all of the other scatterers excluding scatterer $j$). Similarly, "$\langle\ \rangle_{sj}$" is the conditional configuration average by fixing both scatterer $s$ and scatterer $j$. $P(\overline{R_j})$, $P(f_j)$ are respectively the probability density function for the scatterer to have position $\overline{R_j}$ and scattering amplitude $f_j$, while $P(\overline{R_s}|\overline{R_j})$ and $P(f_s|f_j)$ are the conditional probability density functions for the configuration of scatterer $s$ given that of scatterer $j$.

Note the quantity $\langle E(\overline{R},\omega)\rangle$ is defined as the *coherent field* since the total electric field can be decomposed as $E(\overline{R},\omega) = \langle E(\overline{R},\omega)\rangle + \epsilon(\overline{R},\omega)$ with $\epsilon(\overline{R},\omega)$ denoting the *incoherent field*. In this work along with [80, 81], only the scattering of coherent fields is considered while ignoring the incoherent counterparts (or equivalently using the *Distorted Born Approximation* as detailed in Section 2.1.3). This is convenient since firstly the coherent field is expected to dominate; secondly, the coherent field can be calculated by using the *Foldy-Lax* multiple scattering equations with the result being a refracted field propagating inside a random medium with an effective permittivity. In contrast, the computation of the incoherent field is more difficult, and implies a concise analytical expression of the InSAR correlation (as will be presented later in this work) might be prohibited. However, if sufficient accuracy is desired, the incoherent terms must be incorporated to the models presented in the current work.

From (2.4), it can be seen that the conditional average with one scatterer fixed, depends on the conditional average where two scatterers are fixed. It can be shown that after taking the conditional average of (2.2) with any number of scatterers fixed, that the right-hand side of the resulting equation can always be written as a conditional average with one more scatterer fixed than the left-hand side. This successive set of conditional averages creates a set of hierarchical equations that becomes as large as the number of scatterers in the medium. Instead of solving for the set of equations which is computationally impossible when the number of scatterers $N$ is large, the Quasi-Crystalline Approximation (QCA) [36, 82] is used to truncate the series so that a reasonable solution of $\langle E^{ex}(\overline{R_j}, \omega)\rangle_j$ can be obtained.

Using the Quasi-Crystalline Approximation, an approximation is made such that

$$\langle E^{ex}(\overline{R_s}, \omega)\rangle_{sj} \approx \langle E^{ex}(\overline{R_s}, \omega)\rangle_s, \tag{2.5}$$

which has the physical interpretation that the electric field at particle $s$, when the location and scattering amplitudes of particles $s$ and $j$ are known, is equivalent to the electric field at particle $s$ when only the location and scattering amplitude of particle $s$ are known. This approximation is suitable for dense media, with a dense medium defined here as one where it is important to take into account multi-particle scattering interactions. In the sparse case, QCA reduces to the well-known *Foldy's* approximation [82], where

$$\langle E^{ex}(\overline{R_s}, \omega)\rangle_s \approx \langle E(\overline{R_s}, \omega)\rangle, \tag{2.6}$$

which is simply the coherent field.

To implement the Quasi-Crystalline Approximation, we define the average scattering amplitude, $\widetilde{f_s}$ as

$$\int f_s P(f_s|f_j) df_s = \widetilde{f}_s \tag{2.7}$$

and the pair distribution function, $g(r)$, of one scatterer's position given the position of another, as

$$P(\overline{R_s}|\overline{R_j}) = \frac{g(|\overline{R_s} - \overline{R_j}|)}{V}, \tag{2.8}$$

where $V$ is the scattering volume within which $g(r)$ is considered stationary such that only the relative distance between two scatterers, $r = |\overline{R_s} - \overline{R_j}|$, matters in the formulation. We can then rewrite (2.4) as

$$\langle E^{ex}(\overline{R_j}, \omega)\rangle_j = E_{inc}(\overline{R_j}, \omega) + \tau_0 \int \langle E^{ex}(\overline{R_s}, \omega)\rangle_s g(|\overline{R_s} - \overline{R_j}|) \frac{e^{jk|\overline{R_s} - \overline{R_j}|}}{|\overline{R_s} - \overline{R_j}|} \widetilde{f}_s d\overline{R_s}, \tag{2.9}$$

where $\tau_0 = \frac{N}{V}$ is the particle number density (assumed constant throughout the medium).

In the above, the pair distribution function, $g(r)$ can take on a number of functional forms. One of these is the *Percus-Yevick* pair distribution function (illustrated in Figure 2.2; [59]), and is appropriate for liquid media where particles in close proximity to one another cause a radially symmetric ripple in the pair distribution function. These ripples diminish with distance, and their magnitude and effect are dependent on the scatterer size, $l$, and the volume fraction, $f_v$, of scatterers within the volume. Here, $f_v$ is defined as the ratio of the volume occupied by the scatterers to the total volume of the dense medium, where $0 \leq f_v \leq 1$. For conciseness, the Percus-Yevick pair distribution function is written as

$$g(r) = g(r; l, f_v). \tag{2.10}$$

where the scatterer size, $l$, and volume fraction, $f_v$, are omitted for conciseness.

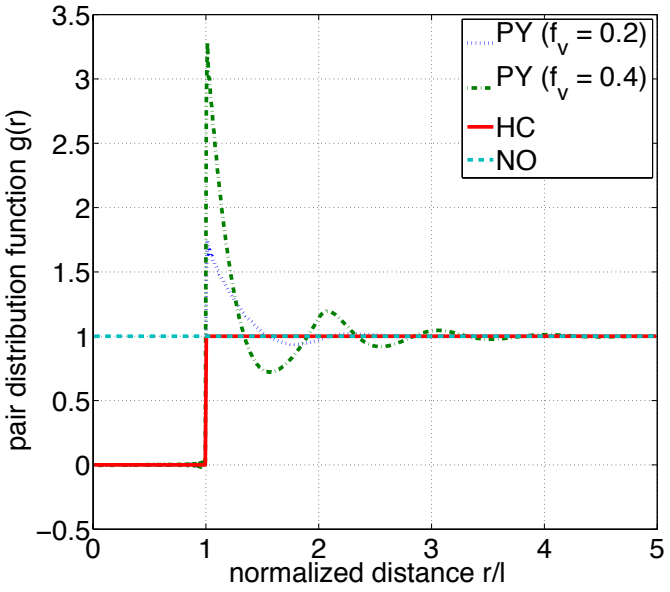


Figure 2.2: Different forms of the pair distribution function: Percus-Yevick function with volume fraction of 0.2 (denoted as "PY ($f_v = 0.2$)"), Percus-Yevick function with volume fraction of 0.4 (denoted as "PY ($f_v = 0.4$)"), Hole-Correction function (denoted as "HC"), and the simplified scenario where the pair distribution function is ignored (denoted as "NO"). The horizontal axis represents the normalized distance $r/l$, where $l$ is the grain size.

Although the Percus-Yevick function is obtained for a liquid-like medium, and more complicated functional forms are expected for dry snow, the Percus-Yevick function is useful to demonstrate the variability of InSAR correlation measurements with respect to the dense-medium parameters (such as grain size and volume fraction). It can be seen from Figure 2.2 that the Percus-Yevick function has oscillation near $r/l = 1$ with the degree of oscillation dependent on the volume fraction of the dense medium. For a sparse medium case with small volume fraction, it becomes indistinguishable with the Hole-Correction formula. The Hole-Correction formula [82] is appropriate for an ideal gas where the physical dimensions of one particle exclude all particles from within its boundary.

Note that in the simplest case where the particle is considered to be infinitely small or a sparse concentration of discrete scatterers is considered (e.g. gas [82],

vegetation [80, 81]), the pair distribution function becomes $g(r) = 1$ and (2.9) reduces to Foldy's approximation [82] as expected. In this extreme case, the InSAR scattering model reduces to the one presented in [80]. For dense media such as snow however, the pair distribution function will have an effect on the InSAR correlation and for this reason has been included both in the theoretical models and the simulated results (Section 4.1).

The truncated conditional average in (2.9) was derived from the Foldy-Lax equation, (2.2), and the Quasi-Crystalline Approximation, (2.5). The solution of (2.9) provides an estimation for the effective propagation constant, $K$, in the scattering medium. For a dense random medium such as snow, the constant should take into account the dielectric and scattering effects within the medium. This is accomplished by enforcing energy conservation for fields within the medium and is solved numerically via the generalized Lorentz-Lorenz law, as discussed in [82]. Once determined, $K$ is used to model both the effects of refraction and signal extinction in the volume-scattering medium.

In order to implement the full scattering model by taking into account the geometry of the observing platform, a local Cartesian coordinate system $(x, y, z)$ is constructed with an origin referenced to the center of the resolution cell, $\overline{R_0}$, located at the air-medium interface (denoted by the $x$-$y$ plane) as illustrated in Figure 2.1.

Following [82] and assuming that the incident field on the half-space dense random medium is a plane wave $e^{jk(y\sin\theta_i - z\cos\theta_i)}$ with incidence angle, $\theta_i$, and free-space wavenumber, $k$, (2.9) can thus be solved with the discrete random medium characterized, on average, as a medium with effective propagation constant $K = K_R + jK_I$. Here, $K$ is determined via (2.9) and depends on the medium's bulk characteristics of number density, pair distribution function and mean-scattering amplitude. These bulk characteristics themselves depend on the physical characteristics of the medium's constituents, parameters such as the scatterer size, $l$, and volume fraction, $f_v$. In

short, the medium's dielectric properties are dependent on the physical properties of the scatterers, and the effective permittivity is written as a function of these characteristics, as in

$$K = K(l, f_v). \tag{2.11}$$

The relationship between the physical characteristics of the medium and the complex permittivity in (2.11) is important in that it is through the estimation of the effective permittivity that these characteristics can be inferred, and that the snow-pack parameters of grain size, density and snow water equivalent thus determined.

By utilizing a series of mathematical manipulation (see Section 6.1), we have the configuration-averaged effective field given by

$$\langle E^{ex}(\overline{R_j}, \omega)\rangle_j = a^{ex} \frac{e^{jk|\overline{R_1}-\overline{R_0}|}}{|\overline{R_1}-\overline{R_0}|} e^{K_I z_j/\cos\theta_t} e^{jk(y_j \sin\theta_i - n z_j \cos\theta_t)}, \tag{2.12}$$

where $a^{ex}$ is the amplitude factor introduced by the air-medium interface, $\overline{R_1}$ is the antenna position, $\overline{R_0}$ represents the center of the resolution cell, $n$ is the index of refraction, and $\theta_t$ is the refraction angle, which satisfies Snell's law

$$n = \frac{K_R}{k} = \frac{\sin\theta_i}{\sin\theta_t}. \tag{2.13}$$

Substituting (2.12) into (2.3) with a little more mathematical derivation (see Section 6.2), the coherent field at an arbitrary point $\overline{R}$ in the random medium is thus given by

$$\langle E(\overline{R}, \omega)\rangle = a \frac{e^{jk|\overline{R_1}-\overline{R_0}|}}{|\overline{R_1}-\overline{R_0}|} e^{K_I z/\cos\theta_t} e^{jk(y \sin\theta_i - n z \cos\theta_t)}, \tag{2.14}$$

where $a$ is the transmission coefficient of the air-medium interface. This coherent field is also illustrated in Figure 2.1b.

### 2.1.3 Backscattering of the coherent field from a single scatterer: *Distorted Born Approximation*

Since we have obtained the coherent field inside the discrete random medium, let us now consider the backscattered field from a finite extent of volume scatterers. In this work, only the backscattering of the coherent field is considered, which is equivalent to the *Distorted Born Approximation* [82], with the mathematical proof shown in Section 6.3. Consider a finite extent of discrete random medium that is illustrated in Figure 2.3. From the Distorted Born Approximation, the total electric field incident on scatterer $j$ is assumed equal to the coherent field at $\overline{R_j}$, *i.e.*, $\langle E(\overline{R_j},\omega)\rangle$, so the backscattered field at $\overline{R_j}$ is $\langle E(\overline{R_j},\omega)\rangle$ multiplied by $f_j$. Due to reciprocity, this backscattered field will exactly reverse the same path through the medium back to the antenna position $\overline{R_1}$ just as the coherent field propagates through the intervening medium to reach the scatterer. Therefore, the backscattered field at $\overline{R_1}$ due to scatterer $j$ is given by

$$E(\overline{R_1},\omega;j) = \langle E(\overline{R_j},\omega)\rangle \cdot f_j \cdot \langle E(\overline{R_j},\omega)\rangle, \tag{2.15}$$

which is only a function of scatterer $j$'s configuration and thus does not vary with any other scatterer's configuration. By fixing scatterer $j$'s configuration (*i.e.*, both $\overline{R_j}$ and $f_j$ are given), $E(\overline{R_1},\omega;j)$ can be considered a constant, and the configuration-averaged backscattered field is thus written as (by holding scatterer $j$ fixed)

$$\begin{aligned}\langle E(\overline{R_1},\omega;j)\rangle_j &= E(\overline{R_1},\omega;j) \\ &= \langle E(\overline{R_j},\omega)\rangle \cdot f_j \cdot \langle E(\overline{R_j},\omega)\rangle,\end{aligned} \tag{2.16}$$

Now that the coherent field that is incident on scatterer $j$ is known, (2.14) is substituted into (2.16), resulting in the backscattered field from the contribution of scatterer $j$ only, *i.e.*

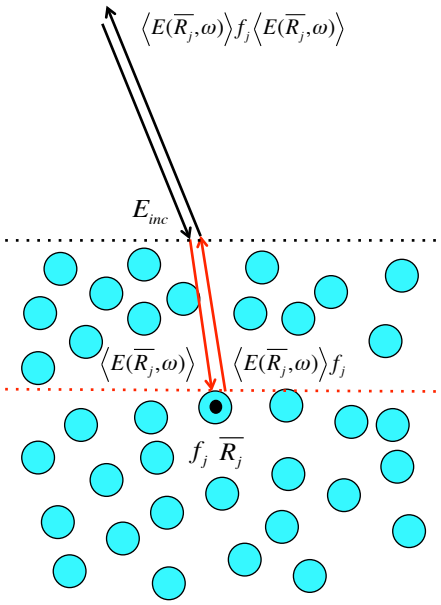


Figure 2.3: Illustration of the backscattering of the coherent field through using the Distorted Born Approximation (DBA). The incident field $E_{inc}$ penetrates through the slab of discrete scatterers (between the "black" and "red" dashed lines) and hits the scatterer with $E(\overline{R_j},\omega)$, where DBA approximates $E(\overline{R_j},\omega)$ with the coherent component $\langle E(\overline{R_j},\omega)\rangle$. The coherent field incident on the scatterer is then backscattered with the scattering amplitude $f_j$. By reversing the same path through the intervening medium back to the radar receiver, the backscattered field due to that particular scatterer is thus $\langle E(\overline{R_j},\omega)\rangle \cdot f_j \cdot \langle E(\overline{R_j},\omega)\rangle$.

$$\begin{aligned}\langle E(\overline{R_1},\omega;j)\rangle_j =& a^2 f_j \frac{e^{j2k|\overline{R_1}-\overline{R_0}|}}{|\overline{R_1}-\overline{R_0}|^2} e^{2K_I z_j/\cos\theta_t} e^{j2k(y_j\sin\theta_i - n z_j\cos\theta_t)} \\ =& A_1 f_j e^{2K_I z_j/\cos\theta_t} e^{j2kr_{1j}} \end{aligned} \tag{2.17}$$

where

$$A_1 = \frac{a^2}{|\overline{R_1}-\overline{R_0}|^2}, \tag{2.18}$$

and

$$r_{1j} \;=\; |\overline{R_1}-\overline{R_0}| + y_j\sin\theta_i - n\cos\theta_t z_j. \tag{2.19}$$

Although the field transmission coefficient of the air-to-medium interface is a little different from that of the medium-to-air interface, we assume they are the same in this work (denoted by a single variable $a$) only for simplicity and conciseness of notation. As shown later, this treatment does not affect the following model derivations and analysis since the constant factor(s) will be cancelled out when calculating the normalized InSAR correlation coefficient defined as in (1.1).

So far, we have obtained the backscattered field due to a single scatterer at a particular frequency. Next, this single-tone expression will be summed up in the frequency domain to derive the single-scatterer SAR backscattered field.

Here, a useful property of the backscattered coherent field can be obtained as below through using the Distorted Born Approximation. As shown in (2.15), once scatterer $j$'s configuration is fixed, the backscattered coherent field is considered a constant. Therefore, a similar interpretation can be made for two independent scatterers, e.g., scatterer $j$ and scatterer $k$, that are separately observed by two antennas at $\overline{R_1}$ and $\overline{R_2}$, such that the following relationship can be obtained,

$$\begin{aligned}\langle E(\overline{R_1},\omega;j)E^*(\overline{R_2},\omega;k)\rangle_{jk} &= \left\langle \langle E(\overline{R_1},\omega;j)\rangle_j \langle E^*(\overline{R_2},\omega;k)\rangle_k \right\rangle_{jk} \\ &= \langle E(\overline{R_1},\omega;j)\rangle_j \langle E^*(\overline{R_2},\omega;k)\rangle_k. \end{aligned} \tag{2.20}$$

### 2.1.4 Single-scatterer SAR backscattered field

Once the backscattered coherent field due to scatterer $j$ is determined from (2.17) for each frequency $\omega$, it is possible to determine the average reflected field from this scatterer through SAR processing. Following [80, 11], the conditional average of the SAR backscattered field from scatterer $j$ is written as

$$\langle E(\overline{R_1};j)\rangle_j = A_1 f_j e^{2K_I z_j/\cos\theta_{t_1}} e^{j2k_0 r_{1j}} W_r(r_{10}-r_{1j}) W_a(a_0-a_j), \tag{2.21}$$

where

$$
\begin{aligned}
a_j &= a_0 + x_j, \\
r_{10} &= |\overline{R_1} - \overline{R_0}|, \\
r_{1j} &= |\overline{R_1} - \overline{R_0}| + y_j \sin\theta_{i_1} - n\cos\theta_{t_1} z_j.
\end{aligned} \tag{2.22}
$$

In the above, $r_{1j}$ and $a_j$ are the slant range and azimuth coordinates of scatterer $j$ as seen from an antenna at $\overline{R_1}$, and $r_{10}$ and $a_0$ are the coordinates for the center of the resolution cell at $\overline{R_0}$. Further, the weighting functions of $W_r$ and $W_a$ refer to the slant range and azimuth resolution functions, both of which are band-limited and thus have a "sinc-like" functional form. In (2.21), $k_0$ is the free-space wavenumber for frequency $\omega_0$, where $\omega_0$ is the center frequency of the radar, and $\theta_{i_1}$ and $\theta_{t_1}$ are the incidence and refraction angles as seen from $\overline{R_1}$.

Note both $r_{10}$ and $r_{1j}$ represent the equivalent path lengths as if the waves only propagated in free space. This means: in the air, the equivalent path length is equal to the physical path length, while inside the random medium, it refers to the physical path length multiplied by the refractive index. This definition of the equivalent path length is the well known *Optical Path Length* and is used in (2.21) because whether or not the backscattered signal travels through the air or the medium, the SAR processing cannot distinguish between the two and will always focus the collected observations according to, $k_0$, the free-space wavenumber at the center frequency of the SAR receiver. Further, since each scatterer is focused to its zero-doppler plane, $r_{10}$ and $r_{1j}$ are only calculated in the cross-track direction (*i.e.* with $y$- and $z$- dependence only).

After substituting the above relations into (2.21) and rearranging terms in Cartesian coordinates, we obtain

$$
\begin{aligned}
\langle E(\overline{R_1}; j)\rangle_j = & A_1 f_j e^{2K_I z_j/\cos\theta_{t_1}} W_a(x_j) W_r\left(y_j \sin\theta_{i_1} - n\cos\theta_{t_1} z_j\right) \\
& e^{jk_0 2\left[|\overline{R_1} - \overline{R_0}| + y_j \sin\theta_{i_1} - n\cos\theta_{t_1} z_j\right]},
\end{aligned} \tag{2.23}
$$

To determine the interferometric correlation, we introduce a second antenna at $\overline{R_2}$, and assuming the *ping-pong* observing mode, where both antennas are allowed to alternately transmit (equivalent to repeat-pass interferometry), the single-scatterer field from scatterer $k$ observed by the second antenna is given as

$$\begin{aligned}\langle E(\overline{R_2};k)\rangle_k =& A_2 f_k e^{2K_I z_k/\cos\theta_{t_2}} W_a(x_k) W_r\left(y_k \sin\theta_{i_2} - n\cos\theta_{t_2} z_k\right) \\ & e^{jk_0 2\left[|\overline{R_2}-\overline{R_0}|+y_k\sin\theta_{i_2}-n\cos\theta_{t_2}z_k\right]},\end{aligned} \tag{2.24}$$

where $A_2 = \frac{a^2}{|\overline{R_2}-\overline{R_0}|^2}$, and $\theta_{i_2}$, $\theta_{t_2}$ are the incidence and refraction angles as seen from the second antenna.

Similar to the property (2.20) derived from the Distorted Born Approximation, and by using the relationship between (2.17) and (2.21), another useful property can be achieved for the single-scatterer SAR backscattered field, *i.e.*,

$$\begin{aligned}\langle E(\overline{R_1};j)E^*(\overline{R_2};k)\rangle_{jk} &= \left\langle \langle E(\overline{R_1};j)\rangle_j \langle E^*(\overline{R_2};k)\rangle_k \right\rangle_{jk} \\ &= \langle E(\overline{R_1};j)\rangle_j \langle E^*(\overline{R_2};k)\rangle_k,\end{aligned} \tag{2.25}$$

which will be used in the following sections for deriving the InSAR correlation models.

## 2.2 Single-pass InSAR scattering model for snow

In Section 2.1, the single-scatterer SAR backscattered field was derived. Using this expression for a pair of antennas with the random medium characteristics being the same, the single-pass InSAR correlation is determined from the cross-product between two single-scatterer SAR backscattered fields. While the InSAR correlation coefficient after normalization is an important InSAR metric, it can be further decomposed so that the volume correlation component can be obtained for the future use of retrieving snow characteristics. Unlike the case where single-pass InSAR observation

of vegetation was studied and the effect of pair distribution function was ignored [80, 81], the Percus-Yevick function as mentioned in Section 2.1.2 is exploited for a dense medium like snow so that the effective propagation constant of the dense medium can be calculated more precisely.

### 2.2.1 Model formulation

For a dense discrete random medium with $N$ independent scatterers in a resolution cell, the total electric field that is received by the SAR antenna at $\overline{R_1}$ is a superposition of the single-scatterer backscattered electric fields, as in

$$E(\overline{R_1}) = \sum_{j=1}^{N} E(\overline{R_1}; j), \tag{2.26}$$

where $E(\overline{R_1}; j)$ is the SAR received electric field due to a single scatterer, $j$. It has been shown in (2.23) that the single scatterer field, $E(\overline{R_1}; j)$, depends on its backscattering amplitude, $f_j$, and its position $\overline{R_j}$.

Since we are mostly interested in the InSAR cross-correlation, using (2.26) for a pair of antennas at the two ends of the baseline, we have

$$\begin{aligned}
&\langle E(\overline{R_1})E^*(\overline{R_2})\rangle \\
&\quad = \sum_{j=1}^{N}\sum_{k=1}^{N}\langle E(\overline{R_1}; j)E^*(\overline{R_2}; k)\rangle \\
&\quad = \sum_{j\neq k}\iiiint \langle E(\overline{R_1}; j)E^*(\overline{R_2}; k)\rangle_{jk} P(\overline{R_j}, \overline{R_k}, f_j, f_k) d\overline{R_j} df_j d\overline{R_k} df_k \\
&\qquad + \sum_{j=k}\iint \langle E(\overline{R_1}; j)E^*(\overline{R_2}; j)\rangle_{j} P(\overline{R_j}, f_j) d\overline{R_j} df_j \\
&\quad = \sum_{j\neq k}\iiiint \langle E(\overline{R_1}; j)E^*(\overline{R_2}; k)\rangle_{jk} P(\overline{R_j}, \overline{R_k}) P(f_j, f_k|\overline{R_j}, \overline{R_k}) d\overline{R_j} df_j d\overline{R_k} df_k \\
&\qquad + \sum_{j=k}\iint \langle E(\overline{R_1}; j)E^*(\overline{R_2}; j)\rangle_{j} P(\overline{R_j}) P(f_j|\overline{R_j}) d\overline{R_j} df_j,
\end{aligned} \tag{2.27}$$

where $P(\overline{R_j}, \overline{R_k}, f_j, f_k)$ and $P(\overline{R_j}, f_j)$ are the joint probability density function for the scatterers' configuration, $P(\overline{R_j}, \overline{R_k})$ and $P(\overline{R_j})$ are the probability density function for the scatterers' position, and $P(f_j, f_k|\overline{R_j}, \overline{R_k})$ and $P(f_j|\overline{R_j})$ are the conditional probability density function for the scattering amplitude given the scatterers' position.

Substituting (2.25) into (2.27) gives

$$\begin{aligned}
&\langle E(\overline{R_1})E^*(\overline{R_2})\rangle \\
&\quad = \sum_{j\neq k} \iiiint \langle E(\overline{R_1}; j)\rangle_j \langle E^*(\overline{R_2}; k)\rangle_k P(\overline{R_j}, \overline{R_k}) P(f_j, f_k|\overline{R_j}, \overline{R_k}) \\
&\qquad d\overline{R_j} df_j d\overline{R_k} df_k + \sum_{j=k} \iint \langle E(\overline{R_1}; j)\rangle_j \langle E^*(\overline{R_2}; j)\rangle_j P(\overline{R_j}) P(f_j|\overline{R_j}) d\overline{R_j} df_j,
\end{aligned} \tag{2.28}$$

It is apparent that in order to solve for the above cross-correlation, one has to know the configuration average of the single-scatterer SAR backscattered field, *i.e.* $\langle E(\overline{R_1}; j)\rangle_j$ and $\langle E(\overline{R_2}; k)\rangle_k$, which have already been shown as (2.23) and (2.24) in Section 2.1.4.

### 2.2.2 Single-pass InSAR correlation

Before substituting (2.23) and (2.24) into (2.28) to solve for the single-pass InSAR correlation, (2.28) can be simplified by eliminating the terms with $j \neq k$ [80]. This is because the phase in (2.23) depends on the electrical path from $\overline{R_j}$ to $\overline{R_1}$, while the phase in (2.24) relies on the electrical path from $\overline{R_k}$ to $\overline{R_2}$. Since it is assumed that individual discrete scatterers are independent of each other, the phase difference of (2.23) and (2.24) will follow a uniform distribution and the double integral with respect to the spatial coordinates in (2.28) will vanish for the case $j \neq k$. Similarly, the double integral with respect to the scattering amplitude in (2.28) will also disappear for $j \neq k$. Therefore, only the configuration integrals with $j = k$ remain, and (2.28) can be rewritten as

$$\langle E(\overline{R_1})E^*(\overline{R_2})\rangle = \sum_{j=1}^{N} \iint \langle E(\overline{R_1};j)\rangle_j \langle E^*(\overline{R_2};j)\rangle_j P(\overline{R_j})P(f_j|\overline{R_j})d\overline{R_j}df_j$$
$$= \iint \tau_0 \langle E(\overline{R_1};j)\rangle_j \langle E^*(\overline{R_2};j)\rangle_j P(f_j|\overline{R_j})d\overline{R_j}df_j, \tag{2.29}$$

where $\tau_0 = \frac{N}{V}$ is the average number density defined in (2.9). Through substituting (2.23) and (2.24) and separating the $y_j$- and $z_j$-dependent terms as detailed in Section 6.4, the interferometric correlation is

$$\langle E(\overline{R_1})E^*(\overline{R_2})\rangle = A_1 A_2 e^{jk_0 2\left(|\overline{R_1}-\overline{R_0}|-|\overline{R_2}-\overline{R_0}|\right)} \cdot \int |W_a(x_j)|^2 dx_j \cdot$$
$$\int |W_r\left(y_j \sin\theta_i\right)|^2 e^{j\kappa_y y_j} dy_j \cdot \int \tau_0 \sigma(z_j) e^{\left(\frac{2k_e}{\cos\theta_t}+j\kappa_z\right)z_j} dz_j, \tag{2.30}$$

where $\theta_i = \frac{\theta_{i_1}+\theta_{i_2}}{2}$, $\theta_t = \frac{\theta_{t_1}+\theta_{t_2}}{2}$. Further,

$$\sigma(z_j) = \int |f_j|^2 P(f_j|z_j) df_j, \tag{2.31}$$

is the vertical profile of the averaged backscatter intensity that here is considered constant in the $z$-direction such that $\sigma(z_j) = \sigma_0$, and

$$k_e = 2K_I \tag{2.32}$$

is the extinction coefficient that is dependent on the imaginary component of the effective permittivity. The interferometric vertical wavenumber, $\kappa_z$ in (2.30) relates the phase of the interferometric correlation for a dense medium to the configurational geometry of the interferometer, and can be written as [89]

$$\kappa_z = 2k_0(\sin\theta_{i_1} - \sin\theta_{i_2})\frac{n\cos\theta_t}{\sin\theta_i} + 2k_0(n\cos\theta_{t_2} - n\cos\theta_{t_1}) \tag{2.33}$$

and

$$\kappa_y = 2k_0(\sin\theta_{i_1} - \sin\theta_{i_2}) \tag{2.34}$$

is the interferometric ground-range wavenumber from [96].

Using Snell's law, (2.13), and trigonometric identities, it can be shown that (see Section 6.5)

$$\kappa_z = \tilde{\kappa_z} \frac{n \cos\theta_i}{\cos\theta_t} \tag{2.35}$$

where

$$\tilde{\kappa_z} = \frac{4\pi B_\perp}{\lambda R \sin\theta_i} \tag{2.36}$$

is the conventional form of the interferometric wavenumber given in [64, 49]. In (2.36), $B_\perp$ is the perpendicular baseline, $\lambda$ is the wavelength, $R$ is the slant range from the radar to the center of the resolution cell. Further, following this same methodology, it can be shown that the interferometric ground-range wavenumber can be written as

$$\kappa_y = \frac{4\pi B_\perp}{\lambda R} \cos\theta_i. \tag{2.37}$$

In the above, when modeling sparse concentrations of volume scatterers (e.g. vegetation), the effect of refraction is not strong enough to bias $\kappa_z$ from $\tilde{\kappa_z}$ since $n \approx 1$ and $\theta_t \approx \theta_i$ [23, 80]. However, for dense media like snow, this effect is significant and the use of (2.35) is warranted.

After dropping the subscript $j$ for conciseness, and normalization of the correlation by the geometric mean of the reflected power, the complex InSAR correlation coefficient conforms to the expressionns given by [80, 96, 89] where

$$\begin{aligned} \gamma &= \frac{\langle E(\overline{R_1}) E^*(\overline{R_2}) \rangle}{\sqrt{\langle |E(\overline{R_1})|^2 \rangle \langle |E(\overline{R_2})|^2 \rangle}} \\ &= e^{jk_0 2\left(|\overline{R_1} - \overline{R_0}| - |\overline{R_2} - \overline{R_0}|\right)} \frac{\int |W_r(y \sin\theta_i)|^2 e^{j\kappa_y y} dy}{\int |W_r(y \sin\theta_i)|^2 dy} \frac{\int \tau_0 \sigma_0 e^{\left(\frac{2k_e}{\cos\theta_t} + j\kappa_z\right) z} dz}{\int \tau_0 \sigma_0 e^{\frac{2k_e}{\cos\theta_t} z} dz}. \end{aligned} \tag{2.38}$$

The physical interpretation of this equation is that first term is the interferometric phase at the center of the resolution cell, the second describes the baseline decorre-

lation (that can be calibrated by common-band filtering [19]), and the last term is the desired volumetric correlation that can be used for retrieving the vertical characteristics of the medium. The thermal noise decorrelation, which would show up as additional terms to the received electric fields at $\overline{R_1}$ and $\overline{R_2}$ is not included in (2.38), and can be corrected separately, as in [96].

These results are derived for the ping-pong mode of SAR interferometry. In the case where a single antenna is used for transmit and two antennas are used for receive (often termed the *standard* mode of InSAR), similar proofs apply. These results are given in Section 6.6.

Also, note that in (2.38), both the number density and the backscatter intensity are considered constant in the vertical direction. These constants are not removed from (2.38) however because this formulation enables a convenient generalization of the InSAR correlation model should those variables depend on $z$. For example, if the dense medium is layered, the effective propagation constant $K$ (and thus $k_e$ and $\kappa_z$) will also be $z$-dependent, and the estimation of the layer parameters would require an observing configuration similar to multibaseline interferometry (e.g. [80]) which is beyond the scope of this work.

### 2.2.3 Simplified dense-medium InSAR correlation model

#### 2.2.3.1 Connection of the InSAR volumetric correlation to the dense medium parameters

From (2.38), the $y$-integration can be computed by using known forms of $W_r$ or offsetting the signal center-frequency during the processing step [19], and hence the effects of baseline decorrelation removed. The remaining correlation signal is the InSAR volumetric correlation (denoted as $\gamma_v$) and is written as

$$\begin{aligned}\gamma_v &= e^{j\phi_0}\frac{\int \tau_0\sigma_0 e^{(\frac{2k_e}{\cos\theta_t}+j\kappa_z)z}dz}{\int \tau_0\sigma_0 e^{\frac{2k_e}{\cos\theta_t}z}dz} \\ &= e^{j\phi_0}\frac{\int_{-d}^{0} \tau_0\sigma_0 e^{(\frac{2k_e}{\cos\theta_t}+j\kappa_z)z}dz}{\int_{-d}^{0} \tau_0\sigma_0 e^{\frac{2k_e}{\cos\theta_t}z}dz},\end{aligned} \tag{2.39}$$

where the volume layer depth, $d$, is explicitly specified, $\phi_0 = 2k_0\left(|\overline{R_1} - \overline{R_0}| - |\overline{R_2} - \overline{R_0}|\right)$ is the interferometric phase at the center of the resolution cell $\overline{R_0}$. Substitutions are made to connect the extinction coefficient, $k_e$, to the imaginary part of the effective permittivity, $K_I$,

$$\frac{2k_e}{\cos\theta_t} = \frac{4K_I}{\cos\theta_t} = \frac{4K_I}{\sqrt{1-\frac{k_0^2\sin^2\theta_i}{K_R^2}}}, \tag{2.40}$$

as well as to connect the interferometric vertical wavenumber for a dense medium, $\kappa_z$, to the real part of the effective permittivity, $K_R$, as in

$$\kappa_z = \tilde{\kappa_z}\frac{n\cos\theta_i}{\cos\theta_t} = \tilde{\kappa_z}\frac{\frac{K_R}{k_0}\cos\theta_i}{\sqrt{1-\frac{k_0^2\sin^2\theta_i}{K_R^2}}}. \tag{2.41}$$

From (2.40) and (2.41), it can be seen that the unknown parameters have been translated into the real and imaginary parts (*i.e.* $K_R$ and $K_I$) of the dense-medium effective propagation constant along with the InSAR instrumental parameters (e.g. $\theta_i$ and $\tilde{\kappa_z}$). Since the instrumental parameters are already known, and also the effective propagation constant $K$ relates to the medium characteristics (e.g. scatterer size $l$ and volume fraction $f_v$) as in (2.11), a relationship can thus be established between the InSAR volumetric correlation measurements and the desired dense medium characteristics via the effective propagation constant $K$. A flowchart illustration that connects the dense-medium parameters (grain size, volume fraction, layer depth) to the InSAR volumetric correlation is shown in Figure 2.4.

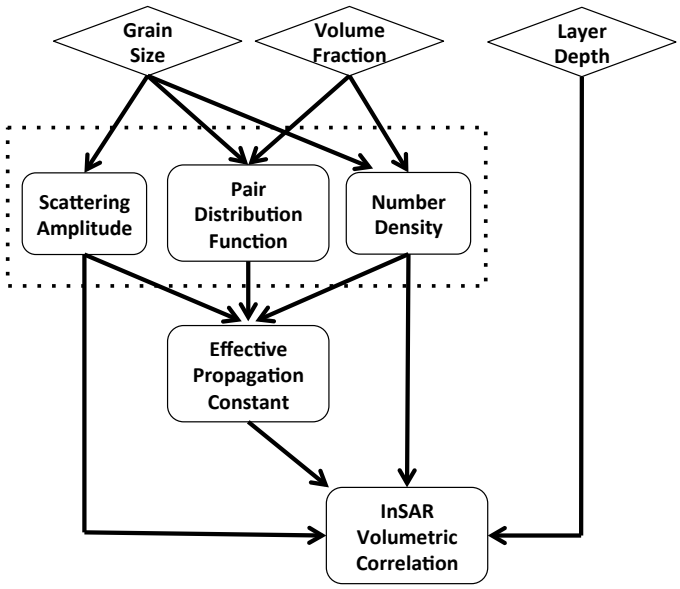


Figure 2.4: Flow chart illustration that connects the dense-medium parameters (grain size, volume fraction, layer depth) to the InSAR volumetric correlation. The dashed rectangular window indicates the implicit connection of grain size and volume fraction to the effective propagation constant as modeled by (2.11). The sets of arrows following the dashed window indicate that the inputs and outputs are related through solving (2.9) and (2.39), respectively.

Compared to previous work on snow InSAR models [89, 49], the InSAR volumetric correlation model as expressed in (2.39) explicitly have both the extinction coefficient and the interferometric vertical wavenumber connected to the real and imaginary parts of the effective propagation constant. This constant in turn is shown to depend on the dense medium parameters (such as grain size and volume fraction) as modeled by (2.11).

#### 2.2.3.2 Random Volume (RV) model of the dense medium InSAR volumetric correlation

In order to study the sensitivity of InSAR correlation measurements to the physical parameters that describe a dense medium, the InSAR correlation model for the random volume (RV) without a contribution from ground scattering is first considered. Such a model is appropriate for a dense-medium half-space, or one where the

surface scattering from the ground interface is small compared to the volume above it. In this formulation, after canceling out the constant number density and backscatter intensity from (2.39), we have

$$\begin{aligned}\gamma_v &= e^{j\phi_0}\frac{\int_{-d}^{0} e^{(\frac{2k_e}{\cos\theta_t}+j\kappa_z)z}dz}{\int_{-d}^{0} e^{\frac{2k_e}{\cos\theta_t}z}dz} \\ &= e^{j\phi_0}\cdot\frac{\frac{2k_e}{\cos\theta_t}}{\frac{2k_e}{\cos\theta_t}+j\kappa_z}\cdot\frac{1-e^{-(\frac{2k_e}{\cos\theta_t}+j\kappa_z)d}}{1-e^{-\frac{2k_e}{\cos\theta_t}d}}. \end{aligned} \tag{2.42}$$

Combining (2.42) with (2.40) and (2.41), where the real and imaginary parts of the effective propagation constant are known as functions of the scatterer size and the volume fraction, the random volume model establishes a connection between the complex InSAR volumetric correlation measurement $\gamma_v$ and the parameters that describe the medium characteristics (volume depth $d$, scatterer size $l$, volume fraction $f_v$). If we assume that the interferometric phase $\phi_0$ is referenced to a fixed point $\overline{R_0}$, and thus does not vary with the parameters of the random volume, the functional relationship between the interferometric correlation and the dense medium parameters can be written as

$$\gamma_v = M\left(\begin{bmatrix} l \\ f_v \\ d \end{bmatrix}\right). \tag{2.43}$$

The model dependence on these three parameters is illustrated as Figure 2.5, where each of the three dense medium parameters is allowed to vary while keeping constant the other two parameters.

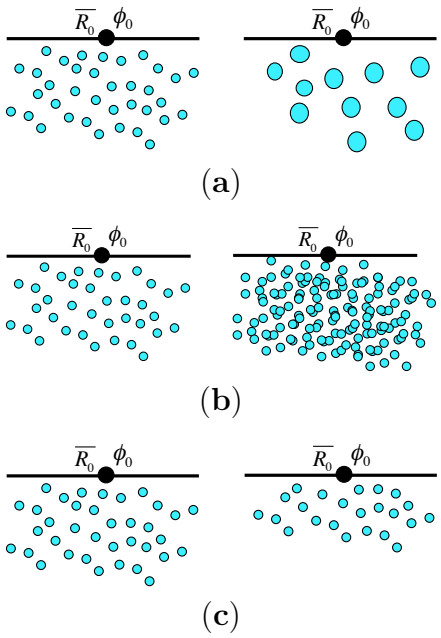


Figure 2.5: Illustration of the Random Volume (RV) model as a function of the snow volume parameters, *i.e.* grain size (**a**), volume fraction (**b**), and layer depth (**c**). Each parameter is investigated by fixing the other two parameters constant. $\phi_0$ denotes the interferometric phase referenced to the center of the resolution cell $\overline{R_0}$.

#### 2.2.3.3 Random Volume over Ground (RVoG) model of the dense medium InSAR volumetric correlation

The inclusion of a more physical model that incorporates a return from the ground surface increases the number of parameters, and specifically includes a term that characterizes the ratio of scattered power from the ground to the total volume. Such a model is termed the random volume over ground (RVoG) model (similar to [81, 57] for a sparse medium like vegetation).

This model is developed through a change of variables $z' = z + d$ that shifts the reference point from the top of the dense medium, to the bottom. Hence, (2.39) can be rewritten as

$$\gamma_v = e^{j\phi_0} e^{-j\kappa_z d} \frac{\int_0^d \tau_0 \sigma_0 e^{\frac{2k_e}{\cos\theta_t}(z'-d)} e^{j\kappa_z z'} dz'}{\int_0^d \tau_0 \sigma_0 e^{\frac{2k_e}{\cos\theta_t}(z'-d)} dz'}. \tag{2.44}$$

Given the ground surface at $z' = 0$, the two-layer backscatter intensity profile can be defined as

$$\tau(z')\sigma(z') = \tau_0\sigma_0 + \sigma_G\delta(z'), \tag{2.45}$$

where $\sigma_G$ represents the reflected power from the ground (here, the term that would be related to ground scatterer density, $\tau_G$, is removed), and $\delta(z')$ is a Dirac delta function at $z' = 0$.

By replacing $\tau_0\sigma_0$ with $\tau(z')\sigma(z')$ as defined in (2.45), (2.44) can be rewritten as

$$\begin{aligned}\gamma_v =& e^{j\phi_0}e^{-j\kappa_z d}\frac{\int_0^d \tau_0\sigma_0 e^{\frac{2k_e}{\cos\theta_t}(z'-d)+j\kappa_z z'}dz' + \sigma_G e^{-\frac{2k_e}{\cos\theta_t}d}}{\int_0^d \tau_0\sigma_0 e^{\frac{2k_e}{\cos\theta_t}(z'-d)}dz' + \sigma_G e^{-\frac{2k_e}{\cos\theta_t}d}} \\ =& e^{j\phi_g}\frac{\gamma_{vol}+m}{1+m},\end{aligned} \tag{2.46}$$

where

$$\phi_g = \phi_0 - \kappa_z d, \tag{2.47}$$

is the interferometric phase referenced to the ground surface (and thus depends on the ground topographic height, denoted as $h$),

$$\gamma_{vol} = \frac{\int_0^d \tau_0\sigma_0 e^{\frac{2k_e}{\cos\theta_t}(z'-d)}e^{j\kappa_z z'}dz'}{\int_0^d \tau_0\sigma_0 e^{\frac{2k_e}{\cos\theta_t}(z'-d)}dz'} \tag{2.48}$$

is the InSAR volumetric correlation component that is due to the dense medium (volume scatterers) only, and

$$m = \frac{\sigma_G e^{-\frac{2k_e}{\cos\theta_t}d}}{\int_0^d \tau_0\sigma_0 e^{\frac{2k_e}{\cos\theta_t}(z'-d)}dz'} \tag{2.49}$$

is the "ground-to-volume" ratio. Further, by canceling terms for the constant number density and backscatter intensity for volume scatterers as in (2.42), (2.48) can be written as

$$\gamma_{vol} = \frac{\frac{2k_e}{\cos\theta_t}}{\frac{2k_e}{\cos\theta_t} + j\kappa_z} \cdot \frac{e^{(\frac{2k_e}{\cos\theta_t}+\kappa_z)d} - 1}{e^{\frac{2k_e}{\cos\theta_t}d} - 1}, \tag{2.50}$$

Similar to the Random Volume model (RV), the Random Volume over Ground model connects the complex InSAR volumetric correlation measurement $\gamma_v$ to the three dense medium parameters (volume depth $d$, scatterer size $l$, volume fraction $f_v$) and two ground parameters, which are ground interferometric phase $\phi_g$ (or equivalently a function of the ground topographic height, $h$) and ground-to-volume ratio $m$, *i.e.*,

$$\gamma_v = M\left(\begin{bmatrix} l \\ f_v \\ d \\ h \\ m \end{bmatrix}\right). \tag{2.51}$$

This is illustrated in Figure 2.6, where the reference interferometric phase, $\phi_0$ and the ground interferometric phase, $\phi_g$ are indicated.

## 2.3 Repeat-pass InSAR scattering model for vegetation

Similar to Section 2.2, by using the expression of the single-scatterer SAR backscattered field for a pair of antennas allowing the random medium characteristics (both scatterers' dielectric property and spatial position) to change between overpasses, one can also determine the repeat-pass InSAR correlation from the cross-product between two single-scatterer SAR backscattered fields. The normalized repeat-pass

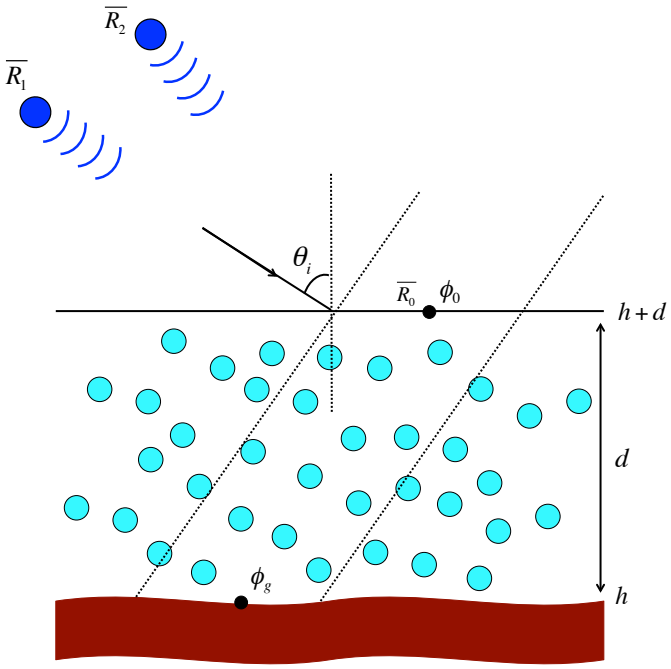


Figure 2.6: Illustration of the Random Volume over Ground (RVoG) model. The topographic height of the underlying ground surface and the top of the medium are indicated as $h$ and $(h+d)$, respectively. Within a resolution cell that is marked by a pair of dashed lines, the interferometric phase referenced to the top of the medium at $\overline{R_0}$ is denoted as $\phi_0$, while the interferometric phase referenced to the bottom (where the ground resides) is denoted by $\phi_g$.

InSAR correlation coefficient can be further decomposed so that the coupled correlation component due to volume scattering and temporal change can be obtained for the future use of retrieving vegetation characteristics.

### 2.3.1 Model formulation

Using (2.26) to represent two SAR observations from a repeat-pass InSAR system, and allowing each scatterer to have a change in the scattering amplitude and its position between overpasses, the repeat-pass InSAR cross-correlation can be written as

$$
\begin{aligned}
\langle E(\overline{R_1})E^*(\overline{R_2})\rangle =& \sum_{j=1}^{N}\sum_{k=1}^{N}\langle E(\overline{R_1};j)E^*(\overline{R_2};k)\rangle \\
=& \sum_{j=1}^{N}\sum_{k=1}^{N}\iiiint \langle E(\overline{R_1};j)E^*(\overline{R_2};k)\rangle_{jk} \\
& P(\overline{R_j}^{(1)},\overline{R_k}^{(2)},f_j^{(1)},f_k^{(2)})d\overline{R_j}^{(1)}d\overline{R_k}^{(2)}df_j^{(1)}df_k^{(2)} \\
=& \sum_{j=1}^{N}\sum_{k=1}^{N}\iiiint \langle E(\overline{R_1};j)E^*(\overline{R_2};k)\rangle_{jk}P(\overline{R_j}^{(1)},\overline{R_k}^{(2)}) \\
& P(f_j^{(1)},f_k^{(2)}|\overline{R_j}^{(1)},\overline{R_k}^{(2)})d\overline{R_j}^{(1)}d\overline{R_k}^{(2)}df_j^{(1)}df_k^{(2)}, \qquad (2.52)
\end{aligned}
$$

where the superscripts "$(i)$" $(i = 1, 2)$ are used to distinguish the position and the scattering amplitude of each scatterer in the $i^{th}$ pass of the SAR platform. The random motion of the volume scatterers is embodied in $P(\overline{R_j}^{(1)}, \overline{R_k}^{(2)})$, which is the joint probability density function for the scatterer $j$ at $\overline{R_j}^{(1)}$ during the $1^{st}$ pass and scatterer $k$ at $\overline{R_k}^{(2)}$ during the $2^{nd}$ pass of the interferometer. The effect of dielectric fluctuations in the scatterers is captured by the joint probability density function for the scattering amplitude $f_j^{(1)}$ of scatterer $j$ at $\overline{R_j}^{(1)}$ during the $1^{st}$ pass and the scattering amplitude $f_k^{(2)}$ of scatterer $k$ at $\overline{R_k}^{(2)}$ during the $2^{nd}$ pass (both $f_j^{(1)}$ and $f_k^{(2)}$ depend on the dielectric constants), which is given by $P(f_j^{(1)}, f_k^{(2)}|\overline{R_j}^{(1)}, \overline{R_k}^{(2)})$.

The temporal change effects of volume scatterers in (2.52) are illustrated in Figure 2.7. Note that Figure 2.7 is a notional illustration. Volume scatterers are assumed randomly oriented with various polarization signatures in each pass and the position as well as orientation can change between passes.

Substituting (2.25) into (2.52) gives

$$
\begin{aligned}
\langle E(\overline{R_1})E^*(\overline{R_2})\rangle =& \sum_{j=1}^{N}\sum_{k=1}^{N}\iiiint \langle E(\overline{R_1};j)\rangle_j\langle E^*(\overline{R_2};k)\rangle_k P(\overline{R_j}^{(1)},\overline{R_k}^{(2)}) \\
& P(f_j^{(1)},f_k^{(2)}|\overline{R_j}^{(1)},\overline{R_k}^{(2)})d\overline{R_j}^{(1)}d\overline{R_k}^{(2)}df_j^{(1)}df_k^{(2)}. \qquad (2.53)
\end{aligned}
$$


(**a**) Dielectric Fluctuation Only


(**b**) Random Motion Only


(**c**) Dielectric Fluctuation + Random Motion

Figure 2.7: Illustration of the temporal change effects (dielectric fluctuation and/or random motion) associated with each scattering element (illustrated as a cylinder with the "black dot" being its position in each pass).

In order to model the cross-correlation, it is important to know the SAR backscattered field contributed from individual scatterers between overpasses, *i.e.* $\langle E(\overline{R_1}; j)\rangle_j$ and $\langle E(\overline{R_2}; k)\rangle_k$.

By using (2.23), the single-scatterer SAR backscattered field due to scatterer $j$ from the $1^{st}$ pass can be rewritten as

$$\langle E(\overline{R_1}; j)\rangle_j = A_1 f_j^{(1)} X_1(\overline{R_j}^{(1)}) \tag{2.54}$$

with

$$X_1(\overline{R_j}^{(1)}) = e^{2K_I^{(1)} z_j^{(1)} / \cos\theta_{t_1}} W_a(x_j^{(1)}) W_r\left(y_j^{(1)} \sin\theta_{i_1} - n\cos\theta_{t_1} z_j^{(1)}\right)$$
$$e^{j2k_0\left(|\overline{R_1}-\overline{R_0}|+y_j^{(1)}\sin\theta_{i_1}-n\cos\theta_{t_1} z_j^{(1)}\right)}. \tag{2.55}$$

where the subscript "1" is used to describe the incidence and refraction angles during the $1^{st}$ pass while the superscript "(1)" is also used to allow for changes of the scatterer's spatial coordinates and scattering amplitude from pass to pass. The geometric relationship is illustrated in Figure 2.8.

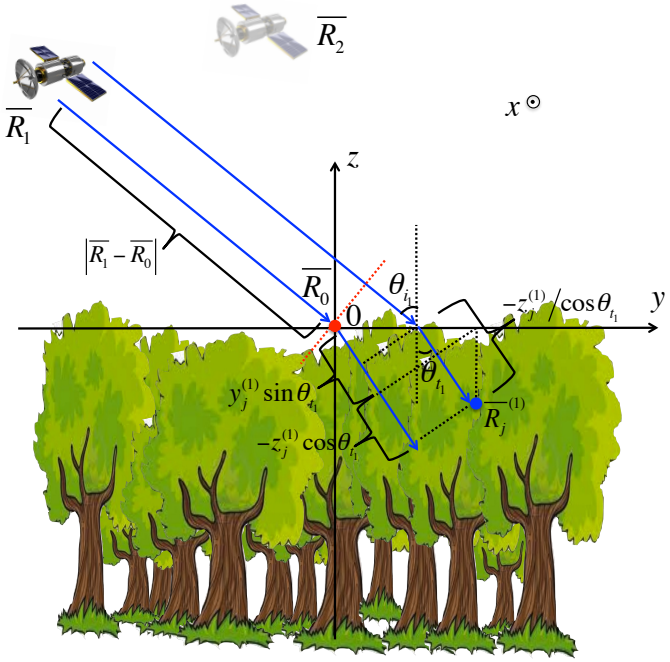


Figure 2.8: Viewing geometry of the repeat-pass InSAR observation. The center of the resolution cell, $\overline{R_0}$, is marked as a "red" dot, while the $j^{th}$ scatterer is shown in "blue". The spatial coordinates of the scatterer at $\overline{R_j}^{(1)}$ are represented in its local Cartesian coordinates $(x_j^{(1)}, y_j^{(1)}, z_j^{(1)})$ that is referenced at $\overline{R_0}$. The reference phase plane at the center of the resolution cell, $\overline{R_0}$, is shown as a "red" dashed line. The range path length from $\overline{R_1}$ to $\overline{R_j}^{(1)}$ is equivalent to the one that starts from $\overline{R_1}$, passes through $\overline{R_0}$ and reaches the same phase front as $\overline{R_j}^{(1)}$, which equals to $|\overline{R_1} - \overline{R_0}| + n(y_j^{(1)} \sin\theta_{t_1} - z_j^{(1)} \cos\theta_{t_1})$. The attenuation path length that the wave traveled within the medium to reach $\overline{R_j}^{(1)}$ is obviously $-z_j^{(1)}/\cos\theta_{t_1}$.

Similarly, using (2.24) for the repeat observation, we have the single-scatterer SAR backscattered response from scatterer $k$ given as

$$\langle E(\overline{R_2}; k)\rangle_k = A_2 f_k^{(2)} X_2(\overline{R_k}^{(2)}) \tag{2.56}$$

with

$$\begin{aligned} X_2(\overline{R_k}^{(2)}) =& e^{2K_I^{(2)} z_k^{(2)}/\cos\theta_{t_2}} W_a(x_k^{(2)}) W_r\left(y_k^{(2)}\sin\theta_{i_2} - n\cos\theta_{t_2} z_k^{(2)}\right) \\ & e^{j2k_0\left(|\overline{R_2}-\overline{R_0}|+y_k^{(2)}\sin\theta_{i_2}-n\cos\theta_{t_2} z_k^{(2)}\right)}. \end{aligned} \tag{2.57}$$

Note in (2.55) and (2.57), the superscript "(i)" $(i = 1, 2)$ is used to distinguish $K_I$, the imaginary part of the effective propagation constant between overpasses, since it varies with the moisture-induced dielectric/scattering amplitude fluctuation of the scatterers. However, the real part $K_R$, equivalently the refractive index $n$, is assumed constant between passes since $n \approx 1$ for a sparse random medium such as a forest canopy [23].

### 2.3.2 Repeat-pass InSAR correlation

Before substituting (2.54) and (2.56) into (2.53) to solve for the repeat-pass InSAR correlation, the same argument can be applied as has been used in deriving (2.29) such that the terms with $j \neq k$ can be eliminated. Therefore, (2.53) can be rewritten as

$$\begin{aligned}\langle E(\overline{R_1})E^*(\overline{R_2})\rangle =& \sum_{j=1}^{N}\iiiint \langle E(\overline{R_1};j)\rangle_j \langle E^*(\overline{R_2};j)\rangle_j P(\overline{R_j}^{(1)},\overline{R_j}^{(2)}) \\ & P(f_j^{(1)},f_j^{(2)}|\overline{R_j}^{(1)},\overline{R_j}^{(2)})d\overline{R_j}^{(1)}d\overline{R_j}^{(2)}df_j^{(1)}df_j^{(2)} \\ =& \sum_{j=1}^{N}\iiiint \langle E(\overline{R_1};j)\rangle_j \langle E^*(\overline{R_2};j)\rangle_j P(\overline{R_j}^{(2)}|\overline{R_j}^{(1)})P(\overline{R_j}^{(1)}) \\ & P(f_j^{(1)},f_j^{(2)}|\overline{R_j}^{(1)},\overline{R_j}^{(2)})d\overline{R_j}^{(1)}d\overline{R_j}^{(2)}df_j^{(1)}df_j^{(2)} \\ =& \iiiint \tau(\overline{R_j}^{(1)})\langle E(\overline{R_1};j)\rangle_j \langle E^*(\overline{R_2};j)\rangle_j P(\overline{R_j}^{(2)}|\overline{R_j}^{(1)}) \\ & P(f_j^{(1)},f_j^{(2)}|\overline{R_j}^{(1)},\overline{R_j}^{(2)})d\overline{R_j}^{(1)}d\overline{R_j}^{(2)}df_j^{(1)}df_j^{(2)}, \end{aligned} \tag{2.58}$$

where $\tau(\overline{R_j}^{(1)})$ is the scatterer number density, and $P(\overline{R_j}^{(2)}|\overline{R_j}^{(1)})$ is the conditional probability of the scatterer's position during the $2^{nd}$ pass given its position in the $1^{st}$ pass. For single-pass SAR interferometry (Section 2.2.2), setting $j = k$ in (2.53) eliminates all of the joint and/or conditional probabilities; however, for repeat-pass InSAR, since there are changes in both the scatterer's position and scattering amplitude between passes, the joint or conditional probabilities still exist and will be utilized to characterize the dielectric fluctuation and random motion effects on the repeat-pass InSAR correlation.

By substituting (2.54) and (2.56) into (2.58), it reduces to

$$\begin{aligned}\langle E(\overline{R_1})E^*(\overline{R_2})\rangle =& \iiiint \tau(\overline{R_j}^{(1)})A_1 f_j^{(1)} X_1(\overline{R_j}^{(1)})A_2 f_j^{(2)*} X_2^*(\overline{R_j}^{(2)})P(\overline{R_j}^{(2)}|\overline{R_j}^{(1)}) \\ & P(f_j^{(1)},f_j^{(2)}|\overline{R_j}^{(1)},\overline{R_j}^{(2)})d\overline{R_j}^{(1)}d\overline{R_j}^{(2)}df_j^{(1)}df_j^{(2)} \\ =& A_1A_2\iint \tau(\overline{R_j}^{(1)})D(\overline{R_j}^{(1)},\overline{R_j}^{(2)})X_1(\overline{R_j}^{(1)})X_2^*(\overline{R_j}^{(2)}) \\ & P(\overline{R_j}^{(2)}|\overline{R_j}^{(1)})d\overline{R_j}^{(1)}d\overline{R_j}^{(2)} \end{aligned} \tag{2.59}$$

with

$$D(\overline{R_j}^{(1)},\overline{R_j}^{(2)}) = \iint f_j^{(1)} f_j^{(2)*} P(f_j^{(1)},f_j^{(2)}|\overline{R_j}^{(1)},\overline{R_j}^{(2)})df_j^{(1)}df_j^{(2)}, \tag{2.60}$$

where $D$ is a function of the spatial coordinates of scatterer $j$. It can be noticed that the statistical averaging over scattering amplitude $f_j^{(i)}$ $(i = 1, 2)$ by using the joint probability is treated differently from averaging over scatterer's position $\overline{R_j}^{(i)}$ $(i = 1, 2)$ where the conditional probability is used. The reason is that there is lack of statistical information for the scattering amplitude change, so the most general treatment that can be made is by using the joint probability; however, for the random motion of a scatterer, it is usually assumed that the position in the $2^{nd}$ observation given its position in the $1^{st}$ observation follows some statistical distribution (e.g. Gaussian [96, 33]), hence the conditional probability is more suitable to characterize this temporal change as will be shown later. Here, the expression of $D(\overline{R_j}^{(1)}, \overline{R_j}^{(2)})$ is consistent with the definition of the covariance between $f_j^{(1)}$ and $f_j^{(2)}$ given the scatterer's positions, *i.e.*

$$D(\overline{R_j}^{(1)}, \overline{R_j}^{(2)}) = \langle f_j^{(1)} f_j^{(2)*} \rangle_{\boldsymbol{f}|\boldsymbol{R}}, \tag{2.61}$$

where "$\langle\ \rangle_{\boldsymbol{f}|\boldsymbol{R}}$" is averaging only over the scattering amplitude given the scatterer's positions, which is part of the configuration averaging by fixing the spatial coordinates of the scatterer. Further, we can define the Pearson correlation coefficient for the scattering amplitudes of scatterer $j$ between the $1^{st}$ and the $2^{nd}$ pass of the instrument, *i.e.*, $f_j^{(1)}$ and $f_j^{(2)}$ as,

$$S_t(\overline{R_j}^{(1)}, \overline{R_j}^{(2)}) = \frac{\langle f_j^{(1)} f_j^{(2)*} \rangle_{\boldsymbol{f}|\boldsymbol{R}}}{\sqrt{\langle |f_j^{(1)}|^2 \rangle_{\boldsymbol{f}|\boldsymbol{R}} \langle |f_j^{(2)}|^2 \rangle_{\boldsymbol{f}|\boldsymbol{R}}}}, \tag{2.62}$$

which is a complex-valued number with a magnitude less than or equal to one. Also, we refer to the backscatter profile as the average of the backscatter intensity, *i.e.*

$$\sigma_1(\overline{R_j}^{(1)}) = \langle |f_j^{(1)}|^2 \rangle_{\boldsymbol{f}|\boldsymbol{R}} = \int |f_j^{(1)}|^2 P(f_j^{(1)}|\overline{R_j}^{(1)}) df_j^{(1)} \tag{2.63}$$

for the SAR observation during the $1^{st}$ pass, and

$$\sigma_2(\overline{R_j}^{(2)}) = \langle |f_j^{(2)}|^2 \rangle_{\boldsymbol{f}|\boldsymbol{R}} = \int |f_j^{(2)}|^2 P(f_j^{(2)}|\overline{R_j}^{(2)}) df_j^{(2)} \tag{2.64}$$

for the $2^{nd}$ SAR observation after the repeat period. Therefore, (2.61) can be written as

$$D(\overline{R_j}^{(1)}, \overline{R_j}^{(2)}) = S_t(\overline{R_j}^{(1)}, \overline{R_j}^{(2)}) \sqrt{\sigma_1(\overline{R_j}^{(1)}) \sigma_2(\overline{R_j}^{(2)})}. \tag{2.65}$$

Assuming that the random motion effect of the volume scatterers is not large such that

$$S_t(\overline{R_j}^{(1)}, \overline{R_j}^{(2)}) \approx S_t(\overline{R_j}^{(1)}, \overline{R_j}^{(1)}) = S_t(\overline{R_j}^{(1)}), \tag{2.66}$$

and

$$\sigma_2(\overline{R_j}^{(2)}) \approx \sigma_2(\overline{R_j}^{(1)}), \tag{2.67}$$

then by substituting (2.65), (2.66) and (2.67) into (2.59), we achieve

$$\begin{aligned} \langle E(\overline{R_1}) E^*(\overline{R_2}) \rangle =& A_1 A_2 \iint \tau(\overline{R_j}^{(1)}) S_t(\overline{R_j}^{(1)}) \sqrt{\sigma_1(\overline{R_j}^{(1)}) \sigma_2(\overline{R_j}^{(1)})} X_1(\overline{R_j}^{(1)}) \\ & X_2^*(\overline{R_j}^{(2)}) P(\overline{R_j}^{(2)}|\overline{R_j}^{(1)}) d\overline{R_j}^{(1)} d\overline{R_j}^{(2)} \\ =& A_1 A_2 \int \tau(\overline{R_j}^{(1)}) S_t(\overline{R_j}^{(1)}) \sqrt{\sigma_1(\overline{R_j}^{(1)}) \sigma_2(\overline{R_j}^{(1)})} X_1(\overline{R_j}^{(1)}) \\ & F(\overline{R_j}^{(1)}) d\overline{R_j}^{(1)}, \end{aligned} \tag{2.68}$$

where

$$F(\overline{R_j}^{(1)}) = \int X_2^*(\overline{R_j}^{(2)}) P(\overline{R_j}^{(2)}|\overline{R_j}^{(1)}) d\overline{R_j}^{(2)}. \tag{2.69}$$

It can be noticed that in (2.68) the goal is to express each component as a function of $\overline{R_j}^{(1)}$. Hence, in (2.69), it is also preferred to replace the argument in $X_2^*$ from $\overline{R_j}^{(2)}$ to $\overline{R_j}^{(1)}$ by accounting for the extra phase shift caused by the change of scatterer position. In particular, by assuming that the effect of scatterer motion is not large, e.g., as in (2.66) and (2.67), such that the amplitude of $X_2^*(\overline{R_j}^{(2)})$ in (2.57) can be approximated as the amplitude of $X_2^*(\overline{R_j}^{(1)})$, but not necessarily the phase. This is accomplished by letting the $j^{th}$ scatterer displacement be $\Delta\overline{R_j} = \overline{R_j}^{(2)} - \overline{R_j}^{(1)} = [\ \Delta x_j\ \Delta y_j\ \Delta z_j\ ]$ in Cartesian coordinates and substituting into the phase term of (2.57). This gives

$$X_2^*(\overline{R_j}^{(2)}) = X_2^*(\overline{R_j}^{(1)}) e^{j2k_0(\Delta y_j \sin\theta_{i_2} - n\cos\theta_{t_2}\Delta z_j)}. \tag{2.70}$$

Within the conditional probability $P(\overline{R_j}^{(2)}|\overline{R_j}^{(1)})$, it is assumed that the displacement vector obeys a three dimensional Gaussian distribution [33, 96] with zero-mean and standard deviation of $\sigma_r(\overline{R_j}^{(1)})$, as in

$$\begin{aligned} P(\overline{R_j}^{(2)}|\overline{R_j}^{(1)}) = P(\Delta\overline{R_j}|\overline{R_j}^{(1)}) &= \frac{1}{(\sqrt{2\pi})^3\sigma_r^3(\overline{R_j}^{(1)})} \exp\left(-\frac{|\Delta\overline{R_j}|^2}{2\sigma_r^2(\overline{R_j}^{(1)})}\right) \\ &= \frac{1}{(\sqrt{2\pi})^3\sigma_r^3(\overline{R_j}^{(1)})} \exp\left(-\frac{\Delta x_j^2 + \Delta y_j^2 + \Delta z_j^2}{2\sigma_r^2(\overline{R_j}^{(1)})}\right) . \end{aligned} \tag{2.71}$$

Substituting (2.70) and (2.71) into (2.69), and integrating over $x$ (which has no effect on the interferometric phase), we have

$$
\begin{aligned}
F(\overline{R_j}^{(1)}) = & \int X_2^*(\overline{R_j}^{(2)}) P(\Delta\overline{R_j}|\overline{R_j}^{(1)}) d\Delta\overline{R_j} \\
= & X_2^*(\overline{R_j}^{(1)}) \iiint e^{j2k_0(\Delta y_j \sin\theta_{i_2} - n\cos\theta_{t_2}\Delta z_j)} \frac{1}{(\sqrt{2\pi})^3 \sigma_r^3(\overline{R_j}^{(1)})} \\
& \exp\left(-\frac{\Delta x_j^2 + \Delta y_j^2 + \Delta z_j^2}{2\sigma_r^2(\overline{R_j}^{(1)})}\right) d\Delta x_j d\Delta y_j d\Delta z_j \\
= & X_2^*(\overline{R_j}^{(1)}) \iint e^{j2k_0(\Delta y_j \sin\theta_{i_2} - n\cos\theta_{t_2}\Delta z_j)} \frac{1}{(\sqrt{2\pi})^2 \sigma_r^2(\overline{R_j}^{(1)})} \\
& \exp\left(-\frac{\Delta y_j^2 + \Delta z_j^2}{2\sigma_r^2(\overline{R_j}^{(1)})}\right) d\Delta y_j d\Delta z_j. \qquad (2.72)
\end{aligned}
$$

By assuming that the effective refractive index $n \approx 1$ (and thus $\theta_{i_2} \approx \theta_{t_2}$) for a sparse medium like a forest canopy [23], we can thus define the radial displacement along the line of sight as $\Delta r_j = \Delta y_j \sin\theta_{i_2} - n\cos\theta_{t_2}\Delta z_j \approx \Delta y_j \sin\theta_{i_2} - \cos\theta_{i_2}\Delta z_j$, and express (2.72) through a change of variables [33], *i.e.*

$$
\begin{aligned}
F(\overline{R_j}^{(1)}) &= X_2^*(\overline{R_j}^{(1)}) \int e^{jk_0 2\Delta r_j} \frac{1}{\sqrt{2\pi}\sigma_r(\overline{R_j}^{(1)})} \exp\left(-\frac{\Delta r_j^2}{2\sigma_r^2(\overline{R_j}^{(1)})}\right) d\Delta r_j \\
&= X_2^*(\overline{R_j}^{(1)}) \exp\left[-\frac{(2k_0)^2}{2}\sigma_r^2(\overline{R_j}^{(1)})\right] \\
&= X_2^*(\overline{R_j}^{(1)}) \rho_r(\overline{R_j}^{(1)}) \qquad (2.73)
\end{aligned}
$$

with

$$
\rho_r(\overline{R_j}^{(1)}) = \exp\left[-\frac{(2k_0)^2}{2}\sigma_r^2(\overline{R_j}^{(1)})\right], \qquad (2.74)
$$

which is the term associated with the random motion of the scatterers. For the height-dependent motion variance, different functional forms have been assumed in various studies: [33] uses a linear form while [5] and this work exploit a quadratic form. No matter what functional form is used, the expression for $\rho_r(\overline{R_j}^{(1)})$ in (2.74) serves as the general model of the vertical random motion profile, which is also consistent with

previous works [33, 34, 5]. This section only focuses on the derivation of the general repeat-pass InSAR model, leaving the selection of the functional form of the motion variance to be discussed in Section 3.2 and Section 5.3.

By substituting (2.73) into the repeat-pass InSAR correlation (2.68), we obtain

$$\langle E(\overline{R_1})E^*(\overline{R_2})\rangle = A_1 A_2 \int \tau(\overline{R}) S_t(\overline{R}) \sqrt{\sigma_1(\overline{R})\sigma_2(\overline{R})}\rho_r(\overline{R}) X_1(\overline{R}) X_2^*(\overline{R}) d\overline{R}, \quad (2.75)$$

where the superscript "(1)" and subscript "$j$" have been dropped since the volume integration is taken only over $\overline{R_j}^{(1)}$. The effect of the baseline and the signal extinction have been incorporated into $X_1(\overline{R})X_2^*(\overline{R})$ at this stage and will be factored out as shown below.

Before we further utilize the expression in (2.75) to derive the normalized repeat-pass InSAR correlation coefficient, we first compare this result with the single-pass scenario, which has been shown in Section 2.2.2. Following (2.29), the single-pass InSAR correlation can be written as

$$\langle E(\overline{R_1})E^*(\overline{R_2})\rangle = A_1 A_2 \int \tau(\overline{R}) \sigma(\overline{R}) X_1(\overline{R}) X_2^*(\overline{R}) d\overline{R}, \quad (2.76)$$

where the number density profile, $\tau(\overline{R})$, and the backscatter profile, $\sigma(\overline{R})$, are further assumed only dependent on the vertical coordinate, $z$. Since the normalized InSAR correlation coefficient is defined as [64]

$$\gamma = \frac{\langle E(\overline{R_1})E^*(\overline{R_2})\rangle}{\sqrt{\langle |E(\overline{R_1})|^2\rangle \langle |E(\overline{R_2})|^2\rangle}}, \quad (2.77)$$

after representing (2.76) in Cartesian coordinates (*i.e.* $x$, $y$ and $z$) and separating the integrals associated with each variable (see Section 2.2.2 along with Section 6.4), the

normalized InSAR volumetric correlation (*i.e.* the correlation component associated with $z$) is given by

$$\gamma_v = \frac{\int \tau(z)\sigma(z)e^{(\frac{2k_e}{\cos\theta_t}+j\kappa_z)z}dz}{\int \tau(z)\sigma(z)e^{\frac{2k_e}{\cos\theta_t}z}dz}, \tag{2.78}$$

where $k_e = 2K_I$ is the extinction coefficient, and $\kappa_z = \frac{2k_0 B_\perp}{R\sin\theta_i}$ is the interferometric vertical wavenumber under the condition of the refractive index $n \approx 1$ (and thus $\theta_i \approx \theta_t$) for a sparse concentration of volume scatterers such as a forest canopy [23]. Here, $B_\perp$ is the perpendicular baseline and $R$ is the slant range from SAR to the resolution center.

Therefore, by assuming $S_t(\overline{R})$ (which is a correlation profile that depends on the dielectric/scattering amplitude fluctuation), random motion profile $\rho_r(\overline{R})$ and the backscatter profiles $\sigma_1(\overline{R})$ and $\sigma_2(\overline{R})$ are only $z$-dependent, we utilize the similarity between (2.75) and (2.76) to further simplify the derivation. That is, by separating the $z$-dependent components, the repeat-pass InSAR coupled correlation coefficient due to volume scattering and temporal changes (both dielectric fluctuation and random motion) is given by

$$\begin{aligned}\gamma_{v\&t} &= \frac{\int \tau(z)S_t(z)\rho_r(z)\sqrt{\sigma_1(z)\sigma_2(z)}e^{\frac{k_{e_1}}{\cos\theta_{t_1}}z}e^{\frac{k_{e_2}}{\cos\theta_{t_2}}z}e^{j\kappa_z z}dz}{\sqrt{\int \tau(z)\sigma_1(z)e^{\frac{2k_{e_1}}{\cos\theta_{t_1}}z}dz\cdot\int \tau(z)\sigma_2(z)e^{\frac{2k_{e_2}}{\cos\theta_{t_2}}z}dz}} \\ &= \frac{\int S_t(z)\rho_r(z)\sqrt{\sigma_1(z)\sigma_2(z)}e^{j\kappa_z z}dz}{\sqrt{\int \sigma_1(z)dz\cdot\int \sigma_2(z)dz}},\end{aligned} \tag{2.79}$$

where $k_{e_i}$ $(i = 1, 2)$ is the extinction coefficient for the $i^{th}$ pass. Note the number density profile, $\tau(z)$, and the exponential extinction profile, $e^{\frac{2k_{e_i}}{\cos\theta_{t_i}}z}$, have been assimilated into the backscatter profile in the last equation for conciseness of notation. That is, (2.63) and (2.64) can be rewritten as

$$\sigma_1(z) = \tau(z) e^{\frac{2k_{e_1}}{\cos\theta_{t_1}} z} \int |f_j^{(1)}|^2 P(f_j^{(1)}|z) df_j^{(1)} \tag{2.80}$$

and

$$\sigma_2(z) = \tau(z) e^{\frac{2k_{e_2}}{\cos\theta_{t_2}} z} \int |f_j^{(2)}|^2 P(f_j^{(2)}|z) df_j^{(2)}, \tag{2.81}$$

where $\sigma_1(z)$ and $\sigma_2(z)$ are the *extinction-weighted* backscatter profiles.

In order to further understand how different decorrelation components (*i.e.*, dielectric fluctuation, random motion, volume structure) contribute to the repeat-pass InSAR correlation in (2.79), we enumerate these three causes below and analyze each one individually.

- ***Moisture-induced Dielectric/Scattering Amplitude Fluctuation***

  In this scenario, the random motion is eliminated from the problem and the baseline is set to zero, which implies $\rho_r(z) = 1$ and $\kappa_z = 0$. The repeat-pass InSAR correlation in (2.79) can be simplified as

  $$\gamma_{v\&t} = \frac{\int S_t(z) \sqrt{\sigma_1(z)\sigma_2(z)} dz}{\sqrt{\int \sigma_1(z) dz \cdot \int \sigma_2(z) dz}}, \tag{2.82}$$

  In the above, the source of decorrelation is from two components: one is $S_t(z)$ (which is defined in (2.62)), the other is everything that remains except $S_t(z)$, which consists of integrals of the extinction-weighted backscatter profiles that are defined in (2.80) and (2.81). There is decorrelation due to this second source since the numerator and denominator have different functional forms. As shown in (2.82), both of the sources of decorrelation are coupled. Further, the two sources of decorrelation are correlated, as both depend on the scattering amplitude (and thus dielectric) fluctuation. Therefore, the overall decorrelation

due to moisture-induced dielectric/scattering amplitude fluctuation will involve the coupled effect from both sources mentioned here.

To take into account the effect of dielectric fluctuations on the observed InSAR correlation, it is desired to follow a similar functional form as has been used for characterizing random motion and baseline effects, which is to have a single backscatter profile, *i.e.*, the geometric mean between observations that is defined as

$$\overline{\sigma}(z) = \sqrt{\sigma_1(z)\sigma_2(z)} \tag{2.83}$$

and a single profile in the numerator to characterize the net effect of these moisture-induced dielectric fluctuations, denoted as $\gamma_d(z)$.

In order to achieve this goal, (2.82) is manipulated as

$$\begin{aligned}
\gamma_{v\&t} &= \frac{\int \sqrt{\sigma_1(z)\sigma_2(z)}dz}{\sqrt{\int \sigma_1(z)dz \int \sigma_2(z)dz}} \frac{\int S_t(z)\sqrt{\sigma_1(z)\sigma_2(z)}dz}{\int \sqrt{\sigma_1(z)\sigma_2(z)}dz} \\
&= R \cdot \frac{\int S_t(z)\overline{\sigma}(z)dz}{\int \overline{\sigma}(z)dz} \\
&= \frac{\int \gamma_d(z)\overline{\sigma}(z)dz}{\int \overline{\sigma}(z)dz},
\end{aligned} \tag{2.84}$$

where

$$R = \frac{\int \sqrt{\sigma_1(z)\sigma_2(z)}dz}{\sqrt{\int \sigma_1(z)dz \int \sigma_2(z)dz}}, \tag{2.85}$$

can be considered a constant normalization factor that can be absorbed into the dielectric correlation profile $\gamma_d(z)$, as

$$\gamma_d(z) = RS_t(z) \tag{2.86}$$

which characterizes the overall decorrelation due to moisture-induced dielectric/scattering amplitude fluctuation.

With this new functional form in (2.84), it is clear that the geometric mean profile, $\overline{\sigma}(z)$, is shown in both of the numerator and denominator, while the overall decorrelation due to moisture-induced dielectric fluctuation is incorporated as a new correlation profile $\gamma_d(z)$, which fulfills the motivation of rewriting (2.82) as mentioned above.

Further, it can be seen from the *Cauchy-Schwartz Inequality*,

$$\left( \int \sqrt{\sigma_1(z)\sigma_2(z)} dz \right)^2 \leq \int \sigma_1(z) dz \int \sigma_2(z) dz, \tag{2.87}$$

that $0 \leq R \leq 1$, and $|S_t(z)| \leq 1$ as defined in (2.62), and thus $|\gamma_d(z)| \leq 1$.

In the extreme case of single-pass SAR interferometry, where there is no moisture-induced dielectric change, *i.e.*, $f_j^{(1)} = f_j^{(2)}$ (and thus $\sigma_1(z) = \sigma_2(z)$), we have $R = S_t(z) = 1$ (thus $\gamma_d(z) = 1$), and (2.84) comes up with the expected result of having no decorrelation.

It is useful to make the clarification that, although the geometric mean profile $\overline{\sigma}(z)$ is a function of the extinction-weighted backscatter profiles $\sigma_i(z)$ $(i = 1, 2)$ which are affected by the dielectric change, it is reasonable and equivalent to treat the geometric mean profile $\overline{\sigma}(z)$ as an independent profile. This is because in (2.84), $\overline{\sigma}(z)$ itself does not introduce decorrelation; rather, $R$ is the component that represents the decorrelation effect due to the variation of $\sigma_i(z)$.

- ***Zero-baseline Wind-induced Random Motion***

In the case of wind-induced random motion, the moisture-induced dielectric change is set to zero, *i.e.*, $f_j^{(1)} = f_j^{(2)}$ (and thus $S_t(z) = 1$, $\sigma_1(z) = \sigma_2(z) = \overline{\sigma}(z)$), and if the baseline is zero, $\kappa_z = 0$. Hence, (2.79) can be simplified as

$$\gamma_{v\&t} = \frac{\int \rho_r(z)\overline{\sigma}(z)dz}{\int \overline{\sigma}(z)dz}, \tag{2.88}$$

which is consistent with previous work [33, 34, 5], and clearly shows that the motion profile $\rho_r(z)$ accounts for the decorrelation due to wind-induced motion. In the extreme case of single-pass SAR interferometry, where there is no random motion among the scatterers, *i.e.*, the motion standard deviation is zero, from (2.74), $\rho_r(z) = 1$ and (2.88) reduces to unity, as expected.

- ***Single-pass Baseline-induced Volume Structure***

  In the simplest scenario, equivalent to single-pass SAR interferometry, where the interferometric vertical wavenumber, $\kappa_z \neq 0$ and the temporal decorrelation is not present, $f_j^{(1)} = f_j^{(2)}$ (and thus $S_t(z) = 1$, $\sigma_1(z) = \sigma_2(z) = \overline{\sigma}(z)$), and $\rho_r(z) = 1$. Therefore, (2.79) can be simplified to

$$\gamma_{v\&t} = \frac{\int \overline{\sigma}(z)e^{j\kappa_z z}dz}{\int \overline{\sigma}(z)dz}, \tag{2.89}$$

  which is consistent with previous work (e.g., [80, 81, 57]), and shows the effect of $\kappa_z$, or equivalently the baseline accounts for the decorrelation due to volume structure, *i.e.* often termed the *Volumetric Decorrelation*. In the extreme case that the baseline is zero, *i.e.* $\kappa_z = 0$, (2.89) reduces to unity, as expected.

- ***Generic Form***

From the above analysis, by using the geometric mean profile and factoring out $R$ as in (2.84), (2.79) can be rewritten as

$$\begin{aligned} \gamma_{v\&t} &= R\frac{\int S_t(z)\rho_r(z)\overline{\sigma}(z)e^{j\kappa_z z}dz}{\int \overline{\sigma}(z)dz} \\ &= \frac{\int \gamma_d(z)\rho_r(z)\overline{\sigma}(z)e^{j\kappa_z z}dz}{\int \overline{\sigma}(z)dz} \end{aligned} \tag{2.90}$$

where $\gamma_d(z)$ is defined in (2.86).

Similar to [33, 34, 5], $\rho_r(z)$ is associated with the random motion within the volume scatterers (with $\sigma_r(z)$ being the height-dependent motion standard deviation). Different from [33, 34, 5], (2.90) now contains the term $\gamma_d(z)$, which may also be spatially varying and depends on the target dielectric change (perhaps due to rain), and also the geometric mean backscatter profile $\overline{\sigma}(z)$ is considered rather than just using the conventional single-pass backscatter profile $\sigma_i(z)$ $(i = 1, 2)$.

### 2.3.3 Modified Random Volume over Ground (RVoG) model

In Section 2.3.2, the repeat-pass InSAR correlation model (2.90) was derived that took into account the effects of the dielectric fluctuation and random motion. The derivation is based on the center of the resolution cell being at the top of the canopy as illustrated in Figure 2.8, *i.e.*, $z = 0$ for the top of the canopy and $z = -h_v$ for the bottom, where $h_v$ denotes the physical canopy height. For a two-layer scenario (with the random volume over the ground surface), it is useful to perform a change of variables $z' = z + h_v$ so that $z' = 0$ for the ground surface and $z' = h_v$ for the top of the canopy, as illustrated in Figure 2.9(a). Therefore, (2.90) can be rewritten as

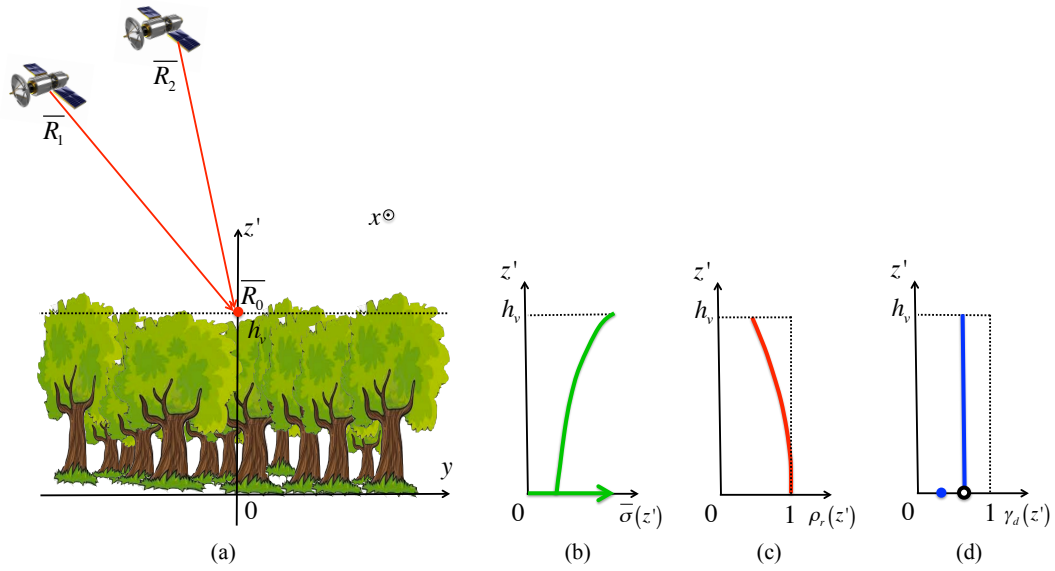


Figure 2.9: (**a**) Illustration of the viewing geometry of the Random Volume over Ground (RVoG) model along with the vertical profiles characterizing the repeat-pass InSAR correlation components. (**b**) is the extinction-weighted backscatter profile which is comprised by an exponential decaying function characterizing the volume and a delta function at the ground surface, (**c**) is the random motion profile which has a magnitude of one at the ground level and starts decorrelating as the height increases, and (**d**) is the dielectric fluctuation profile which has a differential change between the volume and the ground. Note through a change of variables, (a), (b), (c) and (d) have their vertical profiles as a function of $z'$ that is referenced at the ground surface ($z' = 0$).

$$\begin{aligned}
\gamma_{v\&t} &= \frac{\int_{-h_v}^{0} \gamma_d(z)\rho_r(z)\overline{\sigma}(z)e^{j\kappa_z z}dz}{\int \overline{\sigma}(z)dz} \\
&= \frac{\int_{0}^{h_v} \gamma_d(z'-h_v)\rho_r(z'-h_v)\overline{\sigma}(z'-h_v)e^{j\kappa_z(z'-h_v)}dz'}{\int_{0}^{h_v} \overline{\sigma}(z'-h_v)dz'} \\
&= e^{-j\kappa_z h_v}\frac{\int_{0}^{h_v} \gamma_d(z'-h_v)\rho_r(z'-h_v)\overline{\sigma}(z'-h_v)e^{j\kappa_z z'}dz'}{\int_{0}^{h_v} \overline{\sigma}(z'-h_v)dz'} \,. \qquad (2.91)
\end{aligned}$$

Note $\rho_r(z)$ is the random motion profile referenced at the top of the canopy ($z = 0$) with $z$ varying from $-h_v$ to 0; however, $\rho_r(z' - h_v)$ is a new function of $z'$, which characterizes the same segment of the profile but referenced at the ground surface ($z' = 0$) with $z'$ varying from 0 to $h_v$. To keep the concise notation, $\rho_r(z' - h_v)$ can be written as $\rho_r(z')$ with the definition of the motion profile allowed to be inferred

from the context (e.g., from the "prime" notation used in the $z$ coordinate), with a similar interpretation made for $\gamma_d(z')$ and $\overline{\sigma}(z')$. The profiles $\overline{\sigma}(z')$, $\rho_r(z')$ and $\gamma_d(z')$ are shown by example in Figure 2.9(b), (c), (d). Under this change of variables, (2.91) becomes

$$\gamma_{v\&t} = e^{-j\kappa_z h_v} \frac{\int_0^{h_v} \gamma_d(z')\rho_r(z')\overline{\sigma}(z')e^{j\kappa_z z'}dz'}{\int_0^{h_v} \overline{\sigma}(z')dz'} \tag{2.92}$$

To take into account a specific term for the ground scattering component, the extinction-weighted backscatter profiles can be modified as (*i.e.* Figure 2.9(b))

$$\begin{aligned} \sigma_1'(z') &= \sigma_1(z') + G_1\delta(z'); \\ \sigma_2'(z') &= \sigma_2(z') + G_2\delta(z'), \end{aligned} \tag{2.93}$$

where $G_1$ and $G_2$ represent the extinction-weighted Radar Cross Section (RCS) of the ground return at $z' = 0$. Thus by replacing $\sigma_1(z)$ and $\sigma_2(z)$ in (2.85) with $\sigma_1'(z')$ and $\sigma_2'(z')$, it can be shown that

$$\begin{aligned} R_{wg} &= \frac{\int_0^{h_v} \sqrt{\sigma_1'(z')\sigma_2'(z')}dz'}{\sqrt{\int_0^{h_v} \sigma_1'(z')dz' \int_0^{h_v} \sigma_2'(z')dz'}} \\ &= \frac{\int_0^{h_v} \sqrt{\sigma_1(z')\sigma_2(z')}dz' + \sqrt{G_1G_2}}{\sqrt{(\int_0^{h_v} \sigma_1(z')dz' + G_1)(\int_0^{h_v} \sigma_2(z')dz' + G_2)}} \leq 1, \end{aligned} \tag{2.94}$$

where $R_{wg}$ is the $R$ factor now with a ground scattering contribution.

If the effect of dielectric fluctuation is ergodic and stationary (such a formulation characterizes its mean behavior) throughout the random medium, the $z$-dependence of $S_t(z')$ can be ignored within the random volume. By allowing for there to be a

differential change in $S_t(z')$ (and thus $\gamma_d(z')$) for the volume scatterers and the ground as illustrated in Figure 2.9(d), we thus have

$$S_t(z') = \begin{cases} S_t^v & 0 < z' \leq h_v \\ S_t^g & z' = 0 \end{cases}, \tag{2.95}$$

and the total correlation component due to dielectric fluctuation from the ground and the volume is then

$$\gamma_d(z') = R_{wg} S_t(z') = \begin{cases} \gamma_d^v & 0 < z' \leq h_v \\ \gamma_d^g & z' = 0 \end{cases}. \tag{2.96}$$

Assuming that the random motion at the ground level is negligible, *i.e.* $\sigma_r^2(z' = 0) = 0$, using (2.74), we have $\rho_r(z' = 0) = \exp\left[-\frac{(2k_0)^2}{2}\sigma_r^2(z' = 0)\right] = 1$ as shown in Figure 2.9(c).

By replacing $\sigma_1(z')$ and $\sigma_2(z')$ in (2.92) with $\sigma_1'(z')$ and $\sigma_2'(z')$ and following [81, 57, 33], the modified double-layer Random Volume over Ground (RVoG) model is given as

$$\begin{aligned} \gamma_{v\&t} &= e^{-j\kappa_z h_v} \frac{\gamma_d^v \int_0^{h_v} \rho_r(z')\overline{\sigma}(z') e^{j\kappa_z z'} dz' + \gamma_d^g \sqrt{G_1 G_2}}{\int_0^{h_v} \overline{\sigma}(z') dz' + \sqrt{G_1 G_2}} \\ &= e^{-j\kappa_z h_v} \frac{\gamma_d^v \frac{\int_0^{h_v} \rho_r(z')\overline{\sigma}(z') e^{j\kappa_z z'} dz'}{\int_0^{h_v} \overline{\sigma}(z') dz'} + \gamma_d^g m}{1 + m}, \end{aligned} \tag{2.97}$$

where $m = \sqrt{G_1 G_2} / \int_0^{h_v} \overline{\sigma}(z') dz'$ is the ground-to-volume ratio in repeat-pass SAR interferometry.

This gives the general model for the volume and temporal interferometric correlation as

$$\gamma_{v\&t} = e^{-j\kappa_z h_v} \frac{\gamma_d^v \gamma_{v\&m} + \gamma_d^g m}{1 + m}, \tag{2.98}$$

with

$$\gamma_{v\&m} = \frac{\int_0^{h_v} \rho_r(z')\overline{\sigma}(z')e^{j\kappa_z z'}dz'}{\int_0^{h_v} \overline{\sigma}(z')dz'}. \tag{2.99}$$

Note that the first term in (2.98) is associated with the ground interferometric phase. Similar to [33, 34, 5], $\gamma_{v\&m}$ is the correlation associated with the coupled effect from volume scattering and random motion, while different from [33, 34, 5], $\gamma_d^v$ ($|\gamma_d^v| \leq 1$) and $\gamma_d^g$ ($|\gamma_d^g| \leq 1$) are the complex correlation components characterizing the dielectric fluctuation for the volume and the ground, respectively. Note importantly, $\gamma_d^v$, $\gamma_d^g$ and $m$ are expected to be polarization-dependent.

Equation (2.98) is derived for a simplified scenario, where the dielectric fluctuation is assumed ergodic and stationary throughout the random medium, and thus becomes a multiplicative factor that is decoupled from the volume scattering and random motion effects. Despite the simplification, this modified RVoG model is expected to characterize the temporal dielectric fluctuation to the first order (the ergodic and stationary assumption allows us to characterize the mean effect of dielectric fluctuation) while also taking account of the random motion and volume scattering effects. For the case where the temporal change effect of dielectric fluctuation is spatially varying, the random medium can be considered as a layered ergodic and stationary medium where all of the above analyses (such as (2.92)) can be adapted.

### 2.3.4 The physical mechanism of the dielectric fluctuation effect

#### 2.3.4.1 Statement of problem

In order to study the physical mechanism of the dielectric fluctuation effect, it is desired to consider the electromagnetic wave scattering by individual tree components (*i.e.* leaf, branch, trunk) that can be further modeled as dielectric cylinders and/or circular disks [30]. In this work, we investigate the model at L-band for simplicity, in which case the contributions from the branches and trunks (modeled as dielectric

cylinders) dominate the scattered fields. However, similar results at a higher frequency can be shown by considering the contributions from leaves (modeled as dielectric circular disks).

Ulaby [87] proposes a physical dielectric model that relates the dielectric constant, $\epsilon_r$, of vegetation components (e.g. leaf, stalk, branch, trunk) to the gravimetric moisture content, $M_g$. Typical values of $M_g$ are: 0.07 (low value), 0.26 (intermediate value) and 0.68 (high value). As for vegetation samples with various moisture contents, it is found that both the real and imaginary parts of the dielectric constants have a large dynamic range, which implies that the scatterer's dielectric constant could be highly target-dependent. During a long period of time between overpasses that is usually on the order of months, it is reasonable to expect obvious moisture change (and thus changes in the dielectric constants; perhaps due to rainfall), *i.e.*

$$\nu_{M_g}(\overline{R_j}) = \frac{M_g^{(2)}(\overline{R_j})}{M_g^{(1)}(\overline{R_j})}, \tag{2.100}$$

where $M_g^{(i)}(\overline{R_j})$ $(i = 1, 2)$ is the moisture content of the scatterer at position $\overline{R_j}$ during the $i^{\text{th}}$ satellite pass, and $\nu_{M_g}(\overline{R_j})$ is the corresponding ratio that characterizes the moisture change. In response to the moisture-induced dielectric changes, there is thus fluctuation in the complex scattering amplitude (that is a function of the dielectric constant). We thus define the ratio associated with the scattering amplitude change as

$$\nu_f(\overline{R_j}) = \frac{f_j^{(2)}(\overline{R_j})}{f_j^{(1)}(\overline{R_j})}. \tag{2.101}$$

#### 2.3.4.2 A dielectric fluctuation model

To begin, we note that the averaging "$\langle\ \rangle_{\boldsymbol{f}|\boldsymbol{R}}$" defined in (2.62), (2.63) and (2.64) for the complex scattering amplitude is an ensemble averaging. Assuming the dielectric/scattering amplitude fluctuation is an ergodic and stationary random process

throughout the random medium, the ensemble averaging can be replaced by the spatial averaging for the convenience of calculation [22]. That is, the ratio characterizing the scattering amplitude change at any spatial position $\overline{R_j}$ has the same statistics, *i.e.* a stationary mean value $\alpha_0$ plus a zero-mean random fluctuation term $\alpha_1(\overline{R_j})$ with the stationary variance $\langle \alpha_1(\overline{R_j})^2 \rangle = \delta^2$, where both $\alpha_0$ and $\delta^2$ are invariant of the spatial coordinates $\overline{R_j}$ under this assumption of ergodicity and stationarity.

Note such a formulation characterizes the mean behavior of the dielectric fluctuation effect throughout the random medium, which is analogous to the permittivity fluctuation model by Vallese and Kong (1981; [88]), where ergodicity and stationarity are utilized to characterize the permittivity fluctuation in snow and ice samples.

Based on the above analysis, a simple dielectric fluctuation model is thus given as follows,

$$\nu_f(\overline{R_j}) = \frac{f_j^{(2)}(\overline{R_j})}{f_j^{(1)}(\overline{R_j})} = \alpha_0 + \alpha_1(\overline{R_j}) \tag{2.102}$$

where $\alpha_0$ is the stationary mean value of the scattering amplitude change, and $\alpha_1(\overline{R_j})$ is a random fluctuation term describing the scattering amplitude fluctuation during the repeat period with $\langle \alpha_1(\overline{R_j}) \rangle = 0$ and $\langle |\alpha_1(\overline{R_j})|^2 \rangle = \delta^2$ for any spatial point $\overline{R_j}$. Note both $\alpha_0$ and $\alpha_1(\overline{R_j})$ can be complex-valued with the real and imaginary parts satisfying the same equation (2.102).

To take into account the collection of discrete vegetation components, noting that both of the branches and trunks can be modeled as finite-length dielectric cylinders, the fluctuation uncertainty of $\nu_f(\overline{R_j})$ is primarily attributed to the following four aspects:

- Scatterers have different orientations with respect to the line of sight and/or the incidence polarization.

- Scatterers have different physical dimensions (e.g. branches and trunks can be modeled as dielectric cylinders with different radius $a$ and length $l$).
- Scatterers have different levels of moisture contents (*i.e.* $M_g^{(1)}(\overline{R_j})$).
- Scatterers have different ratios characterizing the moisture change (*i.e.* $\nu_{M_g}(\overline{R_j})$).

In Section 4.2.3, electromagnetic simulations will be presented for the effects as enumerated above. In the following analysis, the introduced small-scale dielectric fluctuation parameters (*i.e.* $\alpha_0$ and $\alpha_1(\overline{R_j})$) are related to the macroscopic repeat-pass InSAR correlation components $S_t(z)$ and $R$ in (2.90). Here, only the vertical coordinate $z$ is used to represent the spatial (*i.e.* $\overline{R_j}$) dependence of the associated quantities.

#### 2.3.4.3 Effect of dielectric fluctuation on $S_t(z)$

Substituting (2.102) and denoting the backscatter intensity in the $1^{st}$ SAR observation as $p(z) = |f_j^{(1)}(z)|^2$, we have the following results

$$\begin{aligned}
\langle f_j^{(1)}(z) f_j^{(2)*}(z)\rangle &= \alpha_0^*\langle p(z)\rangle + \langle p(z)\alpha_1^*(z)\rangle, \\
\langle |f_j^{(1)}(z)|^2\rangle &= \langle p(z)\rangle, \\
\langle |f_j^{(2)}(z)|^2\rangle &= |\alpha_0|^2\langle p(z)\rangle + \langle p(z)|\alpha_1(z)|^2\rangle + 2\langle p(z)\Re[\alpha_0\alpha_1^*(z)]\rangle,
\end{aligned} \tag{2.103}$$

where $\Re$ is the real part operator. Here, the subscript "$\boldsymbol{f}|\boldsymbol{R}$" in (2.62) has been dropped to keep the notation concise, and the spatial dependence is explicitly written out by incorporating the vertical coordinate, $z$.

From (2.62), $S_t(z)$ can be calculated as

$$\begin{aligned} S_t(z) &= \frac{\langle f_j^{(1)}(z) f_j^{(2)*}(z)\rangle}{\sqrt{\langle|f_j^{(1)}(z)|^2\rangle\langle|f_j^{(2)}(z)|^2\rangle}} \\ &= \frac{\alpha_0^*\langle p(z)\rangle + \langle p(z)\alpha_1^*(z)\rangle}{\sqrt{\langle p(z)\rangle}\sqrt{|\alpha_0|^2\langle p(z)\rangle + \langle p(z)|\alpha_1(z)|^2\rangle + 2\langle p(z)\Re[\alpha_0\alpha_1^*(z)]\rangle}} \end{aligned} \tag{2.104}$$

In Section 4.2.3, it will be noticed that the ratio of scattering amplitude change fluctuates around its mean value, while the backscatter intensity changes independently. In other words, the statistical correlation between the fluctuation term $\alpha_1(z)$ and the backscatter intensity $p(z)$ is very low, *i.e.* $\alpha_1(z)$ can be considered independent of $p(z)$. This can be mathematically expressed as $\langle\psi(p(z))\phi(\alpha_1(z))\rangle = \langle\psi(p(z))\rangle\langle\phi(\alpha_1(z))\rangle$ for any given functions of $\psi$ and $\phi$ [22].

Noticing that $\langle\alpha_1(z)\rangle = 0$, (2.104) is simplified as

$$S_t(z) = \frac{\alpha_0^*}{\sqrt{|\alpha_0|^2 + \langle|\alpha_1(z)|^2\rangle}} = \frac{\alpha_0^*}{|\alpha_0|}\cdot\frac{1}{\sqrt{1+\frac{\langle|\alpha_1(z)|^2\rangle}{|\alpha_0|^2}}}. \tag{2.105}$$

Since the dielectric fluctuation of the random medium is assumed ergodic and stationary, after substituting the constant variance of dielectric fluctuation $\langle|\alpha_1(z)|^2\rangle = \delta^2$, (2.105) is rewritten as

$$S_t(z) = \frac{\alpha_0^*}{|\alpha_0|}\cdot\frac{1}{\sqrt{1+\frac{\delta^2}{|\alpha_0|^2}}} = S_t, \tag{2.106}$$

which is also a constant value independent of the vertical coordinate.

If there is no dielectric fluctuation, *i.e.* $\alpha_1(z) = 0$ for all $z$, (2.106) reduces to

$$S_t = \frac{\alpha_0^*}{|\alpha_0|}. \tag{2.107}$$

Then, $|S_t| = 1$ and there is no decorrelation effect as expected (in the case of single-pass interferometry). Also, if the fluctuation uncertainty is very small, *i.e.* $\frac{\delta^2}{|\alpha_0|^2} \ll 1$, a Taylor series expansion of (2.106) can be performed as

$$S_t = \frac{\alpha_0^*}{|\alpha_0|} \cdot \left(1 - \frac{1}{2}\frac{\delta^2}{|\alpha_0|^2} \cdots \right) \tag{2.108}$$

It is clearly shown that decorrelation occurs due to dielectric/scattering amplitude fluctuation.

#### 2.3.4.4 Effect of dielectric fluctuation on $R$

Similarly, with the use of (2.102), and denoting the extinction-weighted backscatter intensity in the $1^{st}$ SAR observation as $q(z) = \tau(z)e^{\frac{2k_e}{\cos\theta_t}z}|f_j^{(1)}(z)|^2$, we can thus express (2.80) and (2.81) as

$$\begin{aligned} \sigma_1(z) &= \langle q(z)\rangle, \\ \sigma_2(z) &= |\alpha_0|^2\langle q(z)\rangle + \langle q(z)|\alpha_1(z)|^2\rangle + 2\langle q(z)\Re[\alpha_0\alpha_1^*(z)], \end{aligned} \tag{2.109}$$

where the change in the extinction profile has been ignored.

Assuming that the fluctuation term, $\alpha_1(z)$, is independent of the extinction-weighted backscatter intensity term, $q(z)$ (similar to the argument in Section 2.3.4.3), the constant normalization factor $R$ in (2.85) can be calculated as

$$\begin{aligned} R &= \frac{\int \sqrt{\sigma_1(z)\sigma_2(z)}dz}{\sqrt{\int \sigma_1(z)dz \int \sigma_2(z)dz}} \\ &= \frac{\int \sqrt{\langle q(z)\rangle}\sqrt{|\alpha_0|^2\langle q(z)\rangle + \langle q(z)|\alpha_1(z)|^2\rangle + 2\langle q(z)\Re[\alpha_0\alpha_1^*(z)]\rangle}dz}{\sqrt{\int \langle q(z)\rangle dz \int \left(|\alpha_0|^2\langle q(z)\rangle + \langle q(z)|\alpha_1(z)|^2\rangle + 2\langle q(z)\Re[\alpha_0\alpha_1^*(z)]\rangle\right) dz}} \\ &= \frac{\int \sqrt{\langle q(z)\rangle}\sqrt{|\alpha_0|^2\langle q(z)\rangle + \langle q(z)\rangle\langle|\alpha_1(z)|^2\rangle}dz}{\sqrt{\int \langle q(z)\rangle dz}\sqrt{\int (|\alpha_0|^2\langle q(z)\rangle + \langle q(z)\rangle\langle|\alpha_1(z)|^2\rangle)dz}}. \end{aligned} \tag{2.110}$$

Also, noticing $\langle \alpha_1(z) \rangle = 0$ with $\langle |\alpha_1(z)|^2 \rangle = \delta^2$ under the assumption of ergodicity and stationarity, (2.110) can be further simplified as

$$R = \frac{\int \langle q(z) \rangle \sqrt{|\alpha_0|^2 + \delta^2} dz}{\sqrt{\int \langle q(z) \rangle dz} \sqrt{\int \langle q(z) \rangle (|\alpha_0|^2 + \delta^2) dz}} = 1 \tag{2.111}$$

Therefore, there is no decorrelation effect due to $R$ under the condition of ergodic and stationary dielectric fluctuation. In this case where $\langle \alpha_1(z) \rangle = 0$ and $\langle |\alpha_1(z)|^2 \rangle = \delta^2$, since $R$ does not introduce decorrelation, the decorrelation from $S_t$ dominates the temporal decorrelation due to dielectric fluctuation. Note if the statistics of the dielectric fluctuation is spatially varying along the vertical coordinate, we can treat the random medium as a layered medium with each vertical layer still being ergodic and stationary. In such a scenario, (2.105) and (2.110) still hold with both the stationary mean and variance dependent on the vertical coordinate. However, when the fluctuation uncertainty $\frac{\langle |\alpha_1(z)|^2 \rangle}{|\alpha_0|^2}$ is small, a Taylor series expansion is performed on both equations. It can be found that $R$ always introduces higher order infinitesimals than $S_t(z)$; in other words, $S_t(z)$ is the dominant term that accounts for the temporal decorrelation due to dielectric fluctuation.

# CHAPTER 3

# PARAMETER RETRIEVAL APPROACHES

In this chapter, parameter retrieval algorithms will be developed so as to exploit the InSAR scattering models derived in Chapter 2. First, in Section 3.1, a dual-frequency InSAR observational configuration is proposed to relate the volume parameters (such as snow grain size, volume fraction, layer depth) as well as those aspects that characterize ground scattering contributions (such as ground topographic height and ground-to-volume ratio) to the single-pass InSAR correlation data. Further, in Section 3.2, a simple and efficient approach is developed to retrieve forest height from repeat-pass InSAR correlation measurements, where temporal decorrelation effects such as target dielectric change and random motion dominate.

## 3.1 Retrieval of snow characteristics using single-pass InSAR

### 3.1.1 Schematic outline for retrieving snow characteristics

The actual design of the snow retrieval approach for using single-pass InSAR data relies on the sophisticated investigation of the experimentally collected InSAR data along with a reliable error analysis, which is beyond the scope of this dissertation and serves as an important future work. In contrast, this section only provides the schematic outline and examines the feasibility for retrieving snow characteristics from single-pass InSAR correlation data, which is based on the derived InSAR scattering models in Section 2.2.3 and the simulated results that will be shown in Section 4.1. From the simulated results (Section 4.1), Ka-band InSAR phase is sensitive to the snow grain size and volume fraction, while L-band InSAR coherence and phase have

a good sensitivity to the snow depth information. Therefore, the combination of Ka-band and L-band InSAR data have the potential of measuring the snow characteristics (grain size, volume fraction, depth). According to the simplified RVoG model, (2.51), it is helpful to consider the following generic form,

$$\begin{bmatrix} \phi^{\mathrm{Ka}} \\ A^{\mathrm{L}}_{\mathrm{HH}} \\ \phi^{\mathrm{L}}_{\mathrm{HH}} \\ A^{\mathrm{L}}_{\mathrm{HV}} \\ \phi^{\mathrm{L}}_{\mathrm{HV}} \\ A^{\mathrm{L}}_{\mathrm{VV}} \\ \phi^{\mathrm{L}}_{\mathrm{VV}} \end{bmatrix} = M \left( \begin{bmatrix} l \\ f_v \\ d \\ m^{\mathrm{L}}_{\mathrm{HH}} \\ m^{\mathrm{L}}_{\mathrm{HV}} \\ m^{\mathrm{L}}_{\mathrm{VV}} \\ h \end{bmatrix} \right) \tag{3.1}$$

where $A^{\mathrm{L}}$ and $\phi^{\mathrm{L}}$ denote the L-band InSAR correlation magnitude and phase, and the subscripts "HH", "HV" and "VV" are used to represent different polarizations of the L-band InSAR observations. Note for L-band data, the ground-to-volume ratio is explicitly written as polarization-dependent. However, the ground scattering can be ignored (*i.e.* $m \approx 0$) for Ka-band since the penetration depth is quite small ($<$ 0.5 m) from the simulated results in Section 4.1. As will be shown in Section 4.1, since the Ka-band InSAR coherence is close to the unity and invariant with respect to snow grain size and volume fraction, it is thus sufficient to only use the Ka-band interferometric phase $\phi^{\mathrm{Ka}}$. Therefore, (3.1) clearly shows that the observable space and the parameter space have been connected via the RVoG model (2.51).

Note that in (3.1), none of the observables is sensitive to all of the parameters. In fact, (3.1) can be decomposed into several components based on the sensitivity of the observable(s) with respect to individual parameters, which is illustrated in Figure 3.1. From Figure 3.1, Ka-band InSAR phase is the only observable that is sensitive to the snow grain size and volume fraction, however, this quantity is also

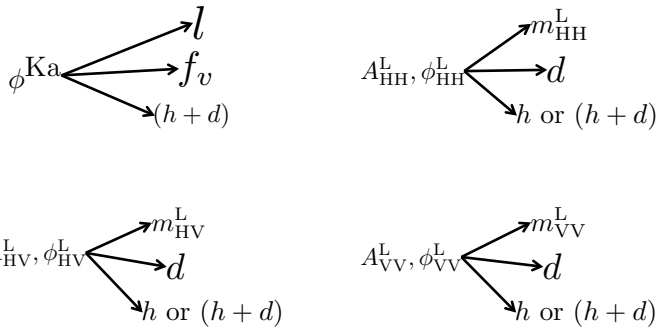


Figure 3.1: Illustration of the observable(s) that have a good sensitivity to the individual parameters. Note $(h+d)$ is the topographic height at the top of the snow surface as indicated in Figure 2.6, which corresponds to the center of the resolution cell. Given the combination of snow bottom $h$ (the topographic height at the ground surface) and the snow layer depth $d$, it is equivalent to know both the depth $d$ and the snow top $(h+d)$.

determined from the topographic height at the snow top surface (or equivalently the reference InSAR phase $\phi_0$) according to the RV model presented in Section 2.2.3. Here, the RV model is sufficient to model the Ka-band InSAR phase, since when $m \approx 0$, the RVoG model reduces to the RV model. For each polarization of L-band data, both the coherence and phase are dependent on the ground-to-volume ratio, the layer depth and the ground topographic height. Hence, all of the sensitivity components in Figure 3.1 rely on the determination of the snow layer depth and the ground topographic height.

There are several methods that can be utilized to measure the snow layer depth and ground topographic height independently, such as the polarimetric InSAR (a.k.a. PolInSAR) techniques [57, 49] (such a method differentiates the volume scattering component from the ground scattering contribution with use of polarimetric signatures), or alternatively 2) retrieval methods using SAR backscatter power [71] as well as 3) radar and/or lidar altimetry techniques [41, 50].

Therefore, given the snow depth and ground topographic height, only the sensitivity component that connects the Ka-band InSAR phase to snow grain size and volume fraction remains in Figure 3.1. By referring to the RV model (2.43), this can

be formulated as

$$\phi^{\mathrm{Ka}} = M\left(\begin{bmatrix} l \\ f_v \end{bmatrix}\right). \tag{3.2}$$

Here, we have two unknown parameters $l$ and $f_v$ along with a single observable $\phi^{\mathrm{Ka}}$, which implies that a unique solution is by no means achievable. Rather, a functional relationship between snow grain size $l$ and volume fraction $f_v$ will be obtained, which will be simulated in Section 4.1.3. This is termed as *Ka-band InSAR phase ambiguity* in measuring the snow grain size and volume fraction.

To this end, it can be concluded that by only using Ka-band and L-band InSAR correlation measurements, the snow layer depth and the ground topographic height can be inverted, as well as a functional relationship between the snow grain size and volume fraction. The unique determination of both the grain size and volume fraction requires to incorporate auxiliary measurements. For example, the volume fraction (equivalently snow density) can be independently retrieved from SAR backscatter power measurements [70]. Once the volume fraction and layer depth are both determined, the Snow Water Equivalent (SWE) measure can be calculated as in (1.2).

### 3.1.2 More discussion on practical implementation

As for the practical design and implementation of the InSAR-based snow retrieval approach, several practical issues that must be addressed in future work are discussed as below.

First, the proposed dual-frequency inversion approach is able to estimate the snow depth to a plausible accuracy, however, it cannot uniquely determine the snow grain size and volume fraction; rather, a functional relationship between these two quantities can be determined. This is similar to [71], although it is the dual-frequency

SAR backscatter power data that were used instead of InSAR correlation data. This relationship can be augmented with auxiliary field data, prior knowledge and results from other methods/sensors such as L-band SAR backscatter power [70] to uniquely determine the grain size and volume fraction.

Also, the dominating error source for the InSAR-based snow retrieval approach is due to the InSAR correlation measurement uncertainty. However, there is a limit of reducing the measurement uncertainty (and thus the error in the inverted snow parameters) through the use of *multi-look averaging* in estimating the InSAR correlation, e.g., as illustrated in Figure 4.7, when the number of looks $L$ reaches 200, the measurement uncertainty does not improve substantially as $L$ continue increases. In order to overcome this performance limit and further enhance the inversion accuracy, *multi-pixel averaging* is therefore proposed to the inverted snow parameters, which is able to reduce the error by a factor of $\sqrt{M}$ where $M$ is the number of pixels in this averaging. So, a trade-off between the inversion accuracy and the spatial resolution must be carefully examined and designed.

In this work, all of the modeled analysis along with the simulated results are based on the Percus-Yevick pair distribution function. Although the Percus-Yevick function is capable of reflecting the variation of InSAR phase as a function of snow parameters, in practice, however, the pair distribution function for densely-packed dry snow could be very complicated in the modeling aspect. As for the accurate inversion performance, experimentally determined pair distribution functions can be incorporated. For example, a look-up table and/or database relating the SAR/InSAR measurements to different choices of snow parameters can be constructed so as to determine the pair distribution function.

The layer effects of dry snow is not considered in this work, since Ka-band data is utilized so that the extinction effect dominates and the penetration depth is quite short. In other words, the inverted snow grain size and volume fraction are only valid

for the top layer. However, given the snow layer depth, and combining with prior geophysical knowledge of snow layer accumulation, it is also possible to recover the vertical structural variation of snow parameters.

Both of the InSAR correlation model and the retrieval method performance rely on the accuracy of the local incidence angle. This is a potential limitation of the InSAR-based snow retrieval approach as well as the one that uses SAR backscatter power in [70, 71]; however, an accurate Digital Elevation Model (DEM) can be incorporated to overcome this restriction.

Even though the above limitations exist, the dense-medium InSAR scattering model derived in this work as well as the associated parameter retrieval analysis have the potential of contributing complimentary observations of snow characteristics to existing snow retrieval techniques, as well as an observational prototype for future Ka-band (e.g. NASA's Surface Water and Ocean Topography or SWOT [18]) and L-band (e.g. NISAR [3]) InSAR missions.

## 3.2 Retrieval of vegetation characteristics using repeat-pass InSAR

In this section, a simplified semi-empirical forest height inversion method is first introduced and then implemented through the use of a Least Squares curve fitting. As an overall guide, the flowchart is demonstrated below in Figure 3.2 showing the associated InSAR processing and inversion procedure. Specifically, Section 3.2.1 discusses the modified RVoG model, Section 3.2.2 derives the simplified Sinc inversion model, Section 3.2.3 describes the semi-empirical forest height inversion approach utilizing nonlinear Least Squares fitting along with the Gauss-Newton numerical method, and the InSAR processing details will be further provided in Section 5.1.

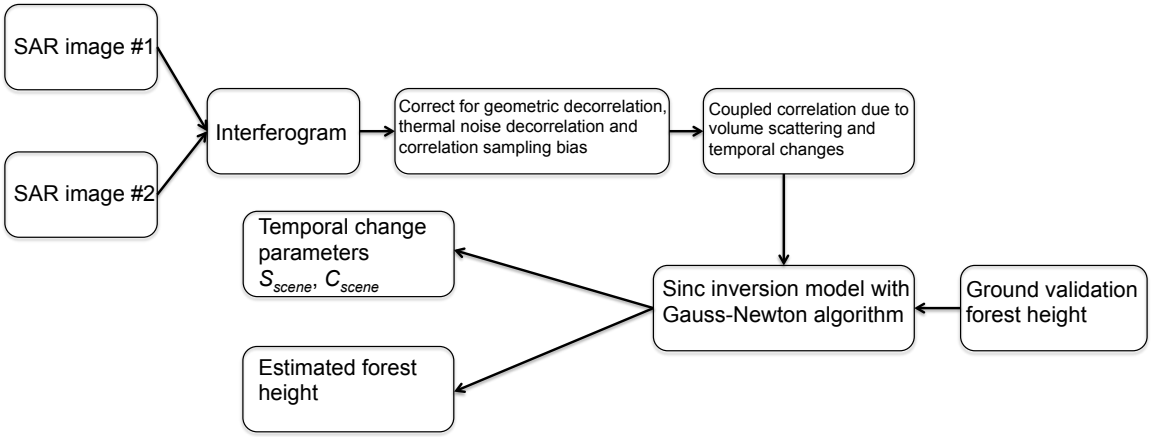


Figure 3.2: Flowchart of the InSAR processing and the inversion procedure. The sinc inversion model and the Gauss-Newton algorithm are discussed in Section 3.2.2 and Section 3.2.3, respectively, while InSAR processing details are to be provided in Section 5.1.

### 3.2.1 Discussion on the modified RVoG model

From the modified RVoG model that is derived in Section 2.3.3, the correlation component of the coupled effect from volume scattering and temporal change is written as (with the ground interferometric phase omitted)

$$\gamma_{v\&t} = \frac{\gamma_d^v \gamma_{v\&m} + \gamma_d^g m}{1+m} \tag{3.3}$$

with

$$\gamma_{v\&m} = \frac{\int \exp\left[-\frac{1}{2}(\frac{4\pi}{\lambda})^2 \sigma_r^2(z)\right] \sigma_V(z) \exp\left(-j\kappa_z z\right) dz}{\int \sigma_V(z) dz} \tag{3.4}$$

where $m$ is the ground-to-volume ratio, and $\sigma_V(z)$ is the extinction-weighted backscattering profile (*i.e.* the geometric mean of those from the two passes) for the volume only. The variables $\gamma_d^v$ and $\gamma_d^g$ represent the temporal correlation component due to dielectric change for the volume and the underlying ground, respectively, and $\gamma_{v\&m}$ is the coupled correlation component due to volume scattering and random motion. In

the above, $\kappa_z$ is the interferometric vertical wavenumber (in units of rad/m), $\sigma_r(z)$ is the random motion standard deviation along the line of sight, and $\lambda$ is the wavelength.

The motion standard deviation in (3.4) is here assumed to be linear as a function of height, *i.e.*,

$$\sigma_r(z) = \frac{\sigma_{\text{ref}}}{h_{\text{ref}}} z \tag{3.5}$$

where $\sigma_{\text{ref}}$ denotes the motion standard deviation at some reference height $h_{\text{ref}}$ (selected to be 15 m in this work and also as in [33]). Equation (3.5) is equivalent to [5] and in contrast to [33] (where the motion variance is assumed linear in the vertical coordinate) because results created using the assumption in (3.5) created a "best fit" between ground validation observations and height in this application (to be discussed later in Section 5.3). Moreover, the ground motion term used in [33] is not used in this model since the wind-induced ground-motion is expected to be small in comparison to volume-motion. In contrast, dielectric change of the ground surface is accounted for by including a term for ground dielectric change, $\gamma_g^d$, as in [5, 40, 56].

The model parameters, $\gamma_d^v$, $\gamma_d^g$ and $\sigma_r$, in (3.3) through (3.5) are a function of the temporal decorrelation, which is target dependent [2, 76] and results from a combination of factors, including wind and rain effects [33, 40, 56, 5]. Even though these factors are expected to be spatially varying throughout a scene, it is reasonable to assume that they follow some degree of *mean* behavior (Appendix A), and it is this behavior that the model is meant to use for estimating forest height. For those interferograms where the spatial variation is non-stationary, or that the spatial variation is the dominant signature, the interferogram may be eliminated and another used in its place given plenty of interferograms over the same area (e.g., it is not uncommon that dozens of interferograms from ALOS/PALSAR are available). This is possible, because the errors that appear due to spatially varying temporal decorrelation, are detectable within individual scenes (showing up as non-physical height estimates),

and when scenes are mosaicked together, because of large differences in forest height solutions between adjacent scenes.

By setting $\gamma_d^v = S_{scene}$ and $\gamma_d^g = S'_{scene}$, and substituting (3.5) into (3.3), a general model for the combined volumetric and temporal decorrelation can be written as

$$\gamma_{v\&t} = S_{scene} \frac{\gamma_{v\&m} + \mu m}{1 + m} \tag{3.6}$$

with

$$\gamma_{v\&m} = \frac{\int \exp\left[-\frac{1}{2}(\frac{4\pi\sigma_{\text{ref}}}{\lambda h_{\text{ref}}})^2 z^2\right] \sigma_V(z) \exp(-j\kappa_z z)\, dz}{\int \sigma_V(z) dz} \tag{3.7}$$

and

$$\mu = \frac{S'_{scene}}{S_{scene}} \tag{3.8}$$

where $S_{scene}$ and $S'_{scene}$ are complex numbers with magnitudes less than or equal to one, and $\mu$ being the "ground-to-volume ratio" of the temporal decorrelation induced by dielectric fluctuations, which has a complex value with $|\mu| \in [0, \infty)$.

The values of $S_{scene}$, $S'_{scene}$ and $m$ are polarization-dependent, making the use of (3.6) through (3.8) potentially very difficult. Simplified scenarios where this polarization dependence is reduced (e.g., [56, 9]) are often used under the assumption of short temporal baselines [56, 40], in order to apply PolInSAR techniques [57]. When the time between observations for an interferometric pair is on the order of months, both $S_{scene}$ and $S'_{scene}$ are expected to be strongly polarization-dependent, which makes the PolInSAR formulation of determining the vegetation height an underdetermined problem. In this study, we investigate the effect of this polarization-dependence on the inversion using HH-pol and HV-pol channels (Appendix B), although ultimately, it is the HV-pol data that is used for forest height inversion.

### 3.2.2 Sinc inversion model

In practice, there is always a ground scattering component (*i.e.*, $m \neq 0$ in (3.6)) over bare surfaces or sparse forests. It is also possible that a polarization-dependence exists for the parameters $m$ and $\mu$ (see previous section). In Appendix B, simulation results are demonstrated on the performance of the forest height inversion model presented here for HH-pol (characterized by a large value for $m$) and HV-pol (characterized by a small value for $m$) data with various choices of $\mu$. Because of the second-order scattering dependence of cross-polarized fields, it is observed that for HV-pol data, the assumption of a small $m$ (not necessarily to be zero) with $\mu$ close to 1 works well over almost the entire height range and hence performance of this inversion approach is equivalent to the case of $m = 0$. Therefore, the absence of a ground-scattering term (*i.e.*, $m = 0$ [24, 33]; see also Appendix B), for cross-polarized fields is assumed here only in order to simplify the analysis and the derivation of the semi-empirical forest height inversion model.

By making this assumption for HV-pol InSAR correlation data, (3.6) is reduced to

$$\gamma_{v\&t}^{\mathrm{HV}} = S_{scene} \frac{\int \exp\left[-\frac{1}{2}(\frac{4\pi\sigma_{\mathrm{ref}}}{\lambda h_{\mathrm{ref}}})^2 z^2\right] \sigma_V(z) \exp\left(-j\kappa_z z\right) dz}{\int \sigma_V(z) dz} \tag{3.9}$$

This expression is further simplified under the zero-baseline scenario (only to simplify the derivation; to be discussed later), when $\kappa_z = 0$, where (3.9) is rewritten as

$$\gamma_{v\&t}^{\mathrm{HV}} = S_{scene} \frac{\int \exp\left[-\frac{1}{2}(\frac{4\pi\sigma_{\mathrm{ref}}}{\lambda h_{\mathrm{ref}}})^2 z^2\right] \sigma_V(z) dz}{\int \sigma_V(z) dz} \tag{3.10}$$

By utilizing the mean value theorem for integration, it can be shown that there exists an intermediate height, $\xi$, between the ground and the maximum forest height,

$h_v$, (*i.e.*, $\xi \in [0, h_v]$) such that (3.10) can be rewritten as

$$\gamma_{v\&t}^{\mathrm{HV}} = S_{scene} \cdot \exp\left[-\frac{1}{2}(\frac{4\pi\sigma_{\mathrm{ref}}}{\lambda h_{\mathrm{ref}}})^2\xi^2\right] \tag{3.11}$$

Assuming forests with different height values are of the scaled versions of extinction-weighted backscattering profile and height-dependent motion profile (in Section 4.2.1 both extinction coefficient and random motion level are considered constant in the mean's sense in order to ensure this assumption; see Appendix A), $\xi$ is thus proportional to $h_v$, *i.e.*, $\xi = \alpha h_v$ with the proportionality constant $0 \leq \alpha \leq 1$. Therefore, we have

$$\begin{aligned} |\gamma_{v\&t}^{\mathrm{HV}}| &= S_{scene} \cdot \exp\left[-\frac{1}{2}(\frac{4\pi\sigma_{\mathrm{ref}}\alpha}{\lambda h_{\mathrm{ref}}})^2 h_v^2\right] \\ &\approx S_{scene} \cdot \mathrm{sinc}\left(\frac{h_v}{C_{scene}}\right), \text{for } h_v < \pi C_{scene} \end{aligned} \tag{3.12}$$

where

$$C_{scene} = \frac{\lambda h_{\mathrm{ref}}}{2\pi^2\sigma_{\mathrm{ref}}\alpha} \tag{3.13}$$

After taking the magnitude of $\gamma_{v\&t}$, $S_{scene}$ becomes $|S_{scene}|$; however, in order to maintain a concise notation, $S_{scene}$ is used here instead of $|S_{scene}|$, with the exact definition of $S_{scene}$ allowed to be inferred from the context. Here, the scaling factor $C_{scene}$ primarily relates to the random motion level (e.g., due to wind and/or tree regrowth) of the volume scatterers. At the current stage, we know that the higher dielectric change is, the smaller $S_{scene}$ we have, while the greater random motion is, the smaller $C_{scene}$ we have.

Note, importantly, that the sinc function in (3.12) is used to approximate the "Gaussian-like" function in the derivation. This has the benefit of obtaining an upper

limit (*i.e.*, $\pi C_{scene}$) on the maximum inverted height in the presence of uncertainty in measuring the correlation. Without this simplifying approximation, the expression in (3.12) is significantly more complicated and the inverted height will approach infinity as the observed correlation magnitude becomes very low. This is also important, because there is a large uncertainty in estimating low correlation magnitude signals (<0.2; [79]) when the number of sampled looks is small, as is usually the case for spaceborne missions (e.g., 20 looks were used in the study presented here). In such a scenario, the estimation error encountered in the inversion of the Gaussian function of (3.12) will create significant errors in the long "tail" regions of a Gaussian curve, as the forest heights get larger. The validity of using this Sinc function instead of a Gaussian curve is elaborated in Appendix D.

Futhermore, for spaceborne repeat-pass InSAR systems, it is difficult to have $\kappa_z = 0$, and therefore it is also not possible to separate its effect from (3.9). Small values of $\kappa_z$ (<0.15 rad/m; which is taken as the *effective range* of $\kappa_z$ values for this study in Appendix C) can be accommodated by the model in (3.12) under a small-$\kappa_z$ assumption (described in Appendix C). This assumption manifests itself as a bias in (3.10) and a $\kappa_z$-dependent correction factor is included in $\alpha$ (and thus $C_{scene}$) in (3.13). Hence, under the small-$\kappa_z$ assumption, $\alpha$ depends on the extinction-weighted backscattering profile, the height-dependent motion profile, and $\kappa_z$. If a uniform backscattering profile along with an exponential extinction profile is considered (as used in Section 4.2.1), $\alpha$ (and thus $C_{scene}$) only depends on the extinction coefficient (denoted by $k_e$), random motion level $\sigma_{\text{ref}}$ and interferometric vertical wavenumber $\kappa_z$, and can be written as

$$\alpha = \alpha\left(k_e, \sigma_{\text{ref}}, \kappa_z\right) \tag{3.14}$$

It should be noted that the sinc function of (3.12) is not related to the sinc solution derived for forest height estimation in Polarization Coherence Tomography,

PCT [8], where a uniform extinction-weighted backscattering profile is assumed in the absence of temporal change effects. In deriving (3.12), a small-$\kappa_z$ assumption (see Appendix C) is used, and thus the temporal decorrelation effects from dielectric fluctuations and random motion dominate the repeat-pass InSAR correlation rather than the volumetric component associated with PCT. In (3.12), $S_{scene}$ derives from the target dielectric change (perhaps due to moisture change e.g., rain), while $C_{scene}$ (defined as (3.13)) primarily describes the level of random motion (resulting from wind and/or changes in the forest structure). While the expression in (3.12) is not restricted to uniform profiles, in the simulations that follow (Section 4.2.1), a uniform backscattering profile with an exponential extinction profile are used in order to illustrate how the model behaves under conditions of varying motion and forest height.

Since this model utilizes the temporal change effects (both dielectric change and random motion) under the conditions of small, but not zero, values of $\kappa_z$, the performance of this inversion approach does not rely on the ground topography.

### 3.2.3 Semi-empirical forest height inversion approach

Before we look at the parameter estimation, we first discuss and define the resolution in this work. As will be shown later in Section 5.1, all of the interferograms in this work are at a resolution of 20 m $\times$ 30 m. However, due to the observational error in the correlation measurements (*i.e.*, correlation sampling noise [79]) and the target-dependent behavior of the temporal change effects (which is different from stand to stand), spatial averaging (which is referred to as "*multi-pixel averaging*" in this work) must be performed in order to remove these uncertainties. This gives resolution on the order of 10 hectares with RMSE $<$ 4 m.

The observed repeat-pass HV-pol InSAR correlation magnitude, $|\gamma^{\mathrm{HV}}_{v\&t}|$, due to the coupled effect of volume scattering and temporal change can be related to the desired height estimates, $h_v$, by analytically inverting (3.12) over the region of validity,

$h_v < \pi C_{scene}$. An equivalent, more computationally efficient approach, is to use a look-up table. In either case, forest height estimates are based on the fitting parameters, $S_{scene}$ and $C_{scene}$. These parameters can be determined from overlap with regions of known forest height (such as where lidar data is available), or in overlap regions of scenes created by adjacent orbits or along-track observations of the satellite. The process of estimating values of $S_{scene}$ and $C_{scene}$ follows.

In these overlap areas, the set of known heights can be written as, $h_{v_1}$, which are considered as the reference. The heights determined by (3.12) are specified as $h_{v_2}$, and are dependent on both the observed correlation magnitude and the model parameters, $S_{scene}$ and $C_{scene}$. With a set of initial values for $S_{scene}$ and $C_{scene}$, a scatter plot of $h_{v_1}$ versus $h_{v_2}$ can be made, such as that shown in Figure 3.3, where the cloud of data points, on a pixel-by-pixel basis are illustrated by an ellipse.

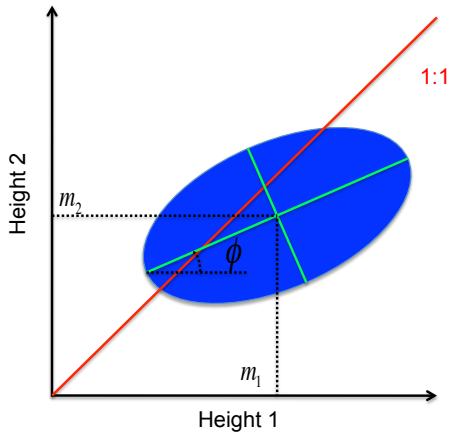


Figure 3.3: Geometric illustration of the comparison between two sets of height estimates. The data cloud is considered an ellipse, with the angle between the major axis and the horizontal axis denoted by $\phi$, and their average heights denoted as $m_1$ and $m_2$. Here Height 1 is considered as the reference height.

Ideally, all points in these overlap regions would follow along the diagonal representing the 1:1 line in Figure 3.3, and in the presence of error sources, would have the ellipse align itself along the line. In general, this is not the case, and there is a offset associated with the location of the ellipse centroid, and its tilt angle. Both of these

parameters can be determined through an optimization procedure which will achieve this alignment.

To achieve this goal, a principal components analysis routine [55] was used here to determine the slope $k$ of the ellipse's major axis (*i.e.*, the tangent of the tilt angle $\phi$ shown in Figure 3.3), and the offset $b$ of the ellipse centroid from the 1:1 line (*i.e.*, the relative difference between the mean heights $m_1$ and $m_2$ in Figure 3.3). Therefore, we have the following definitions for $k$ and $b$, *i.e.*,

$$\begin{aligned} k &= \tan\phi \\ b &= \frac{m_1 - m_2}{(m_1 + m_2)/2} \end{aligned} \tag{3.15}$$

Specifically, in order to solve for the slope $k$, we denote $h_{v_1}^{(i)}$ and $h_{v_2}^{(i)}$ to be the reference height and the InSAR-inverted height for the $i^{th}$ averaged pixel. Suppose there are $N$ averaged pixels in total, we can write the covariance matrix of these two estimates of height as

$$\begin{aligned} \underline{\underline{X}} &= \begin{bmatrix} \sum_{i=1}^{N}(h_{v_1}^{(i)} - m_1)^2 & \sum_{i=1}^{N}(h_{v_1}^{(i)} - m_1)(h_{v_2}^{(i)} - m_2) \\ \sum_{i=1}^{N}(h_{v_1}^{(i)} - m_1)(h_{v_2}^{(i)} - m_2) & \sum_{i=1}^{N}(h_{v_2}^{(i)} - m_2)^2 \end{bmatrix} \\ &= \begin{bmatrix} P_{11} & P_{12} \\ P_{21} & P_{22} \end{bmatrix} \begin{bmatrix} \lambda_1 & 0 \\ 0 & \lambda_2 \end{bmatrix} \begin{bmatrix} P_{11} & P_{12} \\ P_{21} & P_{22} \end{bmatrix}^{-1} \end{aligned} \tag{3.16}$$

where the eigen value decomposition is applied in the last equation. Here, $\lambda_1$ and $\lambda_2$ are the eigen values in the descending order, while $\begin{bmatrix} P_{11} \\ P_{21} \end{bmatrix}$ and $\begin{bmatrix} P_{12} \\ P_{22} \end{bmatrix}$ are their corresponding eigen vectors, respectively. Then, the slope $k$ can be calculated as

$$k = \frac{P_{21}}{P_{11}} \tag{3.17}$$

With $k$ and $b$ determined, $S_{scene}$ and $C_{scene}$ are adjusted such that the long-axis of the ellipse is aligned with the 1:1 line (*i.e.*, $k \approx 1$ and $b \approx 0$). Hence, we come up with the following fitting metric (denoted as the "k-b" fitting metric), *i.e.*,

$$(S^*_{scene}, C^*_{scene}) = \underset{S_{scene}, C_{scene}}{\operatorname{argmin}} \ (k-1)^2 + (b-0)^2 \tag{3.18}$$

which is equivalent to a nonlinear least squares fit (since the fitting parameters $k$ and $b$ are nonlinear functions of the model parameters $S_{scene}$ and $C_{scene}$), where $S^*_{scene}$ and $C^*_{scene}$ are the desired optimum values of the model parameters. To solve the above nonlinear least squares problem, a Gauss-Newton algorithm [54] is applied, *i.e.*,

$$\begin{bmatrix} S^*_{scene} \\ C^*_{scene} \end{bmatrix} = (\underline{\underline{J}}^T \underline{\underline{J}})^{-1} \underline{\underline{J}}^T \begin{bmatrix} 1-k_0 \\ 0-b_0 \end{bmatrix} + \begin{bmatrix} S_{scene_0} \\ C_{scene_0} \end{bmatrix} \tag{3.19}$$

where $S_{scene_0}$ and $C_{scene_0}$ are the initial guess of the model parameters, and $k_0$ and $b_0$ are the fitting parameters corresponding to this initial case. The matrix $\underline{\underline{J}}$ is the Jacobian matrix (calculated at the initial point) that is defined as in (3.20) and can be computed numerically, *i.e.*,

$$\underline{\underline{J}} = \left[ \begin{array}{cc} \frac{\partial k}{\partial S_{scene}} & \frac{\partial k}{\partial C_{scene}} \\ \frac{\partial b}{\partial S_{scene}} & \frac{\partial b}{\partial C_{scene}} \end{array} \right] \Bigg|_{\substack{S_{scene_0} \\ C_{scene_0}}} \tag{3.20}$$

The Gauss-Newton algorithm is an iterative numerical method, which iteratively considers the derived model parameters on the left-hand side of (3.19) as the new initial point for another circulation of (3.19). Regardless of the accuracy of the initial point, convergence for the type of data in the present work has been achieved after the third iteration.

An alternative to the "k-b" fitting metric would be to use the Euclidean norm instead. This is successful when the Root Mean Squared Error (RMSE) between the

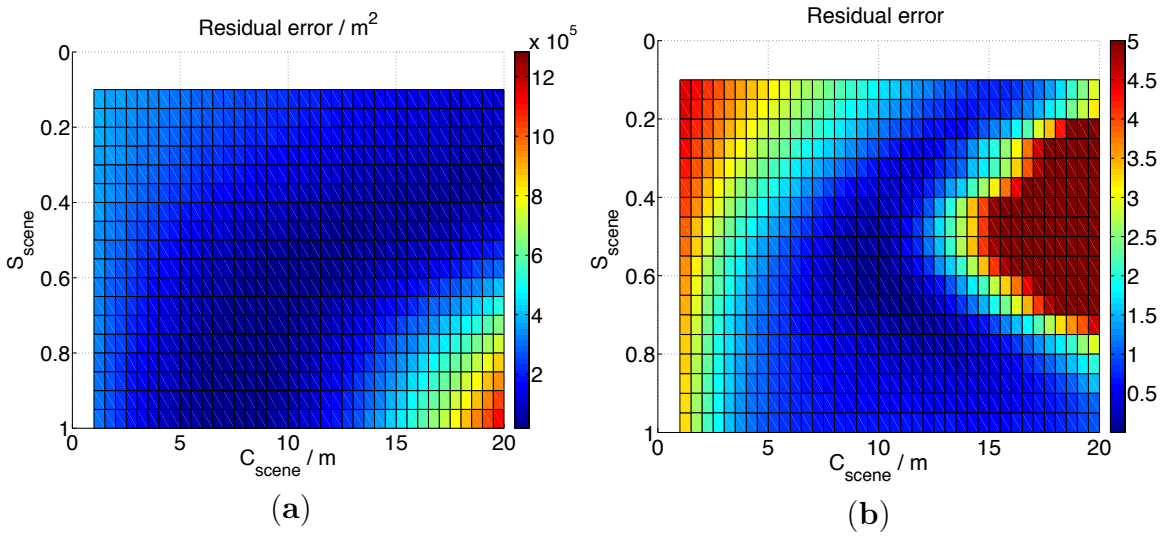


Figure 3.4: The two dimensional residual error distribution over the $S_{scene}$ and $C_{scene}$ plane with (**a**) the Euclidean norm as the fitting metric and (**b**) the "k-b" fitting metric for the experimental data with RMSE of 3.9 m.

ground validation and initial height estimates is small. However, when the RMSE is large, *i.e.*, $> 3$ m, the "k-b" fitting metric proves more robust. An example is shown in Figure 3.4, where the input data RMSE is 3.9 m. This figure shows the residual error plotted as a function of $S_{scene}$ and $C_{scene}$, the two parameters that are being determined, using the two different error metrics: the Euclidian norm (Figure 3.4a) and the "k-b" fitting metric (Figure 3.4b). As can be seen in the set of figures, it is difficult to determine the global minimum using the Euclidean norm, whereas the "k-b" fit is much more well behaved. The reason is that when the RMSE is large, the Euclidean norm metric is not sensitive to the orientation of the data cloud depicted in Figure 3.3. Here, even though the RMSE will be small, it will not guarantee a good linear relationship with the ground validation data. Use of the "k-b" metric, as described in (3.18), and illustrated in Figure 3.4b, the global minimum is better defined and guarantees this linear relationship (since $k \approx 1$) while also maintaining a small RMSE.

# CHAPTER 4

# SIMULATED VALIDATION RESULTS

In this chapter, simulated results are presented so as to validate the InSAR scattering models in Chapter 2 and the inversion algorithms proposed in Chapter 3. These results are shown for the single-pass InSAR observation of snow (Section 4.1) and repeat-pass InSAR observation of vegetation (Section 4.2), respectively.

## 4.1 Single-pass InSAR observation of snow

### 4.1.1 Optimal InSAR observing configuration

It can be seen in (2.43) and (2.51) that any one observation of the complex correlation that would contain at most two independent variables (e.g. the magnitude and phase), that it is not possible to invert for the parameters that describe a dense random medium. Further, it should be noted that some of the parameters are considered *nuisance*-parameters, and it may be some combination of their values that is of ultimate interest. Such would be the case when estimating the snow water equivalent (SWE), which is a combination of the snow depth and volume fraction. With the availability of a forward model that relates these desired characteristics to the interferometric observables, it is possible to use simulations of the forward model to determine what combination of observations would best yield a retrieval for these desired parameters.

To begin, we consider a snow layer with spherical ice particles with a dielectric constant of $\epsilon_r = 3.2 + j0.001$ at microwave frequencies [82]. Given a choice of snow particle size and volume fraction, the pair distribution function and the effective

propagation constant can be calculated numerically as described in [82, 85, 83]. In this work, the software package Electromagnetic Wave MATLAB Library (EWML) developed by the University of Washington is utilized and modified to perform these calculations [84].

In this section, the RV model as in (2.42) is utilized by assuming the interferometric phase $\phi_0$ referenced at $\overline{R_0}$ is fixed as illustrated in Figure 2.5, and thus omitted in the simulated InSAR phase results. In such a way, only the dense medium parameters are allowed to vary and thus the sensitivity of the InSAR correlation measurements to the medium parameters can be investigated by isolating the underlying ground. After the InSAR observational configuration with optimal sensitivity to the dense medium parameters is chosen, the RVoG model can be utilized to retrieve snow characteristics which constitutes a potential future work, as outlined in Section 3.1.

For the following simulation, a typical airborne InSAR observational configuration is considered that is consistent with NASA/JPL's UAVSAR viewing geometry [63]. At L-band (operating frequency $f_0 = 1.27$ GHz), the incidence angle is selected as $\theta_i = 30^\circ$, and the perpendicular baseline is set to be $B_\perp = 100$ m at an altitude of $H = 12$ km such that the conventional interferometric wavenumber is calculated as $\tilde{\kappa_z} = 0.76$ rad/m. This is used as the default configuration for the simulations implemented here. When the simulations are performed at different frequencies, the value of $\kappa_z$ is maintained by appropriately scaling the frequency and the baseline but not the incidence angle.

In the simulated InSAR correlations, a Ka-band system with frequency, $f_0 = 35.75$ GHz (the same as NASA's SWOT mission [18]) is used because the wavelength is comparable to the snow grain size, and hence is expected to exhibit a strong volume-scattering signature. As shown in Figure 4.1, both the InSAR coherence and the interferometric phase-inverted penetration depth (phase divided by $\kappa_z$; such a quantity defines the InSAR phase center inside the dense medium with zero phase depth

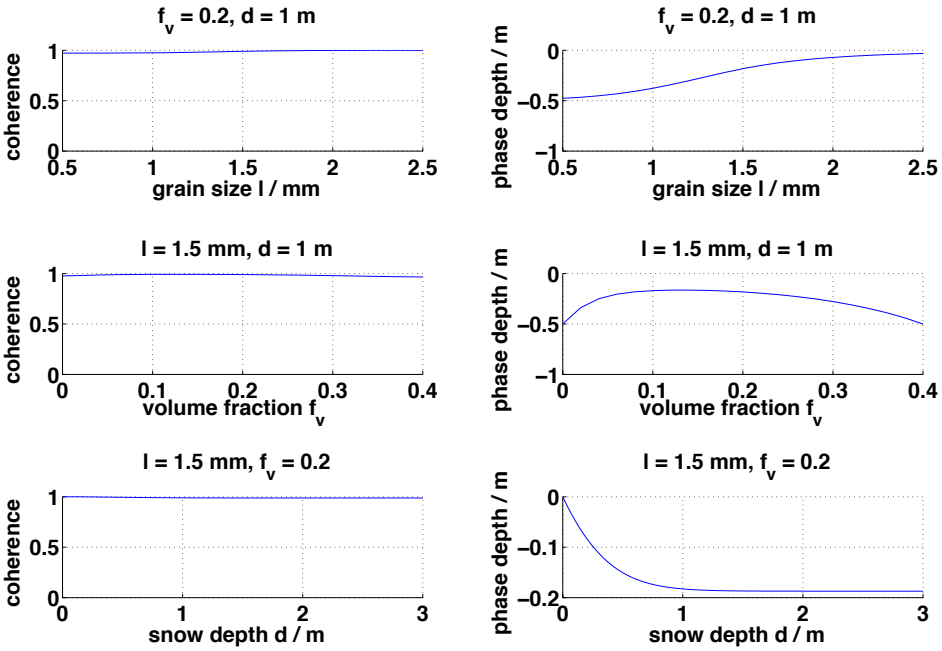


Figure 4.1: InSAR coherence and phase-inverted penetration depth (phase divided by $\kappa_z$) as a function of snow characteristics (grain size $l$, volume fraction $f_v$, layer depth $d$) at Ka-band ($f_0 = 35.75$ GHz). The InSAR viewing geometry is chosen as: incidence angle $\theta_i = 30^\circ$ and perpendicular baseline $B_\perp = 3.5$ m at an altitude of $H = 12$ km ($\tilde{\kappa_z} = 0.76$ rad/m).

representing the top surface) are plotted as a function of the snow characteristics (grain size $l$, volume fraction $f_v$, snow depth $d$). Here, each of the three snow characteristic parameters is studied by keeping the other two parameters fixed.

It can be seen from Figure 4.1 that the interferometric phase is very sensitive to the grain size and volume fraction; however, the InSAR coherence seems to be very close to one and insensitive to the scatterer size and volume fraction. This is due to the fact that the baseline (and thus $\kappa_z$) is small compared to the small layer depth (only 1 m) and thus the coherence in (2.42) is close to the unity. At Ka-band, $k_e$ is large, and strongly dependent on the grain size and volume fraction (e.g. Section 4.1.2). However, the dependence of $k_e$ on grain size or volume fraction is scarcely detectable in the InSAR coherence; rather, its effect is evident in the interferometric phase in (2.42). At 35 GHz, this depth appears to be limited to only

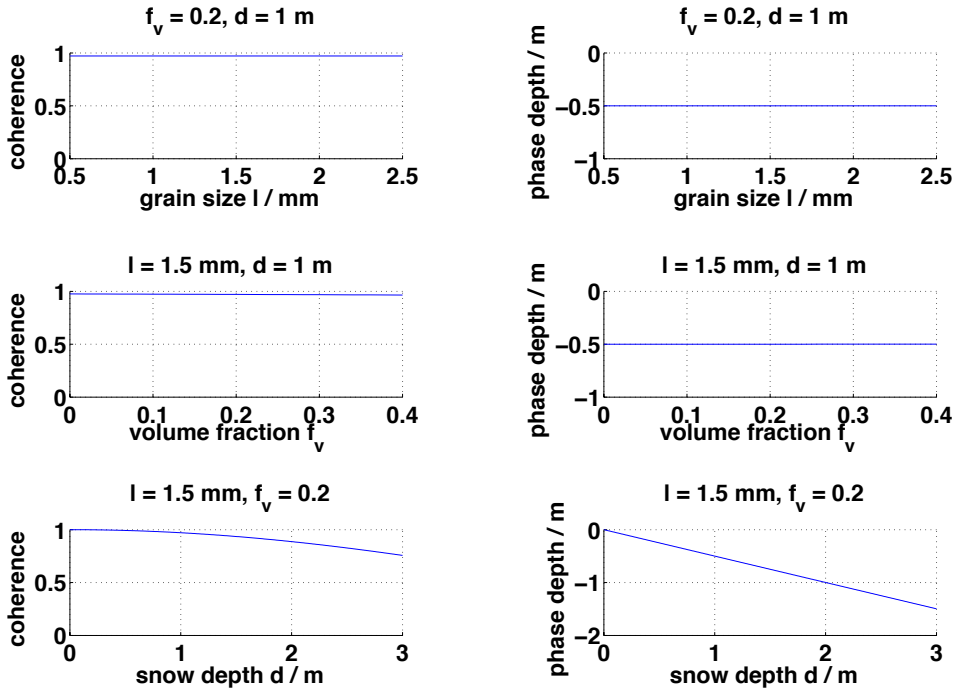


Figure 4.2: InSAR coherence and phase-inverted penetration depth (phase divided by $\kappa_z$) as a function of snow characteristics (grain size $l$, volume fraction $f_v$, layer depth $d$) at L-band ($f_0 = 1.27$ GHz). The InSAR viewing geometry is chosen as: incidence angle $\theta_i = 30°$ and perpendicular baseline $B_\perp = 100$ m at an altitude of $H = 12$ km ($\tilde{\kappa_z} = 0.76$ rad/m).

the top few tens of centimeters of the medium. This can be seen in the bottom-right subplot of Figure 4.1 where the apparent depth of the snow no longer changes after 0.5 m.

The effect of volume scattering on signal extinction is expected to have less an effect on the interferometric signature at frequencies where the snow grain size is significantly smaller than the wavelength. For UAVSAR's L-band radar [63], the free-space wavelength is 24 cm. The results are shown in Figure 4.2 using $\tilde{\kappa_z} = 0.76$ (the same as with Figure 4.1). For this result, both the InSAR coherence and intereferometric phase appear insensitive to the grain size and volume fraction, but are sensitive to the snow depth. This is because the extinction coefficient, $k_e$, is

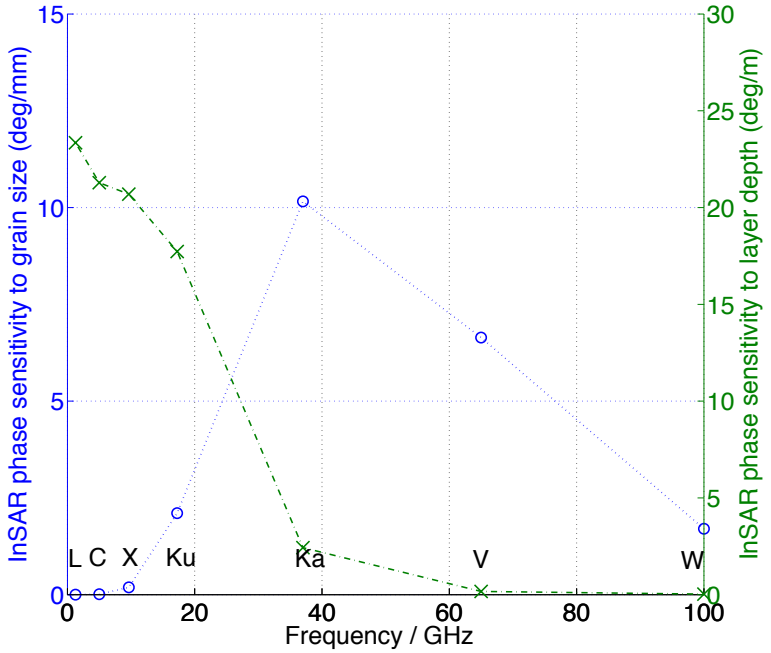


Figure 4.3: InSAR phase sensitivity to the snow grain size and the snow layer depth over the entire range of microwave frequency. The phase sensitivity to the grain size/layer depth is defined as the mean derivative of the phase variation curve with respect to the grain size/layer depth as shown in Figure 4.1 and Figure 4.2.

weakly dependent on snow grain size and volume fraction, but due to $k_e$ is small, the penetration depth is dependent on the total depth of volume scattering.

The combination of Figure 4.1 and Figure 4.2 shows that Ka-band InSAR phase is sensitive to the scatterer information (both the grain size and volume fraction), while L-band InSAR phase and coherence are sensitive to the depth information. This statement can be generalized as illustrated in Figure 4.3, where the mean derivative of InSAR phase variation with respect to the grain size and the layer depth are plotted for a range of microwave bands. The figure shows that the scatterer information is best measured at frequencies where the wavelength is comparable to the scatterer size while lower frequencies (such as L-, C-, X- and Ku-band) are more suited for measuring the depth of the snow layer. To this end, it implies that the combination of Ka- and L-band data has the potential of measuring all three snow parameters

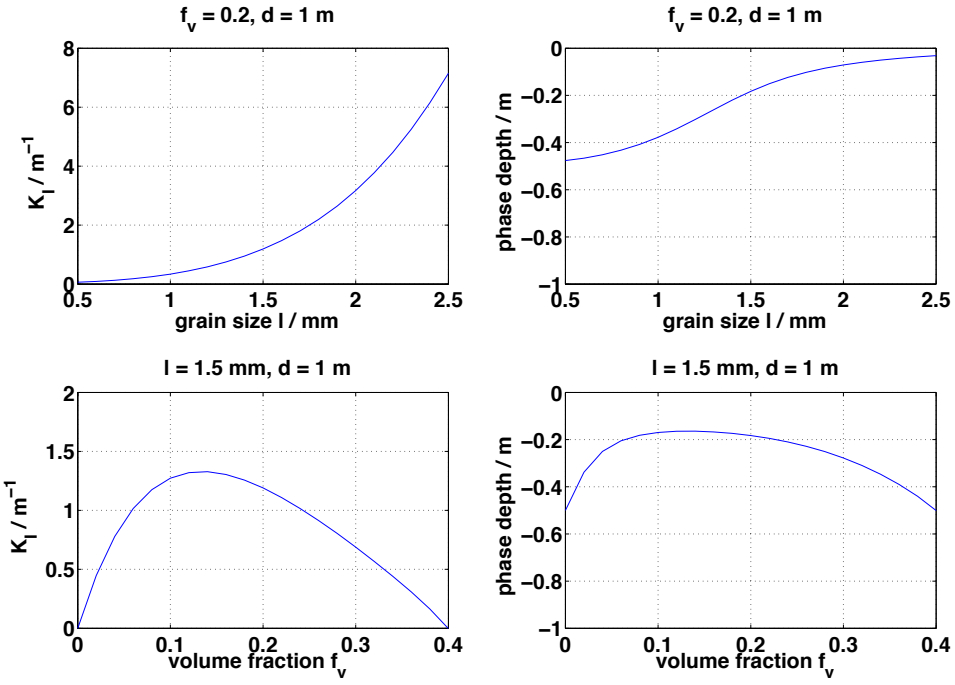


Figure 4.4: The Ka-band InSAR phase analysis with the use of the Percus-Yevick pair distribution function. Both the InSAR phase-inverted penetration depth (phase divided by $\kappa_z$) and the imaginary part of the effective propagation constant (*i.e.* $K_I$) are illustrated, while the same InSAR observational configuration is used as Figure 4.1.

(grain size, volume fraction and layer depth), which constitutes a potential future work for the retrieval of snow characteristics, as outlined in Section 3.1.

### 4.1.2 Effect of pair distribution function on the InSAR phase

In Section 2.1.2, three forms of the pair distribution function were discussed. In this section, the effect of the pair distribution function on Ka-band interferometric phase is further developed. The microwave frequency of Ka-band is chosen here because the wavelength is at a similar scale as the snow grain size, and hence, the most dependent on the pair distribution function. The effects of the pair distribution function using the RV model are shown in Figure 4.4-4.6 for both the Ka-band InSAR penetration depth and the imaginary part of the effective propagation constant, $K_I$.

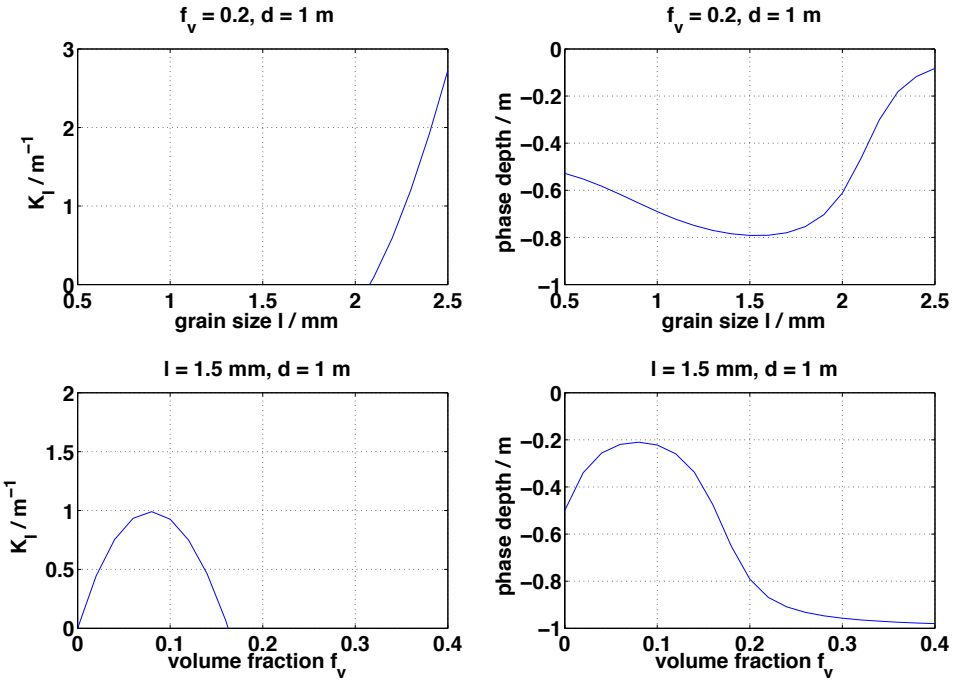


Figure 4.5: The Ka-band InSAR phase analysis with the use of the Hole-Correction pair distribution function. Both the InSAR phase-inverted penetration depth (phase divided by $\kappa_z$) and the imaginary part of the effective propagation constant (*i.e.* $K_I$) are illustrated, while the same InSAR observational configuration is used as Figure 4.1. Note only the positive values of $K_I$ (which have a physical meaning of extinction) are shown in the figure, *i.e.* the missing points in the left-column subplots correspond to the negative values of $K_I$.

In Figure 4.4, the InSAR phase depth variation for the Percus-Yevick pair distribution function is the same as shown in Figure 4.1. As the volume fraction increases from a value of zero to 0.4, the imaginary component of the effective permittivity goes through a resonance effect at $f_v \approx 0.2$ after which $K_I$ decreases as the contrast reduces between the permittivity of the scatterers and the background permittivity of the medium. Eventually, $K_I$ becomes a non-physical number (*i.e.* negative) indicating that (2.5) can no longer be used as an approximation. When the Hole-Correction formula is used as the pair distribution function, shown in Figure 4.5, this point is reached much earlier, when $f_v = 0.15$ (a result that is consistent with [82]). For this reason, care should be used when interpreting plots such as the penetration depth,

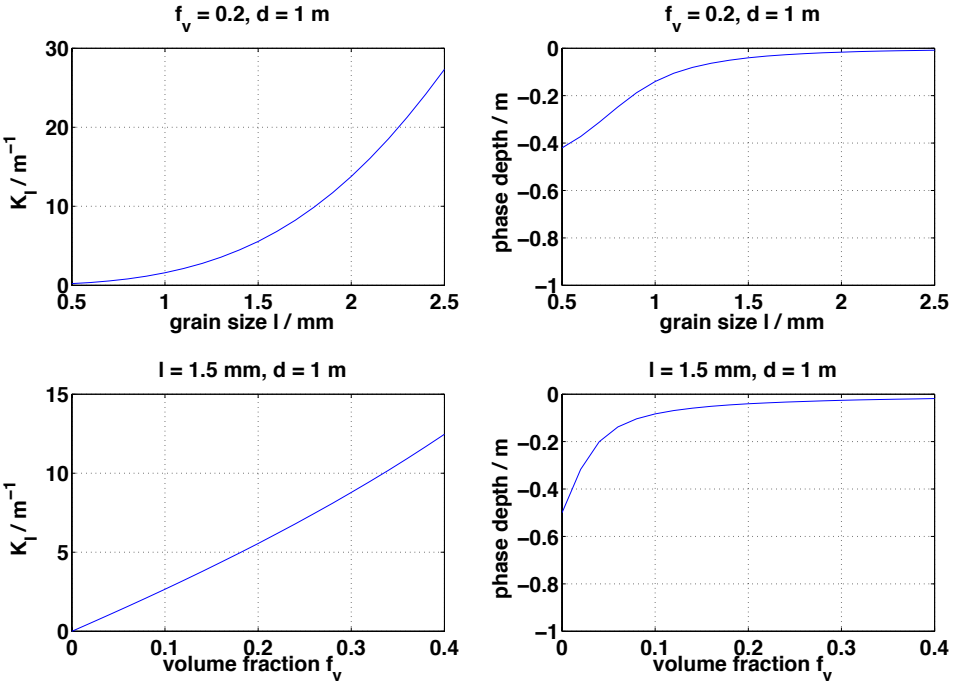


Figure 4.6: The Ka-band InSAR phase analysis by ignoring the pair distribution function. Both the InSAR phase-inverted penetration depth (phase divided by $\kappa_z$) and the imaginary part of the effective propagation constant (*i.e.* $K_I$) are illustrated, while the same InSAR observational configuration is used as Figure 4.1.

where inflection points of the penetration depth are associated with grain sizes of $l \approx 2$ mm and volume fractions of $f_v \approx 0.15$ when the Hole-Correction formula is used.

When the infinitely small scatterer or sparse random medium approximation is used for the pair distribution function, $K_I$ in Figure 4.6 grows almost linearly with volume fraction. For low values of volume fraction, this is expected, as the degree of scattering increases with the number and size of scatterers. At some point, as a function of volume fraction, this trend should reverse when the real part of the effective permittivity approaches that of the inclusions, and the degree of scattering reduces. This effect is not evident in Fig 4.6 and highlights the non-physical nature of this function for volume fraction values larger than a few percent.

This set of simulations and figures illustrates the importance of the pair distribution function in the medium's scattering behavior. While the Percus-Yevick form is sufficient in the current work to demonstrate the potential of using InSAR correlation for modeling the interferomtric signature of snow, more accurate models, perhaps experimentally derived, would be expected to give better results.

### 4.1.3 Ka-band InSAR phase ambiguity in measuring snow grain size and volume fraction

As mentioned in Section 3.1, given the ground topographic height and snow depth, a functional relationship between snow grain size and volume fraction can be inverted from Ka-band InSAR phase. In this section, we show the simulated inversion results using the RV model.

In this simplified scenario, the RV model as expressed in (2.43) reduces to (3.2). Since the relationship between the parameters and the observable cannot be analytically expressed, a direct inversion of (3.2) is not feasible. In order to determine the desired snow parameters, a brute-force search can be performed over the two dimensional space $(l, f_v)$ so that some distance metric between the model-predicted value (denoted as $\phi_{mod}^{\mathrm{Ka}}$) and the observed Ka-band InSAR phase measurement (denoted as $\phi_{obs}^{\mathrm{Ka}}$) can be minimized. In this work, a Least Squares fitting metric is utilized as below,

$$(l^*, f_v^*) = \underset{(l, f_v)}{\operatorname{argmin}} \left(\phi_{obs}^{\mathrm{Ka}} - \phi_{mod}^{\mathrm{Ka}}\right)^2 \tag{4.1}$$

Given the layer depth $d = 1$ m along with a fixed ground topographic height, the actual snow parameters are chosen as: grain size $l = 1.5$ mm, volume fraction $f_v = 0.2$. The Ka-band InSAR instrumental parameters along with the viewing geometry are exactly the same as selected in Section 4.1.1. Therefore, the simulated InSAR observables can be calculated through the use of the RV model.

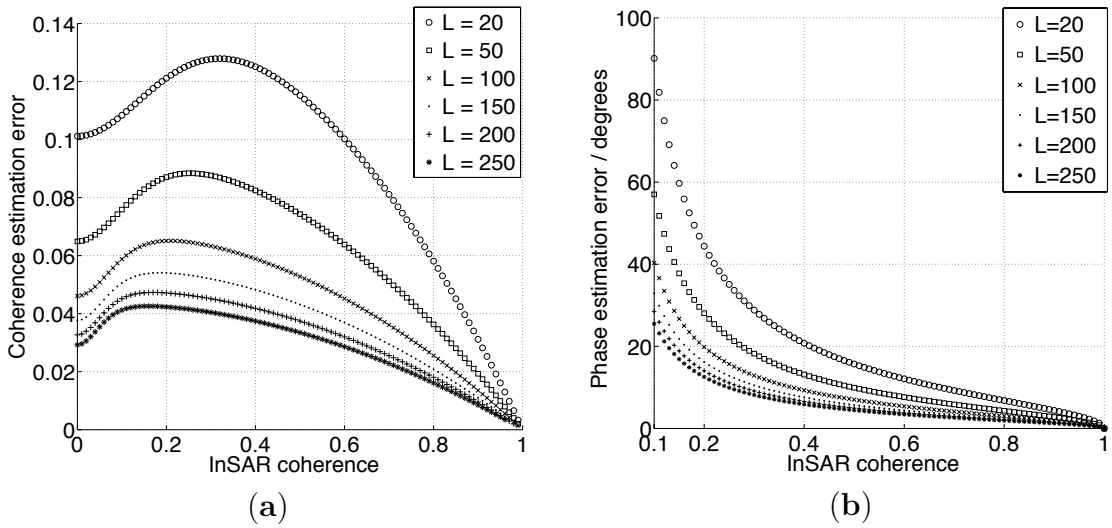


(**a**) (**b**)

Figure 4.7: Standard deviation of the InSAR coherence (**a**) and phase (**b**) measurements as a function of the actual InSAR coherence with different number of looks, $L$, in the InSAR correlation estimation.

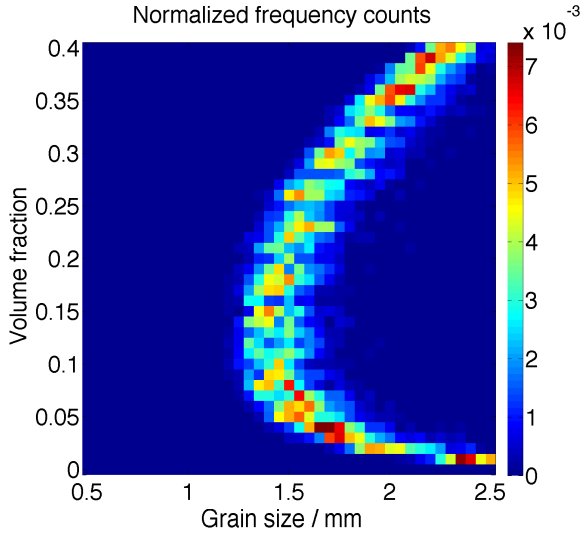


Figure 4.8: The two-dimensional histogram of the inverted snow grain size and volume fraction ("colored value" represents the normalized frequency counts within each bin) from 10,000 Monte Carlo simulations of the inversion only using Ka-band InSAR phase. The actual parameters are: grain size $l = 1.5$ mm and volume fraction $f_v = 0.2$.

Further, the observational error can be introduced to the simulated InSAR phase measurements as illustrated in Figure 4.7. According to [79], the error in the InSAR coherence estimation is dependent on the actual InSAR coherence and the number

of looks $L$, which is illustrated in Figure 4.7a. Similarly, from [38], the estimation uncertainty of the interferometric phase also depends on the actual InSAR coherence and the number of looks L, which is illustrated in Figure 4.7b. In the following simulation, it is assumed 200 independent SAR looks are utilized in estimating the InSAR complex correlation, *i.e.* $L = 200$.

A two dimensional search grid is then established by partitioning the grain size from 0.5 mm to 2.5 mm with step size of 0.05 mm, the volume fraction from 0 to 0.4 with step size of 0.01. The two-dimensional brute-force search as in (4.1) is next performed in order to determine the optimal set of snow parameters. In particular, for each randomized Ka-band InSAR phase measurement, (4.1) will be executed over the two-dimensional search grid with the global minimum determined. After 10,000 Monte Carlo simulations, the two-dimensional histogram of the determined grain size and volume fraction is shown in Figure 4.8, which implies that the desired snow parameters (at the center of Figure 4.8) cannot be uniquely determined; rather, a functional relationship can be determined between the grain size and the volume fraction, which is consistent with the above analysis.

In order to uniquely determine the snow grain size and volume fraction, another measurement must be incorporated into the observation vector in (3.2). For example, in [70], L-band dual-polarized SAR backscatter power is shown to be capable of estimating the volume fraction (and thus snow density) independently with a relative error of 10%. From the functional relationship in Figure 4.8, given a 10% relative error in estimating the volume fraction, the snow grain size can be determined to an absolute error of 0.08 mm (a relative error of 5.3%).

## 4.2 Repeat-pass InSAR observation of vegetation

In this section, simulated results will be presented in order to validate the forest height inversion approach. In particular, the forest height inversion approach is in-

vestigated first by exploiting the analytical model (*i.e.*, the modified RVoG model) as expressed in Section 3.2.1, where the InSAR correlation will be simulated under the noiseless condition. In contrast, we will also simulate the repeat-pass InSAR correlation and validate the inversion method by modifying a numerical simulator PolSARproSim which enables full-polarization electromagnetic simulations of vegetation components at moderately high accuracy. In this case, the PolSARproSim simulated results will be provided under the condition of correlation sampling noise. Finally, we will simulate the electromagnetic scattering by individual dielectric cylinders so as to validate the dielectric fluctuation model proposed in Section 2.3.4.

### 4.2.1 Validation of the forest height inversion approach using the analytical model

In this section, the simulated InSAR correlation magnitude (a Gaussian-like curve) is generated by using the modified RVoG model ((3.9) without any simplification; where the thermal noise and the correlation sampling noise [79] are set to zero), while the estimated forest height is determined from fitting the sinc function in (3.12) into the simulated InSAR data. As a result, under this noiseless scenario, the estimated forest height should correspond to the actual height very well within the non-saturation region of the invertible height range $[0, \pi C_{scene}]$ while small height estimation bias will occur in the saturation region (as detailed in Appendix D). The simulation setup is described as follows.

The correlation due to the coupled effect of volume scattering and temporal change can be simulated by numerically computing the integral in (3.9), while the height estimates obtained from the simulations are determined by inverting (3.12) through the adjustment of the model parameters $S_{scene}$ and $C_{scene}$ (Section 3.2.3). For the extinction-weighted backscattering profile in (3.9), $\sigma_V(z)$, a uniform backscattering profile along with an exponential extinction profile are used. The basic simulation

parameters are chosen such that the extinction coefficient $k_e = 0.1$ dB/m (e.g., a sparse forest; less than the values used in [57, 33] at L-band), the interferometric vertical wavenumber $\kappa_z = 0.05$ rad/m (corresponding to $B_\perp = 500$ m with ALOS's viewing geometry), the magnitude of the correlation component due to dielectric fluctuation $S_{scene} = 0.7$ and the motion standard deviation $\sigma_{\text{ref}} = 2$ cm at the reference height $h_{\text{ref}} = 15$ m (*i.e.*, $\sigma_r(z) = 0.0013z$). By assuming a constant temporal change and forest backscatter profile/extinction coefficient (Appendix A), all of the above parameters are assumed constant in the mean's sense for different values of forest height. The simulation result is illustrated in Figure 4.9a, with the left-hand side plot showing the estimated heights compared to the actual height, and the right-hand side showing the simulated correlation magnitude by using (3.9) compared to the fitted solution of (3.12). Through curve fitting, the parameter $C_{scene}$ is determined to be 10.92, which primarily corresponds to $\sigma_{\text{ref}} = 2$ cm (at a reference height of $h_{\text{ref}} = 15$ m), and $S_{scene}$ fitted to be 0.7. Using (3.13), $\alpha$ is calculated to be 0.82. We make a note here that such simulation parameters are selected to mimic the ground validation results of Section 5.3.

In the remaining three simulations of Figure 4.9, we allow the relevant parameters to vary and study the sensitivity of the inversion results. Specifically, the extinction coefficient is changed to 0.3 dB/m (e.g., a dense forest [33]; Figure 4.9b), the vertical wavenumber is changed to 0 (zero-baseline; Figure 4.9c), and the motion standard deviation is changed to 6 cm at $h_{\text{ref}} = 15$ m (greater level of random motion; Figure 4.9d). It is clear that $\sigma_{\text{ref}}$ is the most important parameter that dominates the value of $C_{scene}$, which is noticed to have a weak dependence on the extinction coefficient. Here, the $\kappa_z$-dependence of $C_{scene}$ can be ignored for $\kappa_z$'s up to 0.05 rad/m, and plays a weak role for $\kappa_z < 0.15$ rad/m (small $\kappa_z$ assumption; Appendix C). Using (3.13), the $\alpha$ values for all of the three subplots are 0.93, 0.82 and 0.65, respectively, which demonstrates the dependence of $\alpha$ on $\sigma_r$ and $k_e$. The $\kappa_z$-dependence of $\alpha$ can

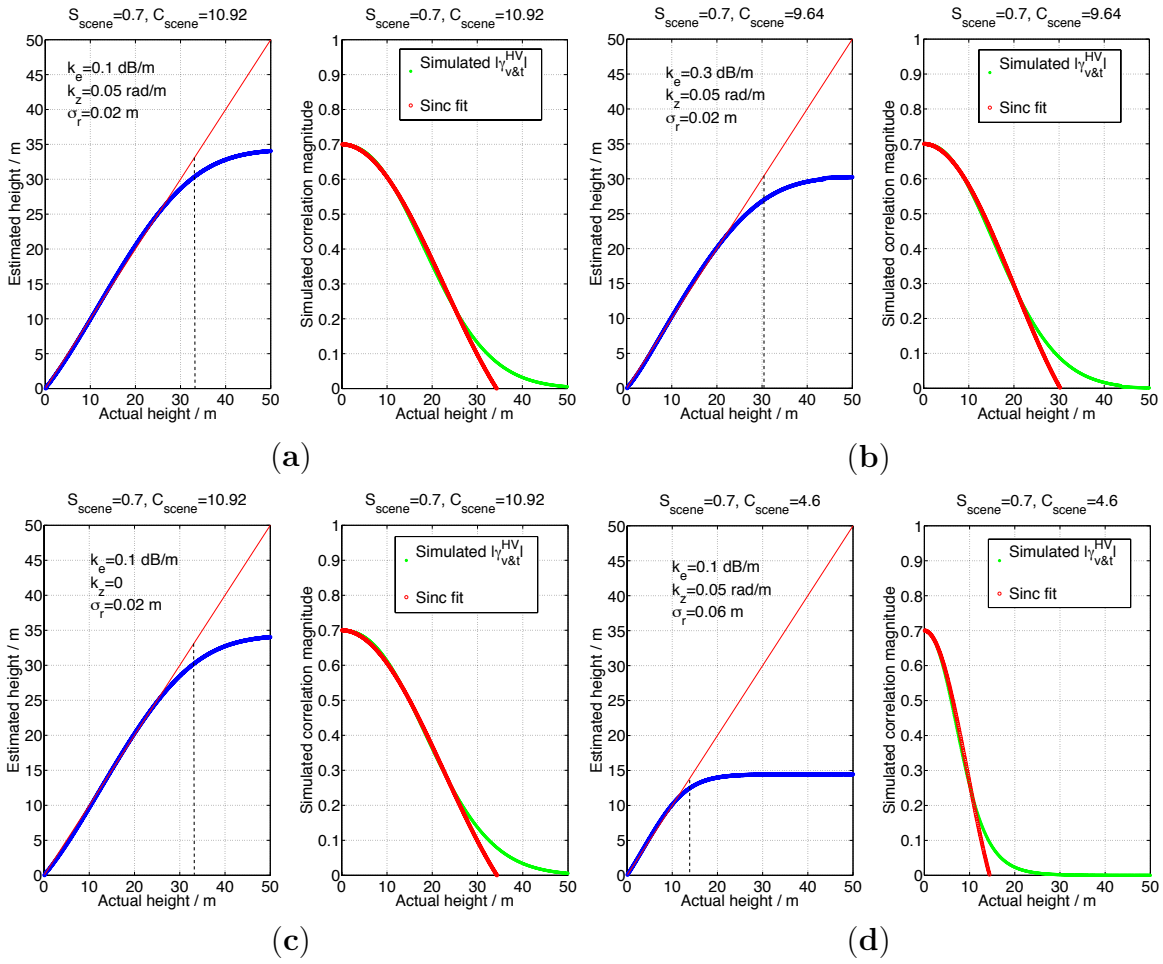


Figure 4.9: Simulation Results. (**a**) serves as the basis of the simulations, showing the estimated height *vs.* the actual height (on the left), and the simulated correlation component *vs.* the sinc approximation (on the right). The simulation parameters for this basic case are: extinction coefficient of 0.1 dB/m, $\kappa_z$ of 0.05 rad/m, $S_{scene}$ of 0.7, motion standard deviation of 2 cm at the reference height of 15 m. (**b**) shows the result with a different extinction coefficient (0.3 dB/m); (**c**) shows the result with a different $\kappa_z$ (0 rad/m); while (**d**) shows the result with a different motion standard deviation (6 cm at the height of 15 m). In all of the subplots, the upper bound of the invertible height range (*i.e.*, $\pi C_{scene}$) is indicated by a dashed vertical line.

be neglected for $\kappa_z < 0.05$ rad/m, although it is noticeable for $\kappa_z$ up to 0.15 rad/m (Appendix C).

Larger random motion levels (possibly induced by higher wind speed) results in smaller values of $C_{scene}$, which will make the saturation point occur at a low height value. In such a scenario, meaningful forest height inversion will be hindered due to

the loss of sensitivity of the model in (3.12) to changes in forest heights. Similarly, larger dielectric changes (possibly due to moisture change) results in smaller values of $S_{scene}$, which will suppress the measured correlation component $\gamma_{v\&t}$ (see (3.9)) by a large amount causing the information to be dominated by the correlation sampling noise [79] as discussed above.

### 4.2.2 Validation of the repeat-pass InSAR model and the forest height inversion approach using the numerical simulator PolSARproSim

In this section, a modified version of the numerical simulator PolSARproSim [91], part of the PolSARpro package developed by the European Space Agency (ESA) for analyzing polarimetric SAR data, is used to perform electromagnetic simulations of the repeat-pass InSAR correlation measurements accounting for the temporal change effects (e.g. both random motion and dielectric change) for a typical forest in a manner that is consistent with the validation of the repeat-pass InSAR model being studied in this work. Simulated results are also shown to validate the forest height inversion approach, as well as to characterize the forest dynamics-induced error in the SAR/InSAR metrics.

#### 4.2.2.1 Introduction to the study area and the simulator

The Harvard forest region (Western Massachusetts, US) has a mean carbon content of 120 MgC/ha, an average height of 30 m, on the order of 800 mature trees/ha, and mostly occupied with red pines, red maples and birch, etc. Because of the study site's long history in forestry and forest ecology, it has been a valuable resource for remote sensing algorithm development. It is expected that the Harvard forest region is a more complex environment in terms of the temporal decorrelation effects, which makes it an attractive test case for extending the work demonstrated, and investigating the associated errors.

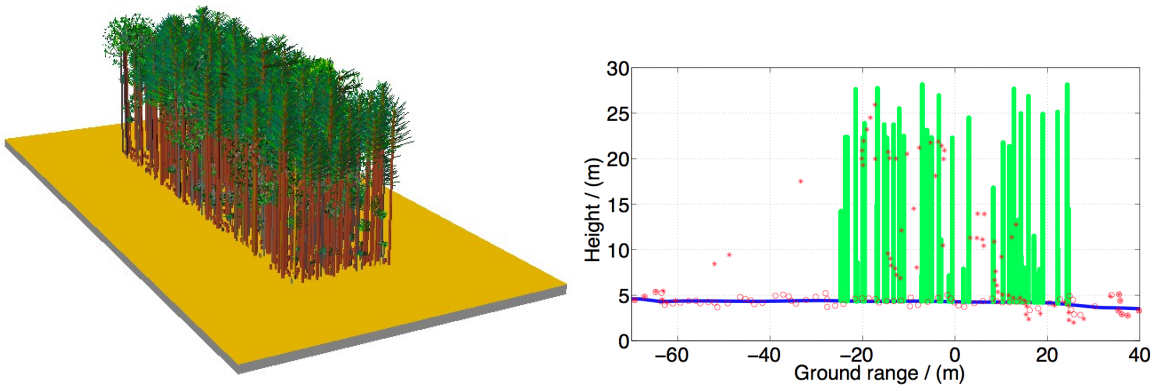


(a) (b)

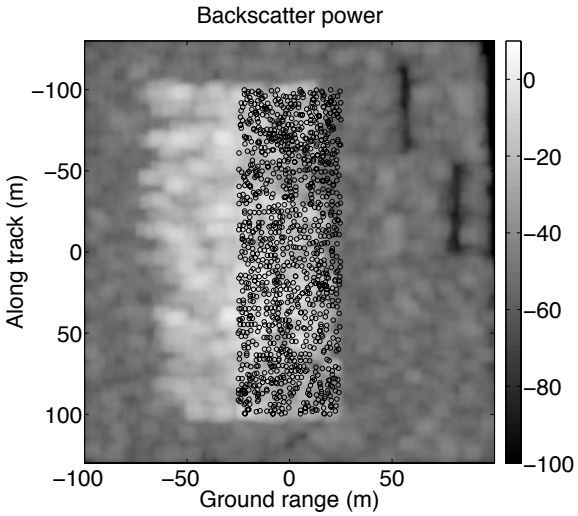


(c)

Figure 4.10: (**a**) A rectangular one-hectare plot in Harvard forest of western Massachusetts. (**b**) Height of the PolSARproSim simulated HV-pol phase center as a function of the ground range for a given azimuth slice of the rectangular plot. The known topography is shown as a "blue" curve while the trees as "green" vertical bars. The phase centers are marked as "red circles" ("red stars") for the simulated HV-pol InSAR measurements with (without) forest canopy above the underlying surface. (**c**) Simulated HV-pol radar backscatter power imagery (in unit of dB) with the dynamic range shown in the color bar. The tree stems are indicated by black circles overlaid on the imagery. Clearly discernible in the image is the radar effect of layover, where the reflection from the top of the trees appears "advanced" by approximately 40 m in the ground range.

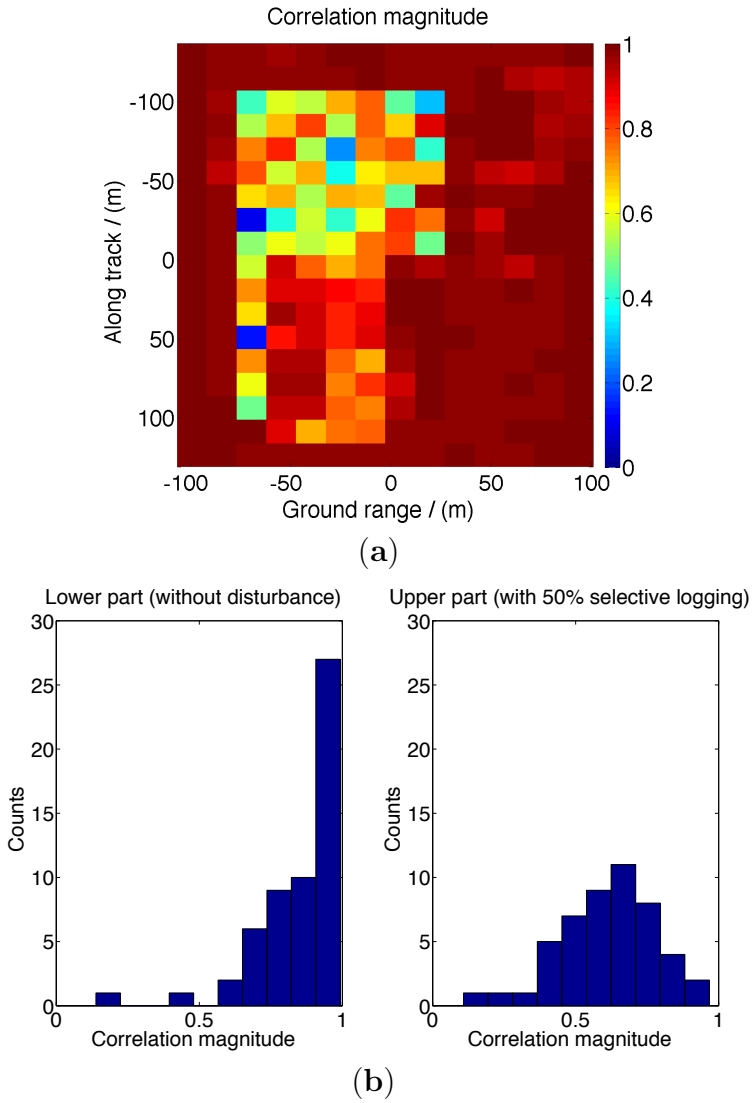


Figure 4.11: (**a**) Simulated HV-pol repeat-pass InSAR correlation magnitude ($\kappa_z$ = 0.1 rad/m) for the above-shown one-hectare plot with randomized selective logging (50% trees are randomly chosen and removed) in the upper half-plot between successive passes. The effect from this disturbance event can also be seen from the histograms (**b**). The one to the left shows the histogram of correlation magnitude without logging while the one to the right with selective logging. With $\kappa_z$ being small, the disturbance effect essentially reduced the repeat-pass InSAR correlation magnitude.

In Figure 4.10, a one-hectare plot modeled from a stem map collected at the Harvard forest is demonstrated through using FVS (Forest Vegetation Simulator; [10]). This plot is mostly occupied with red pines, red maples and birch, etc. Preliminary tests can be shown by using PolSARproSim program. In Figure 4.10, both from the phase center analysis and the radar backscatter power imagery, it seems that the radar instrument observed some trees over the open surface areas in front of (with respect to the line of sight) the forest canopy, which is known to be a standard radar concept termed as "layover". We also tested the PolSARproSim package by simulating repeat-pass InSAR correlation measurements with disturbance events (e.g. selective logging) between overpasses. In Figure 4.11a, 50% trees in the upper half-plot are randomly logged between the two passes. The $\kappa_z$ value is selected as 0.1 rad/m, which implies the volumetric decorrelation is not significant compared to the temporal decorrelation. This is also shown in the comparison plot of Figure 4.11b, where two histograms are demonstrated: the lower half-plot without logging (characterized by high correlation magnitude) and the upper half-plot with logging (characterized by low to moderate correlation magnitude). Also in the simulations of this section, a SAR resolution is 1.5 m $\times$ 1.5 m, while the window size for the estimation of the InSAR correlation is 10 range looks and 10 azimuth looks leading to a resolution of 15 m $\times$ 15 m in the simulated interferograms.

#### 4.2.2.2 Modified PolSARproSim for repeat-pass InSAR observation

As shown in the preliminary results, the PolSARproSim program is capable of characterizing the single-pass and repeat-pass InSAR correlation measurements. In order to simulate the possible remote sensing returns, we propose to modify this program. The primary extension of the PolSARproSim program for this purpose will be the creation of repeat-pass interferometric simulations of existing forest stands taking account of dielectric change and random motion between overpasses. In particular,

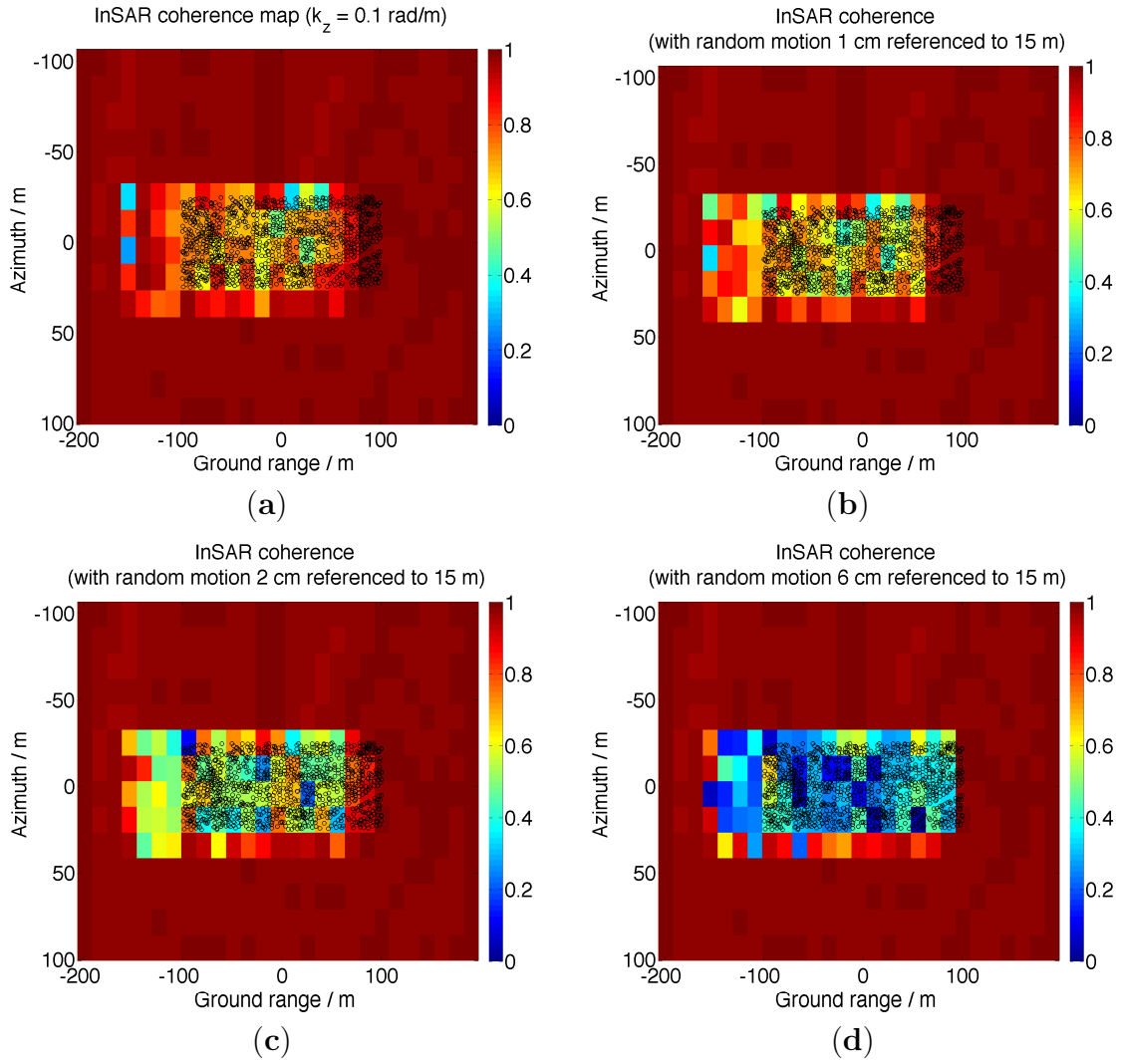


Figure 4.12: The simulation of the HV-pol repeat-pass InSAR correlation magnitude due to the random motion of the volume scatterers. (**a**) shows the single-pass InSAR coherence map, while (**b**), (**c**) and (**d**) show the different choices of the random motion level $\sigma_{\text{ref}} = 1$ cm, $\sigma_{\text{ref}} = 2$ cm and $\sigma_{\text{ref}} = 6$ cm at a reference height of $h_{\text{ref}} = 15$ m, respectively. The interferometric vertical wavenumber is chosen to be $\kappa_z = 0.1$ rad/m indicating the volume decorrelation is minor compared to the temporal decorrelation.

the simulator needs to be parameterized such that the output results better mimic those observed with ALOS/PALSAR and UAVSAR. Note only HV-pol InSAR correlation magnitude data is simulated in this work so as to validate the forest height inversion approach in Section 3.2.

In this example, the PolSARproSim program was modified to incorporate the random motion and the dielectric fluctuation effects of individual volume scatterers. In particular, a Gaussian random motion was introduced to all of the vegetation components (e.g. trunk, branch, leaf) through specifying the vertical dependence of the motion standard deviation $\sigma_r(z)$ as assumed in (3.5), *i.e.*

$$\sigma_r(z) = \frac{\sigma_{\text{ref}}}{h_{\text{ref}}} z, \tag{4.2}$$

where $\sigma_{\text{ref}}$ denotes the motion standard deviation at some reference height $h_{\text{ref}}$. Note $\sigma_{\text{ref}}$ is the only input parameter accounting for the random motion level given that the reference height is set to $h_{\text{ref}} = 15$ m as a constant. The simulated repeat-pass InSAR correlation magnitudes (without the moisture-induced dielectric fluctuation) are shown in Figure 4.12, where the simulated results for the cases of $\sigma_{\text{ref}} = 1$ cm, $\sigma_{\text{ref}} = 2$ cm, $\sigma_{\text{ref}} = 6$ cm are shown. As a comparison, the case where $\sigma_{\text{ref}} = 0$ cm (*i.e.* no random motion effect) is given in Figure 4.12(a). Note, the rectangular one-hectare test site is flipped 90° in order to create a longer projection along the cross-track direction so that the transition regions due to the layover effect occupy a smaller fraction of the entire forest stand.

It can be seen in Figure 4.12 that the temporal decorrelation becomes more dominant as the random motion level increases. Further, a dielectric fluctuation for all of the vegetation components (e.g. trunk, branch, leaf) in PolSARproSim was incorporated by using a Gaussian random number assigned to describe the moisture change ratio, *i.e.* $\nu_{M_g} = M_{g_2}/M_{g_1}$, where $M_{g_1}$ and $M_{g_2}$ are the gravimetric moisture content level for each vegetation component during the two separate passes. However, as assumed in Section 2.3.3 and Section 2.3.4, the moisture change (or dielectric fluctuation) is considered as an ergodic and stationary random process in the spatial domain, *i.e.* the mean and the standard deviation of $\nu_{M_g}$ are constant everywhere in the test site. Therefore, as for this extension, two additional input parameters

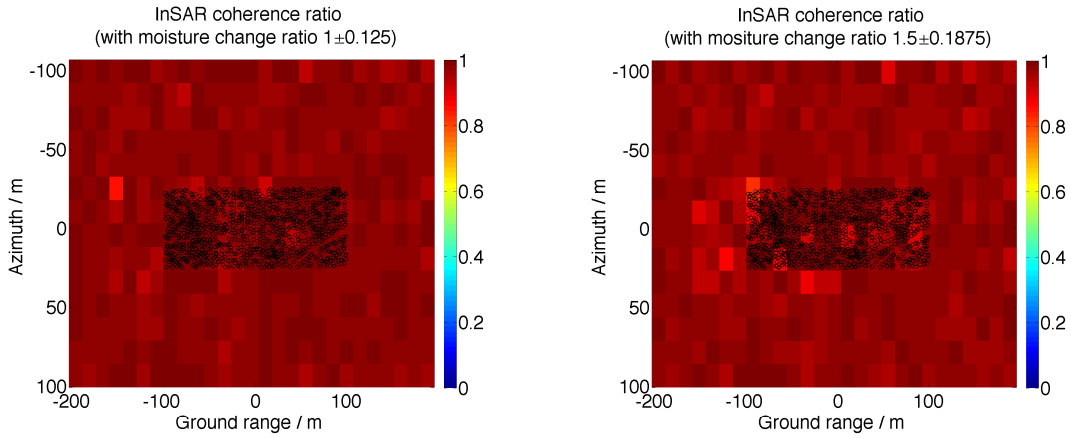


(a)




(b)

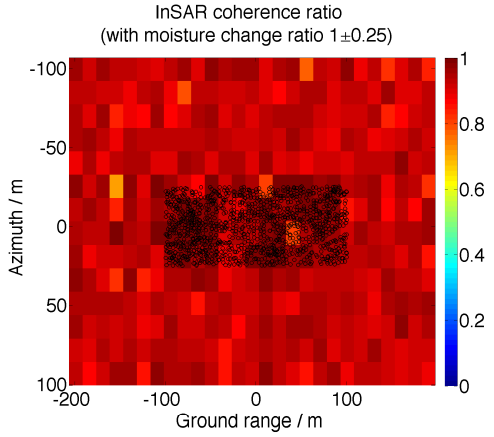


(c)

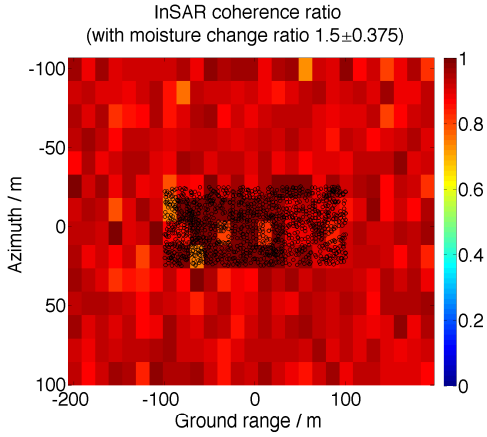


(d)

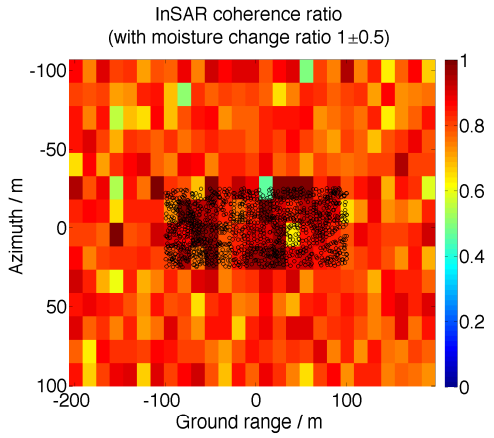


(e)

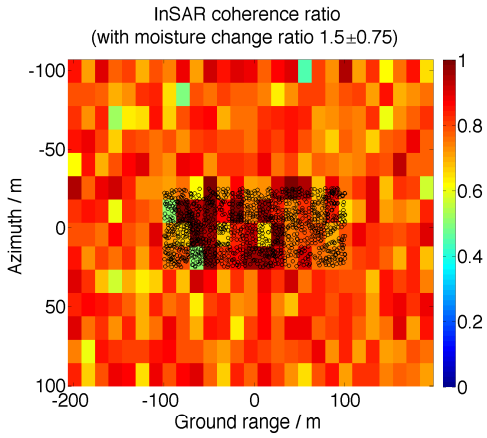


(f)

Figure 4.13: The simulated $|\gamma_{d_v}|$ of the HV-pol repeat-pass InSAR correlation magnitude due to the dielectric fluctuation of the volume scatterers. Different choices of the moisture change ratio $\nu_{M_g}$ are illustrated: (**a**), (**c**) and (**e**) show the results of $1 \pm 0.125$, $1 \pm 0.25$ and $1 \pm 0.5$, respectively; while (**b**), (**d**) and (**f**) show the results of $1.5 \pm 0.1875$, $1.5 \pm 0.375$ and $1.5 \pm 0.75$, respectively. Other simulation parameters are the same as in Figure 4.12(a).

are used for the simulation: the mean and the standard deviation of the moisture change ratio, $\nu_{M_g}$. Since PolSARproSim assigns low vegetation on top of the ground surface, it can be assumed that in (2.98), the temporal correlation component due to ground dielectric change is the same as the one due to volume dielectric change, *i.e.* $\gamma_{d_g} \approx \gamma_{d_v}$. From (2.98) and by only considering the moisture change among the scatterers between overpasses (*i.e.*, the random motion effect is excluded), the ratio of the repeat-pass HV-pol InSAR correlation magnitude $|\gamma^{\mathrm{HV}}_{v\&t}|$ to the single-pass InSAR correlation magnitude $|\frac{\gamma_{v\&m}+m}{1+m}|$ (illustrated in Figure 4.12(a)) can be shown to give the value of $|\gamma_{d_v}|$.

Using this ratio, in Figure 4.13 the simulated $|\gamma_{d_v}|$ from the HV-pol repeat-pass InSAR correlation magnitude due to the dielectric fluctuation effect only is shown. In Figure 4.13, each moisture change ratio $\nu_{M_g}$ is represented as "mean±standard deviation". Particularly, in the left column of Figure 4.13, the cases of $1 \pm 0.125$, $1 \pm 0.25$ and $1 \pm 0.5$ are shown, while in the right column are the cases for $1.5 \pm 0.1875$, $1.5 \pm 0.375$ and $1.5 \pm 0.75$. It can be seen in this figure that for each column (*i.e.* given the same mean value of the moisture change ratio), the larger that standard deviation of the moisture change is, the more temporal decorrelation due to the dielectric fluctuation effect occurs. Moreover, the left column corresponds to the right column visually very well, which implies that the parameter $|\gamma_{d_v}|$ is a function of the relative moisture change (*i.e.* $\frac{\text{standard deviation}}{\text{mean}}$), which validates the dielectric fluctuation model in Section 2.3.4. Under the assumption of ergodicity and stationarity, given a random distribution of the moisture change ratio, the simulated $|\gamma_{d_v}|$ in Figure 4.13 indeed seems to be ergodic and stationary across the image both with and without the presence of vegetation.

Next, we combine the moisture change effect and the random motion effect in simulating the repeat-pass HV-pol InSAR correlation. Particularly, the moisture change ratio is chosen as $1.5 \pm 0.75$ (as illustrated in Figure 4.13(f)), while the random

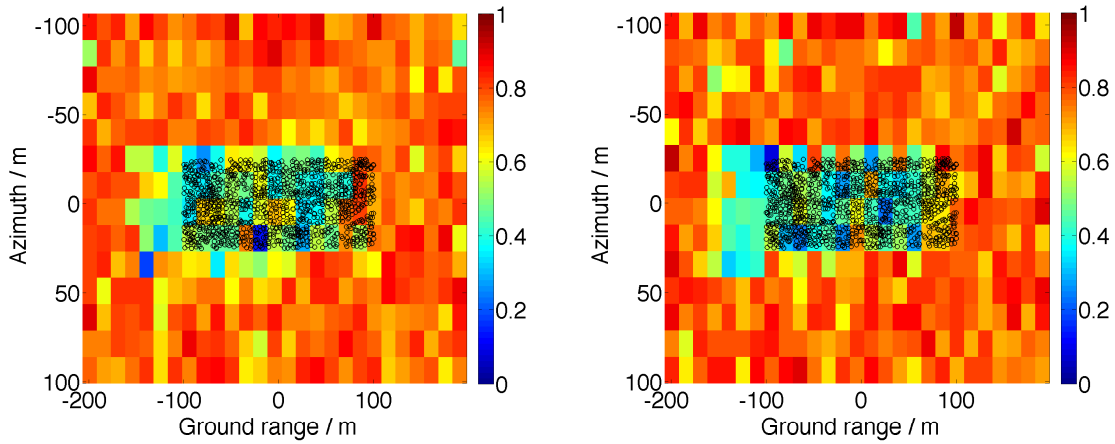


Figure 4.14: (**a**) The simulated HV-pol repeat-pass InSAR correlation magnitude due to both effects of dielectric fluctuation and random motion of the volume scatterers. The moisture change ratio is chosen as $1.5 \pm 0.75$ as illustrated in Figure 4.13(f), while the random motion level is selected to be $\sigma_{\text{ref}} = 2$ cm at a reference height of $h_{\text{ref}} = 15$ m as illustrated in Figure 4.12(c). (**b**) The direct product of the dielectric fluctuation term $|\gamma_{d_v}|$ in Figure 4.13(f) and the term $|\frac{\gamma_{v\&m}+m}{1+m}|$ in Figure 4.12(c) due to the coupled effects of volume scattering and random motion.

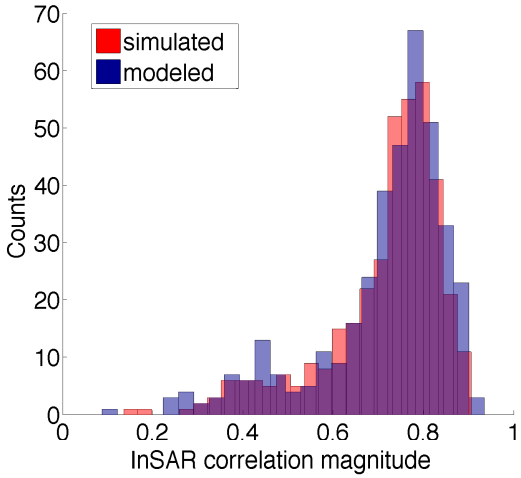


Figure 4.15: Histograms of the simulated repeat-pass InSAR correlation magnitude in Figure 4.14(a) as marked by "transparent red", and the modeled correlation magnitude values in Figure 4.14(b) as indicated by "transparent blue".

motion level is selected to be $\sigma_{\text{ref}} = 2$ cm at a reference height of $h_{\text{ref}} = 15$ m (as illustrated in Figure 4.12(c)). The resulting simulated repeat-pass InSAR correlation magnitude is shown in Figure 4.14(a). However, as implied by the modified RVoG model that is derived in Section 2.3.3 (*i.e.* see (2.98)) and given $\gamma_{d_g} \approx \gamma_{d_v}$ as in the above-mentioned simulation setup, the repeat-pass InSAR correlation can be decomposed into the dielectric fluctuation term $\gamma_{d_v}$ and the term with the coupled effects of volume scattering and random motion, $\frac{\gamma_{v\&m}+m}{1+m}$. Therefore in Figure 4.14(b), we show the direct product of the dielectric fluctuation term $|\gamma_{d_v}|$ in Figure 4.13(f) and the term $|\frac{\gamma_{v\&m}+m}{1+m}|$ in Figure 4.12(c) due to the coupled effects of volume scattering and random motion. Both of the correlation magnitude maps in Figure 4.14 as well as their histograms in Figure 4.15 statistically show very good consistency which implies that the modified RVoG model (as expressed in (2.98)) is capable of characterizing both the dielectric fluctuation and the random motion effects.

As for realizing these extensions to the PolSARproSim software, we used an optimized C implementation (with a multithreaded environment using OpenMP), and found that the repeat-pass InSAR simulation of a typical 15-m tall one-hectare plot can be processed on the order of twenty minutes.

#### 4.2.2.3 Validation of the forest height inversion approach

We next validate the forest height inversion approach presented in Section 3.2 using the PolSARproSim-simulated repeat-pass InSAR observations. By assuming that the test site has experienced some dielectric change (with moisture change ratio $1.5 \pm 0.75$) and random motion (with the motion level 2 cm referenced to 15 m) between the two passes, and by scaling the tree height values in the rectangular one-hectare plot such that a stand-averaged height of 5 m, 10 m, 15 m, 20 m, 25 m and 30 m can be obtained, we can thus perform simulations of repeat-pass InSAR observations for forest stands with various mean heights. After curve fitting as described

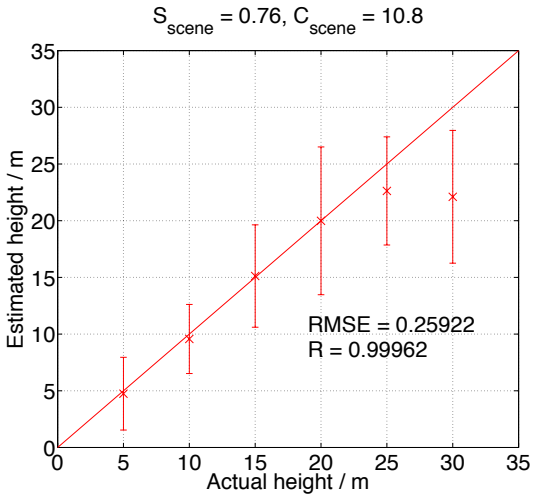


Figure 4.16: Validation of the forest height inversion approach for PolSARproSim-simulated repeat-pass InSAR observations. The moisture change ratio is $1.5 \pm 0.75$ while the random motion level is 2 cm referenced to 15 m. The forest heights in the original stem map of the rectangular one-hectare plot are scaled such that a stand-averaged height of 5 m, 10 m, 15 m, 20 m, 25 m and 30 m can be obtained. In such a manner, simulated forest stands of various mean heights are created. The inverted height *vs.* actual height along with the error bar are illustrated for each mean height value. Both the fitted model parameters ($S_{scene}$ and $C_{scene}$) and the fitting accuracy (RMSE and R) are also indicated.

in Section 3.2.3, the inverted forest height is demonstrated in Figure 4.16 with the model parameters determined to be $S_{scene} = 0.76$ and $C_{scene} = 10.8$. The estimated forest height under the saturation point (*i.e.* 25 m) is well linear in the actual height with RMSE of 0.26 m and R of 0.9996.

To visualize the estimated forest height compared to the actual height, the inversion results are particularly illustrated for a 15 m tall forest stand as in Figure 4.17 with the simulated repeat-pass InSAR correlation magnitude shown in Figure 4.14a. Comparing Figure 4.17d with Figure 4.17c, it is obvious that the layover effect is considerably reduced through the use of the radar viewing geometry and also given the known topography. The forest height that has been corrected for the layover effect corresponds to the ground truth averaged height very well visually. Through multi-pixel averaging (as described in Section 3.2.3), the mean heights are calculated for

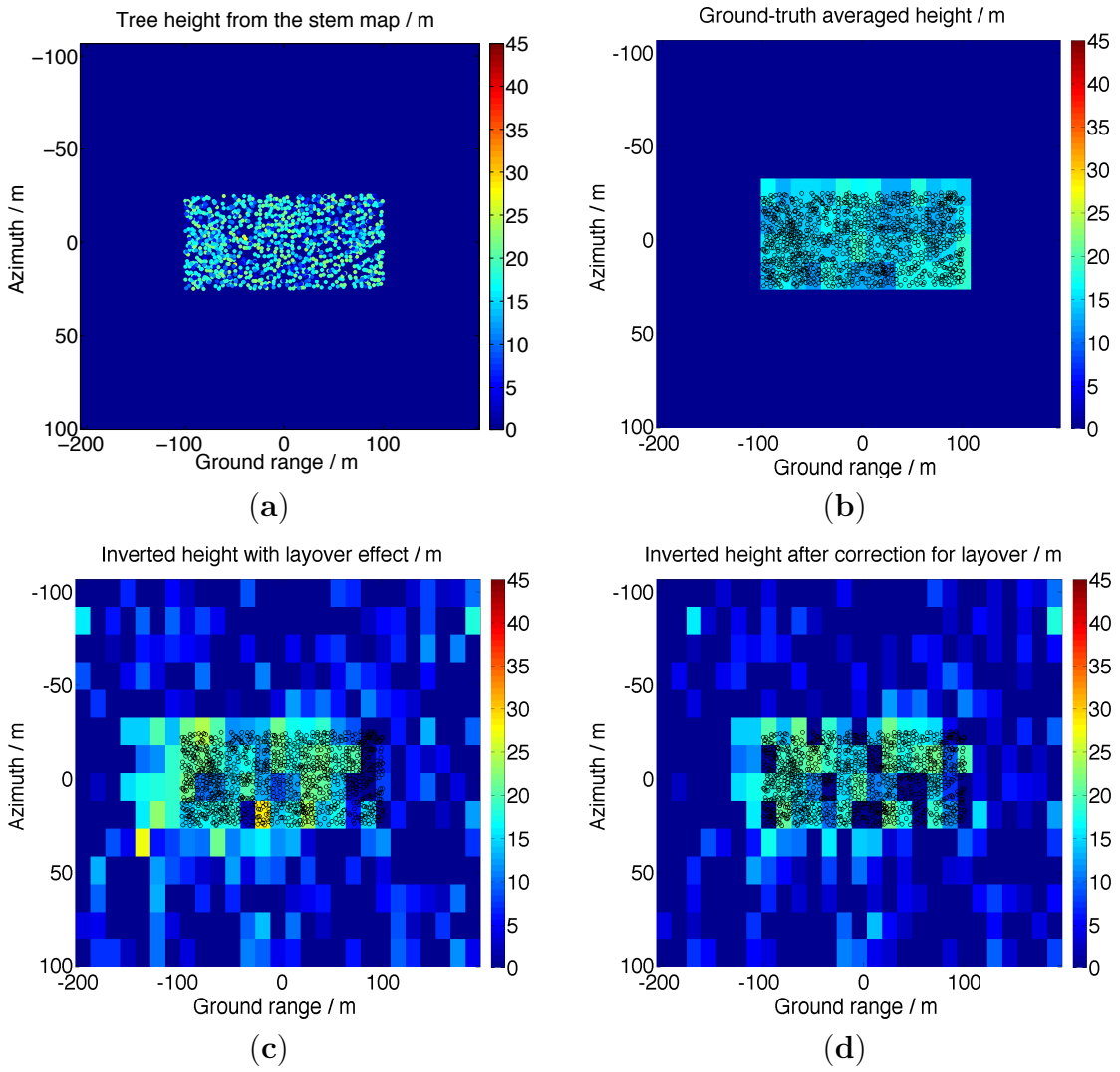


Figure 4.17: Forest height inversion results for a 15 m tall forest stand. (**a**) is the stem map with the mean height scaled to 15 m, (**b**) is the ground truth height after spatial averaging that is consistent with the resolution of the interferogram (each pixel is 15 m $\times$ 15 m), while (**c**) and (**d**) show the inverted forest heights with and without layover effect, respectively. Other simulation parameters are the same as in Figure 4.12a.

both the ground truth height and the InSAR correlation magnitude-inverted height over the rectangular one-hectare plot. By doing so repeatedly for the other mean forest height values, we thus obtain the forest height inversion curve in Figure 4.16.

#### 4.2.2.4 Forest dynamics and error analysis for the SAR/InSAR metrics

For the physical forest realizations (input of the simulator) in the above simulation results, the stem map and forest inventory data have been exploited to serve as the basis for direct simulation of remote sensing observations. However, by utilizing a forest dynamics model FVS, they will serve as a point of initialization resulting in an extension of the inventory and therefore large regions of simulated forest with varying forest density and relocated stem positions. An error analysis of the observed SAR/InSAR quantities can thus be performed by utilizing the extended PolSARproSim program and the FVS program. In particular, we will 1) vary the forest density of the original rectangular one-hectare plot by randomly logging a particular portion of the trees, 2) relocate the stem positions using a pure random number generator, 3) regenerate the stem maps using the FVS program.

First, we will investigate the error propagation to the estimated model parameters ($S_{scene}$ and $C_{scene}$) in the forest height inversion by varying the forest realization. The results are shown in Figure 4.18, Figure 4.19 and Figure 4.20, respectively, which correspond to the three tasks as mentioned above. In Figure 4.18, ten scenarios are demonstrated where the forest density is varied by randomly logging a portion of the trees. For example, 100% represents that the density is 100% of the original stem map (*i.e.* no logging occurred), while 10% means the density is reduced to 10% of the original stem map (*i.e.* 90% of the trees in the original stem map have been logged). It can be observed that as the forest density decreases, $S_{scene}$ will not be affected while $C_{scene}$ tends to increase, which is consistent with the simulated results in Section 4.2.1 by using the analytical model. In Figure 4.19, another ten scenarios are simulated with the tree stem locations randomly distributed through using a pure random number generator, while Figure 4.20 shows those scenarios where the stem maps are simulated with the use of the FVS program. Both cases seem to provide the similar level of fluctuation of the inverted model parameters $S_{scene}$ and $C_{scene}$ around

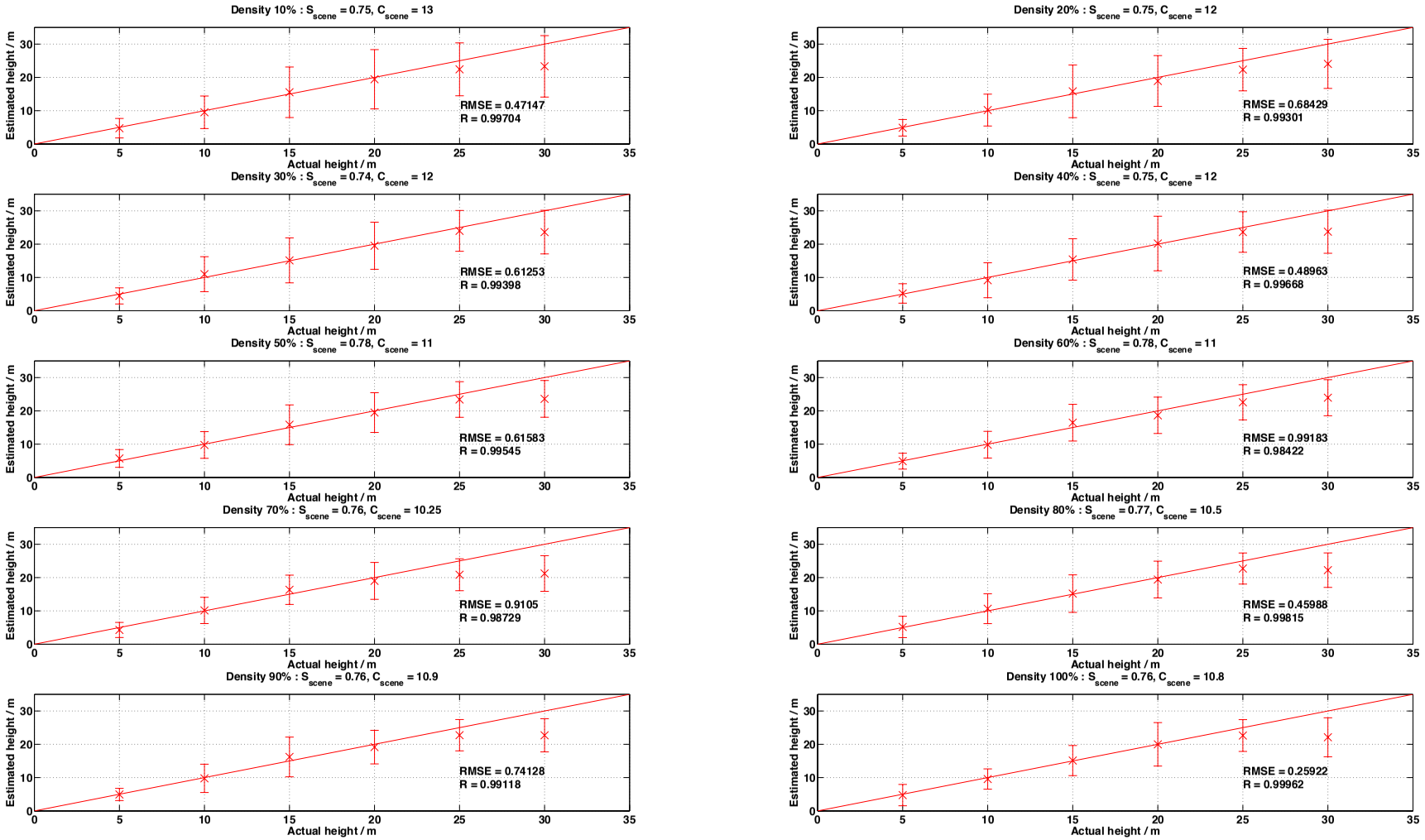


Figure 4.18: The forest height inversion performance along with the model parameters for ten simulated forest stands of varying forest density, where 100% represents that the density is 100% of the original stem map (*i.e.* no logging occurred), while 10% means the density is reduced to 10% of the original stem map (*i.e.* 90% of the trees in the original stem map have been randomly logged). Other simulation parameters are the same as in Figure 4.16.

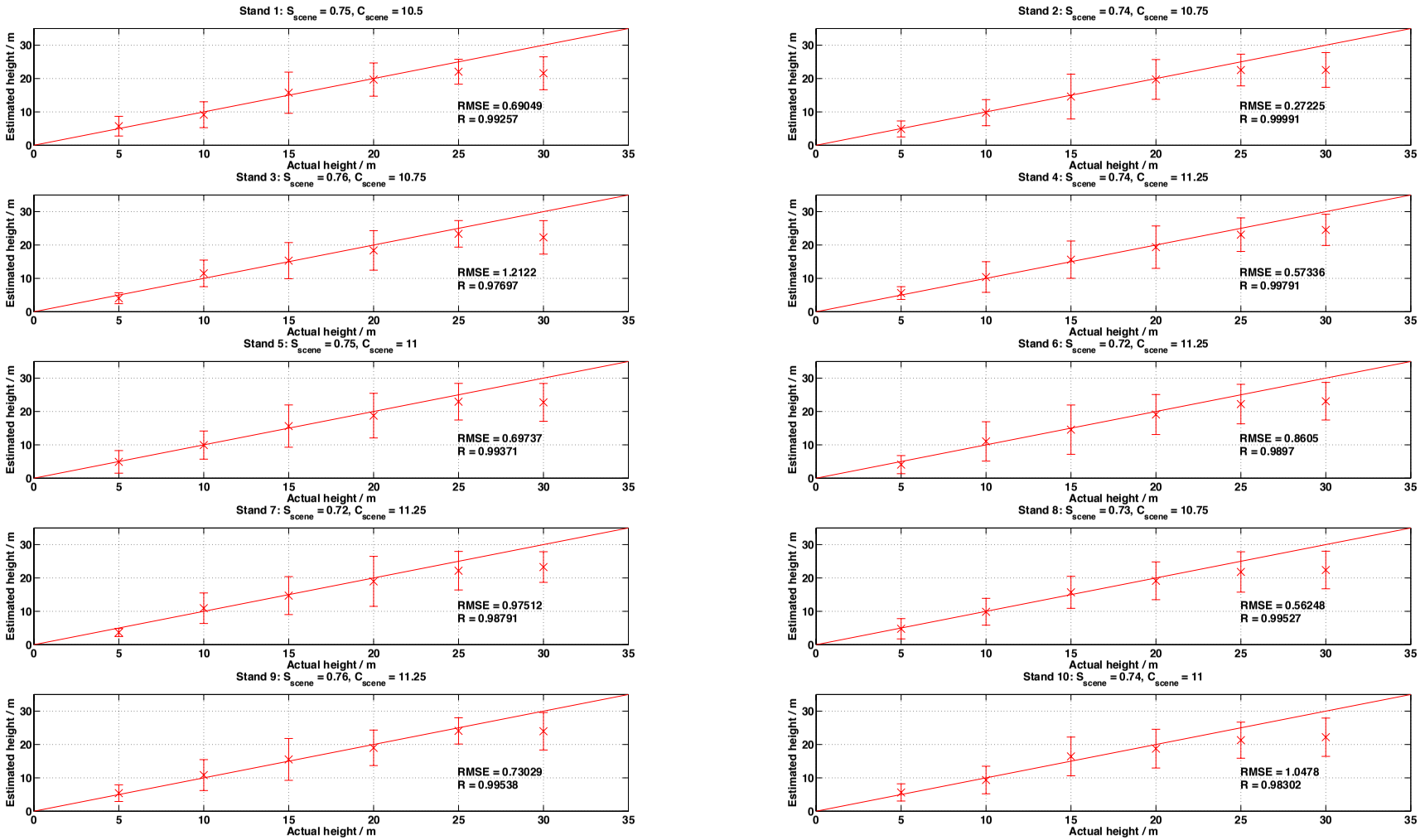


Figure 4.19: The forest height inversion performance along with the model parameters for ten simulated forest stands, where the tree stem positions are relocated by using a pure random number generator. Other simulation parameters are the same as in Figure 4.16.

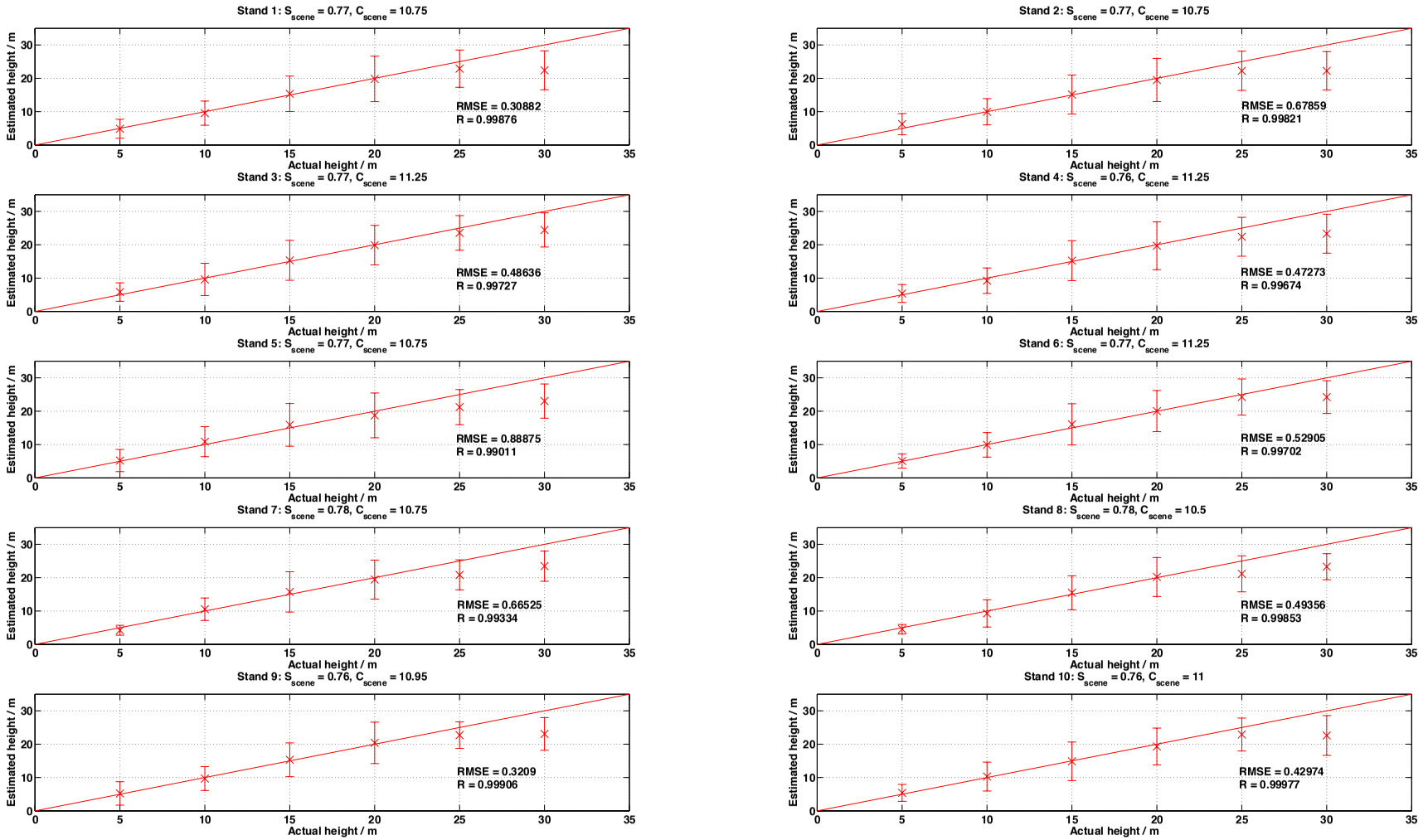


Figure 4.20: The forest height inversion performance along with the model parameters for ten simulated forest stands, where the tree stem maps are regenerated by using the FVS program. Other simulation parameters are the same as in Figure 4.16.

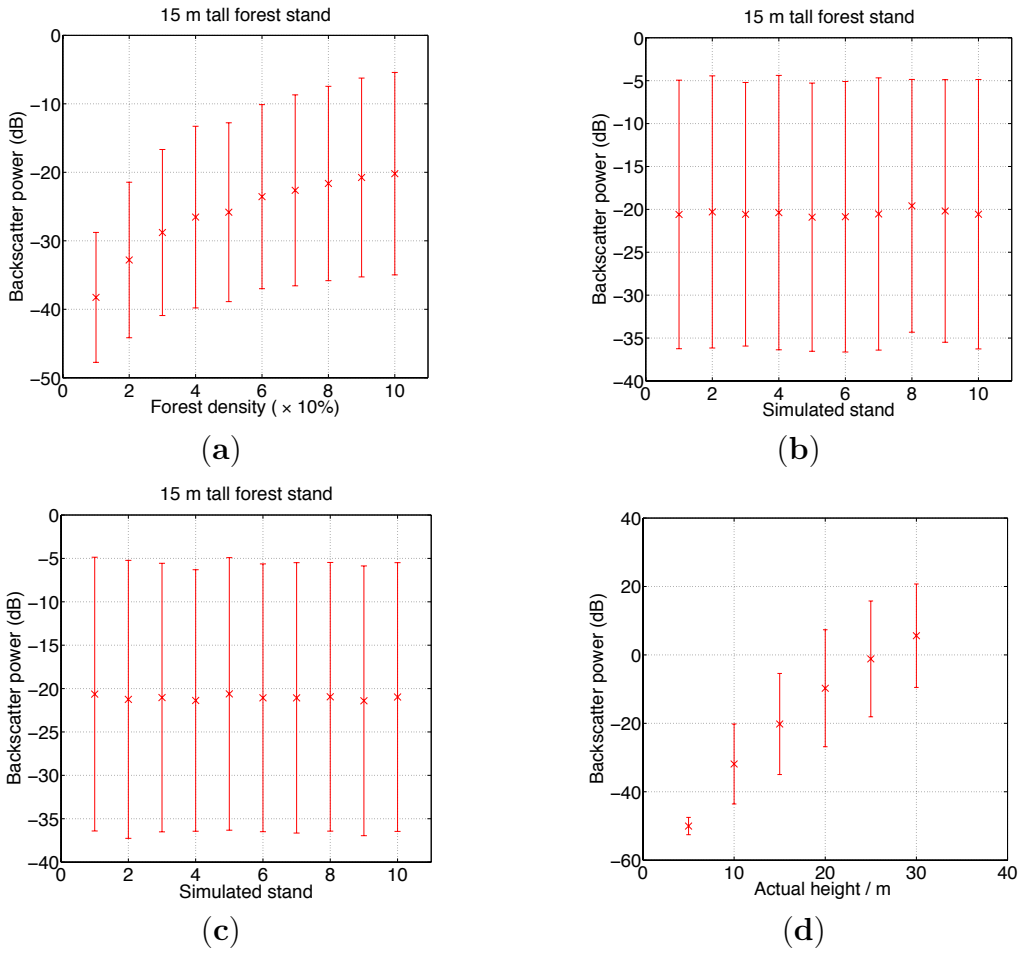


Figure 4.21: The forest dynamics-induced error analysis of the simulated SAR backscatter power for ten realizations of 15 m tall forest stand: (**a**) with varying forest density, (**b**) with relocated tree stem positions through using a pure random number generator, (**c**) with regenerated stem maps through using the FVS program and (**d**) the functional relationship between the SAR backscatter power and forest height. Other simulation parameters are the same as in Figure 4.16.

the point of initialization (shown in Figure 4.16), which implies that given the limited types of tree species (*i.e.* red pine and/or deciduous) in the PolSARproSim program, the stem positions and/or stem maps that are simulated either using a pure random number generator or using the FVS program (which accounts for the ecological and environmental conditions) cannot be discerned from each other.

Further, by varying the forest realization, it is possible to examine the error propagation to the simulated SAR backscatter power. The results for a 15 m tall forest

stand are shown in Figure 4.21. In Figure 4.21a, the simulated SAR backscatter power is shown as a function of the forest density, which seems to obey an exponential curve fitting. The statistics of the simulated SAR backscatter power is illustrated in Figure 4.21b with the tree stem positions relocated by utilizing a pure random number generator and in Figure 4.21c with the tree stem maps regenerated by utilizing the FVS program. As noticed above in Figure 4.19 and Figure 4.20, the signatures in Figure 4.21b and Figure 4.21c essentially demonstrate the same statistical properties, which again implies that the stem positions and/or stem maps that are simulated either using a pure random number generator or using the FVS program cannot be discerned from each other given the current version of the PolSARproSim program (where the types of tree species are limited). In comparison to the forest height inversion result using the InSAR correlation magnitude (*i.e.* Figure 4.16), the capability of inverting forest height through the use of SAR backscatter power is also investigated in Figure 4.21d, where the simulated SAR backscatter power is shown as a function of forest height, which is also observed to follow an exponential fit (consistent with the ground validation results in Section 5.5).

### 4.2.3 Validation of the dielectric fluctuation model

As mentioned in Section 2.3.4, there are four independent effects that induce the fluctuation of the scatterers' dielectric property and/or scattering amplitude. In this section, electromagnetic simulations will be presented individually for those effects as enumerated in Section 2.3.4.

#### 4.2.3.1 The effect of scatterer orientation

We first look at the effect from the orientation of the scattering element (e.g. branch and trunk). At L-band, both branch and trunk can be modeled as finite-length dielectric cylinders. The electromagnetic bi-static scattering amplitudes for finite-length dielectric cylinders are calculated in [29]. Assuming that the cylinder

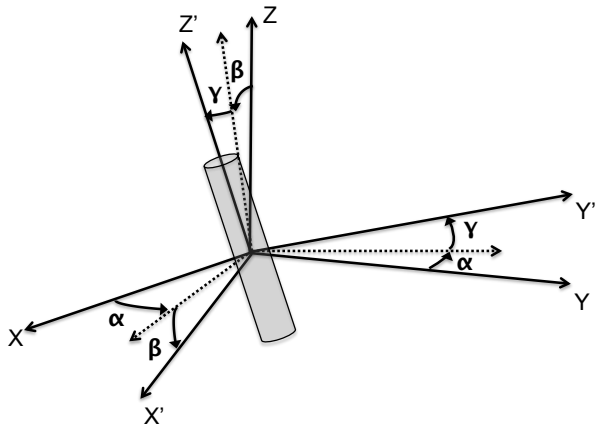


Figure 4.22: Illustration of coordinate transformation of the cylinder from its reference frame $(X, Y, Z)$ to the local frame $(X', Y', Z')$ through the selection of $\alpha$, $\beta$ and $\gamma$ angles [29]. The effective range of $(\alpha, \beta, \gamma)$ is $0° \leq \alpha \leq 90°$, $0° \leq \beta \leq 90°$, $\gamma = 0°$.

is arbitrarily oriented, the observing geometry is illustrated in Figure 4.22. In order to calculate the scattered fields for any orientation of the cylinder, we first solve the problem in the local frame $(X', Y', Z')$ of the cylinder and then transform the fields to the reference frame $(X, Y, Z)$ with a proper choice of $(\alpha, \beta, \gamma)$. Therefore, in the backscattering scenario with the incidence direction/polarization fixed, all of the possible orientations can be covered by varying $(\alpha, \beta, \gamma)$ from $0°$ to $360°$. However, due to cylindrical symmetry, it is sufficient to define the effective range of $(\alpha, \beta, \gamma)$ as $0° \leq \alpha \leq 90°$, $0° \leq \beta \leq 90°$, $\gamma = 0°$, since for any other combinative choice, there exists some point in the effective range such that their scattered fields are either equal to or conjugate of each other (and thus correlated).

For the sake of brevity, we only deal with cross-polarization in this work so as to be consistent with the presented forest height inversion approach (which only utilizes HV-pol data); however, it should be noted that the adaption to co-polarization is straightforward. The simulation results are shown by randomly sampling the effective range of $(\alpha, \beta, \gamma)$ with a resolution of $1°$ (*i.e.* only integer values are sampled).

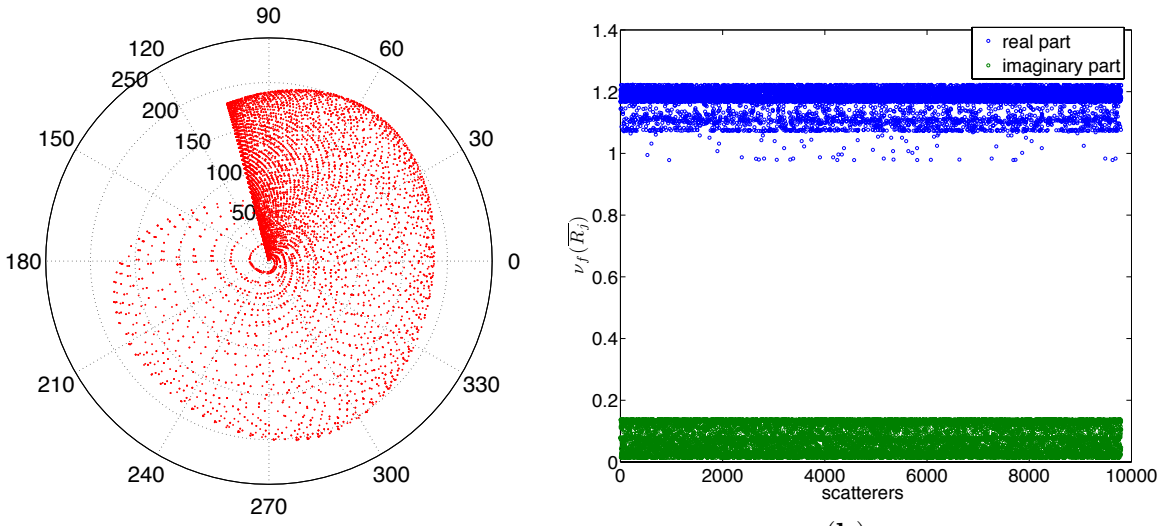


(**a**) (**b**)

Figure 4.23: Simulation results of (**a**) the complex scattering amplitude $f_j^{(1)}(\overline{R_j})$ and (**b**) the ratio characterizing the scattering amplitude change $\nu_f(\overline{R_j})$, where the scatterer's orientation is uniformly randomized within $0° \leq \alpha \leq 90°$, $0° \leq \beta \leq 90°$, $\gamma = 0°$. Other parameters are chosen as $M_g^{(1)} = 0.24$ ($\epsilon_r = 6 - j2$), $\nu_{M_g} = 1.5$ ($M_g^{(2)} = 0.36$), $\lambda = 23.6$ cm, $a = 14$ cm, $l = 15a$.

In order to isolate from the other three fluctuation effects, the relevant parameters are selected as such and fixed as constants: moisture content level $M_g^{(1)} = 0.24$ (*i.e.* $\epsilon_r = 6 - j2$ as in [29] using the dielectric model given by Ulaby [87]), ratio characterizing the moisture change $\nu_{M_g} = 1.5$ (*i.e.* which gives $M_g^{(2)} = 0.36$), wavelength $\lambda = 23.6$ cm (as used by ALOS/PALSAR), cylinder radius $a = 14$ cm (large cylinders at L-band i.e. $\lambda \sim 2a$), cylinder length $l = 15a$ (as used in [29]) for all of the scatterers. In other words, only the orientation angle of the scatterers is allowed to change.

First, 10,000 independent samples are generated, however, for the cases where zero backscatter is observed, $\nu_f(\overline{R_j})$ will be a undetermined number that is meaningless. Therefore, after eliminating the undetermined numbers, only 9799 independent samples remain, as illustrated in Figure 4.23.

From Figure 4.23, we notice that although the complex scattering amplitude is completely random with large uncertainty by varying the orientation of the cylinder, the ratio characterizing the scattering amplitude change tends to have a complex mean value plus a small random fluctuation term. For example, $\nu_f(\overline{R_j})$ in Figure 4.23(b) can be represented as

$$\nu_f(\overline{R_j}) = [1.18 + j0.08] + [\mathbf{rand}(\overline{R_j}; 0, 0.04) + j\mathbf{rand}(\overline{R_j}; 0, 0.04)], \tag{4.3}$$

where $\mathbf{rand}(\overline{R_j}; \mu, \sigma)$ denotes a random number at position $\overline{R_j}$ with mean $\mu$ and standard deviation $\sigma$. By letting $\alpha_0 = 1.18 + j0.08$ and $\alpha_1(\overline{R_j}) = \mathbf{rand}(\overline{R_j}; 0, 0.04) + j\mathbf{rand}(\overline{R_j}; 0, 0.04)$, we have

$$\nu_f(\overline{R_j}) = \alpha_0 + \alpha_1(\overline{R_j}) \quad \text{with} \quad \frac{\langle|\alpha_1(\overline{R_j})|^2\rangle}{|\alpha_0|^2} = 0.0025. \tag{4.4}$$

Note that the fluctuation uncertainty as a function of spatial coordinates, $\langle|\alpha_1(\overline{R_j})|^2\rangle$, relies on the actual stochastic distribution of the scatterer orientation. However, by adopting a uniform randomization over the effective range of the orientation angles as shown in Figure 4.23, a worst-case scenario can be achieved resulting in the largest possible fluctuation uncertainty. For this reason, a uniform randomization of the relevant scatterer parameters will be used in the following sections for investigating the other three effects associated with dielectric/scattering amplitude fluctuation.

#### 4.2.3.2 The effect of scatterer dimension

Next, the effect of dimension is investigated for different scattering elements, *i.e.* branches and trunks have various length and radius. In order to isolate this effect from the other three effects, the orientation of the cylinder is fixed by choosing $\alpha = 0°$, $\beta = 0°$, $\gamma = 45°$. Furthermore, let $M_g^{(1)} = 0.24$ ($\epsilon_r = 6 - j2$), $\nu_{M_g} = 1.5$ ($M_g^{(2)} = 0.36$) as in Section 4.2.3.1. As for the physical dimension of the cylinders, the radius $a$ is allowed

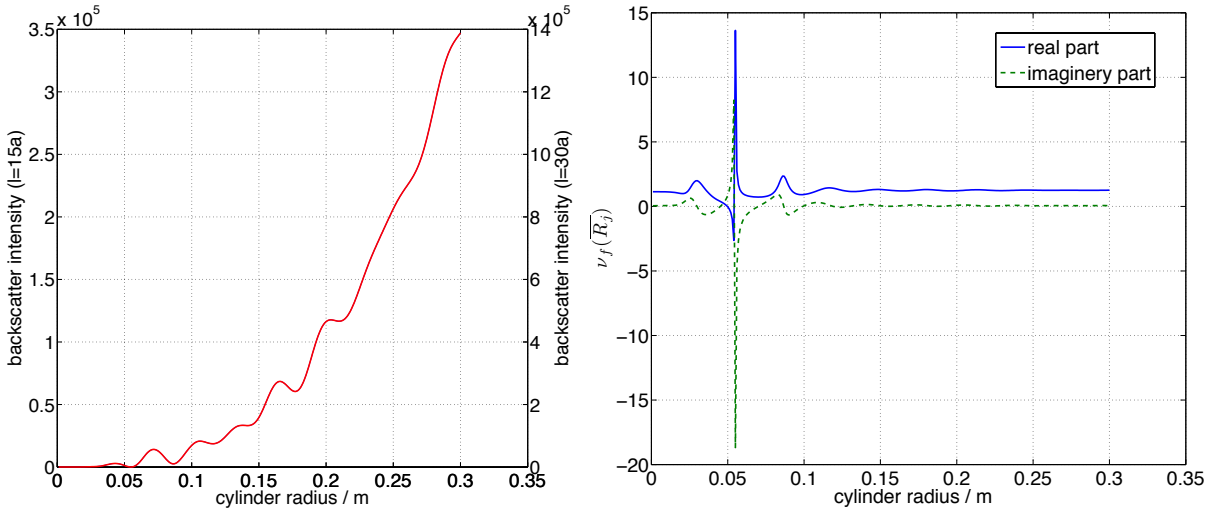


(**a**) (**b**)

Figure 4.24: Simulation results of (**a**) the backscatter intensity $|f_j^{(1)}(\overline{R_j})|^2$ and (**b**) the ratio characterizing the scattering amplitude change $\nu_f(\overline{R_j})$, where $a$ continuously goes from 0 cm to 30 cm. Other parameters are chosen as $\alpha = 0°$, $\beta = 0°$, $\gamma = 45°$, $M_g^{(1)} = 0.24$ ($\epsilon_r = 6 - j2$), $\nu_{M_g} = 1.5$ ($M_g^{(2)} = 0.36$), $\lambda = 23.6$ cm. Both $l = 15a$ and $l = 30a$ are considered: two vertical-axis labels are used to differentiate one another in (a), while both cases result in exactly the same ratio in (b).

to vary from 0 cm to 30 cm with the length proportional to the radius as above, *i.e.* $l = 15a$. However, since the cylinder length (and thus the proportionality) can also vary from scatterer to scatterer, we also examine the case where $l = 30a$ as a comparison. The results are illustrated in Figure 4.24. In Figure 4.24(a), both scenarios have the same type of functional form for the backscatter intensity curves which only differ by a scaling factor. However, in Figure 4.24(b), the ratios characterizing the scattering amplitude change are exactly the same for $l = 15a$ and $l = 30a$.

Although the ratio $\nu_f(\overline{R_j})$ tends to be drastically varying with the dimension of the scatterers (and thus highly target-dependent) in the Rayleigh ($2a \ll \lambda$) and Mie ($2a \sim \lambda$) scattering regions of Figure 4.24(b), it can be noticed that their corresponding backscatter intensities are very small compared to the large scatterers, and thus have much less contributions to the resulting InSAR correlation component.

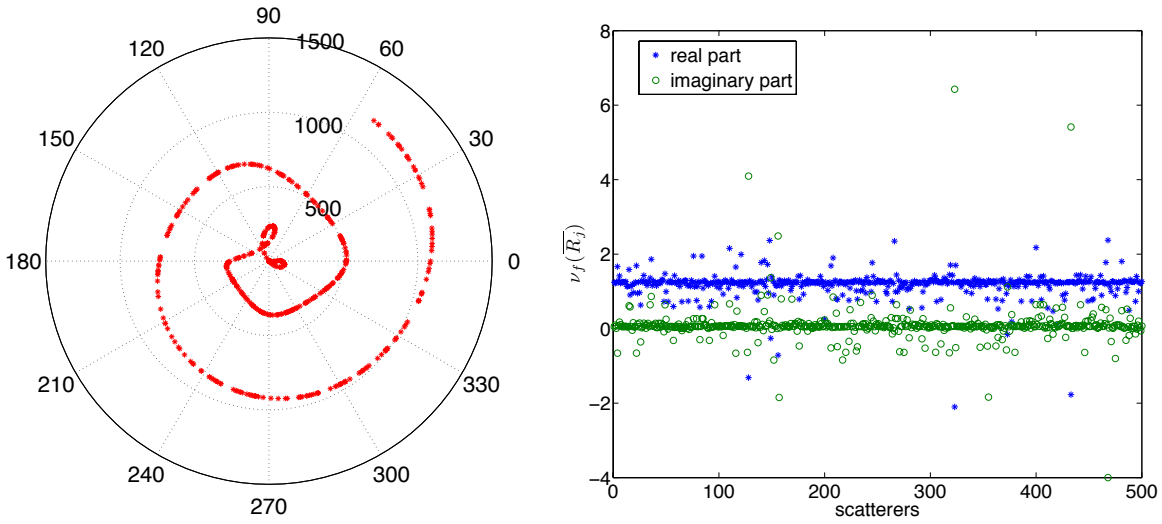


(**a**) (**b**)

Figure 4.25: Simulation results of (**a**) the complex scattering amplitude $f_j^{(1)}(\overline{R_j})$ and (**b**) the ratio characterizing the scattering amplitude change $\nu_f(\overline{R_j})$, where $a$ is uniformly randomized between 0 cm and 30 cm. Other parameters are chosen as $\alpha = 0°$, $\beta = 0°$, $\gamma = 45°$, $M_g^{(1)} = 0.24$ ($\epsilon_r = 6 - j2$), $\nu_{M_g} = 1.5$ ($M_g^{(2)} = 0.36$), $\lambda = 23.6$ cm, $l = 15a$.

Letting $l = 15a$, 500 independent samples are generated by uniformly randomizing $a$ from 0 cm to 30 cm. The randomized results are illustrated in Figure 4.25. Similar to Figure 4.23, the complex scattering amplitude is completely random with large uncertainty; however, the ratio associated with the scattering amplitude change can be represented as

$$\nu_f(\overline{R_j}) = \alpha_0 + \alpha_1(\overline{R_j}), \tag{4.5}$$

where $\alpha_0 = 1.18 + j0.09$ and $\alpha_1(\overline{R_j}) = \mathbf{rand}(\overline{R_j}; 0, 0.36) + j\mathbf{rand}(\overline{R_j}; 0, 0.54)$ with $\frac{\langle|\alpha_1(\overline{R_j})|^2\rangle}{|\alpha_0|^2} = 0.2968$.

Compared to Figure 4.23, it is noticed that given the same moisture level and ratio characterizing the moisture change, the effect due to a scatterer's dimension surpasses that due to the scatterer's orientation in terms of the uncertainty of the scattering amplitude fluctuation.

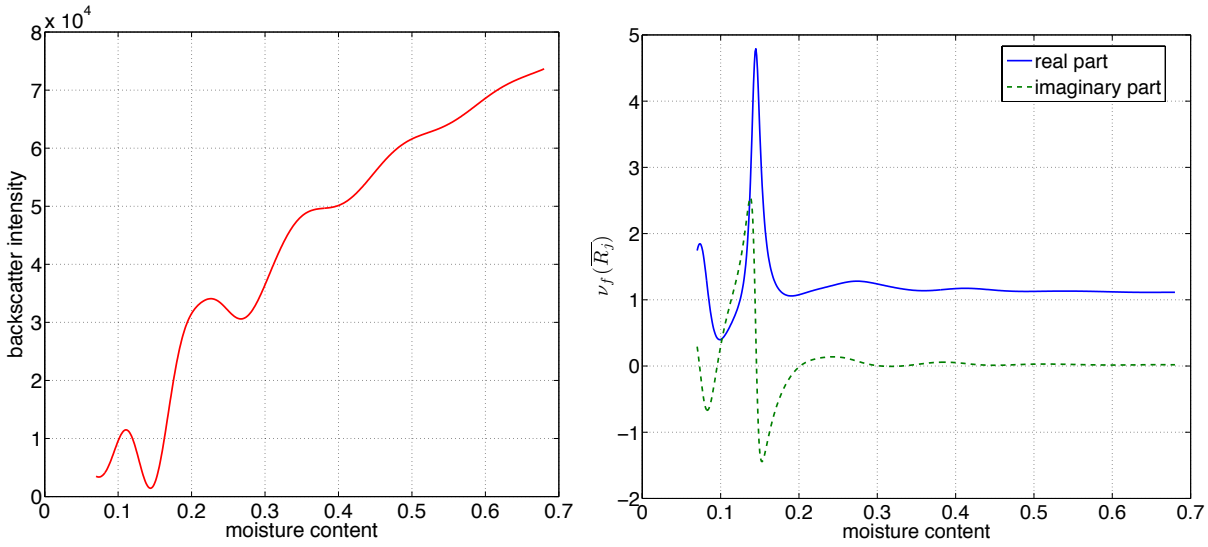


(**a**) (**b**)

Figure 4.26: Simulation results of (**a**) the backscatter intensity $|f_j^{(1)}(\overline{R_j})|^2$ and (**b**) the ratio characterizing the scattering amplitude change $\nu_f(\overline{R_j})$, where $M_g^{(1)}$ continuously varies from 0.07 to 0.68. Other parameters are: $\nu_{M_g} = 1.5$, $\alpha = 0°$, $\beta = 0°$, $\gamma = 45°$, $\lambda = 23.6$ cm, $a = 14$ cm, $l = 15a$.

#### 4.2.3.3 The effect of scatterer moisture content level

Similarly, in order to study the effect from the moisture content level, $M_g^{(1)}$ is allowed to vary between 0.07 (dry) and 0.68 (high) as in [87]. Note typical values that have been used are within this range, e.g. 0.24 (intermediate; $\epsilon_r = 6 - j2$ as in [29]) and 0.51 (high; $\epsilon_r = 18 - j6$ as in [12]). The other parameters are chosen as such: $\nu_{M_g} = 1.5$, $\alpha = 0°$, $\beta = 0°$, $\gamma = 45°$, $\lambda = 23.6$ cm, $a = 14$ cm, $l = 15a$, which are consistent with Section 4.2.3.1-4.2.3.2. The simulated backscatter intensity is shown in Figure 4.26(a), while the ratio characterizing the scattering amplitude change $\nu_f(\overline{R_j})$ is illustrated in Figure 4.26(b). Similar to Figure 4.24, it seems that the ratio $\nu_f(\overline{R_j})$ is strongly varying with the moisture content of the scatterers (and thus target-dependent) only when the backscatter intensity is very small and thus have much less contributions to the resulting InSAR correlation component.

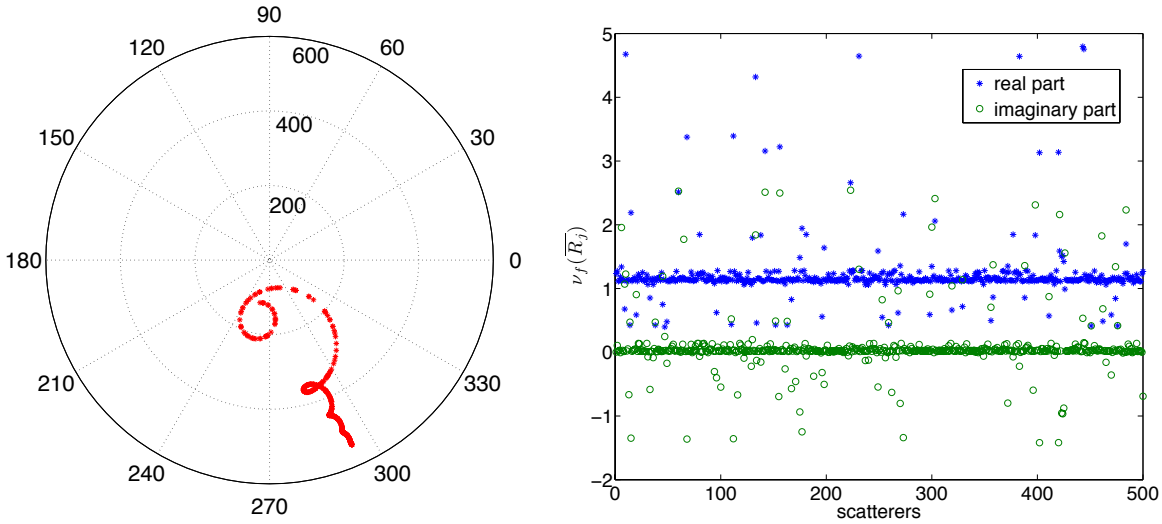


(**a**) (**b**)

Figure 4.27: Simulation results of (**a**) the complex scattering amplitude $f_j^{(1)}(\overline{R_j})$ and (**b**) the ratio characterizing the scattering amplitude change $\nu_f(\overline{R_j})$, where $M_g^{(1)}$ is uniformly randomized between 0.07 and 0.68. Other parameters are: $\nu_{M_g} = 1.5$, $\alpha = 0°$, $\beta = 0°$, $\gamma = 45°$, $\lambda = 23.6$ cm, $a = 14$ cm, $l = 15a$.

Hence, in order to study the spatial fluctuation of $\nu_f(\overline{R_j})$, 500 independent samples are generated by randomizing the moisture content from 0.07 to 0.68. Figure 4.27(a) shows that the simulated complex scattering amplitude is quite random; however, the ratio characterizing the scattering amplitude change is shown in Figure 4.27(b), and can be written as a complex mean value plus a small fluctuation term, *i.e.*

$$\nu_f(\overline{R_j}) = \alpha_0 + \alpha_1(\overline{R_j}), \tag{4.6}$$

where $\alpha_0 = 1.22 + j0.08$ and $\alpha_1(\overline{R_j}) = \mathbf{rand}(\overline{R_j}; 0, 0.49) + j\mathbf{rand}(\overline{R_j}; 0, 0.46)$ with $\frac{\langle|\alpha_1(\overline{R_j})|^2\rangle}{|\alpha_0|^2} = 0.3083$.

#### 4.2.3.4 The effect of scatterer moisture change

In Section 4.2.3.3 and Section 2.3.4, it is known that the moisture content $M_g$ (and thus the dielectric constant $\epsilon_r$) is highly target-dependent. In fact, the ratio $\nu_{M_g}$

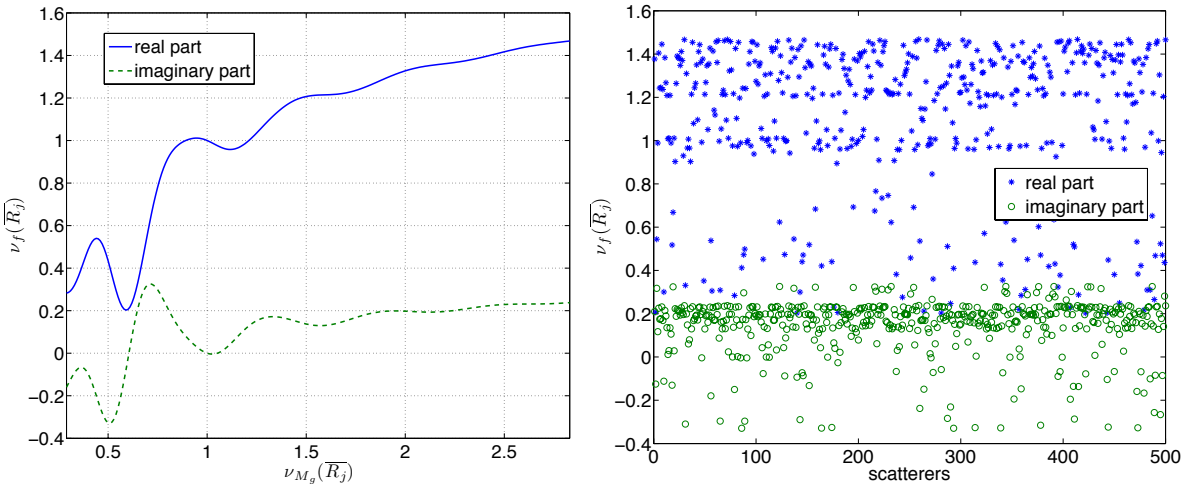


(**a**) (**b**)

Figure 4.28: Simulation results of the ratio characterizing the scattering amplitude change $\nu_f(\overline{R_j})$, where (**a**) $\nu_{M_g}$ continuously varies from 0.29 to 2.83; (**b**) $\nu_{M_g}$ is uniformly randomized between 0.29 and 2.83. Other parameters are chosen as $M_g^{(1)} = 0.24$, $\alpha = 0°$, $\beta = 0°$, $\gamma = 45°$, $\lambda = 23.6$ cm, $a = 14$ cm, $l = 15a$.

characterizing the moisture change between repeat observations is also expected to be target-dependent. As illustrated in Figure 4.28(a), by fixing $M_g^{(1)} = 0.24$ and allowing $M_g^{(2)}$ to vary from 0.07 (dry) to 0.68 (high) [87], $\nu_{M_g}$ goes from 0.29 to 2.83 with the mean around 1.5, which is also consistent with Section 4.2.3.1-4.2.3.3. The simulated ratio characterizing the scattering amplitude change, $\nu_f$, tends to be oscillating and increasing as the ratio characterizing the moisture change, $\nu_{M_g}$, increases.

Based on the above-mentioned reasons, $M_g^{(2)}$ is thus uniformly randomized over the entire range (*i.e.* between 0.07 and 0.68). To see the fluctuation uncertainty of $\nu_f(\overline{R_j})$, 500 independent samples are generated and shown in Figure 4.28(b) that can still be represented by the following form, *i.e.*

$$\nu_f(\overline{R_j}) = \alpha_0 + \alpha_1(\overline{R_j}), \tag{4.7}$$

where $\alpha_0 = 1.10 + j0.14$ and $\alpha_1(\overline{R_j}) = \mathbf{rand}(\overline{R_j}; 0, 0.35) + j\mathbf{rand}(\overline{R_j}; 0, 0.13)$ with $\frac{\langle|\alpha_1(\overline{R_j})|^2\rangle}{|\alpha_0|^2} = 0.1124$.

To this end, we conclude that the dielectric fluctuation model (as expressed in (2.102); Section 2.3.4) is valid, where the fluctuation uncertainty $\langle|\alpha_1(\overline{R_j})|^2\rangle$ is attributed to all of the four effects associated with each scattering element as discussed above as well as in Section 2.3.4, *i.e. orientation*, *dimension*, *moisture content level* and *ratio characterizing the moisture change*.

# CHAPTER 5

# GROUND VALIDATION RESULTS FOR THE RETRIEVAL OF VEGETATION CHARACTERISTICS USING REPEAT-PASS INSAR OBSERVATION

In this chapter, concrete ground validation results will be provided for the forest height inversion model that is presented in Section 3.2. First, the InSAR processing details are described in Section 5.1. Then, the ground validation results over the ILCP in Queensland, Australia and the Howland forest in central Maine, US will be shown in Section 5.2 and Section 5.3, respectively. As an important product of this work, mosaic maps of forest height along with an automatic mosaicking algorithm will be demonstrated in Section 5.4. In Section 5.5, the spaceborne SAR/InSAR metrics are compared in the capabilities of estimating forest height. Finally, generation of the forest disturbance map along with the forest height map is demonstrated in Section 5.6.

## 5.1 Preprocessing of InSAR correlation measurements

In Section 5.1.1, the decomposition of the measured repeat-pass InSAR correlation data is described. Then, the removal of the correlation magnitude bias and the correction for the thermal noise decorrelation will be covered in Section 5.1.2 and Section 5.1.3, respectively.

### 5.1.1 Decomposition of repeat-pass InSAR correlation

A necessary component of the study was to analyze the contribution of different components to the observed repeat-pass InSAR correlation, *i.e.*, geometric, thermal

noise, volumetric and temporal decorrelation. To begin, the InSAR correlation is defined as [64, 60]

$$\gamma = \frac{\langle E_1 E_2^* \rangle}{\sqrt{\langle |E_1|^2 \rangle \langle |E_2|^2 \rangle}}, \tag{5.1}$$

where $E_1$ and $E_2$ are the received signals from two antennas separated by a baseline. In repeat-pass interferometry, $E_1$ and $E_2$ are the received signals observed during different passes (or orbits) of the platform. The ensemble average in (5.1) can be approximated with multi-look averaging, which gives [79]

$$\gamma = \frac{\sum_{i=1}^{L} E_1 E_2^*}{\sqrt{\sum_{i=1}^{L} |E_1|^2 \sum_{i=1}^{L} |E_2|^2}}, \tag{5.2}$$

where $L$ is the number of independent samples (or looks). This correlation can also be factorized into the following components as has been partially derived in (2.38), (2.90) and in [64, 96, 33, 5]

$$\gamma = \gamma_{geo} \gamma_{SNR} \gamma_{v\&t}, \tag{5.3}$$

where $\gamma_{geo}$ is the correlation of the two echoes with slightly different cross-track and along-track viewing geometries in successive passes, $\gamma_{SNR}$ is the correlation attributable to thermal noise contaminating both radar channels, and $\gamma_{v\&t}$ takes into account of the coupled decorrelation effects of volume scattering and temporal changes. Geometric decorrelation is removed by first applying common band filtering [19], to account for a shift in the echo spectrum due to slight changes in the viewing geometry. In order to exploit repeat-pass InSAR correlations to invert forest height, calibration of the InSAR correlation data was first undertaken as below.

### 5.1.2 Removal of correlation magnitude bias

Implementation of (5.2) implies that InSAR correlation measurements are obtained through spatially averaging adjacent multiple looks. It is noted that [79] the sampled correlation magnitude is a biased estimate, and both the bias and the standard deviation decrease as the number of looks increase. For the case where $L = 20$ (as used in this work), the biased mean and standard deviation of the sampled correlation magnitude are plotted as red "x" markers along with error bars in Figure 5.1a. For ground surfaces where low signal-to-noise ratios are usually observed (particularly at HV-polarization), the observed correlation magnitude is often $< 0.5$, even under minimal temporal decorrelation. In such cases, the bias in the correlation measurements becomes challenging. However, this bias can be reduced (if impossible to be removed) by mapping the sampled correlation magnitudes to the true values through the use of the curve in Figure 5.1b, which is the inverse function of the biased mean in Figure 5.1a and considered as a lookup table. By generating 10,000 20-look random samples at each correlation magnitude, in Figure 5.1a, we also show the mean with reduced bias as magenta "o" markers and the corresponding standard deviation as green error bounds, respectively. Since the sampled correlation magnitude is biased to higher values and always greater than 0.2, we can use the curve in Figure 5.1b to remove this bias from the observed correlation magnitudes that are greater than 0.2. However, considering the biased mean curve in Figure 5.1a, no value can be mapped to observed correlation magnitudes that are smaller than 0.2. Therefore, those low correlation magnitudes ($< 0.2$) are mapped to zero in the lookup table. As the new mean curve in Figure 5.1a implies, the bias becomes a problem only when the actual correlation magnitude is below 0.1, which usually occurs for disturbance events (e.g. selective logging) or water bodies, where the inverted height is no longer meaningful because of high temporal decorrelation. Therefore, the above-mentioned bias-reduction method is valid for the present study.

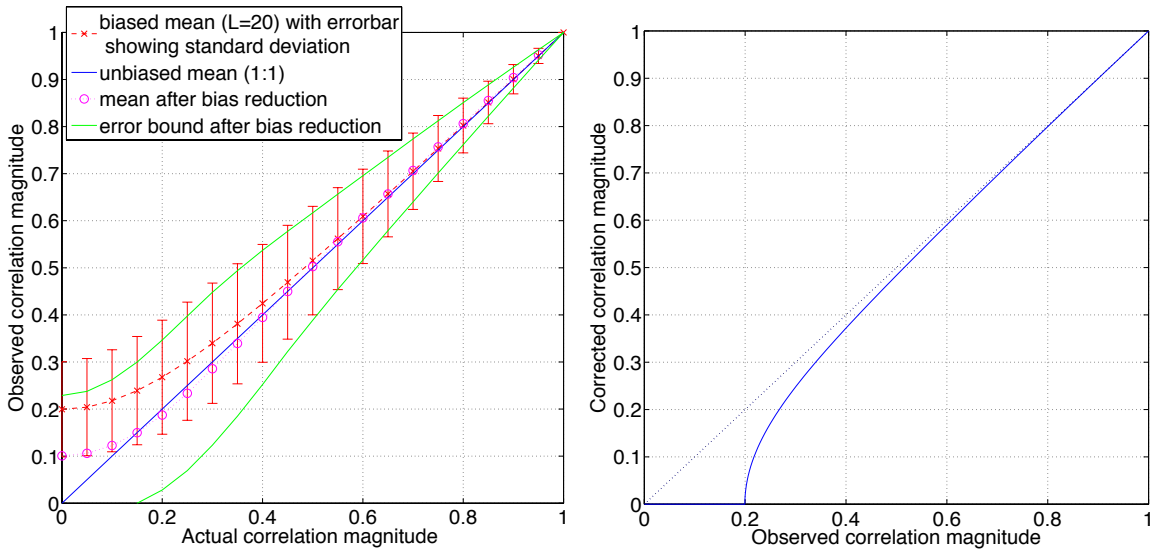


(**a**) (**b**)

Figure 5.1: Correction for the bias in the sampled correlation magnitude: (**a**) shows the biased mean and its standard deviation as red "x" markers and error bars ($L = 20$) with the corrected mean and the associated standard deviation as magenta circles and green error bounds; (**b**) is the correction function, which is the inverse function of the biased mean in (a).

The green error bounds in Figure 5.1a illustrate the confidence in the estimation of correlation magnitudes. Since ground surfaces have a lower reflectivity (and hence reduced SNR and correlation magnitude) it is more difficult to estimate correlations over surfaces compared to bright targets, such as forests, which have a larger reflectivity and better SNR. This will, in turn, translate into noisy ground features in the inverted forest height maps, even though the surfaces are barren.

### 5.1.3 Correction for thermal noise decorrelation

Prior to calibrating observed correlations for thermal noise, common band filtering and bias-reduction will have been applied. Further, additive thermal noise is incoherent with the SAR received signal, and thus affects the inter-channel correlation. The correlation associated with this thermal effect can be modeled as a function of the SAR receiver's signal-to-noise ratio (SNR). By treating the two channels (*i.e.* two

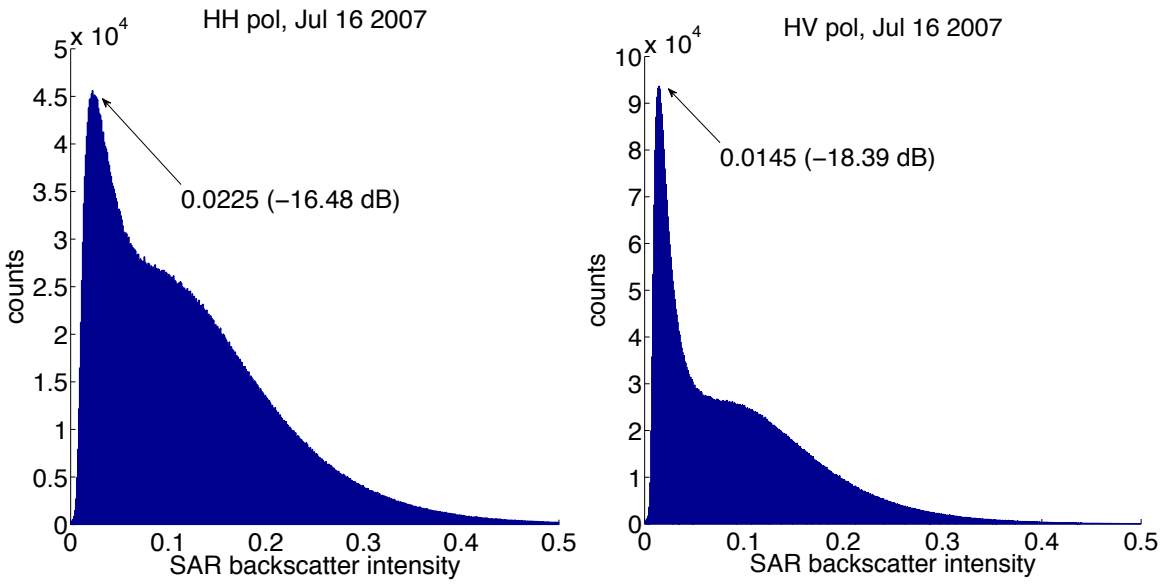


(**a**) (**b**)

Figure 5.2: Histograms of the HH-pol (**a**) and HV-pol (**b**) backscatter intensities of the ALOS/PALSAR data collected on July 16, 2007 over ILCP in Queensland, Australia.

ends of the baseline) differently, $\gamma_{SNR}$ can be expressed as [96]

$$\gamma_{SNR} = \frac{1}{\sqrt{1 + SNR_1^{-1}}\sqrt{1 + SNR_2^{-1}}}, \tag{5.4}$$

where $SNR_1$ and $SNR_2$ are the signal-to-noise ratios for the two SAR channels. Since the observed backscatter intensity is a sum of signal and noise powers, the image data can be converted into pixel-level SNR imagery through the use of an estimate of thermal noise level, which is assumed to be uniform throughout the imagery. Because the SNR depends on the target reflectivity, the thermal noise correlation also varies spatially. Therefore, to achieve accurate estimates of the coupled decorrelation effect of volume scattering and temporal changes, correction of the observed correlations for thermal noise is necessary.

The choice of the thermal noise level can be estimated by analyzing histograms of backscatter intensities within "dark regions" of the imagery. To demonstrate this

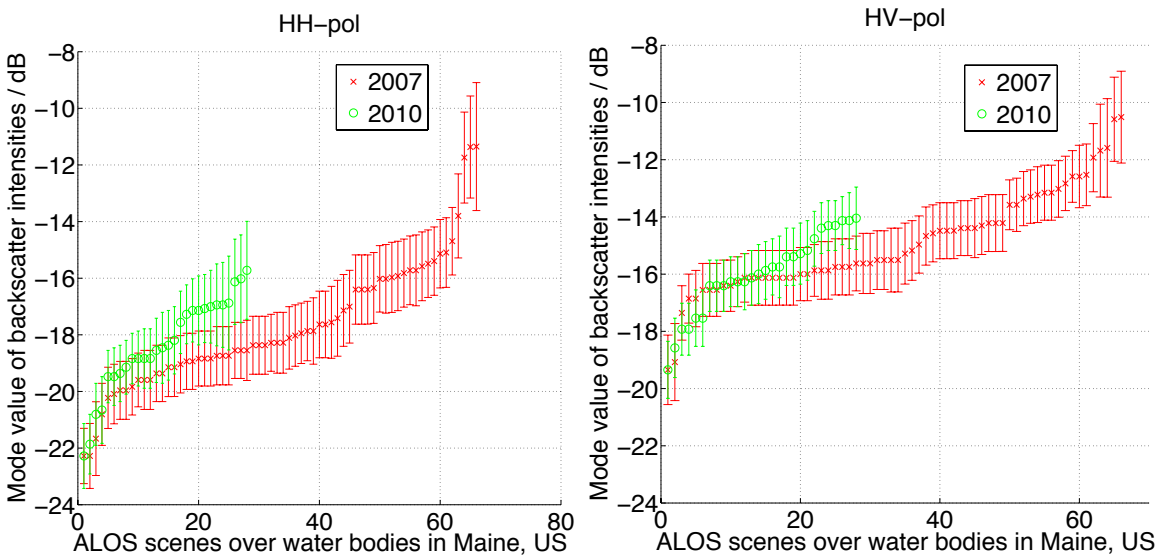


Figure 5.3: The mode values of the HH-pol (**a**) and HV-pol (**b**) ALOS/PALSAR backscatter intensities over all the water bodies in Maine, US between 2007 and 2010.

process, two histograms of the radar backscatter coefficient (intensity) taken from a sample imagery acquired over ILCP in Queensland, Australia, are shown in Figure 5.2. As this section analyzes the SAR backscatter power, we would like to provide the complete results for both the HH-pol and the HV-pol data. As there are a large number of relatively barren surfaces within our study area, the peak values in the histogram (*i.e.*, 0.0225 or -16.48 dB for HH-pol and 0.0145 or -18.39 dB for HV-pol data respectively) represent returns from ground surfaces, and therefore are a combination of the reflected radar signal from the surfaces and thermal noise inherent to the system. In this case, the intensity value of the peak will be greater than the noise level. Figure 5.3 illustrates the mode values (*i.e.*, the most frequent value) of the ALOS/PALSAR backscatter intensities over water bodies (lakes, rivers, and ocean) in the US state of Maine. These scene-wide mode values over water bodies are collected from 94 ALOS InSAR scenes. Both of the HH-pol and HV-pol scenarios have a consistent estimate of thermal noise determined from the histogram mode

of reflectivity for data between 2007 and 2010. Because the thermal noise level is an inherent characteristic of the SAR receiver that operates in a stable condition, we therefore consider these minimum mode values as thermal noise levels, which are -22.3 dB for HH-pol and -19.4 dB for HV-pol. These values are different from reported Noise-equivalent sigma-zero (NESZ) value (-32 dB for FBD HH-pol and -34 dB for FBD HV-pol over wind-slick regions in Hawaii; [74]) that selects the minimum backscatter intensity during the 20 s of PALSAR data, our method is a statistical one that utilizes the minimum mode value of backscatter intensities collected over water bodies, which have extremely low reflectivity.

## 5.2 Ground validation at ILCP, Queensland, Australia

In this section, the ground validation results are demonstrated for the forest height inversion approach over the test site at ILCP, in Queensland, Australia. In particular, Section 5.2.1 introduces the study area of ILCP and the experimental data that is used for the validation, while Section 5.2.2 provides the forest height inversion results in comparison with airborne/spaceborne LiDAR data.

### 5.2.1 Study area and experimental data

#### 5.2.1.1 Study area

The study focused on a 90 × 90 km region (see Figure 5.4a) centered on the Injune Landscape Collaborative Project (ILCP; Latitude $-25°32'$, Longitude $147°32'$) research site, which is located within the Brigalow Belt Bioregion of central southeast Queensland. The area is comprised of open forests (canopy cover > 30 %) and woodlands (between 10 and 30 %) and agricultural land used primarily for cattle production. The forests in the ILCP are mostly comprised of Eucalyptus species, with E. populnea (poplar box) and E. melanaphloia (silver-leaved ironbark) dominating and being up to 25 m tall. Callitris glaucophylla (white cypress pine) also domi-

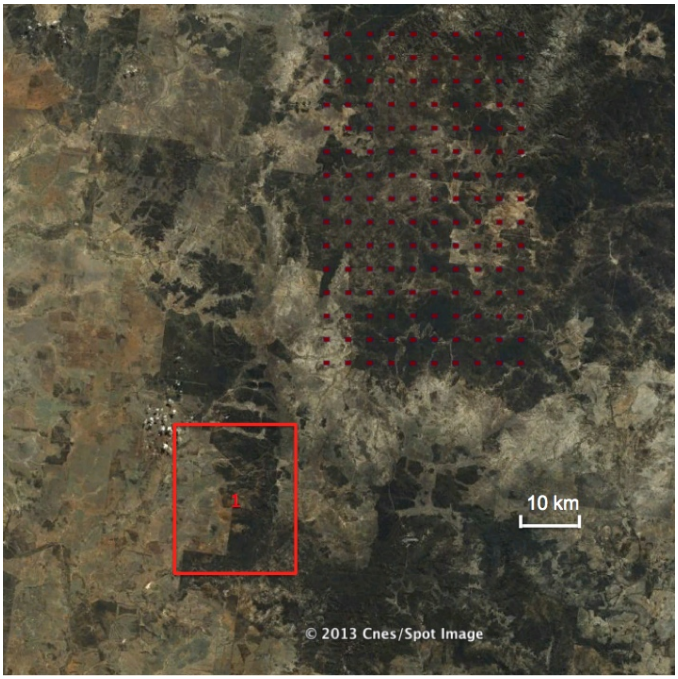


(**a**)

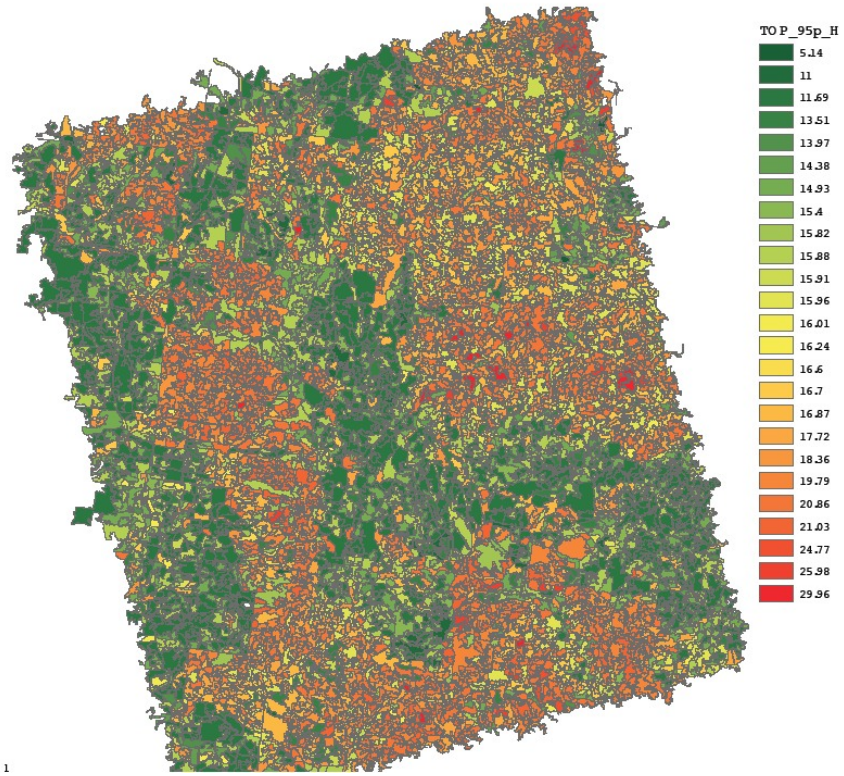


(**b**)

Figure 5.4: (**a**) shows the study area (90 × 90 km) at ILCP, Australia along with validation sites: the grid of PSU sites (500 × 150 m for each grid point) and test site #1 (25 × 20 km). (**b**) shows the clustered ICESAT forest heights over the same study area at ILCP.

nates many stands on sandy soils with heights being between 4 and 12 m although individual trees may exceed 25 m [78]. Stands dominated by Callitris species are harvested commercially through selective logging. Other species occurring include the widely dispersed Angophora leiocarpa and A. floribunda (smooth and rough barked apple respectively), with these often extending 30 m in height. Regrowth following abandonment or neglect of previously cleared agricultural land is often dominated by brigalow (Acacia harpophylla).

As illustrated in Figure 5.4a, two test sites are selected in consideration of different purposes. First of all, a grid within the ILCP research area is marked in red, which consisted of 150 $500 \times 150$ m Primary Sampling Units (PSUs), with each divided into 30 $50 \times 50$ m Secondary Sampling Units (SSUs). The airborne LiDAR data have been acquired over this grid of PSU sites in 2000 and also 2009. Therefore, the ALOS InSAR height estimates will be compared with the airborne LiDAR data over this PSU grid. Test site #1 ($25 \times 20$ km) is selected for the comparison of the ALOS heights with the clustered ICESAT heights (see Figure 5.4b).

#### 5.2.1.2 Available data

Through JAXA's Kyoto and Carbon Initiative (K&C), over 20 dual-pol and quad-pol ALOS/PALSAR scenes were acquired over the ILCP between 2006 and 2010. However, while the site is seasonally dry and semi-arid and hence the likelihood of obtaining InSAR data that are minimally affected by temporal decorrelation is increased, only three interferometric pairs were selected with two of them (acquired in 2007 and 2008, respectively) identified as having a relatively high average of correlation magnitude and hence suitable for retrieving forest height [46]. For each interferometric pair, fine-beam dual-polarization (FBD) data were available. However, due to the regional rainfall occurring over the study area in the InSAR acquisition of 2008, which violated the constant temporal change effects across the scene (see Ap-

pendix A), only the interferogram collected in 2007 has the best correlation magnitude average, and therefore is most suitable for forest height inversion.

To validate the forest height retrieved from InSAR correlation magnitude, estimates of clustered forest height (top 95% height) obtained from ICESAT GLAS data (see Figure 5.4b) were available for objects generated across the entire ILCP through segmentation of ALOS/PALSAR HH and HV data and Landsat-derived Foliage Projective Cover (FPC) data. Using these two datasets, the segments generated were of varying dimension but found to be relatively homogeneous in terms of vertical structure, as determined through reference to airborne LiDAR data acquired in 2000 and also 2009. As mentioned earlier, these airborne data had been acquired previously over the PSU grid. The measures of vertical structure, including median stand height, retrieved from the airborne LiDAR were validated with reference field data collected in 2000 [78]. The clustered ICESAT forest heights and 2009 airborne LiDAR data are used to validate the proposed approach.

### 5.2.2 Results and discussions

#### 5.2.2.1 Interferogram generation

For each interferogram, the complex correlation was calculated by averaging multiple looks (*i.e.*, two range looks along with ten azimuth looks) using the Gamma Remote Sensing processing software [90]. The range and azimuth common band filtering for each interferometric pair were applied to compensate for the effect of geometric decorrelation [19, 68]. The data were then transformed into map coordinates (at a spatial resolution of $30 \times 30$ m) such that they were coincident with the Shuttle Radar Topography Mission (SRTM) Digital Surface Model (DSM), through a lookup table. The observed correlations were then corrected for correlation magnitude bias and thermal noise decorrelation, as described in Section 5.1.2 and Section 5.1.3, resulting in the correlation component attributable to volume scattering and temporal

changes. The inverted pixel-based height estimates will be further averaged to achieve the forest height estimates (on the order of 10 hectares) in order to reduce the noise in the sampled correlation magnitudes.

#### 5.2.2.2 Validation with airborne LiDAR data

To determine the model parameters (*i.e.* $S_{scene}$ and $C_{scene}$) for the 2007 interferometric pair, the 2009 airborne LiDAR data over the grid of PSU sites was used. A similar comparison was made with airborne LiDAR data collected in 2000, which provide almost the same results as data collected in 2009. LiDAR-derived metrics of RH100 and RH70 were tested, with both generating similar results with one another (with the normalized RMSE of 20.1% for RH100 and 20.2% for RH70). In this work, RH100 was used because of its larger dynamic range. The comparison result is illustrated in Figure 5.5 with each point corresponding to a PSU stand of 500 m $\times$ 150 m.

From Figure 5.5a, the HV-pol InSAR correlation magnitude-inverted forest height is comparable to the airborne LiDAR height data. Basically, the estimation error in this forest height inversion approach results from the imperfectness of the assumption that $S_{scene}$ and $C_{scene}$ are constant for all of the targets in an InSAR scene (see Appendix A), *i.e.* spatial variation of these model parameters across the scene cannot be sufficiently described by a unique pair of parameters. However, as we have observed so far, this error source provides a RMSE of 5 m for forest stands of 7.5 hectares, which is good for most cases. Figure 5.5a also validates Appendix B, where the HV-pol data can be characterized by the modified RVoG model (3.6) with a small $m$ and $\mu \approx 1$ (see Figure B.1b). The data points above the "1:1" line are indicators of disturbance events, e.g., selective logging (to be discussed in Section 5.2.2.5).

As a comparison, Figure 5.5b illustrates the HH-pol inverted forest height. Practically, the $S_{scene}$ of HH-pol data is probably different from that of HV-pol. However,

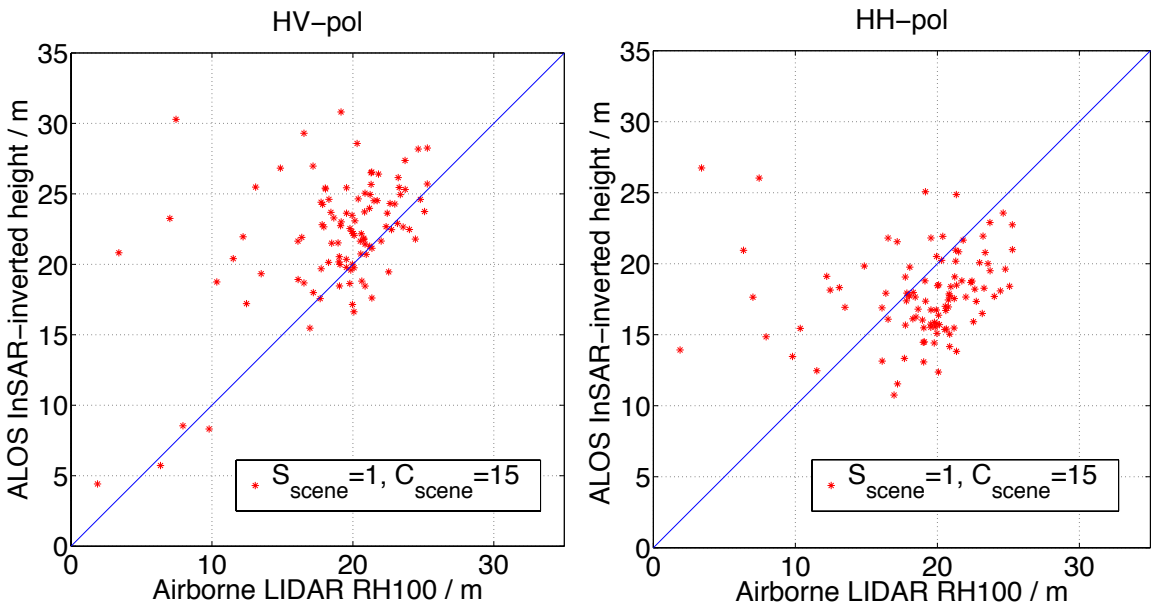


(**a**) (**b**)

Figure 5.5: Quantitative comparison of the ALOS InSAR-inverted heights from the HV-pol (**a**) and HH-pol (**b**) 2007 interferometric pair with the 2009 airborne LiDAR heights over the grid of PSU sites. Each point corresponds to a forest stand of 500 m $\times$ 150 m.

since the HH-pol data is less sensitive to volume scattering and $S_{scene}$ describes the temporal correlation due to volume dielectric change, the HH-pol $S_{scene}$ should be greater than or equal to that of HV-pol. Also, we have $S_{scene} = 1$ for HV-pol data (see Figure 5.5a), which implies the volume dielectric change can be ignored. So it is reasonable to conclude that $S_{scene} = 1$ for HH-pol data. By applying the same $C_{scene}$ as the HV-pol counterpart, it can be seen that the result in Figure 5.5b is similar to Figure B.1a and can be characterized by the modified RVoG model (3.6) with a large m and $\mu \neq 1$ (Appendix B).

#### 5.2.2.3 Forest height map generation

The HV-pol map and the HH-pol map of the InSAR-inverted heights over the study area of ILCP are illustrated in Figure 5.6 by using the model parameters derived from Section 5.2.2.2, and overlain on the optical imagery of Google Earth. Both maps

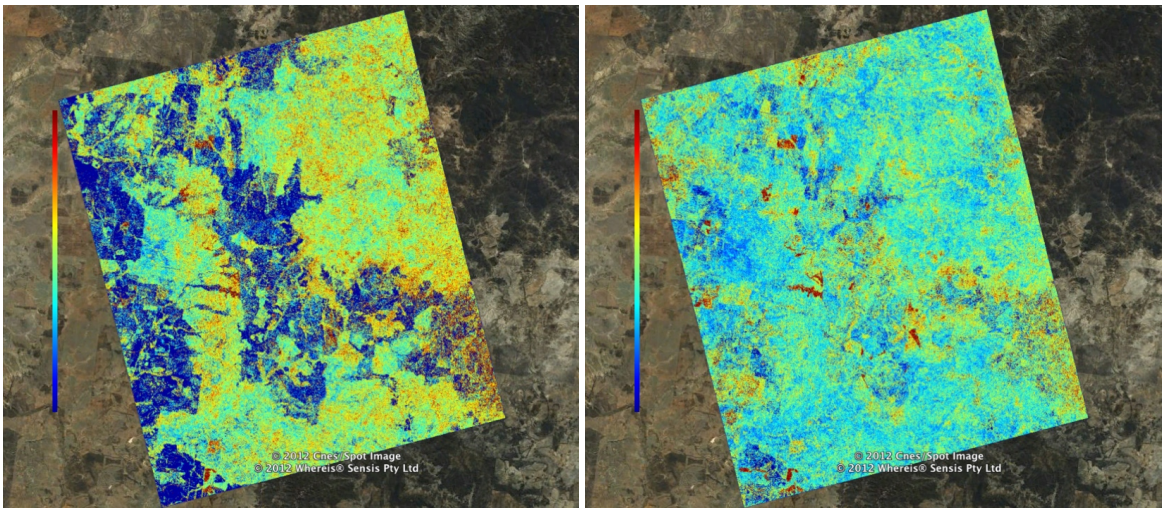


(**a**) (**b**)

Figure 5.6: The InSAR-inverted forest height maps for the study area of ILCP, Australia are shown for HV-pol (**a**) and for HH-pol (**b**). Both maps are coded with a color scale ("red" being 45 m, "blue" being surfaces).

share the same color scale from 0 to 45 m, with "blue" being ground surfaces and "red" being 45 m tall trees. Note both the maps are at the original resolution (*i.e.* 30 m $\times$ 30 m) without spatial averaging. Comparison between Figure 5.6a and Figure 5.6b reveals that the HH-pol map is very sensitive to the ground contribution and therefore the use of this polarimetric combination in this application for estimating forest height in a dry shrubland is problematic.

In regions where drastic changes in the land cover are occurring (e.g. selective logging), an unusually large value of decorrelation is observed with similarly large (and unrealistic) estimates of forest height (as discussed in Section 5.2.2.5). While these regions are considered a source of error in forest height estimation, a threshold can be used in their detection and a highlight in the image made where these sorts of changes are occurring (a useful output as well).

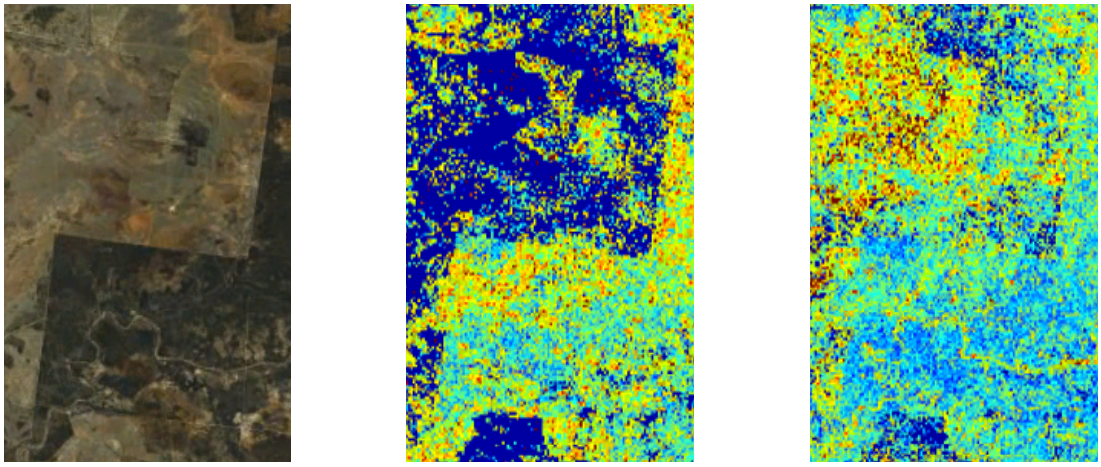

(**a**) (**b**) (**c**)

Figure 5.7: The InSAR-inverted forest height maps over test site #1 superimposed on the optical image (**a**) are shown for HV-pol (**b**) and HH-pol (**c**) data.

#### 5.2.2.4 Validation with the clustered ICESAT data

Test site #1 is selected for verifying the model parameters derived using airborne LiDAR data over the PSU grid. The maps of inverted forest height over test site #1 are shown in Figure 5.7 with the quantitative comparison results plotted in Figure 5.8. In Figure 5.8, each point represents a forest stand of 480 m × 480 m. Although the ICESAT segments are of varying sizes, the mean segment is on the order of 480 m × 480 m. The quantitative plots in Figure 5.8 demonstrate similar features compared to Figure 5.5. In fact, the combination of Figure 5.5 and Figure 5.8 validate the polarization dependence of this inversion approach as discussed in Appendix B.

The comparison of forest height inverted from HV-pol data with the clustered ICESAT data (see Figure 5.8a) shows both underestimation and overestimation of FSH. Data points above the "1:1" line are primarily indicators of disturbance events, e.g., selective logging, but can also result from the error in the ICESAT-derived height estimates. Uncertainties of InSAR-derived forest height at lower heights in Figure 5.8a can be attributed to the fact that no ICESAT heights are under 10 m for test site #1. This error in the ICESAT height data is known for this region, and is evident

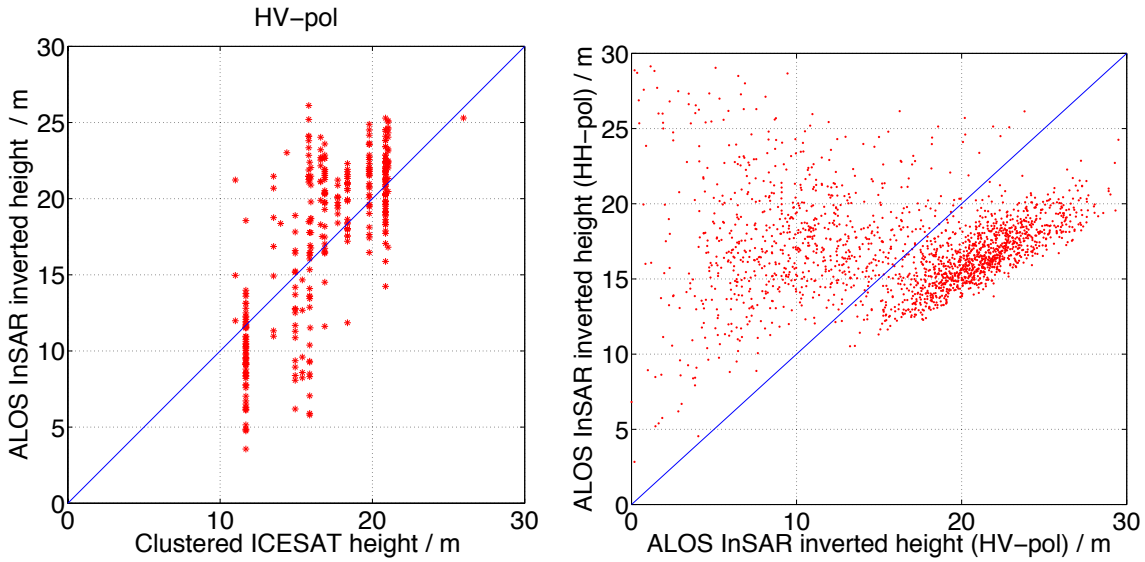


(**a**) (**b**)

Figure 5.8: Quantitative comparison of the HV-pol (**a**) and HH-pol (**b**) ALOS InSAR inverted heights with the clustered ICESAT heights and themselves over test site #1. Each point in (b) corresponds to a forest area of 480 m × 480 m, while that in (a) corresponds to a segment having a similar size to a 480 m × 480 m area.

upon examination of optical imagery. As for the HH-pol comparison (Figure 5.8b), we utilized the HV-pol ALOS InSAR inverted height as the ground truth height instead of using the clustered ICESAT height data since it can be noticed that from Figure 5.8a, the clustered ICESAT data has low accuracy for this type of study. Moreover, from both Figure 5.5a and Figure 5.8a, the HV-pol InSAR inverted height is observed to be consistently comparable to the ground validation heights.

A comparison between Figure 5.7b and Figure 5.7c illustrates that the HH-pol inverted forest height is very sensitive to not only temporal changes of the ground dielectric properties but also the disturbances of the ground dielectric change (shown as "red" spots in Figure 5.7c), while the HV-pol inverted height are much more sensitive to the volume than the ground.

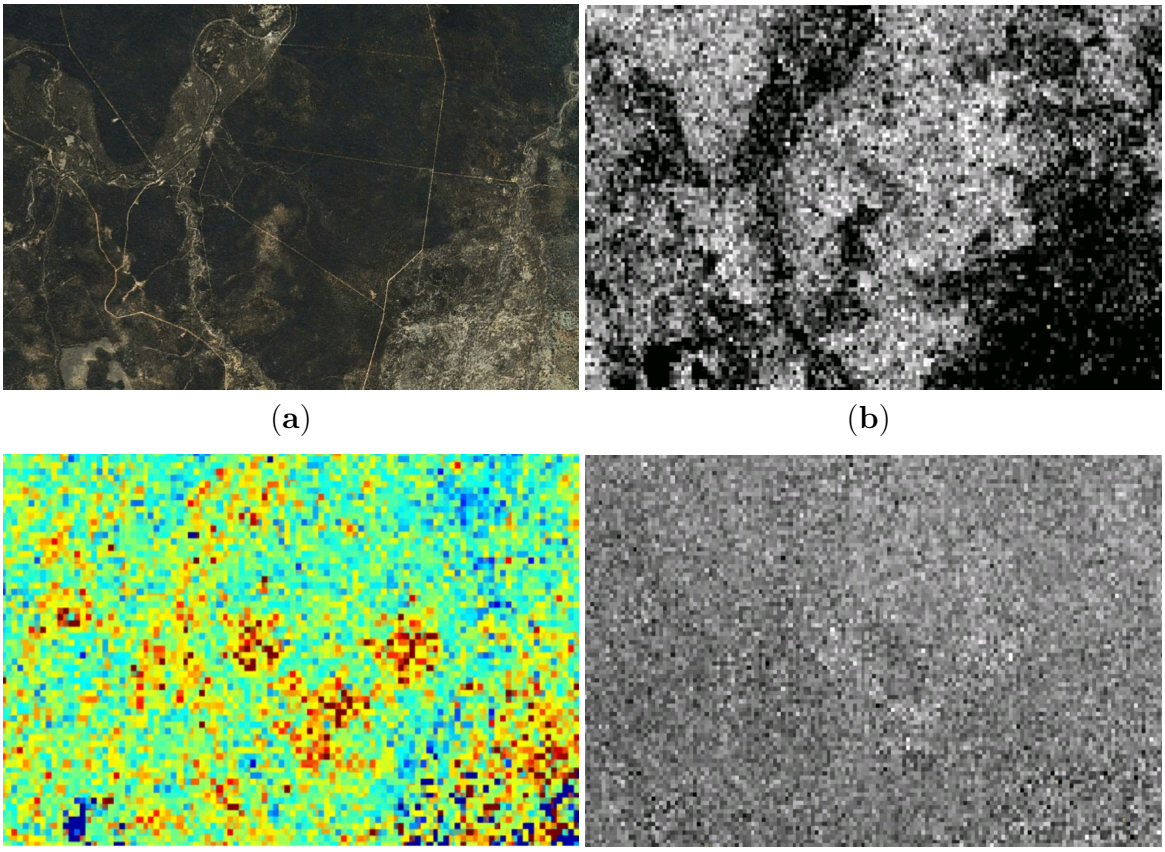

(**a**) (**b**)

(**c**) (**d**)

Figure 5.9: A closeup of the central region of the study area that illustrates the capabilities of the interferometric correlation and the RCS intensity in measuring forest change where selective logging is known to have occurred. (**a**) is the optical image from Google Earth, (**b**) is the RCS/backscatter intensity, (**c**) is the inverted forest height using InSAR correlation magnitude, and (**d**) is the RCS change.

#### 5.2.2.5 Characterization of forest change

In many regions of the inverted forest height maps (see Figure 5.9, which is taken from a central region of Figure 5.6a, the large InSAR-inverted heights (marked in red) are the consequences of change in the forest canopy rather than an indication of taller trees. This is confirmed through reference to hyper-temporal observations using Landsat and MODIS-simulated Landsat sensor data and time-series comparison of high-resolution optical data from the 2000 airborne campaign and Worldview observations in 2010 which concludes that selective logging is occurring at these lo-

cations [52]. Subtle changes such as these are not readily observed in the backscatter intensity image.

Establishing which areas of the image are indicative of structure or a disturbance event is difficult without the use of other datasets (e.g., time-series of Landsat Foliage Projective Cover (FPC), as used for statewide mapping and reporting of change) as the effects from volume scattering, temporal changes and disturbance events are all coupled together. However, if a "best effort" is performed to remove the effect of volume scattering and temporal changes by utilizing part of the test data as training set as well as other validation data (e.g., LiDAR/forest inventory data) to remove $\gamma_{v\&t}$, a quantitative description of the disturbance behavior can be obtained. This effort will be elaborated in Section 5.6, where a forest disturbance map can be generated along with the inverted forest height map.

Taken over a larger area and over a longer time period, this type of work can be extended to provide a model of forest changes that will be important for detecting land cover change, such as selective logging and forest degradation, and is a useful result in its own right. Such information is also important for understanding the limitation of the proposed InSAR technique for estimating vegetation height, and for characterizing this error source for DESDynI-R (now called NISAR) like missions [3].

## 5.3 Ground validation at the Howland Research Forest, Maine, US

In this section, ground validation results are provided for the forest height inversion approach over the Howland research forest in central Maine, US. Particularly, Section 5.3.1 introduces the study area and the experimental data, while Section 5.3.2 demonstrates the forest height inversion results in comparison with airborne LiDAR data.

### 5.3.1 Study area and experimental data

#### 5.3.1.1 Site description

To validate the inversion model, the chosen study area extends over a 83 km $\times$ 71 km region in central Maine (see Figure 5.10), where the Howland Research Forest (Latitude $45°12'$, Longitude $-68°43'$) and the Penobscot Experimental Forest (Latitude $44°51'$, Longitude $-68°37'$) are located. Two climate observing stations that are close to the Howland forest and the Penobscot forest are illustrated in Figure 5.10 with the historical weather record available from National Oceanic and Atmospheric Administration (NOAA)'s National Climate Data Center (NCDC) [1].

About 35 miles north of Bangor, ME, the 202-ha Howland research forest is a boreal-northern hardwood transition forest consisting of spruce-hemlock-fir, aspen-birch, and hemlock-hardwood mixtures with average tree height of 20 m [25]. The forest has not been selectively logged since 1900 and is considered as an "overmature" forest. The climate over this area is primarily cold, humid, and continental with the snowpack being of up to 2 m from December through March. The annual temperature and rainfall in this region are measured as $6.1 \pm 1.0$ °C and $988 \pm 170$ mm. The topography around this area varies from flat to gently rolling with a maximum elevation change of $< 68$ m within 10 km.

Similarly, the 1619-ha Penobscot experimental forest adjacent to Bangor, ME across the Penobscot river is located in Acadian Forest, which is an ecotone between the eastern broadleaf and boreal forests consisting of a mixture of northern conifers and hardwoods dominated by spruces, balsam fir, and eastern hemlock [69]. The average tree height is 18.4 m. The climate is cool and humid with the annual temperature average of 6.6 °C (e.g., $-7.0$ °C for February and 20.0 °C for July). Annual precipitation is about 1060 mm, with 48% falling from May through October, and annual snowfall averages 239 cm.

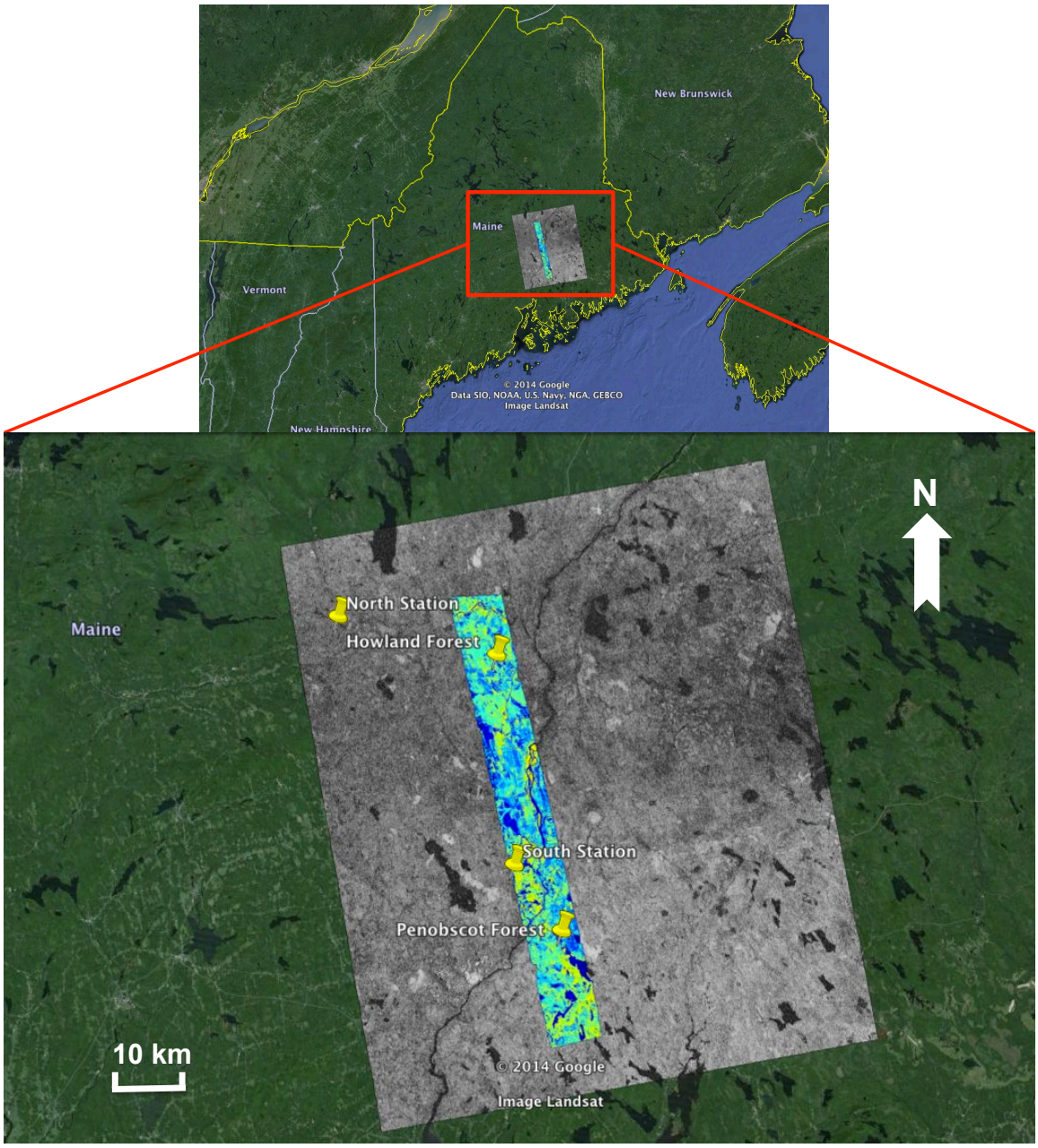


Figure 5.10: Study area in Maine, US. The grey image shows the correlation magnitude of the interferogram 10 July–25 August 2007 over the central Maine area, where the Howland research forest and the Penobscot experimental forest are encompassed and marked. The overlaid color map is an LVIS strip of height, and serves as the ground validation data for forest height inversion. Two climate observing stations ("North Station" and "South Station") are also indicated.

#### 5.3.1.2 LVIS lidar data

Ground validation data exists in the form of a narrow strip (63 km $\times$ 7 km) of Laser Vegetation Imaging Sensor (LVIS; [7]) data collected over the Howland forest and the Penobscot forest in 2009. LVIS is an airborne full-waveform scanning laser altimeter, which is developed by NASA's Goddard Space Flight Center (GSFC). It operates at an altitude of 10 km producing swath up to 1000 km wide and normally with 25-m wide footprints and 10-cm height accuracy. The LVIS height data in this study is demonstrated as a color strip map in Figure 5.10 with a spatial resolution of 50 m $\times$ 50 m in raster grid. The data products of LVIS Lidar data has various metrics: RH50, RH75 and RH100, *etc.* Here, "RH" means relative height, and RH100 height stands for the height above the detected ground at which 100% of the waveform energy has been returned, and is typically associated with the maximum tree height within a resolution beam of the lidar. In this study, RH100 metric is used as the ground truth forest height and found to be well related to the ALOS InSAR-inverted forest heights, as will be shown in Section 5.3.2.2.

#### 5.3.1.3 ALOS/PALSAR data

ALOS/PALSAR is a repeat-pass L-band SAR developed by JAXA through the K&C Initiative [74, 66]. The repeat period of ALOS/PALSAR is 46 days. In this central Maine area, there also exists eight FBS (fine-beam single-polarization) and ten FBD (fine-beam dual-polarization) ALOS/PALSAR scenes (Table 5.1). In Table 5.1, we also show the temperature and the precipitation on the observation date, as well as the accumulated precipitation during the past three days prior to the data collection (denoted as "3-day accumulated precipitation"), all of which are available from NOAA's NCDC [1]. For each observation date, the weather record for both climate observing stations are demonstrated. The "3-day accumulated precipitation" is used because it happens that there might not be rainfall on the observation date; however,

Table 5.1: ALOS/PALSAR acquisitions over the central Maine area between 2007 and 2011. For each acquisition, weather conditions are provided over the "North Station" (denoted by "(N)") as well as the "South Station" (denoted by "(S)"). "3-day Accumulated Precipitation" stands for the accumulated precipitation during the past three days prior to the observation date.

| **Collection Date** | **Data Mode** | **Precipitation (mm)** | **3-day Accumulated Precipitation (mm)** | **Temperature (Max/Min; °C)** |
|---|---|---|---|---|
| 20070107 | FBS | 7.6 (N)<br>0.0 (S) | 20.6 (N)<br>16.3 (S) | 12.8/3.3 (N)<br>6.7/−3.9 (S) |
| 20070222 | FBS | 0.0 (N)<br>0.0 (S) | 1.3 (N)<br>0.0 (S) | 0.0/−15.6 (N)<br>−1.7/−20.6 (S) |
| 20070710 | FBD | 2.8 (N)<br>0.0 (S) | 3.3 (N)<br>0.0 (S) | 19.4/9.4 (N)<br>28.9/12.2 (S) |
| 20070825 | FBD | 19.1 (N)<br>1.0 (S) | 5.3 (N)<br>8.4 (S) | 22.2/17.8 (N)<br>29.4/15 (S) |
| 20071010 | FBD | 0.5 (N)<br>0.0 (S) | 4.6 (N)<br>1.0 (S) | 16.7/3.3 (N)<br>12.2/7.2 (S) |
| 20080110 | FBS | 2.5 (N)<br>0.0 (S) | 0.3 (N)<br>0.3 (S) | 11.1/2.8 (N)<br>6.7/−4.4 (S) |
| 20080225 | FBS | 0.0 (N)<br>0.0 (S) | 3.8 (N)<br>4.3 (S) | 3.9/−12.2 (N)<br>5/−13.3 (S) |
| 20080411 | FBS | 0.0 (N)<br>0.0 (S) | 0.0 (N)<br>0.0 (S) | 12.2/1.1 (N)<br>11.1/0.6 (S) |
| 20080527 | FBD | 0.5 (N)<br>0.0 (S) | 2.3 (N)<br>0.0 (S) | 22.2/11.1 (N)<br>26.7/6.7 (S) |
| 20080712 | FBD | 0.0 (N)<br>0.0 (S) | 8.6 (N)<br>0.0 (S) | 24.4/8.9 (N)<br>26.1/8.3 (S) |
| 20090227 | FBS | 0.3 (N)<br>7.6 (S) | 0.3 (N)<br>0.0 (S) | 2.2/−12.2 (N)<br>8.9/−6.7 (S) |
| 20090830 | FBD | 14.0 (N)<br>0.0 (S) | 2.5 (N)<br>51.3 (S) | 11.7/10 (N)<br>21.1/10.6 (S) |
| 20091015 | FBD | 0.0 (N)<br>0.0 (S) | 9.1 (N)<br>10.2 (S) | 7.8/−3.3 (N)<br>5.6/−3.9 (S) |
| 20100417 | FBS | 0.0 (N)<br>0.0 (S) | 0.0 (N)<br>0.0 (S) | 11.1/0.6 (N)<br>6.1/2.2 (S) |
| 20100602 | FBD | 17.8 (N)<br>0.0 (S) | 0.0 (N)<br>11.4 (S) | 15.6/12.2 (N)<br>22.2/12.2 (S) |
| 20100718 | FBD | 2.5 (N)<br>0.0 (S) | 0.0 (N)<br>0.0 (S) | 30.6/16.7 (N)<br>28.9/17.2 (S) |
| 20101018 | FBD | 0.0 (N)<br>0.0 (S) | 45.2 (N)<br>41.1 (S) | 16.1/4.4 (N)<br>10/1.1 (S) |
| 20110305 | FBS | 0.3 (N)<br>0.5 (S) | 1.0 (N)<br>1.8 (S) | −1.7/−25 (N)<br>5.6/−3.3 (S) |

the humidity level is still high due to the accumulated rainfall in the past few days, e.g., "20101018". It can also be seen that some of the PALSAR scenes have uniform weather conditions over the northern and southern sites, e.g., "20070710", "20071010" and "20100718". However, some of them seem to have nonuniform weather conditions (e.g., "20070825"), which we would like to avoid in order to apply the assumption of constant temporal change parameters as discussed in Section 3.2.1 and in Appendix A (*i.e.*, the weather conditions for each acquisition of the interferogram is uniform). Such an effect can be seen in Figure 5.10 where the grey-scale image shows the correlation magnitude of the interferogram 07/10/2007–08/25/2007. Here, the correlation magnitude is significantly affected by the nonuniform weather conditions on 08/25/2007 due to the rainfall occurred over the northern site.

### 5.3.2 Results and discussions

In this section, we first describe the InSAR processing details and then validate the forest height inversion model by comparing ALOS InSAR correlation magnitude-inverted heights with LVIS heights (*i.e.*, supervised regression) over the Howland and Penobscot forests in central Maine.

#### 5.3.2.1 InSAR processing

All interferograms described in this work were created using Gamma Remote Sensing software [90] with a correlation estimation window size of $5 \times 5$ (*i.e.*, 5 range looks along with 5 azimuth looks for the estimation of InSAR correlation) and a multi-look averaging (two range looks along with ten azimuth looks) afterwards. The data were transformed into map coordinates (at a resolution of 20 m $\times$ 30 m) that are coincident with the Shuttle Radar Topography Mission (SRTM) data through a look-up table. The common-band filtering (both range and azimuth) is applied to ensure the geometric decorrelation is removed [19, 68]. The estimation bias in the sampled correlation magnitudes and the thermal noise decorrelation are corrected as

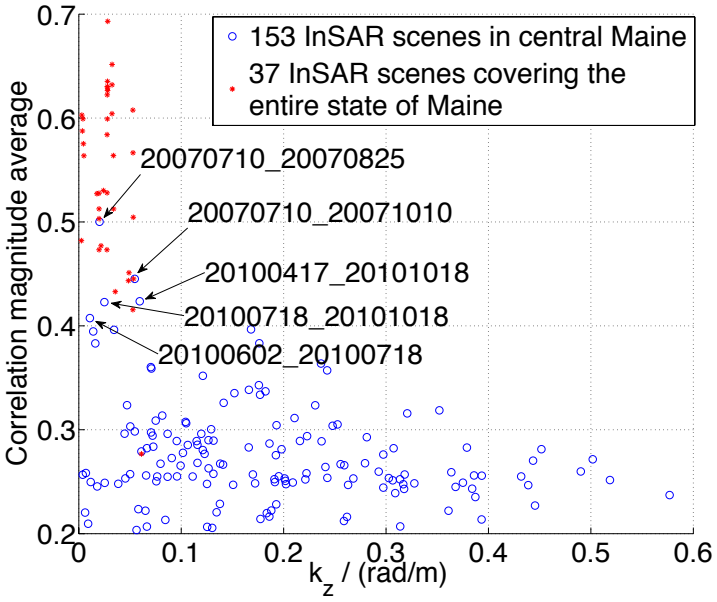


Figure 5.11: Scene-wide correlation magnitude averages and $\kappa_z$ values of the 153 interferometric pairs over central Maine (as blue circles) along with the 37 pairs covering the entire state of Maine (as red stars). All of the scenes have been calibrated for the geometric decorrelation. For the central Maine area, five best scenes are marked by the collection dates with their $\kappa_z < 0.06$ rad/m.

in Section 5.1.2 and Section 5.1.3, respectively. The remaining correlation component only deals with the coupled effect of volume scattering and temporal change.

Specifically, common-band filtering was applied to the eight FBS and ten FBD observations so that interferograms could be formed out of all combinations [90]. These were processed into 153 interferograms with the scene-wide correlation magnitude averages and their $\kappa_z$ values shown as blue circles in Figure 5.11. From Figure 5.11, it can be seen that even for $\kappa_z < 0.06$ rad/m, the ALOS scenes collected between July and October in both 2007 and 2010 have the best correlations amongst the possible combinations (even after accounting for the effects of baseline and volumetric decorrelation). While this may be a surprising result because it implies that the summer/fall data has the best correlations as opposed to winter scenes, we allowed the data to indicate the best scenes to use for this analysis. Such information may be pertinent to future spaceborne missions such as DESDynI-R (now called NISAR) and ALOS-2.

Note that we define the "best" scene as the one with the highest correlation magnitude. Although we utilize the temporal change effects to invert forest height, this does not contradicts considering the "best" scene with highest correlation magnitude (or equivalently the least temporal change effects). As seen in Figure 5.11, even for the best interferometric pair 07/10/2007–08/25/2007 with almost zero baseline, the correlation magnitude average is as low as 0.5, which is primarily dominated by temporal change effects with large temporal baseline (e.g., at least 46 days) and is believed to be sufficient for forest height inversion. Having a lower correlation magnitude average (or equivalently more temporal change effects) will make the inversion less robust and reliable due to the presence of correlation sampling noise [79]. Therefore, for repeat-pass InSAR data with large temporal baselines (on the order of months; at least 46 days for ALOS), we would like to seek the highest level of scene-wide correlation magnitude average in order to have reliable estimates of forest height.

As indicated in Figure 5.11 and also in [77] (under the unfrozen condition), the smaller $\kappa_z$ value, the more likely a high correlation magnitude average can be obtained (although the lower the sensitivity to height and vertical structure from the volume decorrelation). However, at a fixed $\kappa_z$ value, it is the level of the temporal change effects that determines whether a high correlation magnitude could be achieved. By referring to Table 5.1 for the weather conditions that relate to the five best interferometric pairs in Figure 5.11, we noticed that given a fixed $\kappa_z$ value, an interferometric pair with less precipitation on both observation dates and less 3-day accumulated precipitation prior to the observations is more likely to have a higher correlation magnitude average. That is why even for some of the interferometric pairs with almost zero baseline, the observed correlation magnitude average are still very low ($<$0.3). It is possible for them to have larger temporal baselines, *i.e.*, the larger temporal baseline, the more likely to have larger temporal change effects. However, the fundamental reason is that the temporal change effects (e.g., rainfall, wind, forest

growth, selective logging, freezing) are so pronounced for those observations that the SAR returns are barely correlated any more.

#### 5.3.2.2 Validation with LVIS lidar data

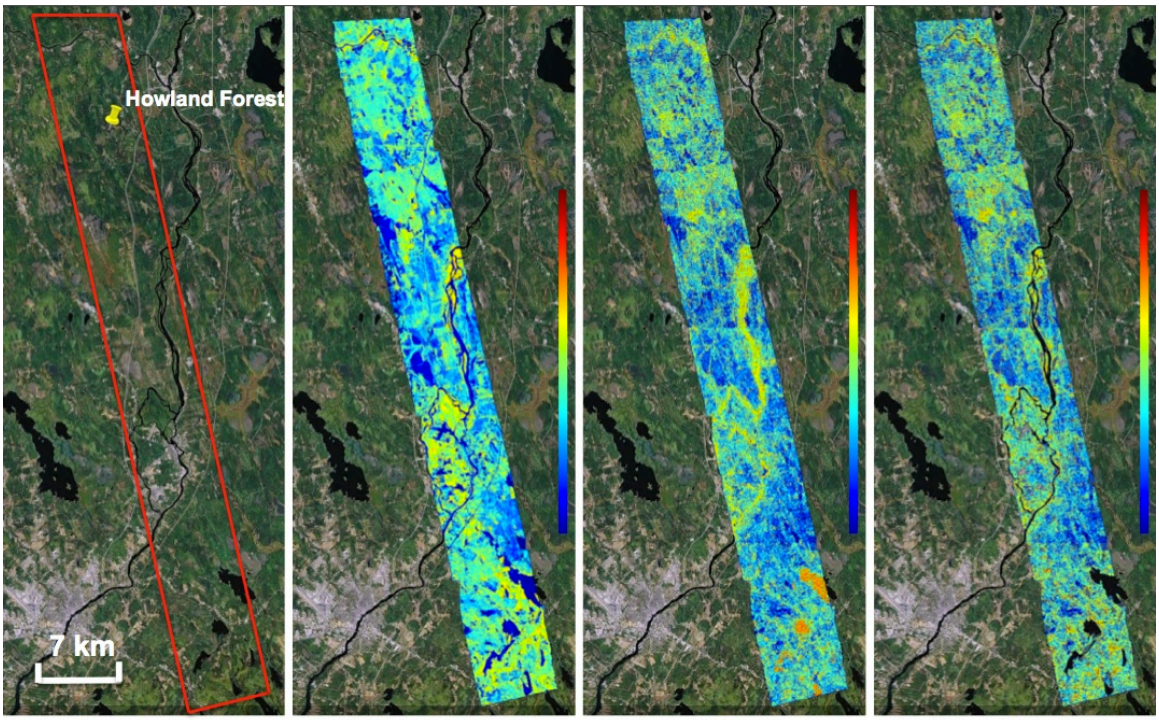


Figure 5.12: The optical image (**a**) from GoogleEarth is compared with the LVIS height data (**b**) and the ALOS correlation magnitude-inverted forest height (**c**) over the Howland research forest in central Maine. (**d**) shows the map from (c) with the values over water bodies removed. (b–d) are coded with the same color scale ("blue" being surfaces, "red" being 45 m). (c,d) are from the interferogram 07/10/2007–08/25/2007, which have been divided into three segments to characterize the spatial variation of temporal change effect. The spatial resolution of (b–d) is 50 m × 50 m.

As seen from Figure 5.11, the ALOS interferometric pair 07/10/2007-08/25/2007 for central Maine had the largest correlation magnitude, and thus was most suitable to be utilized for comparison with LVIS data. Through the proper estimation of the fitting parameters $S_{scene}$ and $C_{scene}$ (as in Section 3.2.3), the ALOS InSAR correlation magnitude-inverted height estimates are comparable with the LVIS RH100 height

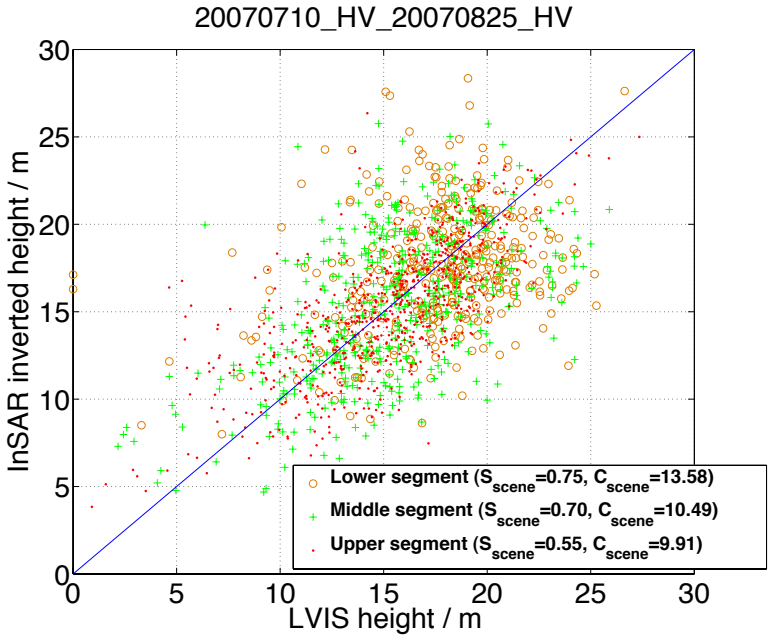


(**a**)

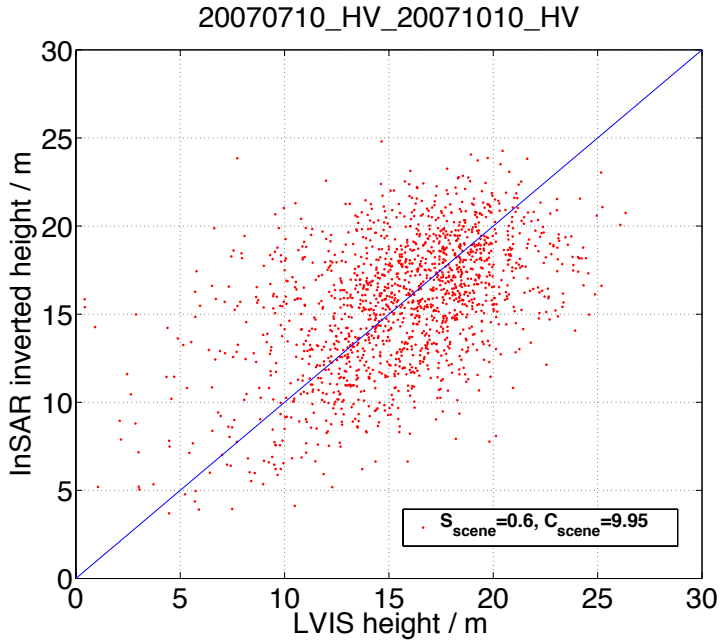


(**b**)

Figure 5.13: Quantitative comparison results between ALOS correlation magnitude-inverted forest height and LVIS height. (**a**) shows the result (comparison between Figure 5.12b and Figure 5.12d) for the interferogram 07/10/2007–08/25/2007, which is divided into three segments to account for different temporal change levels (RMSE = 3.6 m and R = 58%); while (**b**) shows the result of the interferogram 07/10/2007–10/10/2007, which seems to have uniform effect of temporal change (RMSE = 3.9 m and R = 49%). The resolution is 160 m × 480 m after multi-pixel averaging.

data as illustrated in Figure 5.12. Since repeat-pass InSAR correlation magnitude is sensitive to temporal decorrelation, the inverted height estimates are expected to be very large over water bodies (as shown by Figure 5.12c). After removing those height values by identifying open water regions with the National Land Cover Database 2006 (NLCD2006; [17]), the resulting map (*i.e.*, Figure 5.12d) corresponds well to the LVIS data (*i.e.*, Figure 5.12b). A quantitative comparison between these two images is shown in Figure 5.13a, where the resolution is 160 m $\times$ 480 m after multi-pixel averaging. In order to compensate for a spatial variation in the temporal decorrelation, the strip of InSAR height map (in both Figure 5.12c and Figure 5.12d) is divided into three segments with each segment allowed to have its own unique model parameters in order to fit best to the LVIS observations (as shown by the three different markers and their associated model parameters in Figure 5.13a). This spatial variation of temporal change effect (and thus the model parameters) has been verified with the use of the precipitation data from the National Climate Data Center (NCDC; [1]) in Appendix A, where the characterization of the spatial homogeneity is also discussed.

In comparison, Figure 5.13b shows the result for the second best interferometric pair 07/10/2007–10/10/2007, which tends to have a uniform degree of temporal decorrelation throughout the image, *i.e.*, a single pair of model parameters can be applied to all of the targets in the same test region. In Figure 5.13a, the RMSE of the ALOS InSAR correlation magnitude-inverted heights compared to LVIS heights is 3.6 m (correlation coefficient R = 58%), while in Figure 5.13b the RMSE is 3.9 m (R = 49%). In order to test the inherent homogeneity of temporal change parameters from the second best interferometric pair, we evenly divided the LVIS strip into two parts (*i.e.*, northern and southern parts), and performed a cross-validation by taking the northern heights as training samples and inverting the southern heights with the model parameters derived from the northern part. The derived parameters for the northern part are $S_{scene} = 0.59$, $C_{scene} = 9.42$ (as opposed to $S_{scene} = 0.6$,

$C_{scene} = 9.95$ in Figure 5.13b for the entire strip) with RMSE of 3.6 m and R of 56%, while by applying these parameters on the southern part we achieved the regression results with RMSE of 4.4 m and R of 47%. Note, it is the spatially correlated behavior of temporal change parameters that cause the consistency in these regression results over the LVIS strip (about a 44,000-hectare area).

Note the uncertainty at the lower end of the height range is related to extra temporal decorrelation (e.g., where water bodies are not thoroughly removed; farming activities, *etc.*), and poor SNR in ground scattering due to the thermal noise decorrelation (which makes the total correlation magnitude dominated by the sampling noise [79]). These overestimated values can be removed through the utility of a forest/non-forest classification map, which will be discussed later.

To this end, we have noticed the linear relationship between the InSAR correlation magnitude-inverted forest height and lidar height, which is obtained through the use of (3.5) or equivalently as in [5]. However, by using the linear motion variance as in [33], we observed a noticeable quadratic relationship between the InSAR-inverted height and lidar height. This can be explained as below. Given that the InSAR-inverted height using (3.5) is linear with the lidar height (e.g., Figure 5.13), we have (3.12) being the correct relationship between the observed correlation magnitude and actual forest height, *i.e.*, $|\gamma_{obs}| \propto \exp^{-ch_v^2}$ (where $c$ is a constant factor). However, if we used the linear motion variance in [33] to derive a similar model for the correlation magnitude, we would have the modeled correlation magnitude given as $|\gamma_{mod}| \propto \exp^{-c'h'_v}$ (where $c'$ is another constant factor and $h'_v$ is the estimated forest height). Therefore, in order to fit the modeled correlation magnitude to the observed value, we would achieve the estimated height being quadratic in the actual height, *i.e.*, $h'_v \propto h_v^2$.

## 5.4 Generation of forest height mosaic

In this section, we will propagate the inverted forest height as well as the model parameters that are derived over the ground validation site in central Maine area (see Section 5.3) throughout the entire state of Maine utilizing the overlap areas between adjacent interferometric pairs, and therefore create a state mosaic of forest height for the US state of Maine. In particular, Section 5.4.1 describes a manual mosaicking approach, and Section 5.4.2 provides an automatic mosaicking algorithm with the refined mosaic results shown in Section 5.4.3.

### 5.4.1 Mosaic map generation for the entire state of Maine

Based on the observation dates where the highest correlation magnitude average existed for the central Maine region, a set of ALOS images (about 0.6 million hectares for each image) was identified to create a state mosaic (about a 9 million-hectare area) of correlation magnitude (and hence forest height). Specifically, 94 ALOS scenes with multiple dates in the summer/fall 2007 and 2010 timeframe were analyzed, from which 37 interferometric pairs (see Table 5.2) had the best correlations with small $\kappa_z$ values (illustrated as red stars in Figure 5.11).

Assuming the parameters ($S_{scene}$ and $C_{scene}$) of the temporal change effect are constant within each scene (the scenes are selected with high level of homogeneity that is discussed in Appendix A), the spatial overlapping regions of adjacent ALOS interferometric scenes with different frame and orbit numbers in Table 5.2 can be used to propagate the derived model parameters and forest heights from the strip of LVIS data throughout the entire state of Maine. Although the best interferometric pair of Figure 5.13a has a smaller RMSE than the pair of Figure 5.13b, we prefer to utilize the second pair as the basis for propagating the analysis since it has more homogeneous effect of temporal change across the scene.

Table 5.2: Interferometric pairs utilized for generating the state mosaic. Each interferogram is indexed by its unique ALOS coordinate (frame # and orbit #), and named by the collection dates.

| Frame # \ Orbit # | 124 | 123 | 122 | 121 | 120 | 119 | 118 | 117 |
|---|---|---|---|---|---|---|---|---|
| 930 | | | | | 20070727<br>20070911 | 20070710<br>20070825 | 20070808<br>20070923 | |
| 920 | | | | 20100706<br>20100821 | 20070727<br>20070911 | 20070710<br>20070825 | 20070808<br>20070923 | |
| 910 | | | | 20100706<br>20100821 | 20070727<br>20070911 | 20070710<br>20070825 | 20070808<br>20070923 | |
| 900 | | | 20070715<br>20070830 | 20100706<br>20100821 | 20070611<br>20070727 | 20070710<br>20070825 | 20070808<br>20070923 | |
| 890 | | 20070616<br>20070801 | 20070715<br>20070830 | 20100706<br>20100821 | 20070727<br>20070911 | 20070710<br>20071010 | 20070808<br>20070923 | 20070722<br>20070906 |
| 880 | 20070703<br>20071003 | 20070616<br>20070801 | 20070715<br>20070830 | 20100706<br>20100821 | 20070611<br>20070727 | 20070710<br>20071010 | 20070808<br>20070923 | |
| 870 | 20070703<br>20071003 | 20070616<br>20070801 | 20100723<br>20100907 | 20100706<br>20100821 | 20070611<br>20070911 | | | |
| 860 | 20070818<br>20071003 | 20100809<br>20100924 | | | | | | |

The procedure for propagating the LVIS ground validation through the overlap regions of the ALOS data is illustrated in Figure 5.14. Here, we would like to propagate the inverted model parameters (and thus forest heights; Figure 5.14b) from the ALOS InSAR scene (orbit #: 119 and frame #: 890; denoted by "119_890") in central Maine where the LVIS strip is located, to achieve the parameters and forest heights for the ALOS InSAR scene (orbit #: 118 and frame #: 890; denoted by "118_890") on the right side. By choosing the model parameters of the InSAR scene"118_890" as $S_{scene} = 1$ and $C_{scene} = 8.85$ obtained from a rough estimate of these values, we have the resulting forest height map superimposed on the optical image in GoogleEarth (Figure 5.14c).

A quantitative comparison result is shown in Figure 5.15a for the overlapping region of these two scenes. It can be seen here that the estimated heights of the InSAR scene "118_890" do not match the reference heights of the InSAR scene "119_890" well. However, by adjusting the model parameters as $S_{scene} = 0.75$ and $C_{scene} = 13.86$

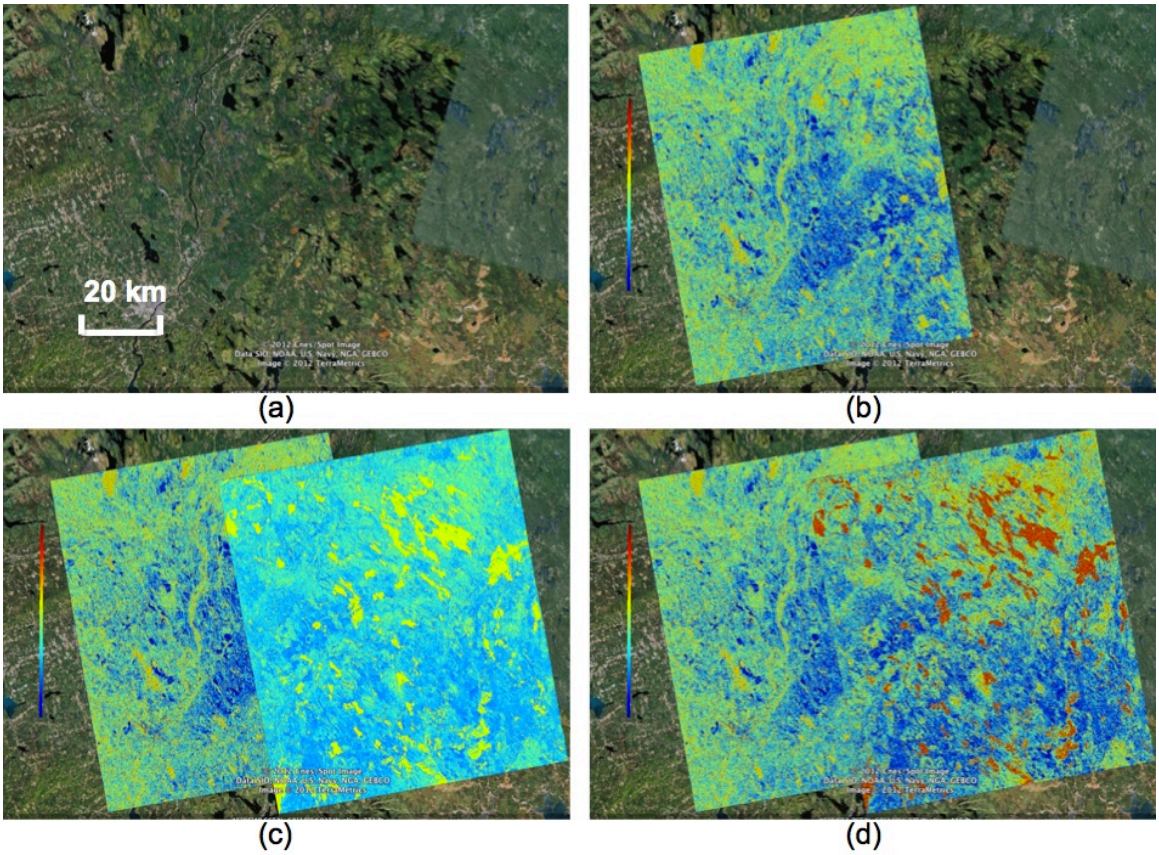


Figure 5.14: Illustration of the propagation procedure: the inverted model parameters and forest heights over central Maine (orbit #: 119 and frame #: 890) are exploited as the basis and propagated through the overlapping area to the interferogram on the right side (orbit #: 118 and frame #: 890). (**a**) shows the optical image available within GoogleEarth. As for the ground reference height, (**b**) shows the inverted forest height of the InSAR scene "119_890". (**c**) shows the inverted forest height of the InSAR scene"118_890" using inaccurate model parameters, while (**d**) shows the result with correct model parameters. All of the forest height maps are color-coded from 0 to 45 m with a spatial resolution of 20 m $\times$ 30 m.

through a curve fit (Section 3.2.3), the inverted forest height map is shown in Figure 5.14d with the quantitative comparison shown in Figure 5.15b, both of which imply that the estimated and ground reference heights correspond with each other well (RMSE = 2.69 m and R = 80% for all of the data points except those from water bodies). Note that the overestimated data points are from water bodies (identified by utilizing the water classification of NLCD2006 and shown as a different color in the figure) where high temporal decorrelation is expected.

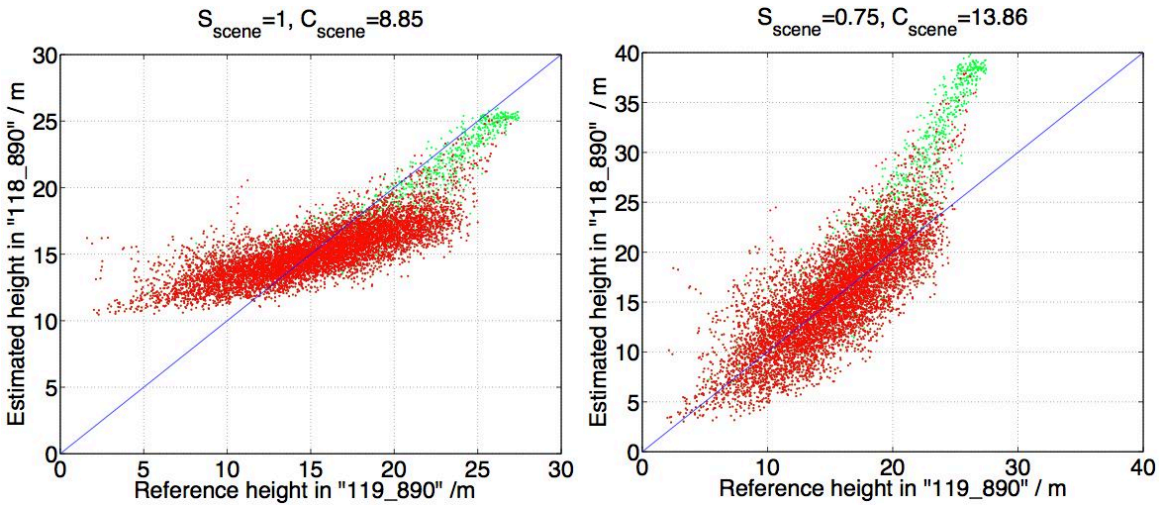


(**a**) (**b**)

Figure 5.15: Quantitative comparison results between the inverted forest heights in the InSAR scene "118_890" and the ground reference heights in the InSAR scene "119_890" (only for their spatial overlap): (**a**) corresponds to Figure 5.14c while (**b**) corresponds to Figure 5.14d (RMSE = 2.69 m and R = 80% for the "red" points). The resolution is 340 m × 750 m after multi-pixel averaging. The height estimates over water bodies are identified by using the water classification of NLCD2006 and represented as green dots.

Following the same procedure to propagate the analysis and the model parameters (and thus forest heights) as outlined in Figure 5.16, a state mosaic of forest height can be generated. This is shown in Figure 5.17. In Figure 5.16, along with the model parameters $S_{scene}$ and $C_{scene}$, an indication of the regression quality measures (*i.e.*, RMSE and R) are included for the cross-track direction (most of the scenes in the along-track direction are collected on the same date giving RMSE $<$ 0.5 m and R $>$ 99%). It can be seen that even though the cross-track scenes are collected with temporal baselines on the order of months (e.g., at least 46 days), there is indeed noticeable consistency (e.g., RMSE as low as 2 m and R up to 80%) between the inverted forest heights. Again, this verifies the homogeneity of temporal change parameters and implies that the errors in this type of inversion are manageable. Note

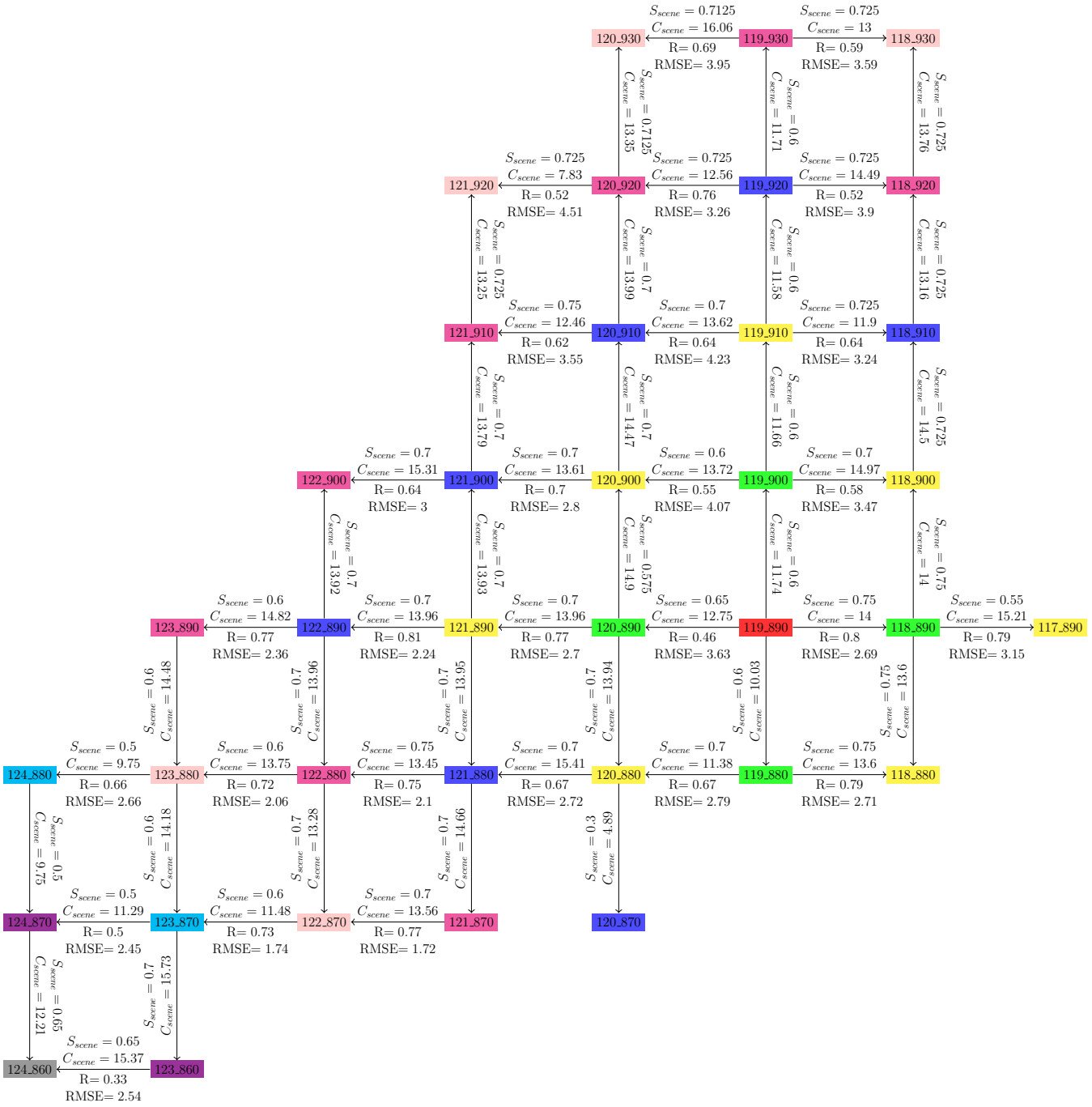


Figure 5.16: The outline of the mosaicking scheme. Each interferogram in Table 5.2 is represented by "orbit#_frame#". The mosaicking process starts from the InSAR scene "119_890" (marked in "red"), and propagates the analysis as well as the inverted forest heights by sequentially going through the interferograms marked in "green", "yellow", "blue", "magenta", "pink", "cyan", "violet" and finally "grey". The model parameters $S_{scene}$ and $C_{scene}$ along with RMSE (in units of m) and R in the cross-track direction are indicated.

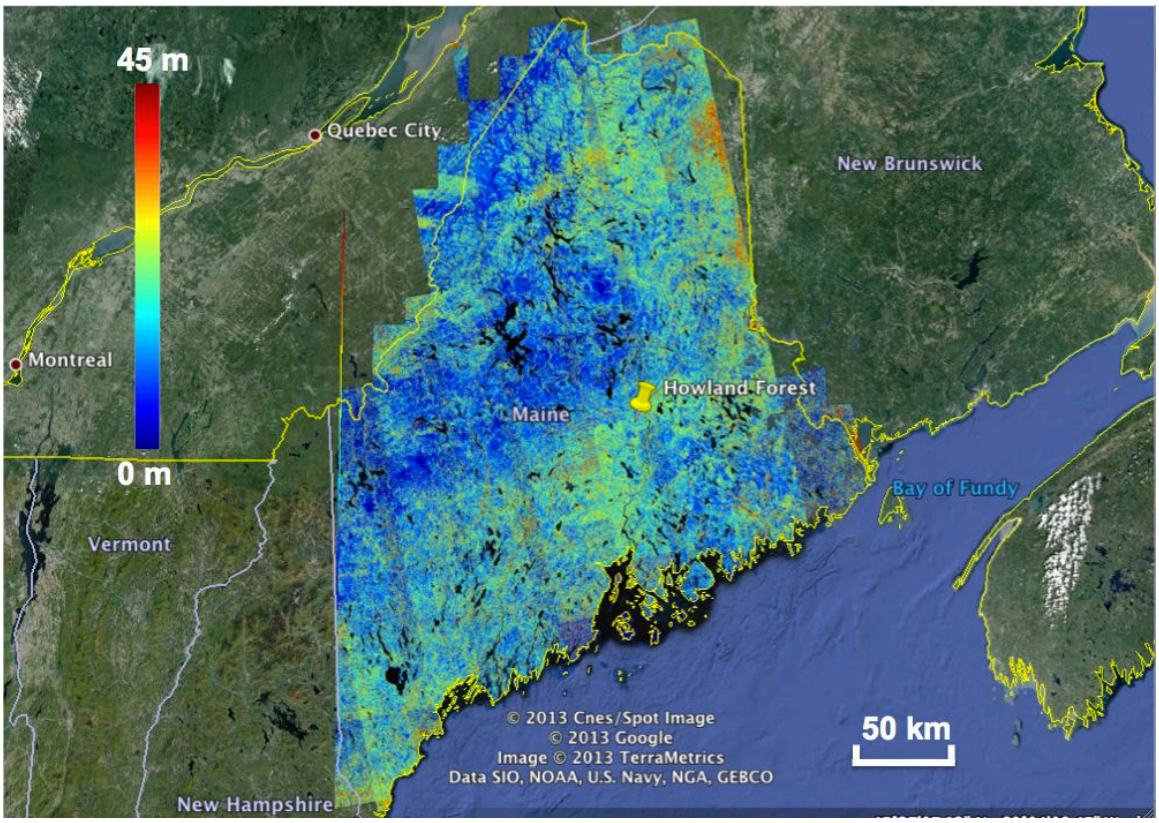


Figure 5.17: A map of forest height for the state of Maine, US. The state mosaic is color-coded as indicated ("blue" being 0 m and "red" being 45 m). All of the values over water bodies have been removed. Most of the "orange" and "red" spots are indicators of high temporal decorrelation rather than large trees.

that regions with a small R value are more indicative of a small dynamic range of forest height rather than inhomogeneous temporal change effects.

Because height estimates over water bodies are affected by extreme temporal decorrelation, inverted values over water bodies have been removed by using the water classification of NLCD2006 [17]. The remaining regions of unusually tall trees (*i.e.*, colored orange and red) are most likely due to localized sources of high temporal decorrelation (e.g., farming activity and urban activity), which should be flagged and treated separately. A forest/non-forest map can be utilized to remove those over-estimated values. It can also be noticed that there are artifacts in the mosaic map of Figure 5.17, e.g., striping problem. Note, this does not imply the assumption of

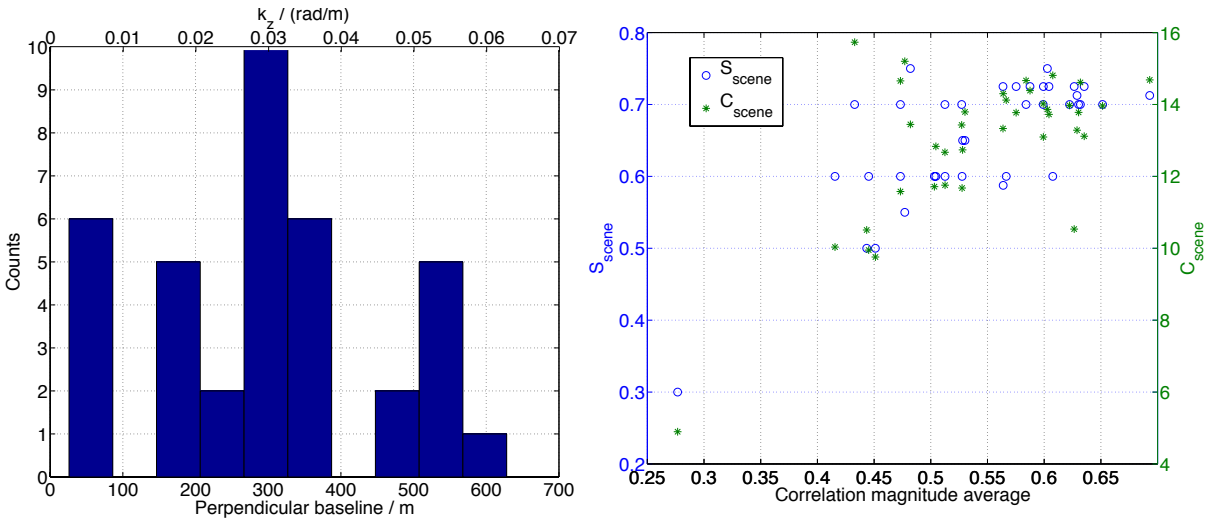


Figure 5.18: The histogram of the utilized instrumental parameters (**a**) and the scene-wide scatter plot of the derived model parameters (**b**) in the mosaic generation.

constant temporal change parameters is wrong; rather, it is due to the drawback (e.g., "wallpapering" problem) of the manual mosaicking algorithm. Improving the mosaic map with the use of an automatic mosaicking algorithm along with a forest/non-forest map will be described in Section 5.4.2 and Section 5.4.3.

The perpendicular baselines (and hence $\kappa_z$'s) for data used in the mosaic are plotted in Figure 5.18a. The range of the utilized $\kappa_z$'s for this application was $< 0.15$ rad/m and most often $< 0.05$ rad/m hence fulfilling the small-$\kappa_z$ assumption (Appendix C). A plot of the model parameters $S_{scene}$ and $C_{scene}$ is shown in Figure 5.18b. The horizontal axis represents the scene-wide correlation magnitude average (from Figure 5.11), which emphasizes the correlated behavior between the model parameters and the temporal changes of weather conditions. As mentioned earlier, a smaller $S_{scene}$ means larger dielectric change, while a smaller $C_{scene}$ implies higher level of wind-induced motion. For rainy and windy days, both $S_{scene}$ and $C_{scene}$ are expected to be small, while for stable weather (e.g., without rainfall), both of the parameters are expected to be large.

### 5.4.2 An automatic mosaicking algorithm

This manual mosaicking approach is prone, however, to what can be termed as the "wallpapering" problem (that is, by fixing one or two points of the wallpaper and gradually attaching the remaining part, larger deviation will occur as distance from the fixed points increases). Here, scenes that are farther away from the ground validation sites result in larger uncertainty in the determined estimates of the model parameters. In addition to this effect, the propagation path/sequence is non-unique, leading to a non-unique solution in determining the model parameters. The solution to this problem is to introduce an automatic mosaicking algorithm that estimates the desired model parameters simultaneously and arrives at a solution that is mathematically traceable and has a globally-minimized error.

In order to propagate the inverted forest height through scene overlap areas, it is necessary to explicitly define a fitting metric given any pair of overlapping forest height estimates. In particular, a nonlinear least squares problem is formulated to characterize the fitting metric. We then investigate the solution for a three-scene mosaicking problem that serves as a simplified scenario and, finally, generalize the matrix formulation for multiple overlapping scenes.

#### 5.4.2.1 Nonlinear least squares fitting metric

To begin, a comparison is made between two sets of forest height estimates in their overlapping region. According to (3.12), the observed repeat-pass HV-polarized InSAR correlation magnitude, $|\gamma_{v\&t}^{\mathrm{HV}}|$, due to the coupled effects of volume scattering and temporal change, is related to the desired forest height estimate $h_v$ as,

$$|\gamma_{v\&t}^{\mathrm{HV}}| = S_{scene} \cdot \mathrm{sinc}\left(\frac{h_v}{C_{scene}}\right), \quad \text{for} \quad h_v < \pi C_{scene} \tag{5.5}$$

where $S_{scene}$ (unitless; $0 \leq S_{scene} \leq 1$) characterizes the dielectric fluctuation of the volume scatterers (perhaps due to moisture change, e.g., rainfall; a smaller $S_{scene}$

indicates a bigger dielectric change), while $C_{scene}$ (in meters; $C_{scene} > 0$) represents the random motion of volume scatterers (perhaps due to wind; a smaller $C_{scene}$ implies a higher level of motion). Only the main lobe of the sinc function is used in (5.5). Through inverting (5.5), the forest height estimates can thus be considered as a function of the correlation measurements $|\gamma^{\mathrm{HV}}_{v\&t}|$ and the fitting parameters ($S_{scene}$ and $C_{scene}$).

Suppose there exist two sets of forest height estimates in an overlap area with the height estimates inverted as below,

$$h_{v_1} = f(|\gamma^{\mathrm{HV}}_{v\&t_1}|, S_{scene_1}, C_{scene_1}) = f_1(S_{scene_1}, C_{scene_1}) \tag{5.6}$$

$$h_{v_2} = f(|\gamma^{\mathrm{HV}}_{v\&t_2}|, S_{scene_2}, C_{scene_2}) = f_2(S_{scene_2}, C_{scene_2}). \tag{5.7}$$

Here, $f$ is the above-mentioned implicit function performing the forest height inversion, where we further omit the variable $|\gamma^{\mathrm{HV}}_{v\&t}|$ to keep the notation concise, since the correlation magnitude is invariant in the process of data fitting. Subscripts $i = 1, 2$ are used to differentiate the forest height estimate, as well as the model parameters from the $i$-th set.

To proceed, it can be assumed that the inverted forest heights from the repeat observations, on average, are comparable to each other, and therefore, a metric is desired so that the difference between $h_{v_1}$ and $h_{v_2}$ can be minimized. In Section 3.2.3, a fitting metric comprised with two parameters was used that was comprised of the slope $k$ and offset $b$, which is illustrated in Figure 3.3.

In Figure 3.3, the two sets of forest height estimates are considered as the horizontal and vertical axes with the data cloud illustrated as an ellipse. The slope parameter $k$ describes the slope of its major axis, while the offset parameter $b$ represents the relative difference between the average forest height estimates. In particular, $k$ and $b$ are written as:

$$k = \tan(\phi) \tag{5.8}$$

$$b = \frac{m_1 - m_2}{\overline{m}} \quad \text{with} \quad \overline{m} = \frac{m_1 + m_2}{2} \tag{5.9}$$

where $\phi$ is the angle between the major axis and the horizontal axis and $m_1$ and $m_2$ are the average forest height estimates. The calculation of these parameters is obtained through a principle component analysis-based method as in Section 3.2.3.

In order to have $h_{v_1}$ and $h_{v_2}$ match one another, a nonlinear least squares criterion is used to seek the proper model parameters $S_{scene_i}$ and $C_{scene_i}$ $(i = 1, 2)$, such that the following residual error can be minimized, *i.e.*,

$$T = (k-1)^2 + (b-0)^2. \tag{5.10}$$

During a non-automated mosaicking process (shown in Section 5.4.1), for a particular overlap area, one set of forest heights is always known prior to the inversion of the other, and thus, (5.10) is repeatedly used as the residual error that is minimized in order to achieve the optimal estimates of the model parameters (and, thus, forest heights) for the other InSAR scene. In other words, only the estimates from one InSAR scene are considered unknown each time the optimization step is run. However, if multiple overlapping scenes are used, it is desired to come up with the estimates simultaneously with the residual fitting error minimized globally. In order to see this, we next consider the three-scene mosaicking problem as a simplified scenario.

#### 5.4.2.2 Three-scene mosaicking problem

As shown in Figure 5.19, we thus apply this fitting metric (characterized by $k$ and $b$) to a simple three-scene mosaicking problem. There are three InSAR scenes along with a narrow validation site, where the forest heights $h_{v_0}$ are predetermined and considered as ground truth data. In this example, three overlap areas can be obtained, *i.e.*, Scene 1 with the validation site, Scene 1 with Scene 2 and Scene 1

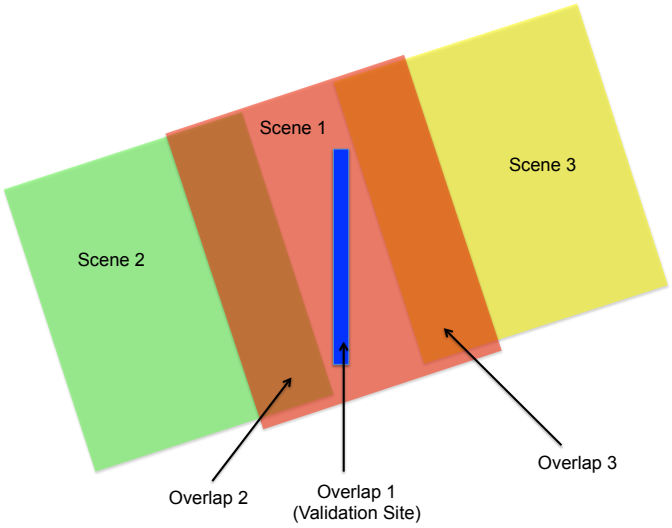


Figure 5.19: Illustration of mosaicking three InSAR scenes. The "blue" bar is a ground validation site with the heights predetermined. In this example, there are three InSAR scenes (*i.e.*, three pairs of model parameters $S_{scene}$ and $C_{scene}$ need to be determined) along with three overlap areas (*i.e.*, three pairs of fitting parameters $k$ and $b$ can be computed).

with Scene 3. A set of three equations, $f_1, f_2$ and $f_3$, for these overlap areas can be summarized as:

$$\begin{cases} h_{v_1} = f_1(S_{scene_1}, C_{scene_1}) & \text{with} \quad h_{v_0} & \text{in Overlap 1} \\ h_{v_1} = f_1(S_{scene_1}, C_{scene_1}) & \text{with} \quad h_{v_2} = f_2(S_{scene_2}, C_{scene_2}) & \text{in Overlap 2} \\ h_{v_1} = f_1(S_{scene_1}, C_{scene_1}) & \text{with} \quad h_{v_3} = f_3(S_{scene_3}, C_{scene_3}) & \text{in Overlap 3} \end{cases} \cdot$$

In the overlap regions (which includes the overlap of the central scene with ground validation data), two fitting parameters, *i.e.*, $k_i$ and $b_i$, are specified, where $i \in \{1, 2, 3\}$. The vector representation is defined as:

$$\underline{\xi} = \mathbf{G}(\underline{\rho}) \tag{5.11}$$

where:

$$\underline{\xi} = \begin{bmatrix} k_1 \\ b_1 \\ k_2 \\ b_2 \\ k_3 \\ b_3 \end{bmatrix}, \underline{\rho} = \begin{bmatrix} S_{scene_1} \\ C_{scene_1} \\ S_{scene_2} \\ C_{scene_2} \\ S_{scene_3} \\ C_{scene_3} \end{bmatrix} \tag{5.12}$$

and $\mathbf{G}$ is the implicit function that relates $\underline{\xi}$ to $\underline{\rho}$. The least squares solution $\underline{\rho}^*$ can be obtained by minimizing the target function:

$$\underline{\rho}^* = \arg\min_{\underline{\rho}} \|\underline{\xi} - \underline{\xi}^*\|^2 = \arg\min_{\underline{\rho}} \|\mathbf{G}(\underline{\rho}) - \underline{\xi}^*\|^2 \tag{5.13}$$

where:

$$\underline{\xi}^* = \begin{bmatrix} 1 \\ 0 \\ 1 \\ 0 \\ 1 \\ 0 \end{bmatrix} \tag{5.14}$$

and "$\|\cdot\|^2$" is the Euclidean norm of a vector. Since $\mathbf{G}$ is a nonlinear function, we can solve this nonlinear least squares problem by utilizing the Gauss-Newton algorithm [54]. Particularly, we first perform the Taylor series expansion of $\mathbf{G}$ at an initial point $\underline{\rho}_0$ (that is close to the optimal point $\underline{\rho}^*$), and keep the terms up to the first order, *i.e.*,

$$\mathbf{G}(\underline{\rho}) \approx \mathbf{G}(\underline{\rho}_0) + \underline{\underline{J}} \cdot (\underline{\rho} - \underline{\rho}_0) \tag{5.15}$$

where $\underline{\underline{J}}$ is the $6 \times 6$ Jacobian matrix calculated at the initial point $\underline{\rho}_0$ and defined as:

$$\underline{\underline{J}} = \left[ \begin{array}{cccccc} \frac{\partial k_1}{\partial S_{scene_1}} & \frac{\partial k_1}{\partial C_{scene_1}} & \frac{\partial k_1}{\partial S_{scene_2}} & \frac{\partial k_1}{\partial C_{scene_2}} & \frac{\partial k_1}{\partial S_{scene_3}} & \frac{\partial k_1}{\partial C_{scene_3}} \\ \frac{\partial b_1}{\partial S_{scene_1}} & \frac{\partial b_1}{\partial C_{scene_1}} & \frac{\partial b_1}{\partial S_{scene_2}} & \frac{\partial b_1}{\partial C_{scene_2}} & \frac{\partial b_1}{\partial S_{scene_3}} & \frac{\partial b_1}{\partial C_{scene_3}} \\ \frac{\partial k_2}{\partial S_{scene_1}} & \frac{\partial k_2}{\partial C_{scene_1}} & \frac{\partial k_2}{\partial S_{scene_2}} & \frac{\partial k_2}{\partial C_{scene_2}} & \frac{\partial k_2}{\partial S_{scene_3}} & \frac{\partial k_2}{\partial C_{scene_3}} \\ \frac{\partial b_2}{\partial S_{scene_1}} & \frac{\partial b_2}{\partial C_{scene_1}} & \frac{\partial b_2}{\partial S_{scene_2}} & \frac{\partial b_2}{\partial C_{scene_2}} & \frac{\partial b_2}{\partial S_{scene_3}} & \frac{\partial b_2}{\partial C_{scene_3}} \\ \frac{\partial k_3}{\partial S_{scene_1}} & \frac{\partial k_3}{\partial C_{scene_1}} & \frac{\partial k_3}{\partial S_{scene_2}} & \frac{\partial k_3}{\partial C_{scene_2}} & \frac{\partial k_3}{\partial S_{scene_3}} & \frac{\partial k_3}{\partial C_{scene_3}} \\ \frac{\partial b_3}{\partial S_{scene_1}} & \frac{\partial b_3}{\partial C_{scene_1}} & \frac{\partial b_3}{\partial S_{scene_2}} & \frac{\partial b_3}{\partial C_{scene_2}} & \frac{\partial b_3}{\partial S_{scene_3}} & \frac{\partial b_3}{\partial C_{scene_3}} \end{array} \right] \Bigg|_{\underline{\rho}=\underline{\rho}_0} \tag{5.16}$$

Thus, by letting $\underline{\rho} = \underline{\rho}^*$ and rearranging the terms in (5.15), we have:

$$\underline{\rho}^* \approx \underline{\rho}_0 + \underline{\underline{J}}^{-1} \cdot [\underline{\xi}^* - \mathbf{G}(\underline{\rho}_0)] \tag{5.17}$$

where $\underline{\underline{J}}$ is assumed invertible (which is usually true in practice). Because it is difficult to express the function $\mathbf{G}$ analytically, derivatives in (5.16) are calculated numerically. If $\mathbf{G}$ is a linear function, the result of (5.17) is exactly the desired optimal point. However, since $\mathbf{G}$ is nonlinear, the Gauss-Newton algorithm is an iterative numerical method, which considers the result of (5.17) as a new initial point and refines the value of $\underline{\rho}^*$ through another circulation of (5.17).

#### 5.4.2.3 Multi-scene mosaicking problem: the matrix formulation

With the matrix form of the least squares solution for the three-scene case established, a generalized treatment of multiple connected InSAR scenes along with multiple validation sites can be formulated. To begin, out of $N$ repeat-pass InSAR scenes that are connected with one another, $M$ will have validation sites. The number of the connected pairs is given by $E$. This is shown in Figure 5.16, where each InSAR scene is represented as a node, each connected pair is described as an edge and only the central scene (marked in "red") has a validation site. For the state

mosaic of Maine, this gives $N = 37$, $M = 1$ and $E = 57$. As another example, in the three-scene case of Figure 5.19, $N = 3$, $M = 1$ and $E = 2$. For the generalized scenario, there are $(E + M)$ overlap areas (and, thus, $2(E + M)$ fitting parameters $k$ and $b$) in total along with $N$ InSAR scenes (and, thus, $2N$ model parameters $S_{scene}$ and $C_{scene}$).

Further, the same vector notation as in Section 5.4.2.2 can be applied to this generalized case. In particular, (5.11) and (5.13) still hold with $\underline{\xi}$ and $\underline{\xi}^*$ being $2(E + M) \times 1$ vectors, $\underline{\rho}$ and $\underline{\rho}^*$ $2N \times 1$ vectors. By letting $\underline{\rho} = \underline{\rho}^*$, (5.15) is rewritten as:

$$\underline{\xi}^* - \mathbf{G}(\underline{\rho}_0) \approx \underline{\underline{J}} \cdot (\underline{\rho}^* - \underline{\rho}_0) \tag{5.18}$$

where the Jacobian matrix is $2(E + M)$ rows by $2N$ columns. More explicitly,

$$\underline{\underline{J}} = \left[ \begin{array}{cccc} \frac{\partial k_1}{\partial S_{scene_1}} & \frac{\partial k_1}{\partial C_{scene_1}} & \cdots & \frac{\partial k_1}{\partial S_{scene_N}} & \frac{\partial k_1}{\partial C_{scene_N}} \\ \frac{\partial b_1}{\partial S_{scene_1}} & \frac{\partial b_1}{\partial C_{scene_1}} & \cdots & \frac{\partial b_1}{\partial S_{scene_N}} & \frac{\partial b_1}{\partial C_{scene_N}} \\ \vdots & \vdots & \ddots & \vdots & \vdots \\ \frac{\partial k_{(E+M)}}{\partial S_{scene_1}} & \frac{\partial k_{(E+M)}}{\partial C_{scene_1}} & \cdots & \frac{\partial k_{(E+M)}}{\partial S_{scene_N}} & \frac{\partial k_{(E+M)}}{\partial C_{scene_N}} \\ \frac{\partial b_{(E+M)}}{\partial S_{scene_1}} & \frac{\partial b_{(E+M)}}{\partial C_{scene_1}} & \cdots & \frac{\partial b_{(E+M)}}{\partial S_{scene_N}} & \frac{\partial b_{(E+M)}}{\partial C_{scene_N}} \end{array} \right] \Bigg|_{\underline{\rho}=\underline{\rho}_0} \tag{5.19}$$

As long as all of the InSAR scenes are connected with one another and there is at least one validation site available, the relationship $(E+M) \geq N$ holds, which satisfies the prerequisite of the Gauss-Newton algorithm [54]. Therefore, in order to solve for the optimal point $\underline{\rho}^*$, the more general form of (5.17) is written as [54]:

$$\underline{\rho}^* \approx \underline{\rho}_0 + (\underline{\underline{J}}^T \underline{\underline{J}})^{-1} \underline{\underline{J}}^T \cdot [\underline{\xi}^* - \mathbf{G}(\underline{\rho}_0)] \tag{5.20}$$

Note that when $\underline{\underline{J}}$ is a square matrix, (5.20) reduces to (5.17).

The manual mosaicking process in Section 5.4.1 sequentially propagates the information from the validation sites throughout the adjacent-scene overlap areas. Therefore, the propagation of errors will manifest itself as the "wallpapering" problem described earlier. However, the nonlinear least squares solution has the benefit of estimating the desired model parameters simultaneously and minimizing the fitting error globally and, thus, resolves the "wallpapering" problem. Moreover, it is a robust system that is mathematically traceable. The accuracy and the computational complexity of this automatic mosaicking algorithm depend on the choice of the initial point, the number of iterations, the number and the quality of the InSAR scenes that are to be mosaicked together, as well as the number and the distribution of the ground validation sites.

### 5.4.3 Refined mosaic results and discussions

In this section, the Gauss-Newton algorithm is used to solve for the nonlinear least squares solution of the model parameters ($S_{scene}$ and $C_{scene}$). With these results, a new mosaic map of forest height for the U.S. state of Maine can be generated and compared with the LVIS height data and the National Biomass and Carbon Dataset (NBCD) Basal Area Weighted (BAW) height.

#### 5.4.3.1 Generation of the new mosaic map

Before running the automatic mosaicking algorithm, we want to exclude one InSAR scene (*i.e.*, "120_870" in Figure 5.16) and its associated pairwise connection (*i.e.*, the directed edge pointing from "120_880" to "120_870" in Figure 5.16), because the temporal change effect occurring within this InSAR scene is so severe (characterized by $S_{scene} = 0.3$ and $C_{scene} = 4.89$) that the global error minimization will be biased. Therefore, in this scenario, we end up with $N = 36$, $M = 1$ and $E = 56$.

The essential part in the implementation of (5.20) is the numerical calculation of the Jacobian matrix $\underline{\underline{J}}$ expressed in (5.19). Because the elements of $\underline{\underline{J}}$ are the

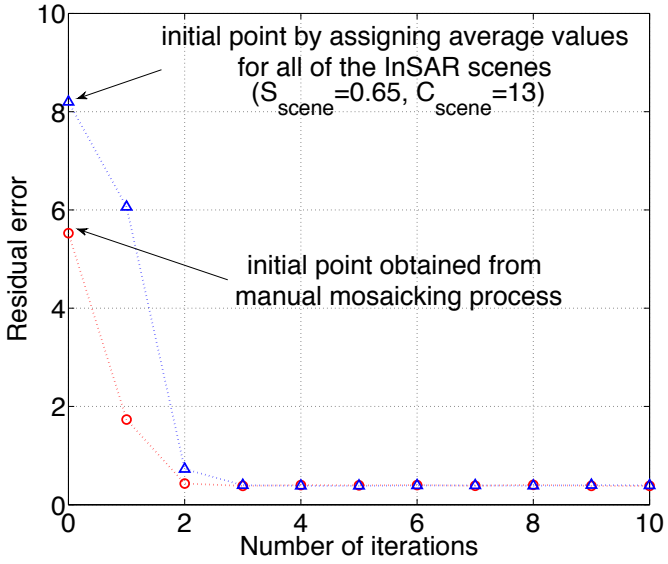


Figure 5.20: Residual error at each iteration of running the automatic mosaicking algorithm. The blue triangles indicate the results by using the average values of the model parameters ($S_{scene} = 0.65$ and $C_{scene} = 13$) for all of the InSAR scenes as the initial point, while the red circles show the results by considering the model parameters determined from the manual mosaicking process as the initial point.

partial derivatives of $k$ and $b$ with respect to $S_{scene}$ or $C_{scene}$, numerical derivatives are calculated by allowing $S_{scene}$ (or $C_{scene}$) to have a small increment of $10^{-6}$ (or $10^{-5}$ m). The Jacobian matrix is then computed on a column-by-column basis. Given a small increment of the $i$-th element of $\underline{\rho}$, the vector derivative of $\underline{\xi}$ is equivalent to the $i$-th column of the Jacobian matrix. The initial point $\underline{\rho}_0$ is chosen from the model parameters determined from the manual mosaicking process in Section 5.4.1. After ten iterations, the residual error (*i.e.*, the Euclidean norm in (5.13)) is plotted as red circles in Figure 5.20.

It can be seen that after the third iteration, the residual error becomes very stable, which implies that the initial point (determined from the manual mosaicking process in Section 5.4.1) is close to the optimal point. The effect of the initial point on convergence can be tested by assigning a uniform value (e.g., $S_{scene} = 0.65$ and $C_{scene} = 13$) for all of the InSAR scenes. As shown by the blue triangles in Figure 5.20,

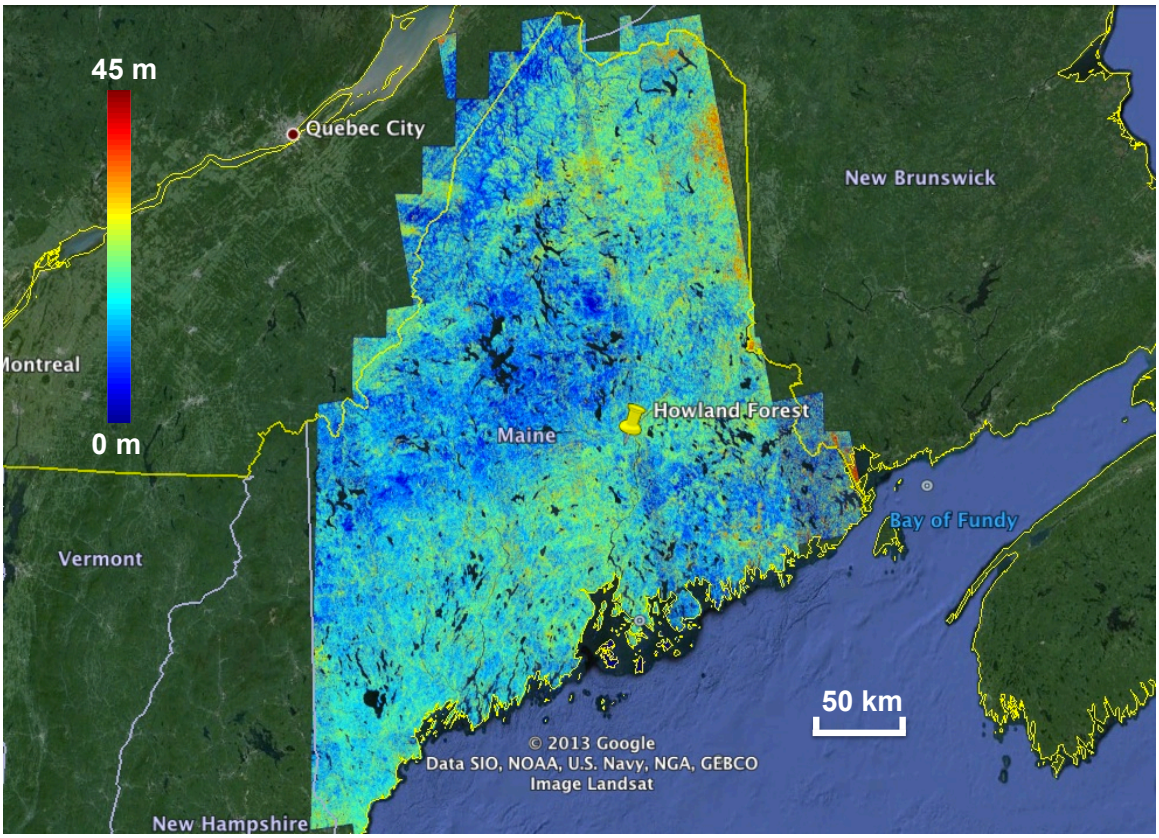


Figure 5.21: The new mosaic map of forest height for the state of Maine, U.S. The state mosaic is color-coded as indicated ("blue" being 0 m and "red" being 45 m). All of the values over water bodies have been removed by using NLCD2006. Most of the "orange" and "red" spots are indicators of high temporal decorrelation rather than large trees.

it is demonstrated that although the initial residual error is higher than that from the manual mosaicking process, the final result after ten iterations is similar to that when initial values were chosen from the manual mosaicking results.

By utilizing the refined model parameters ($S_{scene}$ and $C_{scene}$) after the tenth iteration, a new mosaic map of forest height is created for the U.S. state of Maine, as shown in Figure 5.21, where all of the values over water bodies have been removed by using National Land Cover Database (NLCD) 2006 [17].

A comparison of forest height estimates between the old and new mosaic maps highlights the systematic propagation of errors that occurs in the manual mosaicking

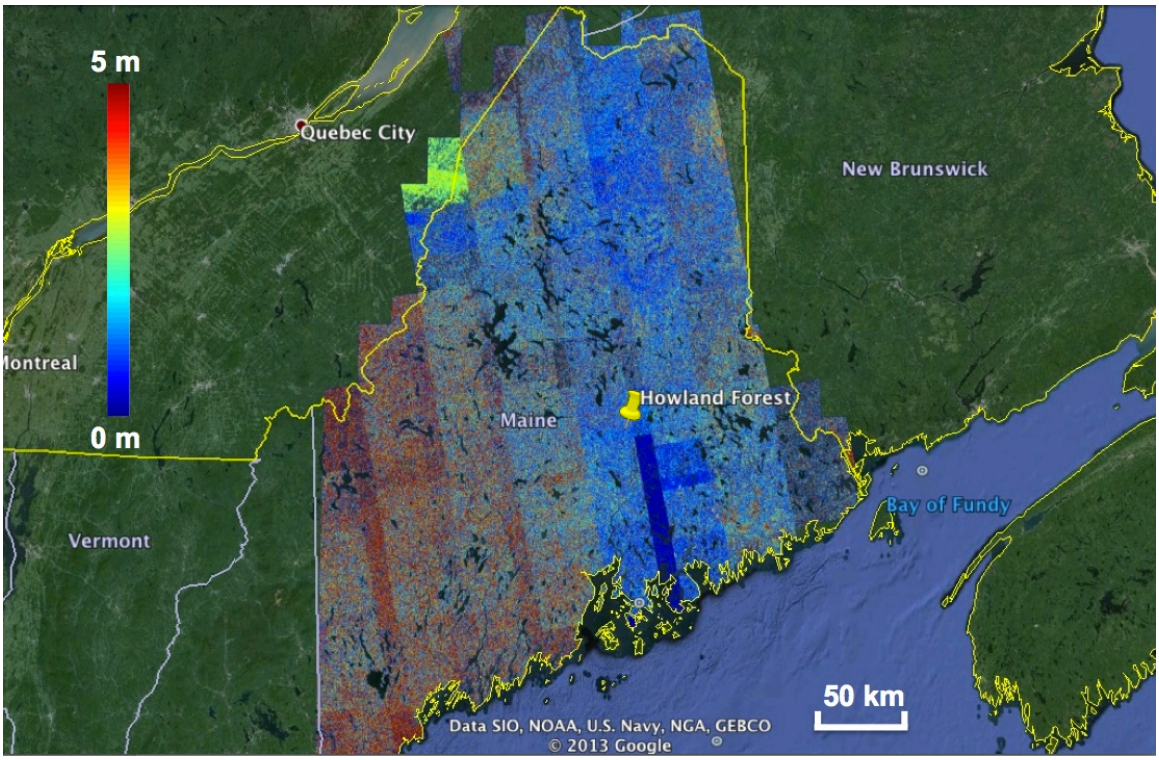


Figure 5.22: Illustration of the residual error between the automated and manual mosaicking approaches. Here, the absolute error in the forest height estimates between the old and new mosaic maps is illustrated and color-coded as indicated ("blue" being 0 m and "red" being 5 m). All of the values over water bodies have been removed by using NLCD2006. It can be observed that the "wallpapering" problem occurs, since the scenes that are far away from the central Maine area (where the Howland Forest is located) are more likely to have larger uncertainty in the forest height estimates.

process (the "wallpapering" problem). This is illustrated in Figure 5.22. It can be seen in the figure that the scenes that are far away from the central Maine area (where the Howland Forest is located) are more likely to have larger uncertainty in the forest height estimates (and, thus, the model parameters).

#### 5.4.3.2 Validation over Howland forest

Once constructed, a comparison can be made of the mosaic map of forest height with heights available from the LVIS sensor [7] (from the year 2009 over the Howland forest in central Maine) and NBCD BAW height [31] (from the year 2000 over the entire state of Maine). Note that it is desirable to compare this mosaic map of forest

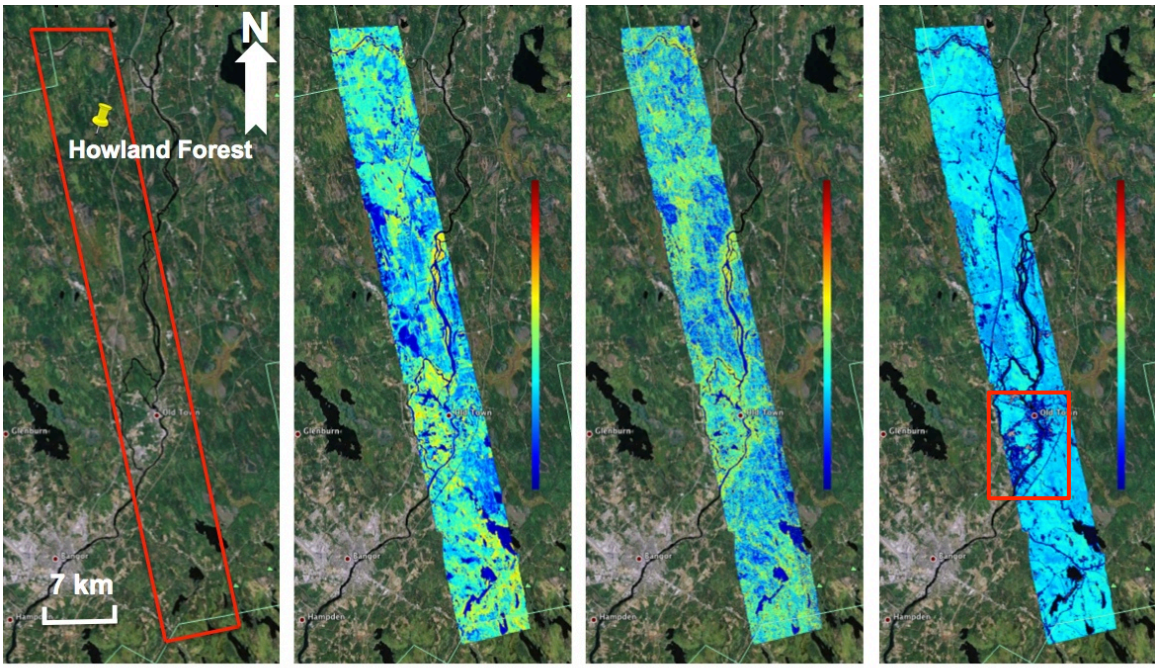


Figure 5.23: The optical image (**a**) from Google Earth is compared with the LVIS height (**b**), the ALOS InSAR correlation magnitude-inverted forest height (**c**) and the NBCD BAW height (**d**) over the Howland research forest in central Maine. The values over water bodies are removed with the use of NLCD2006. The color maps are coded with the same color scale ("blue" being surfaces, "red" being 45 m) and a spatial resolution of 50 m $\times$ 50 m. The inherent bias of the NBCD BAW data, discussed in the text, is highlighted by a "red" rectangular window over the urban area.

height with high spatial resolution LiDAR height data over various sites in Maine; however, this is restricted due to the LVIS data collection, which is restricted to the data strip between the Howland research forest and the Penobscot experimental forest in the state of Maine that has been used in Section 5.3.2.2. Therefore, in this work, we only compare our mosaic results with the NBCD BAW height data over the areas outside the LVIS LiDAR strip. In this section, we first show the comparison results within the LVIS LiDAR strip over the Howland forest.

Although the Maine mosaic of forest height (*i.e.*, Figure 5.21) was determined with the use of the LVIS height at the ground validation site, it is useful to compare

the inverted height estimates from the final mosaic with the LVIS data. As shown in Figure 5.23, it can be seen that the ALOS InSAR correlation magnitude-inverted heights correspond visually well with the LVIS heights. By contrast, the NBCD BAW height seems to have a much shorter dynamic range, although it does indicate similar features as those derived from LVIS and ALOS data. Note that the underestimation (termed as "inherent bias" in this work) of the NBCD BAW height can be observed in comparison to the LVIS height data, especially over the urban area that is marked by a "red" window in Figure 5.23d.

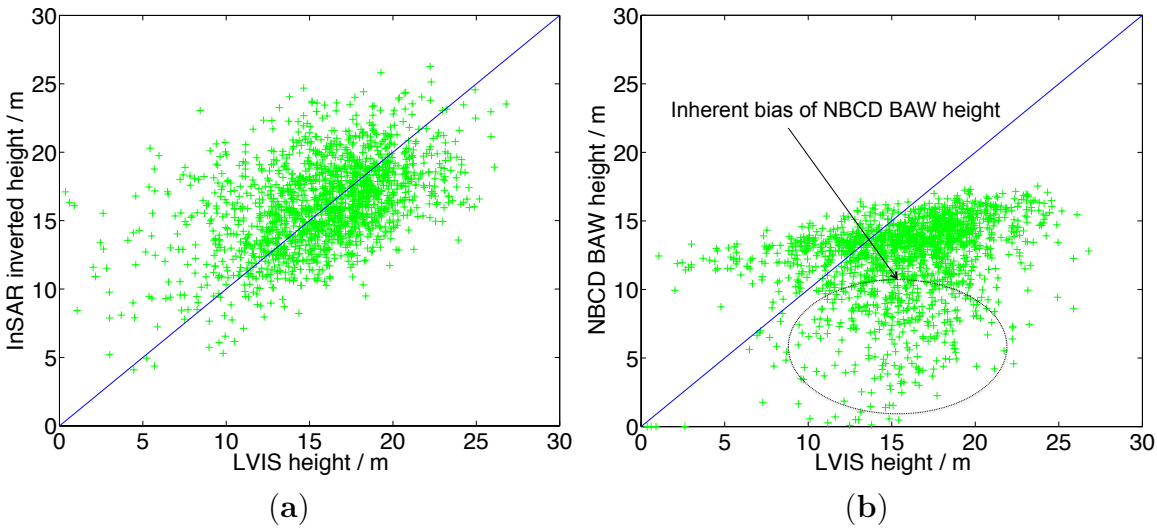


Figure 5.24: Quantitative comparison results between various height metrics. (**a**) The comparison between the ALOS InSAR correlation magnitude-inverted height (Figure 5.23c) and the LVIS height (Figure 5.23b) with RMSE of 3.8 m and R value of 0.48; (**b**) the comparison between the NBCD BAW height (Figure 5.23d) and the LVIS height (Figure 5.23b) with RMSE of 5.6 m and R value of 0.3. Each point corresponds to a forest area of 160 m $\times$ 480 m through multi-pixel averaging. The data points pertaining to the inherent bias of the NBCD BAW height are indicated by a dashed circle.

A quantitative comparison of results is illustrated in Figure 5.24. Each point in Figure 5.24 represents a forest area of 160 m $\times$ 480 m derived from multi-pixel averaging. Figure 5.24a shows the consistency between the ALOS InSAR correlation magnitude-inverted heights and the LVIS heights. The root mean square error

(RMSE) of this fit is 3.8 m, and the statistical R value is 0.48. Figure 5.24b compares the NBCD BAW and LVIS-derived heights. In this part of the figure, it can be seen that the NBCD BAW height has a smaller dynamic range, as well as some inherent bias compared to the LVIS heights. This is likely due to the fact that the NBCD is basal area weighted and less sensitive to the height of dominant trees within a resolution element, as is the case for the LVIS-derived heights.

The presence of unusually high temporal decorrelation (e.g., in agriculture and water-covered regions) is known to bias forest heights derived from the ALOS InSAR correlation measurements. This can be seen in Figure 5.24a at the lower end of the LVIS-derived height range, where water bodies, farmlands and urban activities, not thoroughly removed from the ALOS imagery, yield forest height estimates significantly larger than those observed by LVIS. Regions such as this can be detected because of the estimates of unrealistically large trees (40 m and larger) and/or removed in the larger mosaic using a forest/non-forest classification map, which will be discussed later.

#### 5.4.3.3 Validation over the entire state of Maine

Next, we compare our mosaic results with the NBCD BAW height data over the areas outside the LVIS LiDAR strip. The NBCD data consists of a 30-m resolution estimate of basal area weighted height, aboveground live dry biomass and standing carbon stock for the conterminous United States in 2000. The dataset was derived by utilizing the empirical modeling approach, which combines USDA Forest Service Forest Inventory and Analysis (FIA) data with 2000 SRTM InSAR data and optical remote sensing data acquired from the Landsat ETM+ sensor [31]. The mosaic map of the NBCD BAW height is illustrated in Figure 5.25 for the entire state of Maine.

Compared to Figure 5.21, it can be seen that the mosaic of NBCD BAW height has a much shorter dynamic range. The quantitative comparison result between

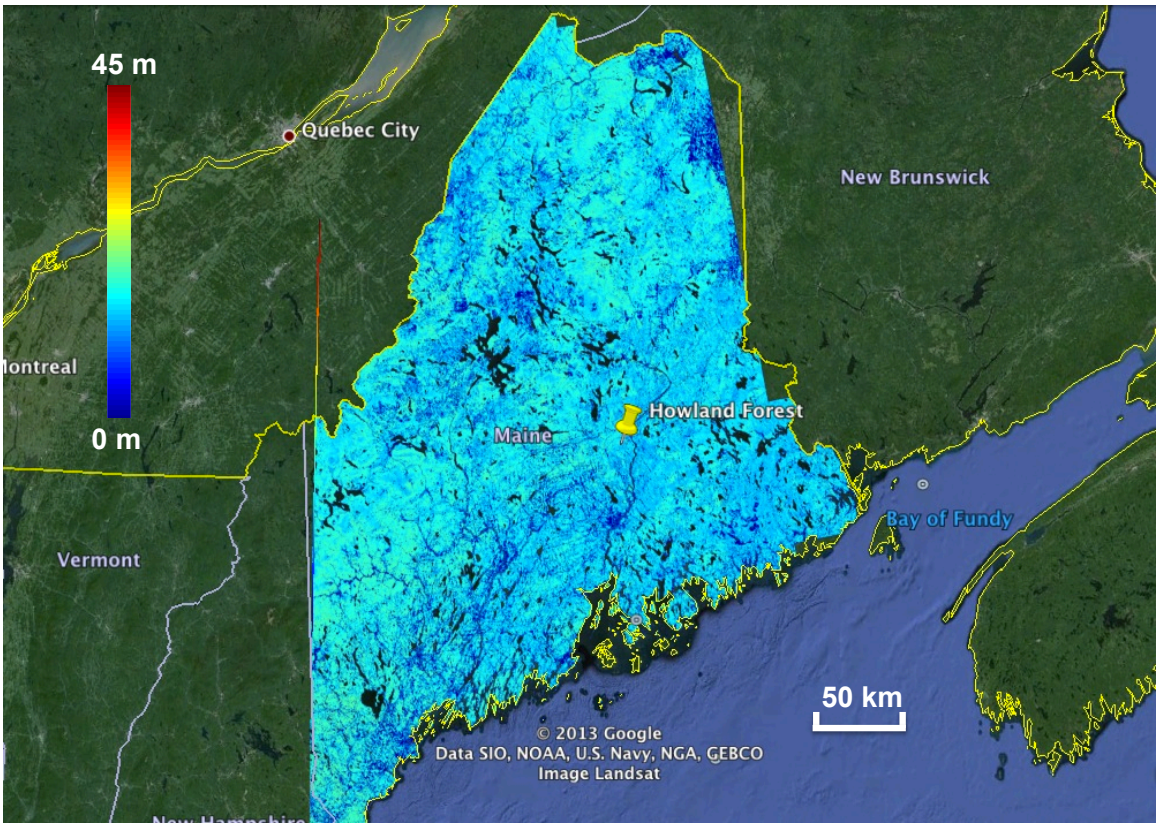


Figure 5.25: The mosaic map of the NBCD BAW height for the state of Maine, U.S. This mosaic is also color-coded as indicated ("blue" being 0 m and "red" being 45 m). All of the values over water bodies have been removed by using NLCD2006.

the mosaic of forest height inverted from ALOS InSAR correlation magnitude (*i.e.*, Figure 5.21) and the mosaic of the NBCD BAW height (*i.e.*, Figure 5.25) is shown in Figure 5.26. Each point in Figure 5.26 corresponds to a forest area of 500 m $\times$ 500 m through multi-pixel averaging. The inherent bias of the NBCD BAW height that appears in Figure 5.24b can also be seen here for the whole mosaic map.

Overestimation of forest height from the ALOS InSAR correlation magnitude-inverted height, due to the temporal decorrelation in urban areas, farmlands *etc.*, is evident in the upper right-hand corner of Figure 5.21. This part of the state of Maine consists of scattered farmlands and shows up as the colors "orange" and "red" in the imagery, indicating heights of 35 m and taller, which is much larger than average tree heights in the region. While this may be a useful tool for detecting change,

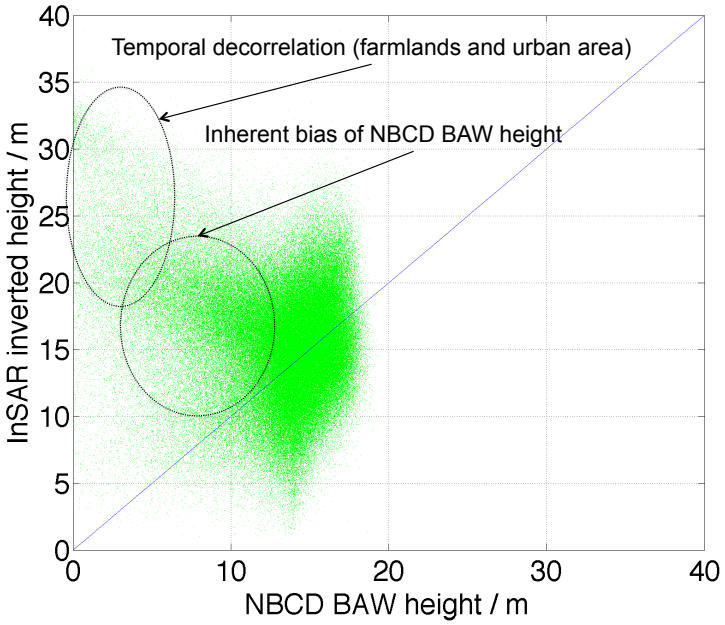


Figure 5.26: Quantitative comparison result between the mosaic of forest height inverted from ALOS InSAR correlation magnitude (*i.e.*, Figure 5.21) and the mosaic of the NBCD BAW height (*i.e.*, Figure 5.25) for the entire state of Maine, U.S. Each point corresponds to a 500 m $\times$ 500 m forest area through multi-pixel averaging. The data points that are affected by the inherent bias of the NBCD BAW height and by the temporal decorrelation of the ALOS InSAR data (e.g., farmlands and urban area) are indicated by dashed circles, respectively.

even within a forest (e.g., selective logging), here, it is considered a primary source of error, which can be improved by combining the mosaic with a land cover database that differentiates forested and non-forested regions. Typical forest/non-forest maps have already been derived from the ALOS SAR backscatter power, as demonstrated in [75, 73]. However, as noticed in this work, another resource for such a classification can be the NBCD BAW height mosaic, where any non-forest region is identified with the use of a flag value. The refined mosaic map is illustrated in Figure 5.27. Comparing with Figure 5.21, it can be seen that the overestimated height values over the non-forest regions (shown as "orange" and "red" spots in Figure 5.21) have been removed in the updated forest height mosaic.

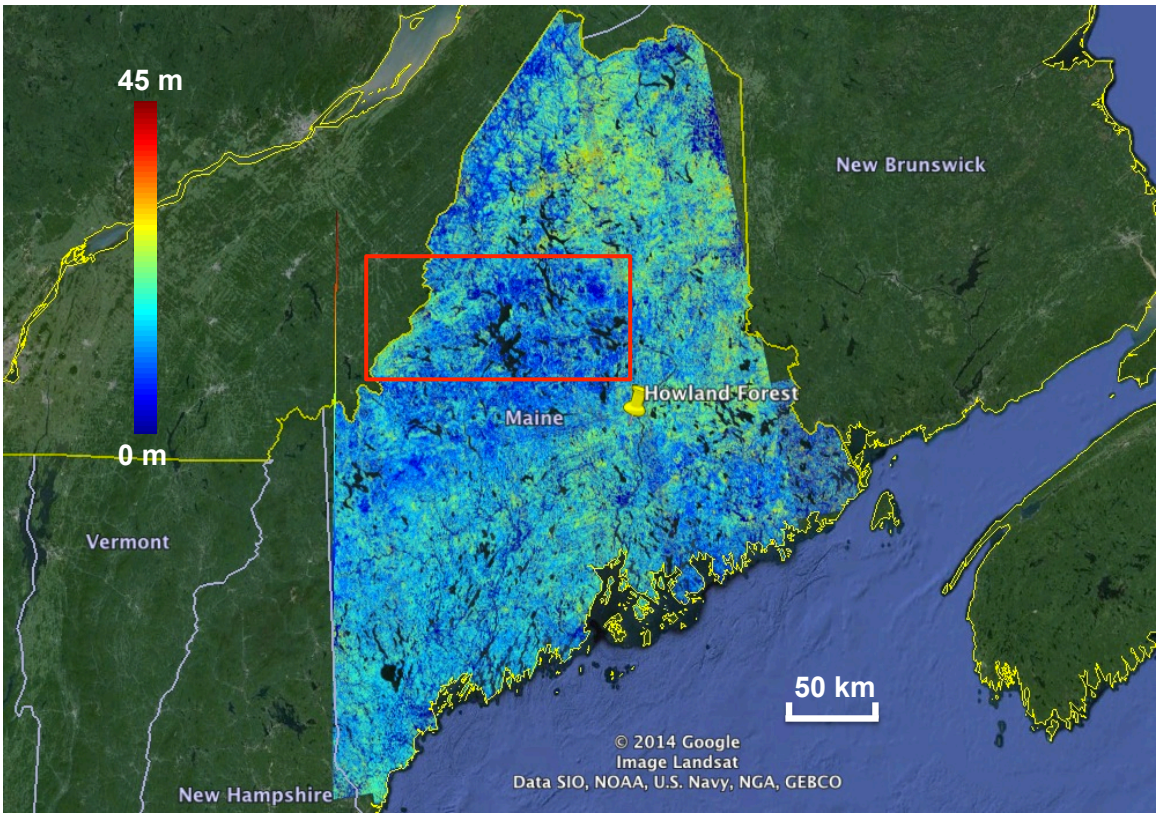


Figure 5.27: The refined mosaic map after removing the height estimates over non-forest regions by using the NBCD mosaic. This mosaic is also color-coded as indicated ("blue" being 0 m and "red" being 45 m). All of the values over water bodies have been removed by using NLCD2006. A large, one million hectare validation site is selected and indicated by the "red" rectangular window.

Although the NBCD mosaic has a small dynamic range of heights compared to the LVIS and ALOS-derived heights, it still captures similar features. In order to better demonstrate this, a large, one million hectare validation site is selected in Figure 5.27 (indicated by a "red" rectangular window). In Figure 5.28, a comparison of results between the refined Maine mosaic and the NBCD mosaic is shown over the selected large validation site. The color scale for the refined Maine mosaic is consistent with the other color maps that are shown throughout this work (*i.e.* "blue" being 0 m and "red" being 45 m); however, in order to improve the contrast in the NBCD mosaic, a different color scale (*i.e.* "blue" being 10 m and "red" being 28 m) is chosen for the

NBCD mosaic. It can be seen that although the NBCD mosaic still lacks some of the height detail evident in the ALOS-derived mosaic, both maps share similar features.

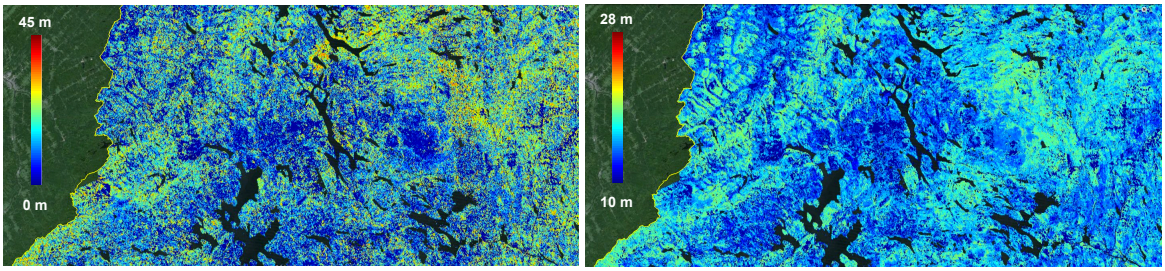


(**a**) (**b**)

Figure 5.28: Illustrative comparison between the refined Maine mosaic and the NBCD mosaic over the large validation site as indicated in Figure 5.27. (**a**) shows the forest heights from the refined Maine mosaic (*i.e.* Figure 5.27) with a color scale from 0 m ("blue") to 45 m ("red"), while (**b**) shows the forest heights from the NBCD mosaic (*i.e.* Figure 5.25) with a color scale from 10 m ("blue") to 28 m ("red").

#### 5.4.3.4 More discussion on practical implementation

In this work, there are several practical concerns that should be considered with the proposed improvements that are related to the implementation of this forest height inversion approach and its automated mosaicking process.

First, temporal decorrelation (e.g., harvesting over farmlands, urban activities) is noticeable and embodied as overestimated height values over the non-forest regions in the mosaic map. One practical approach is to remove the non-forest regions through the use of a forest/non-forest map. For example, in this work, the NBCD mosaic map has been utilized to serve as a forest/non-forest map. However, forest/non-forest maps derived from SAR backscatter power [75, 73] can alternately be used so that SAR/InSAR observations from the same spaceborne mission are fully exploited (*i.e.*, InSAR correlation magnitude data are used to generate a forest height mosaic, while SAR backscatter power is used to create a forest/non-forest map). This would alleviate the need for external maps. Further, a forest/non-forest classification map

can be applied to the InSAR coherence map prior to the forest height inversion, instead of being a post-processing step to the mosaic results, as in this work, so that the accuracy of the forest height inversion can thus be improved by precluding non-forest regions being used in overlap regions. Note that the forested plots that are affected by selective logging and/or forest degradation cannot be removed by using the forest/non-forest map and will also embody themselves as overestimated "large" forest heights, which could be useful for monitoring the global forest change, and will be treated separately as in Section 5.6.

Second, because of the repeatable nature of SAR data collections, there are often many scenes available over the same area, but separated in time by weeks, if not months. However, due to the unreliable nature of the temporal decorrelation effects, only a few of them are suitable for the use of forest height inversion. Compared to a stable weather condition, a windy and/or rainy day will decrease the observed InSAR correlation magnitude by a great amount. Although the data with smaller correlation magnitude still have the vegetation structural and temporal change information that could be utilized for forest height inversion, this bit of information is often masked by correlation sampling noise [79], making the inversion much noisier and less robust. Furthermore, if the weather condition changes non-uniformly, such as a regional rainfall, the temporal change effects may vary across each InSAR scene, so that the model parameters cannot be assumed constant over the whole scene any more. In this work, through a careful selection of ALOS InSAR scenes over the same study area, only one or two out of the dozens of available scenes are best suited for forest height inversion. It is recommended and desired to have more reliable spaceborne repeat-pass InSAR data with moderate (less than a month; 12 days for NISAR [3] and 14 days for ALOS-2 [28]) or large (on the order of months; 46 days for ALOS) temporal baselines, so that the best InSAR scene(s) can be selected and utilized to generate a reliable forest height mosaic.

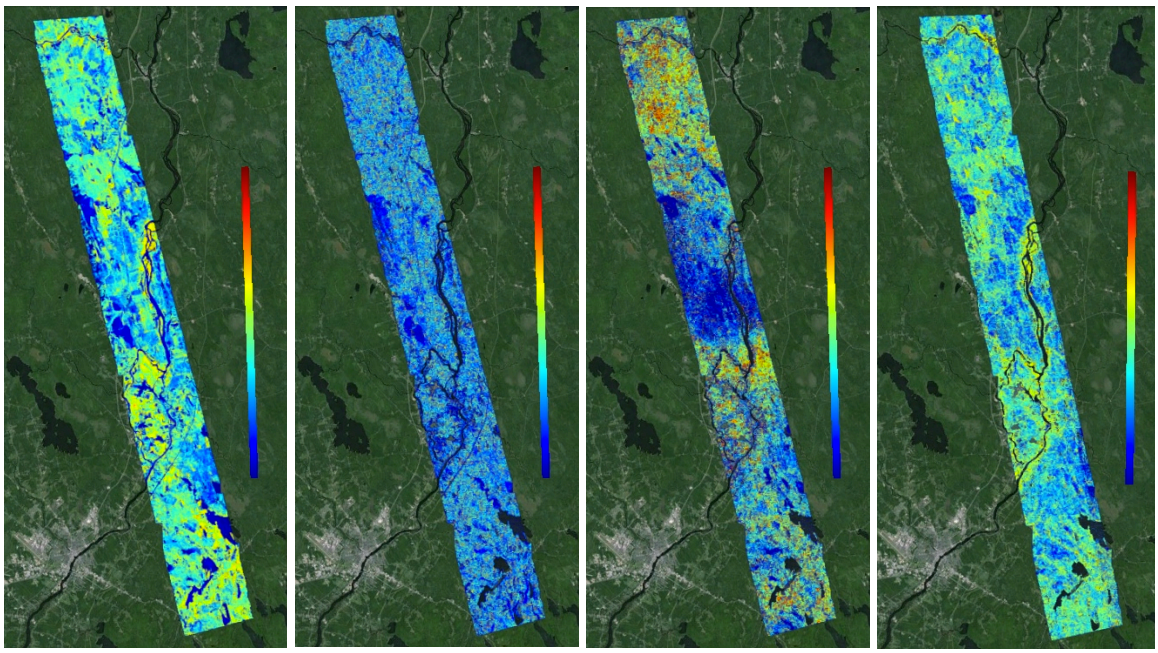


Figure 5.29: Comparison of different spaceborne SAR/InSAR metrics in the capabilities of estimating forest heights over the Howland forest: (a) is the LVIS height, (b) is the forest height inverted from ALOS SAR backscattering power (HV-pol), (c) is the inverted height from ALOS differential InSAR phase (HV-pol), while (d) is the ALOS HV-pol InSAR correlation magnitude-inverted height (from the state mosaic in Figure 5.21). The values over water bodies have been removed for all of the maps that are at a spatial resolution of 50 m $\times$ 50 m and color-coded from 0 m to 45 m.

## 5.5 Comparison of spaceborne SAR/InSAR metrics

It has been shown by others that backscattering intensity/power is an important SAR metric relating to the forest biomass and/or forest height (e.g. [53]) using a simple model fit between lidar heights and the observed radar cross section. Further, using SAR interferometry, the signal phase can be used to derive topography [64]. Through the use of a ground surface Digital Elevation Model (DEM), it can be shown that the differential interferometric phase (by taking out the topographic phase) corresponds to a mean height somewhere between the ground surface and the crown of the canopy [32].

Figure 5.29 shows estimates of inverted forest height maps over the Howland forest and Penobscot experimental forest by using ALOS SAR backscattering power (HV-pol), ALOS differential InSAR phase (HV-pol), and ALOS InSAR correlation magnitude (HV-pol). All of the maps are coded with the same color scale ("blue" being 0 m, "red" being 45 m). The data processing steps are detailed as follows. In particular, the ALOS SAR backscatter intensity map was converted to forest height values through a regression method (e.g. an exponential curve fitting; $y = 0.45 * (1 - \exp^{-0.12*x})$ in deriving Figure 5.29(b) with $y$ denoting the backscatter intensity and $x$ denoting the forest height). As for the use of the ALOS InSAR phase, the effect of the topography was first removed by using the DEM from National Elevation Dataset (NED; [20]), which leads to the differential InSAR phase. This was further calibrated sequentially by correcting for the tropospheric delay effects through using the software package PyAPS [27], fitting and eliminating a $3^{\text{rd}}$-order two-dimensional polynomial function, and applying a constant phase shift factor to the residual differential InSAR phase. The corrected differential InSAR phase was divided by the interferometric vertical wavenumber $\kappa_z$ in order to achieve the inverted forest height in Figure 5.29(c). Figure 5.29(d) is the central strip from the state mosaic of forest height (*i.e.* Figure 5.21) that coincides with the LVIS derived heights. The values over water bodies are removed for all of the maps.

A statistical comparison of the inverted heights is shown in Figure 5.30. The logarithm-like relationship linking SAR backscattering power to biomass [53] is also observed for forest height, and the saturation of the backscatter power occurs at the taller end of the height range. This primarily explains why the estimated forest height by using ALOS SAR backscattering power has the largest uncertainty for tall trees, although it works for small trees quite well. While the forest height obtained from ALOS differential InSAR phase has a smaller standard deviation (with a good R measure) than the backscatter-derived heights, it is still greater than that

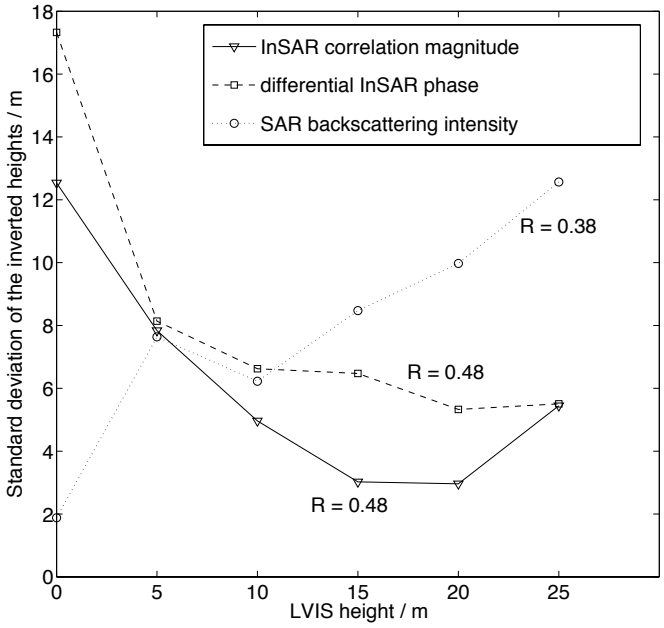


Figure 5.30: Statistical analysis of the inverted forest heights from different spaceborne SAR/InSAR metrics compared to LVIS height. Both the standard deviations (varying with the actual height) and the statistical R values are calculated and shown in the plot.

obtained from ALOS InSAR correlation magnitude. The estimation uncertainty by using ALOS differential InSAR phase is caused by several possible sources of error. The primary reason relates to the fact that the correction of tropospheric delay effect is not sufficient. Although the standard approach for this type of correction is applied through using the PyAPS software (followed by a polynomial fit), there is still spatially-varying large uncertainty in the residual differential InSAR phase (and thus the phase-inverted height; noticeable as the slowly-varying pattern in Figure 5.29(c)). Other reasons involve that 1) the correlation sampling noise that is relevant to the phase (as in [79] for the magnitude) has to be corrected for and 2) region to region variation in forest temporal change effects is enough to distort the phase of the complex $S_{scene}$, but does not appreciably affect the correlation magnitude. It is clear that the forest height inverted by using ALOS InSAR correlation magnitude has the best estimation uncertainty almost across the entire height range (with the overall height

estimation RMSE of 4 m and a R measure of 48% on the order of 10 hectares). Note the higher uncertainty at the lower end of the height range is related to high temporal decorrelation (e.g. where water bodies are not thoroughly removed; farming and urban activities, etc.), poor SNR in ground scattering due to the thermal noise decorrelation (which makes the total correlation magnitude overwhelmed by the sampling noise [79]), and also that there are fewer samples of forest areas below 5 m tall.

From the analysis, it was implied that, due to the saturation effect in the SAR backscattering power and the tropospheric delay effect in the differential InSAR phase, the spaceborne InSAR correlation magnitude is most suitable to create a large-scale mosaic of forest height map. However, the SAR backscattering power and the differential InSAR phase also consist of some meaningful information that may be useful in order to improve the estimation of forest height, e.g., through combining the SAR backscattering power for short vegetation and the InSAR correlation magnitude for the medium to tall trees.

## 5.6 Generation of forest height and disturbance maps

So far, the concentration has been placed on the forest height estimation under the condition of few or no forest disturbance events. However, in reality, forest disturbance, such as selective logging, tree regrowth or forest degradation, is unavoidable. This section improves the forest height inversion approach presented in Section 3.2.3 by generating both the forest height map along with the forest disturbance map.

Given a scene with the presence of (but not dominated by) forest disturbance, the major trend in a scatterplot (e.g. Figure 5.13) captures the Sinc relationship between the repeat-pass InSAR correlation magnitude and the physical tree height. However, with moderate or relatively high level of forest disturbance involved, the forest height estimation based on the multi-pixel averaging described in Section 3.2.3 will be biased

to various degrees. Neither an accurate forest height map nor a forest disturbance map can be generated.

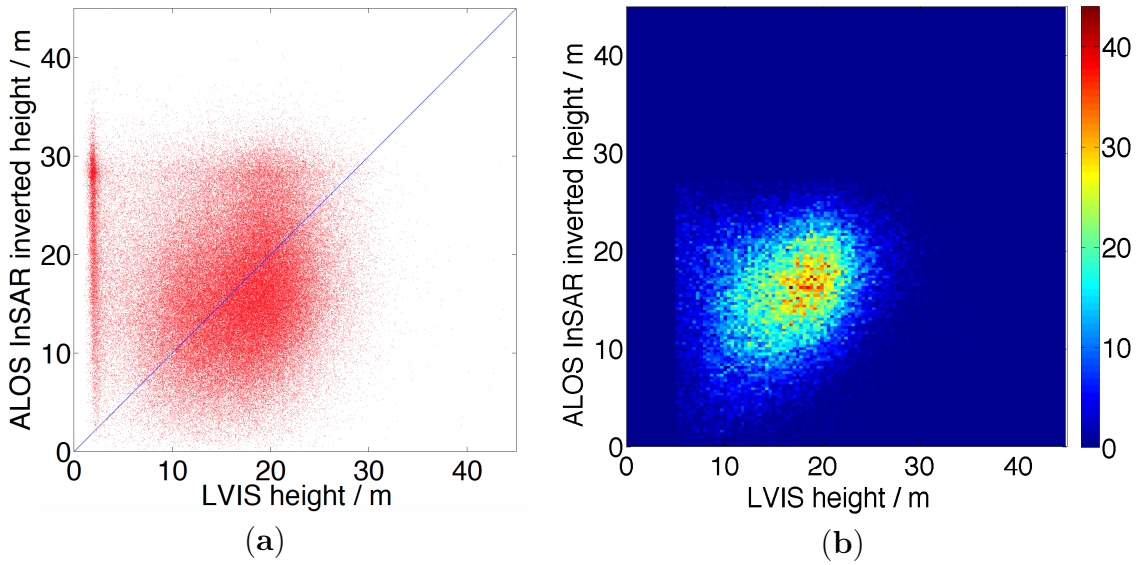


Figure 5.31: Illustrative comparison between the InSAR inverted forest height and the LVIS lidar height over the Howland forest in central Maine with the multi-pixel averaged scatterplot shown previously in Figure 5.13b. (**a**) shows the height comparison without multi-pixel averaging, while (**b**) shows the 2D histogram of (a), where the bin size of the histogram is chosen as 0.5 m.

An improvement step is developed here to replace the plain multi-pixel averaging in Section 3.2.3 such that both of the forest height map and forest disturbance map can be generated for the sites where ground validation height data (such as lidar) is available. As illustrated in Figure 5.31a, this scatterplot shows the pixel-wise InSAR inverted height compared to the LVIS height over the lidar strip in central Maine. Compared to Figure 5.13b, where multi-pixel averaging was applied, Figure 5.31a shows the same set of data but without multi-pixel averaging. This pixel-wise comparison itself does not reveal any significant features of the forest areas. However, since the disturbance events only occupy a smaller portion of the data points, drawing a two-dimensional histogram of the scatterplot will particularly highlight the major trend in the forest height information within the data. This is demonstrated

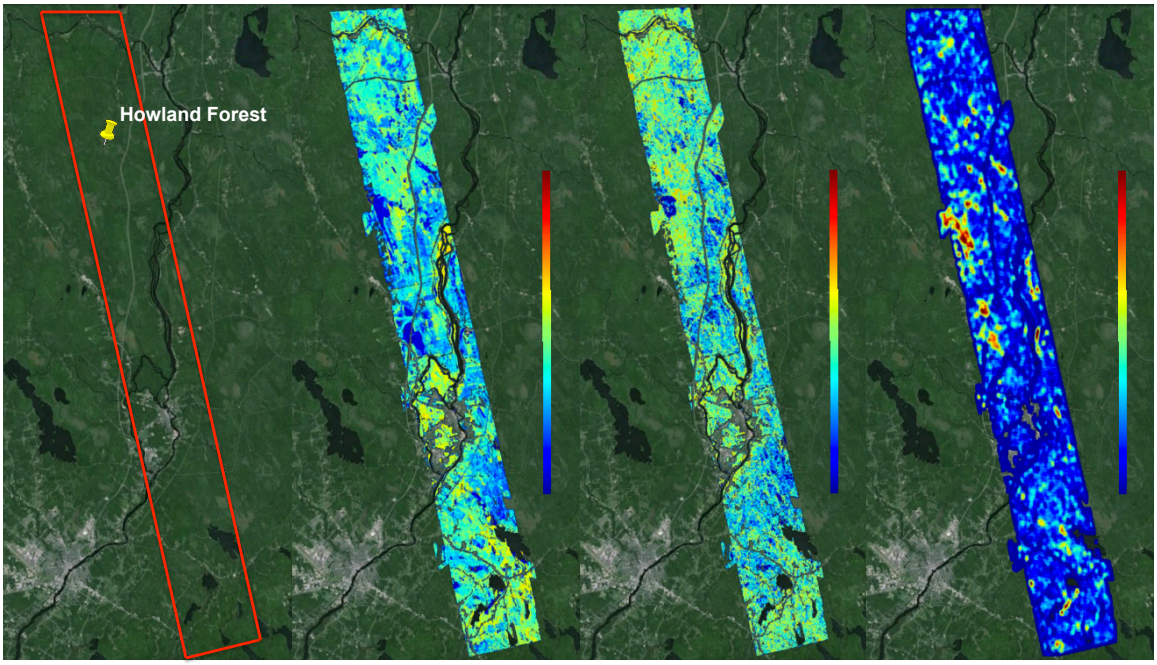


Figure 5.32: Illustration of the forest height and disturbance maps over the Howland research forest in central Maine: (**a**) is the optical image from GoogleEarth that is compared with the LVIS height data (**b**) and the ALOS InSAR correlation magnitude-inverted forest height (**c**). (**d**) shows the forest disturbance map which is the height difference ("absolute value") between (b) and (c). (b–c) are coded with the same color scale ("blue" being surfaces, "red" being 45 m), while (d) is coded from 0 to 10 m. The spatial resolution of (b–d) is 50 m $\times$ 50 m with the height values over non-forest areas removed.

in Figure 5.31b, where the 2D histogram of the scatterplot in Figure 5.31a shows the underlying relationship between the InSAR inverted height and LiDAR height. Since the 2D histogram calculates the density of the data cloud, as for the practical implementation, it is sufficient to use high density data points instead of the conventional multi-pixel averaged data points. This step is then followed by the non-linear least squares fit that is exactly the same as presented in Section 3.2.3. In order to quantitatively define a high-density data point, in this work, a threshold of 0.5 times the maximum density (calculated with the bin size of the 2D histogram being 0.5 m) is selected and proved to be plausibly sufficient.

Utilizing this improvement step, an accurate forest height map can thus be generated for the site where ground validation data exists. Further, a forest disturbance map can be obtained by taking the differential height between the InSAR inverted height and the ground validation height. As for the data cloud in Figure 5.31, both forest height and disturbance maps are demonstrated in Figure 5.32 for the LVIS lidar strip over the Howland forest in central Maine area. In the forest disturbance map, the differential height is induced by two sources: one is due to the disturbance events between the two InSAR collection dates (usually with the InSAR inverted height overestimated), the other source is due to the disturbance occurring between the collection dates of InSAR and lidar (with the InSAR inverted height either greater or lower than the lidar height depending on which data is collected earlier as well as what the cause of the disturbance is, e.g. selective logging or tree regrowth). However, no matter what the potential cause of the disturbance event is, this improved forest height inversion approach is capable of exporting a forest disturbance map along with an accurate forest height map (with RMSE less than 4 m on the order of 10 hectares) for the ground validation site, where low to moderate level of forest disturbance exists.

# CHAPTER 6

# MATHEMATICAL DERIVATION

As this dissertation involves a lot of derivation steps that are associated with the theoretical modeling of multiple scattering effect inside a random medium as well as calculation of the SAR/InSAR metrics, all of these derivation steps are treated rigorously in this chapter. However, it should be noted that this chapter is not necessary to understand the major theme of this work and only serves as the supplementary materials for the readers with particular interests of the mathematical derivation.

## 6.1 Solution of the configuration-averaged effective field

In this section, we will derive the configuration-averaged effective field as discussed in Section 2.1.2. In order to determine the averaged effective field at particle $j$, the location of the particle is taken into account with respect to the reference origin of the coordinate system that defines the center of the resolution element, as shown in Figure 6.1. Here, the reference plane is shown as a red dashed line, where the incident wave is assumed to have a unit-amplitude and zero-phase. The path that the signal takes from this reference plane to the scatterer $j$ can be modeled as

$$\langle E^{ex}(\overline{R_j}, \omega)\rangle_j = e^{jk\eta_1} a^{ex} e^{jK\eta_2}, \tag{6.1}$$

where $a^{ex}$ is the amplitude factor introduced by the air-medium interface and the path segments $\eta_1$ and $\eta_2$ are illustrated in Figure 6.1. Using the index of refraction, $n$, and $\theta_t$ to represent the angle of transmission, which satisfies the Snell's law (2.13),

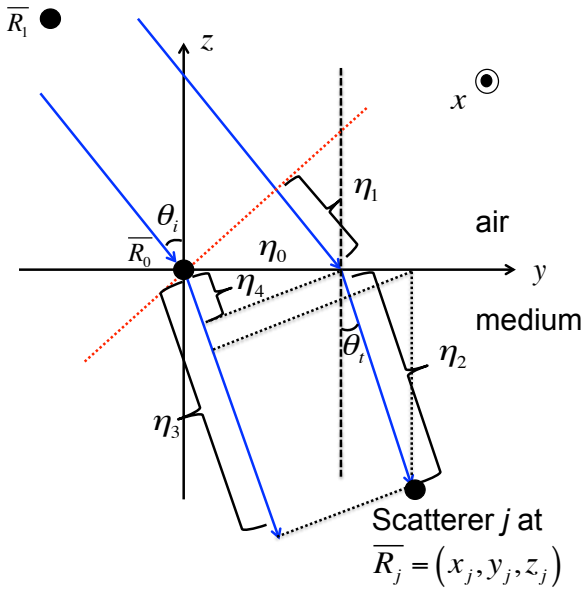


Figure 6.1: Illustration on the derivation of $\langle E^{ex}(\overline{R_j}, \omega)\rangle_j$. The local Cartesian coordinate system $(x, y, z)$ has its origin referenced to the center of the resolution cell, $\overline{R_0}$, on the "air-medium" interface (shown as the $x$-$y$ plane). The reference phase plane is colored in "red". The scatterer $j$ at $\overline{R_j} = (x_j, y_j, z_j)$ is marked as a "black" dot. $\eta_1$, $\eta_2$, $\eta_3$ and $\eta_4$ are the path segments that are associated to the ray tracing from the reference phase plane to the scatterer $j$. $\eta_0$ is the distance between the intersection points of the two "blue" rays crossing the "air-medium" interface. The incident wave is transmitted from the antenna position $\overline{R_1}$, incident upon the "air-medium" interface at the angle $\theta_i$ and refracts within the medium at the angle $\theta_t$.

and, following Figure 6.1, $\eta_1 = \eta_0 \sin\theta_i = n\eta_0 \sin\theta_t = n\eta_4$. Hence, the free-space path length of $\eta_1$ can be related to the within-medium path length of $\eta_4$, as in

$$k\eta_1 = K_R\eta_4. \tag{6.2}$$

By substituting $K = K_R + jK_I$ and (6.2) into (6.1), we have

$$\begin{aligned}
\langle E^{ex}(\overline{R_j}, \omega)\rangle_j &= e^{jk\eta_1} a^{ex} e^{j(K_R + jK_I)\eta_2} \\
&= a^{ex} e^{-K_I\eta_2} e^{j(k\eta_1 + K_R\eta_2)} \\
&= a^{ex} e^{-K_I\eta_2} e^{j(K_R\eta_4 + K_R\eta_2)} \\
&= a^{ex} e^{-K_I\eta_2} e^{jK_R\eta_3}
\end{aligned} \tag{6.3}$$

where $\eta_3 = \eta_2 + \eta_4$ as illustrated in Figure 6.1. Note that now two different path lengths (*i.e.*, $\eta_2$ and $\eta_3$) are used for the real and imaginary parts of $K$, respectively. This is due to the reference of zero-phase to the center of the resolution cell and the path-length difference being associated with the position of scatterer $j$ in relation to this reference point. While this path-length difference $\eta_3$ affects the phase, the attenuation of field amplitude however is only related to the actual propagation path inside the medium (*i.e.* $\eta_2$ in Figure 6.1). Noting that both $\eta_2$ and $\eta_3$ can be represented in the local Cartesian coordinates as $\eta_2 = -z_j/\cos\theta_t$, and $\eta_3 = y_j \sin\theta_t - z_j \cos\theta_t$, the expression can be written as

$$\langle E^{ex}(\overline{R_j}, \omega)\rangle_j = a^{ex} e^{jK_R(y_j \sin\theta_t - z_j \cos\theta_t)} e^{K_I z_j/\cos\theta_t}. \tag{6.4}$$

In order to take into account the spherical wave propagation of the transmitted signal from the source antenna located at $\overline{R_1}$, the incident wave at the center of the resolution cell $\overline{R_0}$ will have an additional factor dependent on the propagation distance, $|\overline{R_1} - \overline{R_0}|$ which affects both the signal amplitude and phase, and (6.4) becomes

$$\langle E^{ex}(\overline{R_j}, \omega)\rangle_j = a^{ex} \frac{e^{jk|\overline{R_1} - \overline{R_0}|}}{|\overline{R_1} - \overline{R_0}|} e^{K_I z_j/\cos\theta_t} e^{jK_R(y_j \sin\theta_t - z_j \cos\theta_t)}. \tag{6.5}$$

Substituting (2.13) into (6.5), we have

$$\begin{aligned} \langle E^{ex}(\overline{R_j}, \omega)\rangle_j &= a^{ex} \frac{e^{jk|\overline{R_1} - \overline{R_0}|}}{|\overline{R_1} - \overline{R_0}|} e^{K_I z_j/\cos\theta_t} e^{jk(y_j \sin\theta_i - n z_j \cos\theta_t)} \\ &= \frac{a^{ex}}{|\overline{R_1} - \overline{R_0}|} e^{K_I z_j/\cos\theta_t} e^{jk(|\overline{R_1} - \overline{R_0}| + y_j \sin\theta_i - n z_j \cos\theta_t)}. \end{aligned} \tag{6.6}$$

This concludes the proof of (2.12).

## 6.2 Solution of the coherent field

In this section, (2.3) and (2.4) will be rewritten such that the generic relationship can be found between the configuration-averaged effective field and the coherent field. In such a manner, the expression of the coherent field can be conveniently obtained by using the configuration-averaged effective field that is already derived as (6.6) in Section 6.1.

Since (2.4) has been rewritten as (2.9) in Section 2.1.2, we now focus on (2.3) with a similar treatment. Hence, it can be shown that (2.3) reduces to

$$\langle E(\overline{R},\omega)\rangle = E_{inc}(\overline{R},\omega) + \int \tau_0 \widetilde{f}_j \langle E^{ex}(\overline{R_j},\omega)\rangle_j \frac{e^{jk|\overline{R}-\overline{R_j}|}}{|\overline{R}-\overline{R_j}|} d\overline{R_j}, \tag{6.7}$$

where $\tau_0 = \frac{N}{V}$ is the number density, and $\widetilde{f}_j = \int f_j P(f_j) df_j$, both of which are consistent with the notation in deriving (2.9).

By rearranging the terms, (6.7) can be rewritten as

$$\begin{aligned}\langle E(\overline{R},\omega)\rangle = &\left\{ E_{inc}(\overline{R},\omega) + \int \tau_0 \widetilde{f}_j \langle E^{ex}(\overline{R_j},\omega)\rangle_j g(|\overline{R}-\overline{R_j}|) \frac{e^{jk|\overline{R}-\overline{R_j}|}}{|\overline{R}-\overline{R_j}|} d\overline{R_j} \right\} \\ &+ \int \tau_0 \widetilde{f}_j \langle E^{ex}(\overline{R_j},\omega)\rangle_j \left[1 - g(|\overline{R}-\overline{R_j}|)\right] \frac{e^{jk|\overline{R}-\overline{R_j}|}}{|\overline{R}-\overline{R_j}|} d\overline{R_j}. \end{aligned} \tag{6.8}$$

where the terms within the curly brackets exactly conforms with the right side of (2.9), and should be equal to the left side, which gives the configuration-averaged effective field evaluated at position $\overline{R}$, *i.e.*, $\langle E^{ex}(\overline{R},\omega)\rangle_j$. Here, the subscript $j$ turns to be a dummy variable once the spatial position $\overline{R}$ is given according to the solution of $\langle E^{ex}(\overline{R_j},\omega)\rangle_j$ presented in Section 6.1.

As for the remaining term in (6.8), noticing that the pair distribution function only deviates from unity when the distance is smaller than several diameters of the scatterer (see Figure 2.2), the volume integral thus only exists for $\overline{R_j}$ being close to

$\overline{R}$. Hence, by factoring out the configuration-averaged effective field, this remaining term can be rewritten as

$$\langle E^{ex}(\overline{R},\omega)\rangle_j \int \tau_0 \widetilde{f}_j \left[1-g(|\overline{R}-\overline{R_j}|)\right] \frac{e^{jk|\overline{R}-\overline{R_j}|}}{|\overline{R}-\overline{R_j}|} d\overline{R_j}. \tag{6.9}$$

As a result, (6.8) reduces to

$$\begin{aligned}\langle E(\overline{R},\omega)\rangle =&\langle E^{ex}(\overline{R},\omega)\rangle_j + \langle E^{ex}(\overline{R},\omega)\rangle_j \int \tau_0 \widetilde{f}_j \left[1-g(|\overline{R}-\overline{R_j}|)\right] \frac{e^{jk|\overline{R}-\overline{R_j}|}}{|\overline{R}-\overline{R_j}|} d\overline{R_j}\\ =&\langle E^{ex}(\overline{R},\omega)\rangle_j \left[1+\int \tau_0 \widetilde{f}_j \left[1-g(|\overline{R}-\overline{R_j}|)\right] \frac{e^{jk|\overline{R}-\overline{R_j}|}}{|\overline{R}-\overline{R_j}|} d\overline{R_j}\right]\\ =&\langle E^{ex}(\overline{R},\omega)\rangle_j \left[1+\beta(\overline{R};l,f_v)\right], \end{aligned} \tag{6.10}$$

where

$$\beta(\overline{R};l,f_v) = \int \tau_0 \widetilde{f}_j \left[1-g(|\overline{R}-\overline{R_j}|)\right] \frac{e^{jk|\overline{R}-\overline{R_j}|}}{|\overline{R}-\overline{R_j}|} d\overline{R_j}, \tag{6.11}$$

is a function of $\overline{R}$ with the functional form dependent on the number density $\tau_0$, scattering amplitude $\widetilde{f}_j$ and pair distribution function $g$, which in turn depend on the scatterer size $l$ and volume fraction $f_v$. This argument is similar to the interpretation in deriving (2.11). Due to the spherical symmetry of $g$, it can be noticed that (6.11) is invariant of $\overline{R}$, *i.e.*, $\beta(\overline{R};l,f_v)=\beta(l,f_v)$.

Therefore, by substituting (6.6), the solution of the coherent field at an arbitrary point $\overline{R}$ can be shown as

$$\begin{aligned}\langle E(\overline{R},\omega)\rangle =&\langle E^{ex}(\overline{R},\omega)\rangle_j \left[1+\beta(l,f_v)\right]\\ =&a^{ex}\frac{e^{jk|\overline{R_1}-\overline{R_0}|}}{|\overline{R_1}-\overline{R_0}|} e^{K_I z/\cos\theta_t} e^{jk(y\sin\theta_i - nz\cos\theta_t)} \left[1+\beta(l,f_v)\right]\\ =&a\frac{e^{jk|\overline{R_1}-\overline{R_0}|}}{|\overline{R_1}-\overline{R_0}|} e^{K_I z/\cos\theta_t} e^{jk(y\sin\theta_i - nz\cos\theta_t)}, \end{aligned} \tag{6.12}$$

where $a = a^{ex}\left[1 + \beta(l, f_v)\right]$ is the transmission coefficient of the air-medium interface. This concludes the proof of (2.14).

Note importantly, for infinitely small scatterers or a sparse concentration of scatterers (e.g. gas, vegetation), *i.e.* $g = 1$ and/or $\tau_0 \approx 0$, (6.11) reduces to zero. Substituting $\beta(l, f_v) = 0$, (6.10) immediately gives $\langle E(\overline{R}, \omega)\rangle = \langle E^{ex}(\overline{R}, \omega)\rangle_j$, which implies that the coherent field can be well approximated as the configuration-averaged effective field. This special case is known as the *Foldy's approximation* [16, 26, 82, 80].

## 6.3 A proof of the Distorted Born Approximation

In Section 2.1.3, the backscattered field has been solved by using the *Distorted Born Approximation*, which approximates the total electric field incident on each scatterer with use of the coherent field. In this section, a mathematical proof is derived in a similar manner as has been done in [80] although a different set of notation that is consistent with the current work has been adopted.

Through denoting the field translated from scatterer $j$ to $\overline{R}$ as $E(\overline{R}, \omega; j)$, we have (2.1) rewritten as

$$E(\overline{R}, \omega) \;=\; E_{inc}(\overline{R}, \omega) + \sum_{j=1}^{N} E(\overline{R}, \omega; j). \tag{6.13}$$

Utilizing (6.13) and assuming the scatterers are identically-distributed, the coherent intensity is given as

$$
\begin{aligned}
&\langle E(\overline{R},\omega)\rangle\langle E(\overline{R},\omega)^*\rangle \\
&\quad = E_{inc}(\overline{R},\omega)E^*_{inc}(\overline{R},\omega) + E_{inc}(\overline{R},\omega)\langle\sum_{j'=1}^{N} E^*(\overline{R},\omega;j')\rangle + \\
&\quad\quad E^*_{inc}(\overline{R},\omega)\langle\sum_{j=1}^{N} E(\overline{R},\omega;j)\rangle + \langle\sum_{j'=1}^{N} E^*(\overline{R},\omega;j')\rangle\langle\sum_{j=1}^{N} E(\overline{R},\omega;j)\rangle \\
&\quad = E_{inc}(\overline{R},\omega)E^*_{inc}(\overline{R},\omega) + NE_{inc}(\overline{R},\omega)\langle E^*(\overline{R},\omega;j)\rangle + \\
&\quad\quad NE^*_{inc}(\overline{R},\omega)\langle E(\overline{R},\omega;j)\rangle + N^2\langle E^*(\overline{R},\omega;j)\rangle\langle E(\overline{R},\omega;j)\rangle. \qquad (6.14)
\end{aligned}
$$

Similarly, substituting (6.13) into the total intensity leads to

$$
\begin{aligned}
&\langle E(\overline{R},\omega)E(\overline{R},\omega)^*\rangle \\
&\quad = E_{inc}(\overline{R},\omega)E^*_{inc}(\overline{R},\omega) + \langle\sum_{j=1}^{N}\sum_{j'=1}^{N} E(\overline{R},\omega;j)E^*(\overline{R},\omega;j')\rangle + \\
&\quad\quad E^*_{inc}(\overline{R},\omega)\langle\sum_{j=1}^{N} E(\overline{R},\omega;j)\rangle + E_{inc}(\overline{R},\omega)\langle\sum_{j'=1}^{N} E^*(\overline{R},\omega;j')\rangle \\
&\quad = E_{inc}(\overline{R},\omega)E^*_{inc}(\overline{R},\omega) + \\
&\quad\quad E_{inc}(\overline{R},\omega)\langle\sum_{j'=1}^{N} E^*(\overline{R},\omega;j')\rangle + E^*_{inc}(\overline{R},\omega)\langle\sum_{j=1}^{N} E(\overline{R},\omega;j)\rangle + \\
&\quad\quad \langle\sum_{j=j'} E(\overline{R},\omega;j)E^*(\overline{R},\omega;j')\rangle + \langle\sum_{j\neq j'} E(\overline{R},\omega;j)E^*(\overline{R},\omega;j')\rangle. \qquad (6.15)
\end{aligned}
$$

Assuming the scatterers are independent of each other and comparing (6.15) with (6.14), the total intensity can be represented as the coherent intensity plus additional terms, *i.e.*,

$$
\begin{aligned}
&\langle E(\overline{R},\omega)E(\overline{R},\omega)^*\rangle \\
&\quad=\langle E(\overline{R},\omega)\rangle\langle E(\overline{R},\omega)^*\rangle + \langle\sum_{j=j'} E(\overline{R},\omega;j)E^*(\overline{R},\omega;j')\rangle+ \\
&\quad\langle\sum_{j\neq j'} E(\overline{R},\omega;j)E^*(\overline{R},\omega;j')\rangle - N^2\langle E^*(\overline{R},\omega;j)\rangle\langle E(\overline{R},\omega;j)\rangle \\
&\quad=\langle E(\overline{R},\omega)\rangle\langle E(\overline{R},\omega)^*\rangle + N\langle E(\overline{R},\omega;j)E^*(\overline{R},\omega;j)\rangle+ \\
&\quad(N^2-N)\langle E(\overline{R},\omega;j)\rangle\langle E^*(\overline{R},\omega;j)\rangle - N^2\langle E^*(\overline{R},\omega;j)\rangle\langle E(\overline{R},\omega;j)\rangle \\
&\quad=\langle E(\overline{R},\omega)\rangle\langle E(\overline{R},\omega)^*\rangle+ \\
&\quad N\left[\langle E(\overline{R},\omega;j)E^*(\overline{R},\omega;j)\rangle - \langle E(\overline{R},\omega;j)\rangle\langle E^*(\overline{R},\omega;j)\rangle\right]. \qquad (6.16)
\end{aligned}
$$

It can be seen from (6.13) that, $E(\overline{R},\omega)$ is on the order of $N$ times $E(\overline{R},\omega;j)$. Therefore, the first term in the last equation of (6.16) is on the order of $N^2$ times $\langle E(\overline{R},\omega;j)\rangle\langle E^*(\overline{R},\omega;j)\rangle$, while the second term (*i.e.* in the square bracket) is on the order of $N$ times the variance of $E(\overline{R},\omega;j)$. As long as the number of scatterers $N$ is very large, and assuming the variance is small, the first term dominates, so that (6.16) immediately reduces to

$$
\langle E(\overline{R},\omega)E(\overline{R},\omega)^*\rangle \approx \langle E(\overline{R},\omega)\rangle\langle E(\overline{R},\omega)^*\rangle. \qquad (6.17)
$$

This result implies that, $E(\overline{R},\omega) = \langle E(\overline{R},\omega)\rangle$ is a deterministic number with zero variance, and thus does not vary with the configuration of the scatterers in the medium. In other words, the total field is thus dominated by the coherent field, which concludes the proof for the Distorted Born Approximation.

## 6.4 Derivation of the InSAR cross-correlation

This section will start from (2.29) and derive the InSAR cross-correlation by separating the $x$-, $y$- and $z$-dependent integrals, which gives the final result of (2.30).

In particular, by substituting (2.23) and (2.24), (2.29) reduces to

$$\begin{aligned}\langle E(\overline{R_1})E^*(\overline{R_2})\rangle &= \int \tau_0 \langle E(\overline{R_1};j)\rangle_j \langle E^*(\overline{R_2};j)\rangle_j P(f_j|\overline{R_j}) d\overline{R_j} df_j \\ &= \int \tau_0 A_1 A_2 \sigma(\overline{R_j}) |W_a(x_j)|^2 W_r\left(y_j \sin\theta_{i_1} - n\cos\theta_{t_1} z_j\right) \\ &\quad W_r^*\left(y_j \sin\theta_{i_2} - n\cos\theta_{t_2} z_j\right) e^{j2k_0\left(|\overline{R_1}-\overline{R_0}|-|\overline{R_2}-\overline{R_0}|\right)} \\ &\quad e^{j2k_0 y_j(\sin\theta_{i_1}-\sin\theta_{i_2})} e^{j2k_0 z_j(n\cos\theta_{t_2}-n\cos\theta_{t_1})} \\ &\quad e^{2K_I z_j(1/\cos\theta_{t_1}+1/\cos\theta_{t_2})} d\overline{R_j}, \end{aligned} \tag{6.18}$$

where

$$\sigma(\overline{R_j}) \;=\; \int |f_j|^2 P(f_j|\overline{R_j}) df_j, \tag{6.19}$$

is the averaged backscatter intensity profile.

Assuming the backscatter intensity profile only depends on the vertical coordinate, (6.18) can be rewritten as

$$\begin{aligned}&\langle E(\overline{R_1})E^*(\overline{R_2})\rangle \\ &\quad = \tau_0 A_1 A_2 e^{j2k_0\left(|\overline{R_1}-\overline{R_0}|-|\overline{R_2}-\overline{R_0}|\right)} \cdot \int |W_a(x_j)|^2 dx_j \cdot \\ &\qquad \int \sigma(z_j) e^{2K_I z_j(1/\cos\theta_{t_1}+1/\cos\theta_{t_2})} e^{j2k_0 z_j(n\cos\theta_{t_2}-n\cos\theta_{t_1})} \\ &\qquad \left\{ \int W_r\left(y_j \sin\theta_{i_1} - n\cos\theta_{t_1} z_j\right) W_r^*\left(y_j \sin\theta_{i_2} - n\cos\theta_{t_2} z_j\right) \right. \\ &\qquad \left. e^{j2k_0 y_j(\sin\theta_{i_1}-\sin\theta_{i_2})} dy_j \right\} dz_j \\ &\quad \approx \tau_0 A_1 A_2 e^{j2k_0\left(|\overline{R_1}-\overline{R_0}|-|\overline{R_2}-\overline{R_0}|\right)} \cdot \int |W_a(x_j)|^2 dx_j \cdot \\ &\qquad \int \sigma(z_j) e^{4K_I z_j/\cos\theta_t} e^{j2k_0 z_j(n\cos\theta_{t_2}-n\cos\theta_{t_1})} \\ &\qquad \left\{ \int \left|W_r\left(y_j \sin\theta_i - n\cos\theta_t z_j\right)\right|^2 e^{j2k_0 y_j(\sin\theta_{i_1}-\sin\theta_{i_2})} dy_j \right\} dz_j, \end{aligned} \tag{6.20}$$

where $\theta_i = \frac{\theta_{i_1}+\theta_{i_2}}{2}$, and $\theta_t = \frac{\theta_{t_1}+\theta_{t_2}}{2}$.

Utilizing the shift property of Fourier transform, we can separate the integral over the ground range, $y_j$, from that over the vertical coordinate, $z_j$. That is,

$$\begin{aligned}
&\langle E(\overline{R_1})E^*(\overline{R_2})\rangle \\
&\quad=\tau_0 A_1 A_2 e^{j2k_0\left(|\overline{R_1}-\overline{R_0}|-|\overline{R_2}-\overline{R_0}|\right)} \cdot \int |W_a(x_j)|^2 dx_j \cdot \\
&\qquad \int |W_r\left(y_j \sin\theta_i\right)|^2 e^{j2k_0 y_j(\sin\theta_{i_1}-\sin\theta_{i_2})} dy_j \cdot \\
&\qquad \int \sigma(z_j) e^{4K_I z_j/\cos\theta_t} e^{j2k_0 z_j(n\cos\theta_{t_2}-n\cos\theta_{t_1})} e^{j2k_0(\sin\theta_{i_1}-\sin\theta_{i_2})\frac{n\cos\theta_t}{\sin\theta_i} z_j} dz_j \\
&\quad=A_1 A_2 e^{j2k_0\left(|\overline{R_1}-\overline{R_0}|-|\overline{R_2}-\overline{R_0}|\right)} \cdot \int |W_a(x_j)|^2 dx_j \cdot \\
&\qquad \int |W_r\left(y_j \sin\theta_i\right)|^2 e^{j\kappa_y y_j} dy_j \cdot \int \tau_0 \sigma(z_j) e^{\left(\frac{2k_e}{\cos\theta_t}+j\kappa_z\right)z_j} dz_j, \qquad (6.21)
\end{aligned}$$

where

$$k_e = 2K_I \qquad (6.22)$$

is the extinction coefficient associated with the vertical penetration,

$$\kappa_z = 2k_0(\sin\theta_{i_1}-\sin\theta_{i_2})\frac{n\cos\theta_t}{\sin\theta_i} + 2k_0(n\cos\theta_{t_2}-n\cos\theta_{t_1}) \qquad (6.23)$$

is the interferometric vertical wavenumber, and

$$\kappa_y = 2k_0(\sin\theta_{i_1}-\sin\theta_{i_2}) \qquad (6.24)$$

is the interferometric ground-range wavenumber. This concludes the derivation for (2.30).

## 6.5 Simplification of the interferometric vertical wavenumber

In this section, we will simplify the expression of $\kappa_z$ in (2.33), which was defined as

$$\kappa_z = 2k_0(\sin\theta_{i_1} - \sin\theta_{i_2})\frac{n\cos\theta_t}{\sin\theta_i} + 2k_0 n(\cos\theta_{t_2} - \cos\theta_{t_1}). \tag{6.25}$$

By denoting $\Delta\theta_i = \theta_{i_1} - \theta_{i_2}$, $\Delta\theta_t = \theta_{t_1} - \theta_{t_2}$ and then using the trigonometric identities

$$\begin{aligned}
\sin\theta_{i_1} - \sin\theta_{i_2} &= \Delta\theta_i \cos\theta_i, \\
\cos\theta_{i_2} - \cos\theta_{i_1} &= \Delta\theta_i \sin\theta_i, \\
\cos\theta_{t_2} - \cos\theta_{t_1} &= \Delta\theta_t \sin\theta_t,
\end{aligned} \tag{6.26}$$

(6.25) can be simplified as

$$\kappa_z \;=\; 2nk_0\frac{\Delta\theta_i\cos\theta_i\cos\theta_t}{\sin\theta_i} + 2nk_0\Delta\theta_t\sin\theta_t. \tag{6.27}$$

Further, using (2.13), $\sin\theta_i = n\sin\theta_t$, and computing the derivatives of both sides gives

$$\cos\theta_i\Delta\theta_i = n\cos\theta_t\Delta\theta_t = \frac{\sin\theta_i\cos\theta_t\Delta\theta_t}{\sin\theta_t}. \tag{6.28}$$

Substituting (6.28) into (6.27), we have

$$\begin{aligned}
\kappa_z &= 2nk_0\frac{\Delta\theta_t\cos^2\theta_t}{\sin\theta_t} + 2nk_0\Delta\theta_t\sin\theta_t \\
&= 2nk_0\frac{\Delta\theta_t}{\sin\theta_t} \\
&= 2k_0\frac{\Delta\theta_i}{\sin\theta_i}\frac{n\cos\theta_i}{\cos\theta_t} \\
&= \tilde{\kappa_z}\frac{n\cos\theta_i}{\cos\theta_t}
\end{aligned} \tag{6.29}$$

which is equivalent to (2.35) with $\tilde{\kappa_z}$ defined in (2.36). Here, the last step used $\Delta\theta_i = \frac{B_\perp}{R}$, where $B_\perp$ is the perpendicular baseline, and $R$ is the slant range from the radar to the volume target.

## 6.6 Standard-mode dense medium InSAR correlation model

In the *standard*-observing mode for SAR interferometry [64], only one antenna is used as the transmitter while two antennas receive. Following the same development in Section 2.1.4, the conditional average of the single-scatterer SAR backscattered field is obtained. This field is the same as (2.23) for the $1^{st}$ antenna, while for the $2^{nd}$ antenna, it is necessary to perform an exchange of variables in (2.24) such that $|\overline{R_2} - \overline{R_0}| \longrightarrow \frac{|\overline{R_1}-\overline{R_0}|+|\overline{R_2}-\overline{R_0}|}{2}$, $\sin\theta_{i_2} \longrightarrow \frac{\sin\theta_{i_1}+\sin\theta_{i_2}}{2}$, $\cos\theta_{t_2} \longrightarrow \frac{\cos\theta_{t_1}+\cos\theta_{t_2}}{2}$. For this field, observed by the second antenna, (2.24) becomes

$$\begin{aligned}\langle E(\overline{R_2};k)\rangle_k =& A_2 e^{2K_I z_k/(\frac{\cos\theta_{t_1}+\cos\theta_{t_2}}{2})} W_a(x_k) \\ & W_r\left(y_k\frac{\sin\theta_{i_1}+\sin\theta_{i_2}}{2} - n\frac{\cos\theta_{t_2}+\cos\theta_{t_1}}{2}z_k\right) \\ & e^{jk_0\left[y_k(\sin\theta_{i_1}+\sin\theta_{i_2})-n(\cos\theta_{t_2}+\cos\theta_{t_1})z_k\right]} e^{jk_0\left[|\overline{R_1}-\overline{R_0}|+|\overline{R_2}-\overline{R_0}|\right]},\end{aligned} \tag{6.30}$$

where $A_2 = \frac{a^2}{|\overline{R_1}-\overline{R_0}||\overline{R_2}-\overline{R_0}|}$.

Substituting (6.30) for (2.24), the normalized InSAR correlation coefficient has the same functional form as (2.38) while the only difference is in the definitions of $\kappa_z$ and $\kappa_y$. Continuing with the same substitution of variables described above, these coefficients become

$$\kappa_z = k_0(\sin\theta_{i_1} - \sin\theta_{i_2})\frac{n\cos\theta_t}{\sin\theta_i} + k_0(n\cos\theta_{t_2} - n\cos\theta_{t_1}), \tag{6.31}$$

and

$$\kappa_y = k_0(\sin\theta_{i_1} - \sin\theta_{i_2}). \tag{6.32}$$

After applying Snell's law and trigonometric identities (as in Appendix 6.5),

$$\kappa_z = \tilde{\kappa_z} \frac{n \cos\theta_i}{\cos\theta_t} \tag{6.33}$$

with $\tilde{\kappa_z} = \frac{2\pi B_\perp}{\lambda R \sin\theta_i}$ (which is the conventional interferometric vertical wavenumber for standard-mode InSAR [64]), and

$$\kappa_y = \frac{2\pi B_\perp}{\lambda R} \cos\theta_i. \tag{6.34}$$

Using the standard-mode interferometric vertical wavenumber derived here, modeling of the interferometric signature for snow parallels that of the "ping-pong" mode derived in Section 2.2.3.

# CHAPTER 7

# CONCLUSIONS AND FUTURE WORK

## 7.1 Summary

In this dissertation, InSAR's capabilities in retrieving characteristics of volume scatterers such as snow and vegetation are systematically studied and expanded. In particular, this work concentrated on two scenarios (that can be adapted from the well-known single-pass InSAR model for a sparse medium like vegetation [80, 81]): 1) single-pass InSAR model for a dense medium like snow, and 2) repeat-pass InSAR model for vegetation. The electromagnetic scattering models of InSAR correlation were derived from a discrete representation of the volume scatterers by utilizing the Foldy-Lax multiple scattering equations, the Quasi-Crystalline Approximation (QCA) and the Distorted Born Approximation. In particular, the coherent field that propagates inside the medium with an effective propagation constant was obtained by solving the Foldy-Lax equations with the use of QCA. The Distorted Born Approximation was then applied to derive the single-scatterer SAR backscattered field. Therefore, through a superposition, the InSAR correlation can be formulated for the above-mentioned two scenarios respectively.

Based on the single-pass InSAR correlation model for snow, a connection was established between the InSAR correlation measurement and the snow volume parameters (grain size, volume fraction and layer depth) as well as those aspects that characterize ground scattering (ground topographic height and ground-to-volume ratio). From simulated validation results, it is noticed that the low-frequency InSAR (Ku-band to L-band) correlation measurements are sensitive to snow depth while the

high-frequency InSAR data (e.g., Ka-band) are sensitive to the microscopic scatterer information such as snow grain size and volume fraction. A dual-frequency (Ka- and L-band) InSAR configuration was then considered having the potential to retrieve the snow characteristics. However, as a restriction, Ka-band InSAR phase is the only InSAR observation that is sensitive to the snow grain size and volume fraction. Therefore, there is an ambiguity in determining both grain size and volume fraction by only using InSAR correlation data, and thus only a functional relationship between the two parameters can be achieved. Also, since the dense medium characteristics is essentially described by the pair distribution function, we examined three functional forms, among which the Percus-Yevick form appears to be more physical and accurate.

Regarding the application of the repeat-pass InSAR correlation model for vegetation, a simple and efficient forest height inversion approach was developed that utilize the temporal change effects (both dielectric change and random motion) of the forest between overpasses. Since the random motion effect has been extensively studied [96, 5, 33], as a complimentary study, this dissertation particularly examines the dielectric fluctuation effect in the repeat-pass InSAR correlation data. Consequently, a dielectric fluctuation model was developed and validated by using the electromagnetic simulations of a finite-length dielectric cylinder. Further, the proposed forest height inversion method was validated through the computer simulation results both using the analytical InSAR correlation model and modifying the numerical simulator PolSARproSim. This approach was also extensively validated with the use of spaceborne repeat-pass InSAR data (*i.e.* ALOS/PALSAR) against with spaceborne lidar (*i.e.* clustered ICESAT) and airborne lidar (e.g. LVIS) data over various test sites such as Queesland, Australia and Northeast, US. For ALOS/PALSAR with the repeat period on the order of months (at least 46 days), the RMSE for this type of height inversion is $< 4$ m at the resolution of 10 hectares. As one of the direct products of

this approach is to create a large-scale mosaic map of forest height, an efficient and automatic mosaicking algorithm was developed with a state mosaic of forest height generated for Maine, US. In the meantime, different spaceborne SAR/InSAR metrics are compared in terms of forest height estimation with the InSAR correlation magnitude (that is particularly used in this work) proved to be the best. Finally, an improvement technique was developed so as to generate a forest disturbance map along with an accurate forest height map for a disturbed forest area, where ground validation data (such as lidar) is also available.

## 7.2 Contributions and Conclusions

Below are the primary conclusions as well as contributions of this dissertation.

- The single-pass InSAR correlation model for a dense medium like snow was rigorously derived. Snow characteristics (such as grain size, volume fraction, and snow depth) is thus related to the InSAR correlation measurements for the first time through incorporating the pair distribution function (and thus an accurate estimate of the effective propagation constant). The derivation of the dense-medium InSAR correlation model for snow is also described in [44, 47].

- The repeat-pass InSAR correlation model for vegetation was derived physically by incorporating the temporal change effects (both dielectric change and random motion). Although this topic has been studied extensively, the previous works [40, 39, 56, 33, 34, 5, 76, 2] have proved to be different variants of the general model derived in this work under simplified conditions. The derivation of the repeat-pass InSAR model for vegetation is also shown in [48].

- Simulations were performed to test the sensitivity of the InSAR correlation measurements to the snow grain size, volume fraction and layer depth (with the product of volume fraction and layer depth characterizing the Snow Water

Equivalent or SWE). A dual-frequency InSAR configuration (e.g. Ka- and L-band) was proposed to have the potential of retrieving snow characteristics which also serves as an observing prototype for the future spaceborne Ka- and L-band InSAR missions, such as SWOT [18] and NISAR [3]. These results and associated analysis expand InSAR's capability to measure the dense medium characteristics, and also is a complimentary tool to existing approaches [70, 71, 72, 67, 58, 93] that use SAR backscatter power observations for the estimation of snow characteristics. The simulation results for validation of the snow InSAR model were also included in [44, 47].

- A simple and efficient forest height inversion approach was proposed to estimate forest height from repeat-pass InSAR correlation measurements and validated through use of simulation results and ground validation data. As a direct application of this approach is to generate large-scale mosaic maps of forest height, an automatic mosaicking algorithm was developed with a state-mosaic of forest height generated for Maine, US. Importantly, this method has found a way to use archival repeat-pass InSAR observations (JAXA's JERS-1 [65], ALOS-1 [66, 75], ALOS-2 [28], NASA's NISAR [3], ESA's BIOMASS [37]) to map vegetation height over large regions, potentially at a continental scale, and to our knowledge, our method is the first one that successfully utilizes spaceborne repeat-pass InSAR data to create large-scale forest height mosaics in the InSAR vegetation community. The present approach described here also serves as an alternative and complementary tool for other PolInSAR inversion techniques when single-pass InSAR and/or full-polarization data may not be available. The forest height inversion approach along with the ground validation results in Maine, US have been published in [43]. The automatic mosaicking algorithm and the state-mosaic generation for Maine, US have been published in [45, 42].

## 7.3 Future Work

The future work entails two separate directions, which are: 1) single-pass InSAR observation of snow, and 2) repeat-pass InSAR observation of vegetation.

For the single-pass InSAR observation of snow, this dissertation only demonstrates the simulated validation results of the dense-medium InSAR scattering model leaving the development of the snow retrieval approach along with experimental data validation for future work. So far, there is no single-pass InSAR mission that is optimized for the snow retrieval problem that was discussed in this dissertation, since the proposed InSAR observing configuration has to exploit two frequencies (e.g. Ka- and L-band) with the incidence angle and interferometric baseline specifically designed in order to extract the microscopic scatterer information. Therefore, it is recommended to first deploy a ground-based interferometer or an airborne InSAR system to test the retrieval algorithm according to the analysis in this work. As simulated in this dissertation, the low-frequency (e.g. Ku-band to L-band) InSAR is most suitable to estimate snow depth, while the high-frequency (essentially Ka-band) InSAR data is very sensitive to snow grain size and volume fraction. The experimental validation can thus be split into two separate parts: the low-frequency one and the high-frequency one, with each case investigated given some prior knowledge of the other. Since only a functional relationship between snow grain size and volume fraction can be determined, auxiliary data and/or allometric equations must be used to uniquely estimate the snow parameters. For example, if SAR backscatter power [70] can be incorporated, snow grain size and volume fraction can thus be uniquely determined, which implies an error analysis can be made directly for the Snow Water Equivalent (SWE), an important snow metric for modeling the hydrological cycle. Through the ground validation experiments, it is also helpful to investigate the actual functional form of the snow pair distribution function, along with its effect in the observed InSAR correlation data.

For the problem of retrieving vegetation characteristics from repeat-pass InSAR observations, both the simulated and ground validation results have been shown in this dissertation. The future work is thus to apply the forest height inversion approach as well as the associated analysis proposed in this work to different test sites where ground validation data (such as lidar) is available. Through extensive validation, it is desirable to characterize the error and validity of this type of inversion approach over different forest types and/or heights under various weather conditions. Since a significant part of this work is to create large-scale mosaic maps of forest height, it is also desired to utilize the archival spaceborne repeat-pass data (especially JAXA's ALOS-2 and NASA's NISAR with a shorter repeat period, *i.e.* 12-14 days, than ALOS-1; and thus more reliable height estimation accuracy) to create mosaic maps of forest height at a national scale, or even at a continental scale. By the time of writing this dissertation, a Python-based forest height inversion and mosaicking software package has been developed from this work through the collaboration of Microwave Remote Sensing Laboratory (MIRSL) at University of Massachusetts (UMass) Amherst and a private company Applied GeoSolutions, and is currently being tested over the entire Northeast region (around 18 million hectares) of the United States. Therefore, in the future, it is desired to seamlessly merge this developed software to existing free SAR/InSAR processing tools such as ROI_PAC [61] or ISCE [62] so as to create an automatic processing line for the generation of large-scale forest height mosaics. Another competitive edge of using InSAR is to detect and monitor the forest change and degradation, which is important to understand the global carbon cycle and climate change. Therefore, through the disturbance analysis in this dissertation, further efforts can be devoted to interpreting the generated forest disturbance maps so as to provide a large-scale map of forest change when equipped with an extensive collection of ground validation data such as spaceborne lidar data, e.g. GEDI [15].

# APPENDIX A

# THE ASSUMPTION OF CONSTANT TEMPORAL CHANGE PARAMETERS AND FOREST BACKSCATTER PROFILE/EXTINCTION COEFFICIENT

In Section 2.3.3 and Section 3.2.1 of this work, a distinction is made between the modified RVoG (*i.e.*, (3.3)) and those of previous works (e.g., [40, 56, 5, 33]). Here, in (3.3), although the parameters of temporal change effects (*i.e.*, $\gamma_d^v$, $\gamma_d^g$ and $\sigma_{\text{ref}}$) tend to be spatially varying (*i.e.*, target-dependent), it is assumed that they follow some scene-wide mean behavior (and thus are constant) for all of the targets in an interferogram (*i.e.*, InSAR "scene"), which implies that both the dielectric change and the wind-induced motion level are uniform. This is different from the target-dependent effect of temporal decorrelation in [40, 56, 76, 2], where the height-dependent term in $\gamma_{v\&m}$ was not introduced, and the wind-induced motion was included in the variable, $\gamma_d^v$. The effect of this difference is that the temporal correlation coefficient $\gamma_d^v$ becomes biased, and is a target (e.g., height) -dependent estimator.

Noting the above difference, in this work, both the height-dependent and height-independent terms are considered with the target-varying parameters set to be constant values, which will have the effect of increasing estimation error with the benefit of employing a simplified model that can be applied scene-wide as shown in Chapter 5. The target-dependence of these parameters across a scene leads to RMSE $< 4$ m on the order of 10 hectares in the forest height estimation. Note importantly, this assumption only works under the conditions that the temporal decorrelation does not exhibit a spatially-varying gradient across the scene. When the temporal decorrelation has a strong gradient across the scene (e.g., see Figure 5.13a; primarily caused

by nonuniform precipitation), the scene can be broken into smaller component parts, and in so much as ancillary measures of forest heights are available, these variations can be accounted for. In the case that the spatial variation of the model parameters is not desired, different time periods for the observations (with no precipitation occurring) can be chosen (as in Figure 5.13b).

To provide more insight into the temporal decorrelation gradient observed in Figure 5.13a, a comparison can be made with ancillary observations of precipitation data that were collected from NOAA's National Climate Data Center (NCDC; [1]) during the time period of the satellite passes. For the inversion shown in Figure 5.13a, it can be seen that the "upper" (*i.e.*, northern) segment has smaller values of $S_{scene}$ and $C_{scene}$ than the "lower" (*i.e.*, southern) portion. This implies that the weather conditions over the northern region were changing more compared to the southern region during the repeat period 07/10/2007–08/25/2007. These results were compared to the inversion shown in Figure 5.13b which used observations from 07/10/2007–10/10/2007, and can be characterized by a single set of temporal change parameters, implying that the weather conditions were uniform over the region.

In Figure 5.10, the locations of two climate observing stations (marked as "North Station" and "South Station") in central Maine are shown. The precipitation data associated with these two stations in July, August and October 2007 are given in Figure A.1. The collection dates of the interferograms are indicated by vertical dashed lines. For interferogram 07/10/2007–08/25/2007, it can be seen that the precipitation for both north and south stations are similar on 07/10/2007, while the north station recorded a heavier rainfall on 08/25/2007 than the south station. In contrast, for interferogram 07/10/2007–10/10/2007, both north and south stations experienced similar level of precipitation on 07/10/2007 and 10/10/2007, hence providing evidence for the source of the temporal decorrelation gradient observed in Figure 5.13a, and not observed in Figure 5.13b.

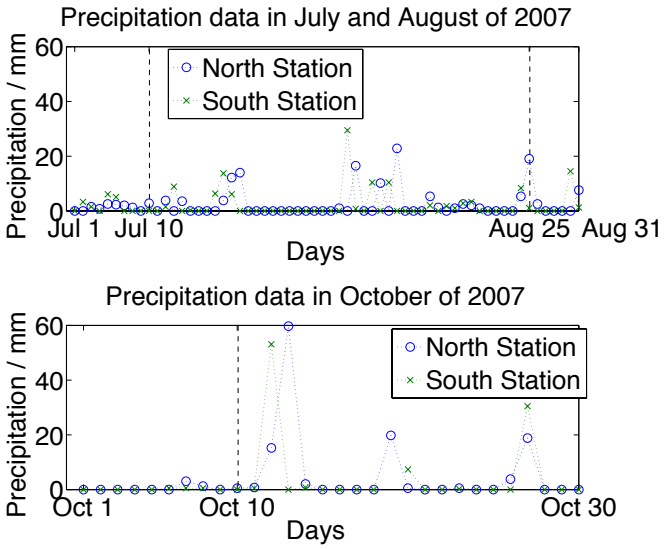


Figure A.1: Precipitation data from NOAA's National Climate Data Center in July, August and October 2007. The data was recorded at both north and south stations in central Maine. The collection dates of the corresponding interferograms are indicated by dashed lines.

An alternative way to look at this homogeneity issue while performing the mosaicking task is through the overlapping regions from adjacent interferometric estimates of forest height. When there is a spatially-varying feature of the temporal change effects across the region, large errors are occurring and scenes should be replaced with alternate or new observations. In Figure A.2, we illustrate an examination of this scene-wide homogeneity utilizing the mosaicking task. By creating a four-scene mosaic, the effect of non-uniform temporal decorrelation on forest height estimation error (R, RMSE and the target function $T$ as defined in (5.10)) can be observed by testing with the above two scenes (interferogram 07/10/2007–08/25/2007 and interferogram 07/10/2007–10/10/2007). In Figure A.2a, the central scene (marked as red) was from interferogram 07/10/2007–08/25/2007 with rainfall occurring over the northern region of the scene, while in Figure A.2b, interferogram 07/10/2007–10/10/2007 was used instead with no rainfall recorded. Measures of the error metrics: R, RMSE and

$T$, show that the inhomogeneous scene can be automatically identified (with much worse error metrics) and removed from the mosaic.

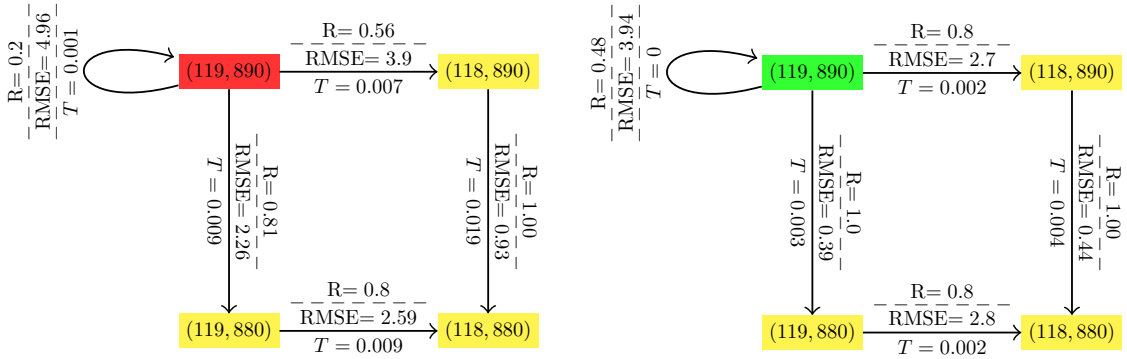


Figure A.2: The forest height estimation error is illustrated for a four-scene mosaic by selecting the central scene (**a**) with and (**b**) without rainfall.

Since we already considered constant wind-induced motion level in the mean sense, for the constant extinction coefficient as mentioned above and utilized in Section 4.2.1, we can still apply the same idea by considering its mean value across the whole scene. As seen from Figure 4.9, the fitting parameter $C_{scene}$ has a weak dependence on the extinction coefficient $k_e$ (Figure 4.9b) compared to the wind-induced motion level $\sigma_r$ (Figure 4.9d). Therefore, if we can consider constant motion level in terms of its mean behavior, we can also safely treat the extinction coefficient in the same way, since the target-dependence of $k_e$ is expected to have a smaller effect on the fitting parameter $C_{scene}$ than that due to $\sigma_r$.

Another assumption that is made in enforcing a constant value for the parameter $C_{scene}$ in deriving (3.12) is that, all of the forests with different height values across the given scene have the scaled versions of extinction-weighted backscattering profile and height-dependent motion profile. To examine this assumption in more detail, the reader is referred to Figure A.3 where a short forest stand of height $h_1$ and a taller forest stand with height $h_2$ ($h_2 = c \cdot h_1$, where $c$ is a scaling constant) are shown.

Denoting the Gaussian motion profile in (3.10) as, $\rho_r(z)$, the mean-value theorem can be applied to (3.10) for $h_1$ and $h_2$ such that

$$\frac{\int_0^{h_i} \rho_r^{(i)}(z)\sigma_V^{(i)}(z)dz}{\int_0^{h_i} \sigma_V^{(i)}(z)dz} = \rho_r^{(i)}(\xi_i) \text{ for } i = 1, 2 \tag{A.1}$$

Mathematically, the choice of the mean value $\xi$ depends on the functional forms of both $\sigma_V(z)$ and $\rho_r(z)$. By using a change of variables, it can be shown that if $\rho_r^{(2)}(z) = \rho_r^{(1)}(\frac{z}{c})$ and $\sigma_V^{(2)}(z) = \sigma_V^{(1)}(\frac{z}{c})$, then $\xi_2 = c \cdot \xi_1$ or equivalently $\frac{\xi_2}{h_2} = \frac{\xi_1}{h_1}$. That is, when the extinction-weighted backscattering profile and the height-dependent motion profile of different forest stands are scaled versions of each other, the proportionality of the mean value with respect to the forest height is the same for all of the forest stands.

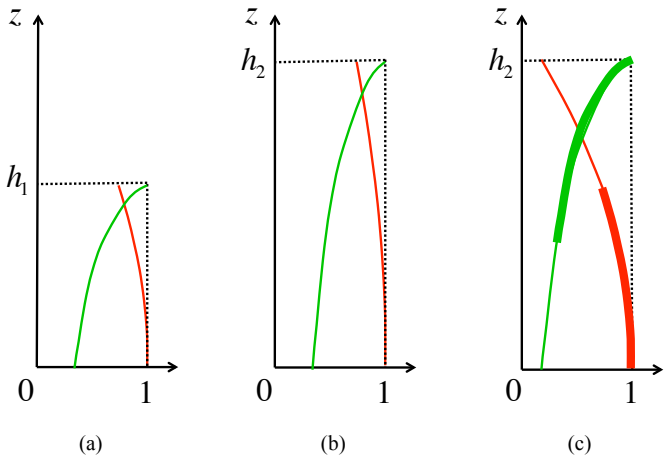


Figure A.3: Illustration of different functional forms of the extinction-weighted backscattering profile (normalized; "green" curve) and the height-dependent motion profile ("red" curve). (**a**) shows the profiles for a short forest stand at height $h_1$, (**b**) shows the profiles that are scaled versions of (a) for a taller forest stand at height $h_2$, while (**c**) shows the profiles for the taller forest stand at height $h_2$ using the same functional forms of $\sigma_V(z)$ (*i.e.*, constant extinction coefficient) and $\rho_r(z)$ (*i.e.*, constant wind-induced motion level) as (a). Note the highlighted curve segments in (c) exactly correspond to the profiles in (a).

In most cases, however, this requirement is not strictly satisfied, as illustrated in Figure A.3. Here, for forests with constant extinction coefficient and constant wind-

induced motion level as assumed in Section 4.2.1 (e.g., Figure 4.9a), the profiles of $\sigma_V(z)$ and $\rho_r(z)$ are illustrated in Figure A.3a,c for heights $h_1$ and $h_2$, respectively. However, in order to guarantee the same proportionality of the mean value, we would desire the profiles at height $h_2$ are nothing more than scaled versions of the ones at height $h_1$, *i.e.*, Figure A.3b. Therefore, the proportionality (denoted by $\alpha$ in Section 3.2.2) will have a perturbation for various forest heights in Figure 4.9a. For example, the standard deviation of $\alpha$ is calculated as 0.07, which in turn results in a standard deviation of 1.11 for $C_{scene}$ through using (3.13). In spite of this small perturbation of $\alpha$ (and thus $C_{scene}$), the overall fit as shown in Figure 4.9a is still quite good (RMSE = 0.25 m and R = 99.97% for heights under the saturation point). So far, we have seen that the requirement of the scaled versions of profiles for different heights could be weakly satisfied with small perturbation occurring but the overall quality of the fitting is still good.

# APPENDIX B

# POLARIZATION-DEPENDENCE OF THE FOREST HEIGHT INVERSION PROCEDURE

The forest height inversion procedure is based on (3.9) which is a version of the correlation model (3.6), simplified by assuming that $m = 0$ for HV-pol data. For the more general case, where both $\mu$, the ground-to-volume temporal decorrelation ratio due to dielectric change, and $m$, the ground-to-volume power ratio, are not trivial values (e.g., for the case of co-polarized transmit and receive channels), the contribution of ground scattering can be further investigated.

To understand these effects of undoing these assumptions, the general correlation model, (3.6), is rewritten as

$$\gamma_{v\&t} = S_{scene} \cdot \gamma'_{v\&m} \tag{B.1}$$

with

$$\gamma'_{v\&m} = \frac{\gamma_{v\&m} + \mu m}{1 + m} \tag{B.2}$$

where $\mu$ and $m$ will bias $\gamma'_{v\&m}$ from $\gamma_{v\&m}$.

To obtain the inverted forest height, (3.12) is used to determine $h_v$, while we maintain the same $S_{scene}$ and $C_{scene}$ as in the simplified model (see Figure 4.9a) but $\gamma_{v\&t}$ is replaced by (B.1) while calculating the simulated correlation magnitude. When $m = 0$, this reduces to the simplified model. Figure B.1 demonstrates the simulated inversion results when $m = 1$ (large $m$, or HH-pol data) and $m = 0.01$ (small $m$ or

HV-pol data), where the value of $m$ is referenced to a 30 m tall canopy as in [57]. Both subplots demonstrate the inversion model performance with $\mu = 1, e^{j\frac{\pi}{8}}, 0.95, 0.95e^{j\frac{\pi}{8}}$ allowing $\mu$ to have magnitude and/or phase bias in comparison with $\mu = 1$.

From the plots shown in Figure B.1 it can be seen that significant contributions from ground scattering (from the HH-polarized case in (a)) create a non-linear relationship between actual and estimated heights, whereas for the HV-pol data (small $m$), the model works well under almost all values of heights. For the small $m$ case, differences between the simulated and estimated heights only exist at the short and very tall extremes of the inversion. It is for this reason that a preference is given for the use of cross-polarized data in the inversion, a fact that has been borne out in observational data as well.

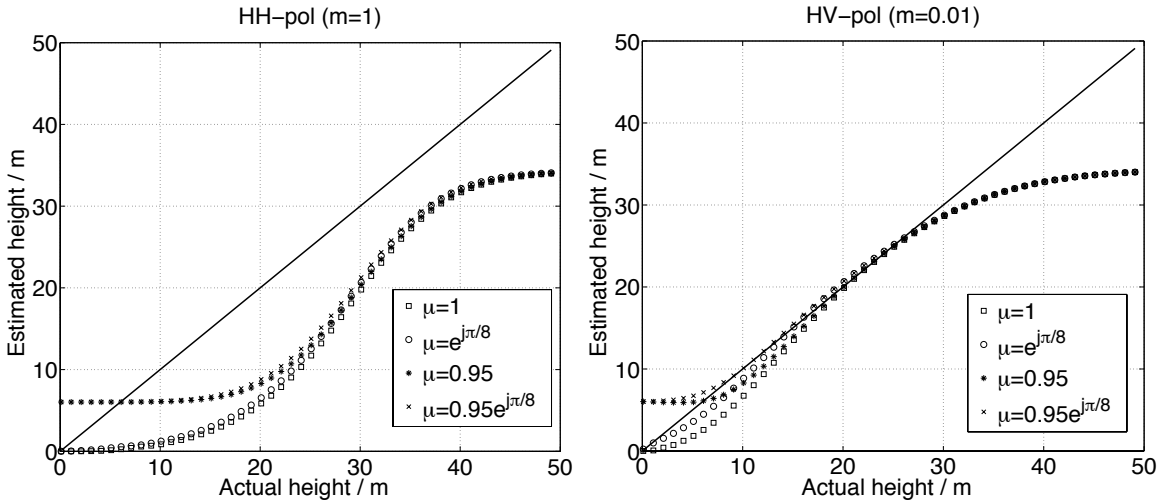


Figure B.1: Simulated forest height inversion results using (**a**) $m = 1$ (HH-pol) and (**b**) $m = 0.01$ (HV-pol). The instrumental and forest parameters are the same as in Figure 4.9a, so are the fitting parameters ($S_{scene}$ and $C_{scene}$). Results are shown with $\mu = 1, e^{j\frac{\pi}{8}}, 0.95, 0.95e^{j\frac{\pi}{8}}$.

Although it would be better to make a rigorous mathematical proof in order to validate this assumption, we note the above simulation method (e.g., Figure B.1) is sufficient at this stage. The purpose of this assumption is to show when $m \neq 0$,

bias exists in the inverted forest height. However, as long as $m$ is small, this only affects the lower end of the height range (e.g., short vegetation and ground), which can be tolerated if $m$ is small enough, or alternatively can be masked out through the use of a forest/non-forest map since there is usually extra temporal decorrelation causing overestimation of the low heights. The fact of HV-polarized data with $m$ being small enough in the present work has been validated both by the simulation results (Figure B.1b) and the experimental results (see Chapter 5, especially Figure 5.5, Figure 5.8, Figure 5.13 and Figure 5.15).

In the above simulation, an extinction coefficient of $k_e = 0.1$ dB/m (less than the values used in [57, 33]) is used to characterize a sparse forest at L-band. If a dense forest is studied with a greater $k_e = 0.3$ dB/m (as in [33]), the bias in the lower end of the height range will become much less pronounced, *i.e.*, the model performs much better. However, if a very spare forest is examined, the extinction effect will be so small that the ground-to-volume ratio will be huge even for a 30 m tall canopy. The inversion result for the HV-polarized data in this case will look very much like the HH-polarized data in the above simulation (Figure B.1a). The forest heights will thus be severely underestimated, however, since the forest is very sparse, the mean ground truth height will also be very small (close to the ground). As this work deals with the forest height through averaging a large area (not the maximum height), the biased difference between the estimated and ground truth heights can be tolerated for very sparse forests.

In the presence of temporal decorrelation, it is important to note that $S_{scene}$, $m$ and $\mu$ will be polarization-dependent. Therefore, the PolInSAR version [9, 40] of this problem will have additional unknowns when temporal decorrelation is expected to play a role in the observations, and thus the inversion becomes an underdetermined problem [56]. While sophisticated techniques (e.g., adapting PolInSAR methods to accommodate (3.6)) might lead to more accurate inversion, the simplified inversion

model shown here (based on HV-pol data only) has been shown to generate meaningful results from repeat-pass InSAR correlation measurements with long repeat periods. Such algorithms thus are important tools for making use of accumulated data from the JERS-1 [65], ALOS-1 & -2 data sets [66, 75, 28], as well as the planned DESDynI-R (now called NISAR) mission [3].

# APPENDIX C

# EFFECTIVE RANGE OF INTERFEROMETRIC VERTICAL WAVENUMBER AND THE SMALL-$\kappa_Z$ ASSUMPTION

Generally speaking, an InSAR correlation magnitude varies with the $\kappa_z$ value as indicated in Figure 5.11 and in [77] (under unfrozen conditions). In this appendix, the range of $\kappa_z$ values that can be used for this inversion model are explored. In order to do this it is useful to differentiate the decorrelation effects from the variety of sources, as they change with respect to $\kappa_z$. Although these decorrelation components are demonstrated here as simulation results, as mentioned in Section 4.2.1, these simulation parameters are intentionally chosen to be such in order to mimic the experimental results in Chapter 5. To create an example, a 20 m tall canopy is used and the $\kappa_z$-dependence of various correlation components is illustrated in Figure C.1 with the same forest parameters as in Figure 4.9a, and using a viewing geometry consistent with ALOS/PALSAR.

In Figure C.1, the "Volume Only" contribution is from volume scattering and no motion, "Dielectric" is the model for the loss of correlation magnitude due to dielectric changes in the volume (a constant factor that manifests itself in the model constant, $S_{scene}$), "Volume+Motion" is the magnitude of the coupled correlation component due to volume scattering and random motion ($|\gamma_{v\&m}|$), and "Total (Volume+Motion+Dielectric)" is the combined correlation magnitude from all volume scattering and temporal changes, $|\gamma_{v\&t}|$. In this example, it is assumed that the geometric decorrelation has been compensated for and that the thermal noise correlation is negligible for 20 m tall canopy.

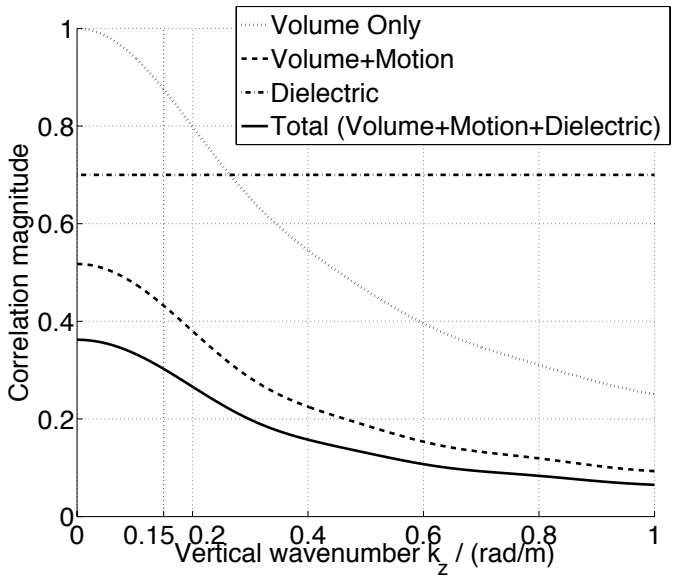


Figure C.1: Illustration of the $\kappa_z$-dependence for all of the correlation components involved in the current work by utilizing ALOS's viewing geometry over a 20 m tall canopy. The forest and temporal change parameters are chosen as in Figure 4.9a. The effective range of $\kappa_z$ for this study is $\kappa_z < 0.15$ rad/m.

From Figure C.1, it can be seen that as the vertical wavenumber increases, the total observed correlation decreases, as expected (which agrees with the observations in Figure 5.11), and that the combined effect of all correlations can make this total correlation quite low (below a value of 0.3). This has the effect of making the correlation magnitude difficult to measure [79], and also is an indication of a loss of information in the observation itself. For these reasons, for any model and subsequent inversion used, it is important to use those correlations that have the highest values, such as those shown in Figure 5.11. Because of the variety of sources of decorrelation when a 46 day repeat-period is introduced (*i.e.*, both dielectric and motion changes occur in the target), those observations with the shortest baselines will have the largest correlations, and hence information content. So long as there is a height-dependent sensitivity of the decorrelation on these changes (e.g., [5, 33]), a signature will exist that can be exploited to estimate forest height.

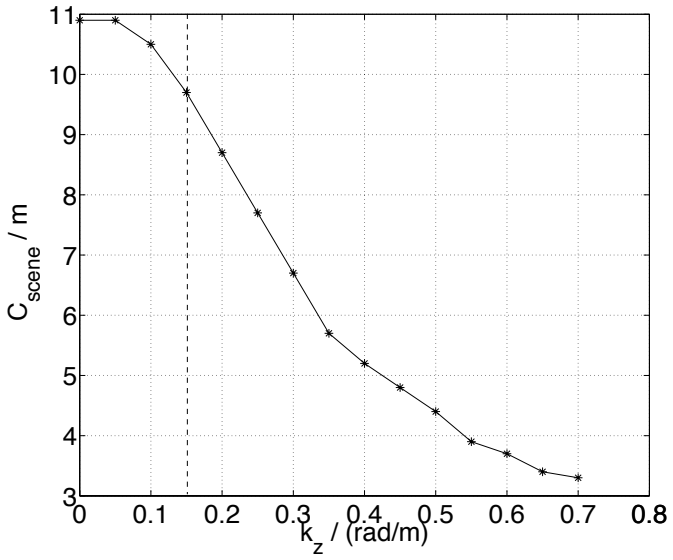


Figure C.2: The $\kappa_z$-dependence of the inversion model degradation. Particularly, the fitted parameter $C_{scene}$ is shown as a function of $\kappa_z$ with $\pi C_{scene}$ related to the invertible range of forest height characterizing the model performance. The smaller $C_{scene}$, the worse model performance. The forest and temporal change parameters in this simulation are set to be the same as Figure 4.9a. The case where $\kappa_z = 0.15$ rad/m (*i.e.*, boundary of the effective range for small $\kappa_z$ in this study) is indicated by a vertical dashed line.

The effect of changing the vertical wavenumber, $\kappa_z$, from zero to some other value, under these circumstances will lead to a graceful degradation in the model's performance, because the effect of this larger wavenumber will only be to decrease the correlation. Note that when $\kappa_z \neq 0$, a non-zero value of $\kappa_z$ will be included in the model via the scene-wide parameter, $C_{scene}$, derived in (3.9) through (3.13). While in that derivation, the vertical wavenumber was assumed to be zero, a non-zero but small value of that parameter will have the effect of scaling the argument of the exponential function given in (3.10), or equivalently, scaling the argument of the sinc function used in (3.12). In other words, the fitting parameter $C_{scene}$ will be $\kappa_z$-dependent in order to compensate the model degradation. This effect can be better illustrated by Figure C.2, which shows the fitted parameter $C_{scene}$ as a function of $\kappa_z$ with other simulation parameters fixed as in Figure 4.9a. As mentioned in Section 3.2.2 and discussed in Appendix D, the value $\pi C_{scene}$ represents the invertible range of forest

height through using the simplified inversion model ("sinc" relationship) with fitting parameters $S_{scene}$ and $C_{scene}$. If $C_{scene}$ becomes very small (e.g., <5 m as seen in Figure C.2), this simplified inversion approach will be insufficient to characterize the height variation of natural forests under the presence of correlation measurement uncertainty. Note for the small $\kappa_z$ values (*i.e.*, $\kappa_z < 0.15$ rad/m and preferably $< 0.05$ rad/m as stated above), the value of $C_{scene}$ is only slightly changed, which is in agreement with Figure 4.9a ($\kappa_z = 0.05$ rad/m) and Figure 4.9c ($\kappa_z = 0$ rad/m). The reason for this can be seen in the effect of $\kappa_z$ on the total decorrelation curve shown in Figure C.1, where the behavior of the curve for small values of $\kappa_z$ is at its peak, and relatively unchanged for values of $\kappa_z < 0.15$ rad/m (as indicated by the vertical dotted line included in Figure C.1), which serves as the effective range of $\kappa_z$ for this study. Therefore, we have demonstrated that for any non-zero small $\kappa_z$, this simplified inversion model (*i.e.*, the sinc relationship as in (3.12)) can always work well with $C_{scene}$ being weakly dependent on $\kappa_z$ (in comparison to (3.13) where $\kappa_z$ was neglected), which is referred to as the "small-$\kappa_z$ assumption" in this study.

# APPENDIX D

# THE VALIDITY FOR THE SINC APPROXIMATION TO THE GAUSSIAN-LIKE FUNCTION

In Section 3.2.2, we utilized the main lobe of a sinc function with a scaling factor to approximate the Gaussian-like curve. In this appendix, we will explain why this is necessary under the presence of measurement uncertainty and quantitatively describe the fitting error by comparing the Gaussian curve with the fitted sinc solution (*i.e.*, (3.12) along with (3.13)) as well as two alternative functional forms. Further, we will look at the translation of the fitting error in the InSAR correlation magnitude to the estimation bias of forest height.

First, we show the Gaussian-like curve of InSAR correlation component compared with the fitted sinc solution in Figure D.1 and explain why the fitted sinc function is used in this study to approximate the Gaussian-like function although there is still fitting error between them as noticed in Figure D.1. This is because that the fitted sinc function has the benefit of obtaining an upper limit (*i.e.*, $\pi C_{scene}$) on the maximum inverted height in the presence of uncertainty for measuring the InSAR correlation [79]. Without this simplifying approximation, the Gaussian expression in (3.12) is significantly insensitive to forest height in the nonlinear long "tail" region, and the inverted height as well as the height estimation uncertainty will approach infinity as the observed correlation magnitude becomes very low (which also implies that characterizing the height estimation uncertainty as a function of forest height is prohibited). This is important, because there is a large uncertainty in estimating low correlation magnitude signals (<0.2 as seen in Section 5.1.2; [79]) when the number of sampled looks is small, as is usually the case for spaceborne missions (e.g., 20-look

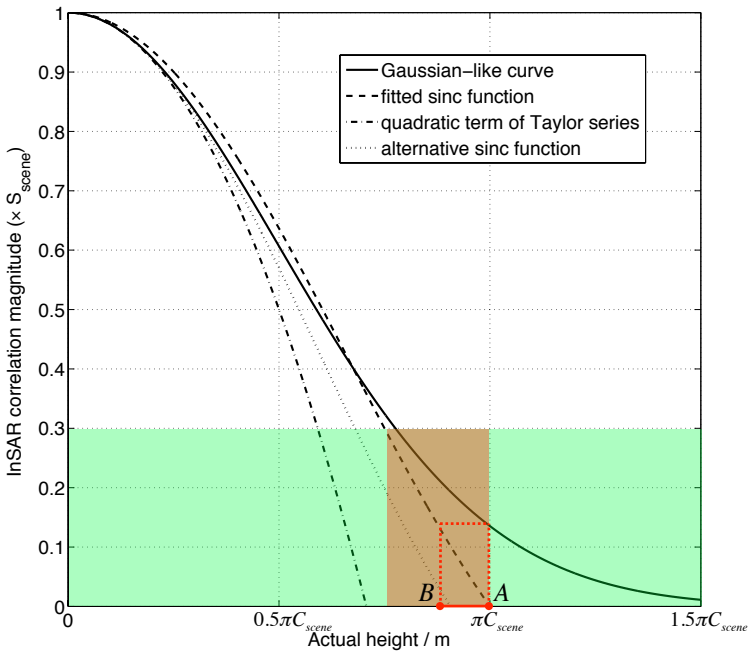


Figure D.1: The Gaussian-like curve of InSAR correlation magnitude as a function of forest height compared to the fitted sinc function along with two alternative functional forms, *i.e.*, the quadratic term of Taylor series and its corresponding sinc function. The illustration of height estimation bias is shown by the "red" lines, with point $A$ and point $B$ denoting the actual and estimated heights, respectively. The uncertainty in measuring the InSAR correlation magnitude and the uncertainty in the forest height estimation are illustrated as shaded areas in "green" and "red", respectively.

averaging was used for the estimation of InSAR correlation in the study presented here, which leads to the pixel size of 20 m $\times$ 30 m). In such a scenario, the InSAR estimation error encountered in the inversion of the Gaussian function of (3.12) will create significant height estimation errors in the long "tail" region of a Gaussian curve, as the forest height gets larger. In Figure D.1, we use the "green" shaded area to indicate the uncertainty (see Section 5.1.2) in measuring the InSAR correlation magnitude at $h_v = \pi C_{scene}$ (point $A$), the upper bound of the invertible height range. By using the Gaussian curve without sinc approximation, this measurement uncertainty is in turn translated into infinity for the height estimation uncertainty; however, by using the fitted sinc function, the height estimation uncertainty can be

remarkably reduced as illustrated by the "red" shaded area, although the mean value is shifted from point $A$ to point $B$ (as illustrated by the "red" lines) leading to a height estimation bias.

Next, we will study the height estimation bias through the use of different fitting functional forms. In Figure D.1, we also illustrate two alternative functional forms: "quadratic term of Taylor series" and "alternative sinc function" along with the fitted sinc function. Note, both sinc function and Gaussian function have their first two terms of Taylor series expansion being in a quadratic form. Therefore, in Figure D.1, "quadratic term of Taylor series" denotes the first two terms (*i.e.*, a quadratic function) in the Taylor series expansion of the Gaussian curve; while "alternative sinc function" denotes the corresponding sinc function that has the same quadratic terms in its Taylor series expansion. It can be noticed that the fitted sinc solution is the closest one on average to the Gaussian curve within the invertible height range $[0, \pi C_{scene}]$ and starts deviating at the higher end of the height range. The quadratic term and the corresponding sinc function fit very well to the Gaussian curve at the lower end of the height range as expected, *i.e.*, even better than the fitted sinc solution, however, they start deviating at a much lower height value. As illustrated by the "red" lines in Figure D.1, an actual forest height at point $A$ will be estimated as the one at point $B$ through using the fitted sinc solution, and the difference between them is referred to as the height estimation bias. We can thus plot the height estimation bias as a function of actual forest height for all of the three fitting functional forms from Figure D.1, and this is shown in Figure D.2. It is observed that, although the quadratic term and its corresponding sinc function have smaller bias at the lower end of the height range, the fitted sinc solution is the best functional form on average within the invertible height range. Particularly, as the "green" lines indicate, the estimation bias within most (almost $\frac{4}{5}$) of the height range $[0, \pi C_{scene}]$ is as small as $0.027\pi C_{scene}$, while for the height values close to the upper bound of the invertible height range,

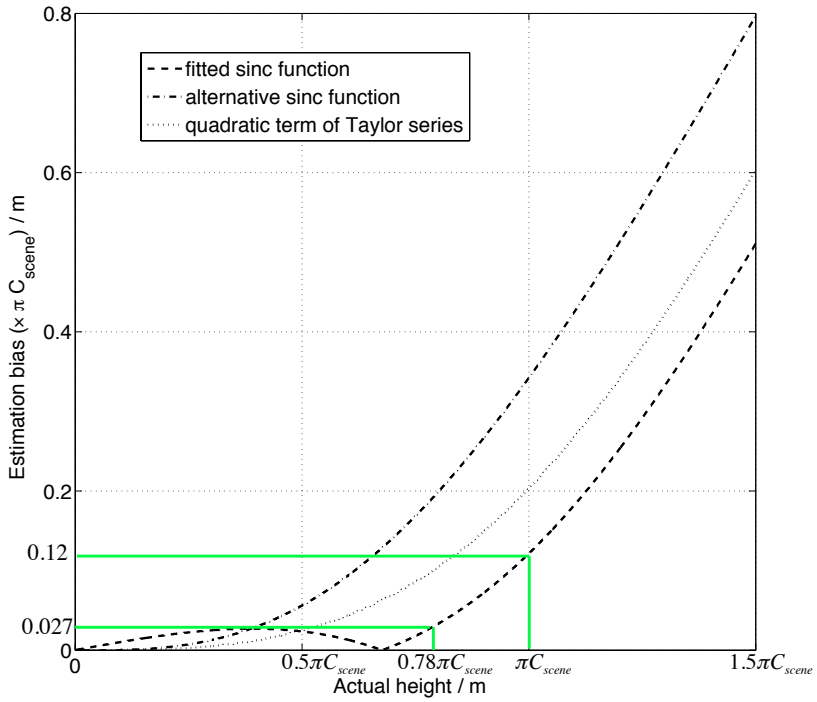


Figure D.2: The height estimation bias as a function of forest height for three different choices of fitting functional form as illustrated in Figure D.1. Here, the estimation bias from this sinc approximation are bounded by the "green" lines.

the estimation bias keeps increasing up to $0.12\pi C_{scene}$ as the estimated height begins to saturate.

Note importantly, the exact mathematical expression of $C_{scene}$ does not affect the practical inversion performance, since $C_{scene}$ along with $S_{scene}$ are just fitting parameters with different factors lumped into them. In practice, both of the fitting parameters $S_{scene}$ and $C_{scene}$ will be optimally estimated given some ground validation heights so that the estimated forest height can match the actual height very well for $h_v \in [0, \pi C_{scene}]$. In other words, the modeled estimation bias (that may not be sufficiently corrected) from this sinc approximation as well as other error sources will result in an overall forest height estimation uncertainty (e.g., $< 4$ m at the resolution of 10 hectares in this study). This has been verified from the simulation in Section 4.2 and the experimental validation in Chapter 5.

# BIBLIOGRAPHY


[1] NOAA's National Climatic Data Center. `http://ncdc.noaa.gov`.

[2] Ahmed, Razi, Siqueira, Paul, Hensley, Scott, Chapman, Bruce, and Bergen, Kathleen. A survey of temporal decorrelation from spaceborne L-Band repeat-pass InSAR. *Remote Sensing of Environment 115*, 11 (2011), 2887–2896.

[3] Alvarez-Salazar, Oscar, Hatch, Sara, Rocca, Jennifer, Rosen, Paul, Shaffer, Scott, Shen, Yuhsyen, Sweetser, Theodore, and Xaypraseuth, Peter. Mission design for NISAR repeat-pass Interferometric SAR. In *SPIE Remote Sensing* (2014), International Society for Optics and Photonics, pp. 92410C–92410C.

[4] Askne, Jan, Santoro, Maurizio, Smith, Gary, and Fransson, Johan ES. Multitemporal repeat-pass SAR interferometry of boreal forests. *Geoscience and Remote Sensing, IEEE Transactions on 41*, 7 (2003), 1540–1550.

[5] Askne, Jan IH, Dammert, Patrik BG, Ulander, Lars MH, and Smith, Gary. C-band repeat-pass interferometric SAR observations of the forest. *Geoscience and Remote Sensing, IEEE Transactions on 35*, 1 (1997), 25–35.

[6] Barnett, Tim P, Adam, Jennifer C, and Lettenmaier, Dennis P. Potential impacts of a warming climate on water availability in snow-dominated regions. *Nature 438*, 7066 (2005), 303–309.

[7] Blair, J.B., Rabine, D.L., and Hofton, M.A. The Laser Vegetation Imaging Sensor: a medium-altitude, digitisation-only, airborne laser altimeter for mapping vegetation and topography. *ISPRS Journal of Photogrammetry and Remote Sensing 54*, 2 (1999), 115–122.

[8] Cloude, Shane R. Polarization coherence tomography. *Radio Science 41*, 4 (2006).

[9] Cloude, SR, and Papathanassiou, KP. Three-stage inversion process for polarimetric SAR interferometry. *IEE Proceedings-Radar, Sonar and Navigation 150*, 3 (2003), 125–134.

[10] Crookston, Nicholas L, and Dixon, Gary E. The forest vegetation simulator: a review of its structure, content, and applications. *Computers and Electronics in Agriculture 49*, 1 (2005), 60–80.

[11] Cumming, Ian G, and Wong, Frank Hay-chee. *Digital processing of synthetic aperture radar data: algorithms and implementation.* Artech House, 2005.

[12] de Matthaeis, Paolo, and Lang, Roger H. Microwave scattering models for cylindrical vegetation components. *Progress In Electromagnetics Research 55* (2005), 307–333.

[13] Ding, Kung-Hau, Xu, Xiaolan, and Tsang, Leung. Electromagnetic scattering by bicontinuous random microstructures with discrete permittivities. *Geoscience and Remote Sensing, IEEE Transactions on 48*, 8 (2010), 3139–3151.

[14] Du, Jinyang, Shi, Jiancheng, and Rott, Helmut. Comparison between a multi-scattering and multi-layer snow scattering model and its parameterized snow backscattering model. *Remote Sensing of Environment 114*, 5 (2010), 1089–1098.

[15] Dubayah, R, Goetz, SJ, Blair, JB, Fatoyinbo, TE, Hansen, M, Healey, SP, Hofton, MA, Hurtt, GC, Kellner, J, Luthcke, SB, et al. The Global Ecosystem Dynamics Investigation. In *AGU Fall Meeting Abstracts* (2014), vol. 1, p. 07.

[16] Foldy, Leslie L. The multiple scattering of waves. I. General theory of isotropic scattering by randomly distributed scatterers. *Physical Review 67*, 3-4 (1945), 107.

[17] Fry, J., Xian, G., Jin, S., Dewitz, J., Homer, C., Yang, L., Barnes, C., Herold, N., and Wickham, J. Completion of the 2006 National Land Cover Database for the Counterminous United States. *Photogrammetric Engineering and Remote Sensing 77*, 9 (2011), 858–864.

[18] Fu, Lee-Lueng, Alsdorf, Douglas, Rodriguez, Erensto, Morrow, Rosemary, Mognard, Nelly, Lambin, Juliette, Vaze, Parag, and Lafon, Thierry. The SWOT (Surface Water and Ocean Topography) Mission: spaceborne radar interferometry for oceanographic and hydrological applications. In *OCEANOBS09 Conference* (2009).

[19] Gatelli, Fabio, Guamieri, A Monti, Parizzi, Francesco, Pasquali, Paolo, Prati, Claudio, and Rocca, Fabio. The wavenumber shift in SAR interferometry. *Geoscience and Remote Sensing, IEEE Transactions on 32*, 4 (1994), 855–865.

[20] Gesch, Dean, Evans, Gayla, Mauck, James, Hutchinson, John, and Carswell Jr, William J. The national map: Elevation. *US geological survey fact sheet 3053*, 4 (2009).

[21] Goetz, Scott. The lost promise of DESDynI. *Remote Sensing of Environment 115*, 11 (2011), 2751.

[22] Gubner, John A. *Probability and random processes for electrical and computer engineers*. Cambridge University Press, 2006.

[23] Guglielmetti, M, Schwank, M, Mätzler, C, Oberdörster, C, Vanderborght, Jan, and Flühler, H. Measured microwave radiative transfer properties of a deciduous forest canopy. *Remote sensing of environment 109*, 4 (2007), 523–532.

[24] Hajnsek, I., Kugler, F., Lee, S.K., and Papathanassiou, K.P. Tropical-forest-parameter estimation by means of PolInSAR: The INDREX-II campaign. *Geoscience and Remote Sensing, IEEE Transactions on 47*, 2 (2009), 481–493.

[25] Hollinger, DY, Goltz, SM, Davidson, EA, Lee, JT, Tu, K, and Valentine, HT. Seasonal patterns and environmental control of carbon dioxide and water vapour exchange in an ecotonal boreal forest. *Global Change Biology 5*, 8 (1999), 891–902.

[26] Ishimaru, Akira. *Wave propagation and scattering in random media*, vol. 2. Academic press New York, 1978.

[27] Jolivet, Romain, Grandin, Raphael, Lasserre, Cécile, Doin, M-P, and Peltzer, G. Systematic InSAR tropospheric phase delay corrections from global meteorological reanalysis data. *Geophysical Research Letters 38*, 17 (2011).

[28] Kankaku, Yukihiro, Osawa, Yuji, Suzuki, Shinichi, and Watanabe, Tomohiro. The overview of the L-band SAR onboard ALOS-2. In *Progress in electromagnetics research symposium proceedings* (2009), pp. 18–21.

[29] Karam, MA, and Fung, AK. Electromagnetic scattering from a layer of finite length, randomly oriented, dielectric, circular cylinders over a rough interface with application to vegetation. *Remote Sensing 9*, 6 (1988), 1109–1134.

[30] Karam, Mostafa A, Fung, Adrian K, and Antar, Yahia MM. Electromagnetic wave scattering from some vegetation samples. *Geoscience and Remote Sensing, IEEE Transactions on 26*, 6 (1988), 799–808.

[31] Kellndorfer, J, Walker, W, LaPoint, E, Bishop, J, Cormier, T, Fiske, G, Hoppus, M, Kirsch, K, , and Westfall, J. NACP Aboveground Biomass and Carbon Baseline Data (NBCD 2000), U.S.A., 2000. Data set. Available on-line at `http://daac.ornl.gov` fr! om ORNL DAAC, Oak Ridge, Tennessee, U.S.A. `http://dx.doi.org/10.3334/ORNLDAAC/1081`, 2012. [Online].

[32] Kellndorfer, Josef, Walker, Wayne, Pierce, Leland, Dobson, Craig, Fites, Jo Ann, Hunsaker, Carolyn, Vona, John, and Clutter, Michael. Vegetation height estimation from shuttle radar topography mission and national elevation datasets. *Remote Sensing of Environment 93*, 3 (2004), 339–358.

[33] Lavalle, M., Simard, M., and Hensley, S. A Temporal Decorrelation Model for Polarimetric Radar Interferometers. *Geoscience and Remote Sensing, IEEE Transactions on 50*, 7 (2012), 2880–2888.

[34] Lavalle, Marco, and Hensley, Scott. Demonstration of repeat-pass POLINSAR using UAVSAR: The RMOG model. In *Geoscience and Remote Sensing Symposium (IGARSS), 2012 IEEE International* (2012), IEEE, pp. 5876–5879.

[35] Lax, Melvin. Multiple scattering of waves. *Reviews of Modern Physics 23*, 4 (1951), 287.

[36] Lax, Melvin. Multiple scattering of waves. II. The effective field in dense systems. *Physical Review 85*, 4 (1952), 621.

[37] Le Toan, Thuy, Quegan, S, Davidson, MWJ, Balzter, Heiko, Paillou, Philippe, Papathanassiou, K, Plummer, S, Rocca, F, Saatchi, S, Shugart, H, et al. The BIOMASS mission: Mapping global forest biomass to better understand the terrestrial carbon cycle. *Remote sensing of environment 115*, 11 (2011), 2850–2860.

[38] Lee, Jong-Sen, Hoppel, Karl W, Mango, Stephen A, and Miller, Allen R. Intensity and phase statistics of multilook polarimetric and interferometric SAR imagery. *Geoscience and Remote Sensing, IEEE Transactions on 32*, 5 (1994), 1017–1028.

[39] Lee, Seung-Kuk, Kugler, Florian, Papathanassiou, Konstantinos P, and Hajnsek, Irena. Quantification of temporal decorrelation effects at L-band for polarimetric SAR interferometry applications. *Selected Topics in Applied Earth Observations and Remote Sensing, IEEE Journal of 6*, 3 (2013), 1351–1367.

[40] Lee, S.K., Kugler, F., Papathanassiou, K., and Hajnsek, I. Quantification and compensation of temporal decorrelation effects in polarimetric SAR interferometry. In *Geoscience and Remote Sensing Symposium (IGARSS), 2012 IEEE International* (2012), IEEE, pp. 3106–3109.

[41] Legresy, Benoit, Papa, Fabrice, Remy, Frederique, Vinay, Gaetan, van den Bosch, Mathias, and Zanife, Ouan-Zan. ENVISAT radar altimeter measurements over continental surfaces and ice caps using the ICE-2 retracking algorithm. *Remote Sensing of Environment 95*, 2 (2005), 150–163.

[42] Lei, Yang, and Siqueira, Paul. An automatic mosaicking algorithm for generating a large-scale forest stand height map using spaceborne repeat-pass InSAR coherence. In *Geoscience and Remote Sensing Symposium (IGARSS), 2014 IEEE International* (2014), IEEE, pp. 84–87.

[43] Lei, Yang, and Siqueira, Paul. Estimation of forest height using spaceborne repeat-pass L-Band InSAR correlation magnitude over the US State of Maine. *Remote Sensing 6*, 11 (2014), 10252–10285.

[44] Lei, Yang, and Siqueira, Paul. A dense-medium InSAR correlation model with its application to the problem of snow characteristics retrieval. In *Geoscience and Remote Sensing Symposium (IGARSS), 2015 IEEE International* (2015), IEEE, pp. 263–266.

[45] Lei, Yang, and Siqueira, Paul. An automatic mosaicking algorithm for the generation of a large-scale forest height map using spaceborne repeat-pass InSAR correlation magnitude. *Remote Sensing 7*, 5 (2015), 5639–5659.

[46] Lei, Yang, Siqueira, Paul, Clewley, Daniel, and Lucas, Richard. Observation of vegetation vertical structure and disturbance using L-band InSAR over the Injune region in Australia. In *Geoscience and Remote Sensing Symposium (IGARSS), 2012 IEEE International* (2012), IEEE, pp. 1637–1640.

[47] Lei, Yang, Siqueira, Paul R, and Treuhaft, Robert N. A dense-medium electromagnetic scattering model for the InSAR correlation of snow. *Radio Science* (In Review).

[48] Lei, Yang, Siqueira, Paul R, and Treuhaft, Robert N. A physical scattering model of repeat-pass InSAR correlation for vegetation. *Waves in Random Media* (In Review).

[49] Leinss, Silvan, and Hajnsek, Irena. Opportunities of snow property extraction based on single and multi pass SAR interferometry: TanDEM-X. In *Geoscience and Remote Sensing Symposium (IGARSS), 2012 IEEE International* (2012), IEEE, pp. 146–149.

[50] Leuschen, Carlton J, Swift, Robert N, Comiso, Josefino C, Raney, R Keith, Chapman, Rickey D, Krabill, William B, and Sonntag, John G. Combination of laser and radar altimeter height measurements to estimate snow depth during the 2004 Antarctic AMSR-E Sea Ice field campaign. *Journal of Geophysical Research: Oceans (1978–2012) 113*, C4 (2008).

[51] Liang, Ding, Tsang, Leung, Yueh, Simon, and Xu, Xiaolan. Modeling active microwave remote sensing of multilayer dry snow using dense media radiative transfer theory. In *Geoscience and Remote Sensing Symposium, 2008. IGARSS 2008. IEEE International* (2008), vol. 3, IEEE, pp. III–39.

[52] Lucas, Richard, Clewley, Daniel, Bunting, Peter, Armston, John, Scarth, Peter, Held, Alex, Phinn, Stuart, Schmidt, Michael, Accad, Arnon, Carreiras, Joao, Siqueira, Paul, and Lei, Yang. 18th ALOS Kyoto & Carbon Initiative Science Team Meeting: Australian R & D Support to Global Forest and Above Ground Biomass Mapping. `http://www.eorc.jaxa.jp/ALOS/en/kyoto/nov2012_kc18/pdf/2-06_KC18_forests_Lucas.pdf`, 2012. [Online].

[53] Lucas, Richard M, Cronin, Natasha, Lee, Alex, Moghaddam, Mahta, Witte, Christian, and Tickle, Phil. Empirical relationships between AIRSAR backscatter and LiDAR-derived forest biomass, Queensland, Australia. *Remote Sensing of Environment 100*, 3 (2006), 407–425.

[54] Michael, T Heath. *Scientific Computing: An Introductory Survey*. The McGraw-Hill Companies Inc., New York, 2002.

[55] Moon, Todd K, and Stirling, Wynn C. *Mathematical methods and algorithms for signal processing*, vol. 1. Prentice hall New York, 2000.

[56] Papathanassiou, KP, and Cloude, Shane R. The effect of temporal decorrelation on the inversion of forest parameters from PolInSAR data. In *INTERNATIONAL GEOSCIENCE AND REMOTE SENSING SYMPOSIUM* (2003), vol. 3, pp. III–1429.

[57] Papathanassiou, K.P., and Cloude, S.R. Single-baseline polarimetric SAR interferometry. *Geoscience and Remote Sensing, IEEE Transactions on 39*, 11 (2001), 2352–2363.

[58] Parrella, Giuseppe, Della Corte, Annalisa, Hajnsek, Irena, and Iodice, Antonio. Snow properties retrieval using TerraSAR-X dual-polarization data. In *Geoscience and Remote Sensing Symposium (IGARSS), 2012 IEEE International* (2012), IEEE, pp. 4410–4413.

[59] Percus, Jerome, and Yevick, George J. Analysis of classical statistical mechanics by means of collective coordinates. *Physical Review* (1958), 1–13.

[60] Rodriguez, E, and Martin, JM. Theory and design of interferometric synthetic aperture radars. In *Radar and Signal Processing, IEE Proceedings F* (1992), vol. 139, IET, pp. 147–159.

[61] Rosen, P, and Fielding, E. Repeat orbit interferometry package (ROI_PAC), 2010.

[62] Rosen, PA, Gurrola, EM, Sacco, G, and Zebker, HA. InSAR Scientific Computing Environment-The Home Stretch. In *AGU Fall Meeting Abstracts* (2011), vol. 1, p. 02.

[63] Rosen, Paul, Hensley, Scott, Wheeler, Kevin, Sadowy, Greg, Miller, Tim, Shaffer, Scott, Muellerschoen, Ron, Jones, Cathleen, Zebker, Howard, Madsen, Soren, et al. UAVSAR: A new NASA airborne SAR system for science and technology research. In *Radar, 2006 IEEE Conference on* (2006), IEEE, pp. 8–pp.

[64] Rosen, Paul A, Hensley, Scott, Joughin, Ian R, Li, Fuk K, Madsen, Soren N, Rodriguez, Ernesto, and Goldstein, Richard M. Synthetic aperture radar interferometry. *Proceedings of the IEEE 88*, 3 (2000), 333–382.

[65] Rosenqvist, A, Shimada, M, Chapman, B, Freeman, A, De Grandi, G, Saatchi, S, and Rauste, Y. The global rain forest mapping project-a review. *International Journal of Remote Sensing 21*, 6-7 (2000), 1375–1387.

[66] Rosenqvist, Ake, Shimada, Masanobu, Ito, Norimasa, and Watanabe, Manabu. ALOS PALSAR: A pathfinder mission for global-scale monitoring of the environment. *Geoscience and Remote Sensing, IEEE Transactions on 45*, 11 (2007), 3307–3316.

[67] Rott, Helmut, Cline, Donald W, Duguay, Claude, Essery, Richard, Etchevers, Pierre, Hajnsek, Irena, Kern, Michael, Macelloni, Giovanni, Malnes, Eirik, Pulliainen, Jouni, et al. CoReH2O, a dual frequency radar mission for snow and ice observations. In *Geoscience and Remote Sensing Symposium (IGARSS), 2012 IEEE International* (2012), IEEE, pp. 5550–5553.

[68] Schwabisch, M, and Geudtner, D. Improvement of phase and coherence map quality using azimuth prefiltering: Examples from ERS-1 and X-SAR. In *Geoscience and Remote Sensing Symposium, 1995. IGARSS'95.'Quantitative Remote Sensing for Science and Applications', International* (1995), vol. 1, IEEE, pp. 205–207.

[69] Sendak, Paul E, Brissette, John C, and Frank, Robert M. Silviculture affects composition, growth, and yield in mixed northern conifers: 40-year results from the Penobscot Experimental Forest. *Canadian Journal of Forest Research 33*, 11 (2003), 2116–2128.

[70] Shi, Jiancheng, and Dozier, Jeff. Estimation of snow water equivalence using SIR-C/X-SAR. I. Inferring snow density and subsurface properties. *Geoscience and Remote Sensing, IEEE Transactions on 38*, 6 (2000), 2465–2474.

[71] Shi, Jiancheng, and Dozier, Jeff. Estimation of snow water equivalence using SIR-C/X-SAR. II. Inferring snow depth and particle size. *Geoscience and Remote Sensing, IEEE Transactions on 38*, 6 (2000), 2475–2488.

[72] Shi, Jiancheng, Yueh, S, and Cline, D. On estimation of snow water equivalence using L-band and Ku-band radar. In *Geoscience and Remote Sensing Symposium, 2003. IGARSS'03. Proceedings. 2003 IEEE International* (2003), vol. 2, IEEE, pp. 845–847.

[73] Shimada, M, Watanabe, M, Motooka, T, Shiraishi, T, Isoguchi, O, Mukaida, A, Okumura, H, Otaki, T, and Itoh, T. Generation of 10m resolution PALSAR and JERS-1 SAR MOSAIC and forest/non-forest maps for forest carbon tracking. In *Synthetic Aperture Radar (APSAR), 2011 3rd International Asia-Pacific Conference on* (2011), IEEE, pp. 1–4.

[74] Shimada, Masanobu, Isoguchi, Osamu, Tadono, Takeo, and Isono, Kazuo. PALSAR radiometric and geometric calibration. *Geoscience and Remote Sensing, IEEE Transactions on 47*, 12 (2009), 3915–3932.

[75] Shimada, Masanobu, and Ohtaki, Takahiro. Generating large-scale high-quality SAR mosaic datasets: Application to PALSAR data for global monitoring. *Selected Topics in Applied Earth Observations and Remote Sensing, IEEE Journal of 3*, 4 (2010), 637–656.

[76] Simard, Marc, Hensley, Scott, Lavalle, Marco, Dubayah, Ralph, Pinto, Naiara, and Hofton, Michelle. An empirical assessment of temporal decorrelation using the uninhabited aerial vehicle synthetic aperture radar over forested landscapes. *Remote Sensing 4*, 4 (2012), 975–986.

[77] Thiel, Christian, and Schmullius, Christiane. Investigating ALOS PALSAR interferometric coherence in central Siberia at unfrozen and frozen conditions: implications for forest growing stock volume estimation. *Canadian Journal of Remote Sensing 39*, 3 (2013), 232–250.

[78] Tickle, PK, Lee, A, Lucas, RM, Austin, J, and Witte, C. Quantifying Australian forest floristics and structure using small footprint LiDAR and large scale aerial photography. *Forest Ecology and Management 223*, 1 (2006), 379–394.

[79] Touzi, R., Lopes, A., Bruniquel, J., and Vachon, P.W. Coherence estimation for SAR imagery. *Geoscience and Remote Sensing, IEEE Transactions on 37*, 1 (1999), 135–149.

[80] Treuhaft, Robert N, Madsen, Søren N, Moghaddam, Mahta, and Zyl, Jakob J. Vegetation characteristics and underlying topography from interferometric radar. *Radio Science 31*, 6 (1996), 1449–1485.

[81] Treuhaft, Robert N, and Siqueira, Paul R. Vertical structure of vegetated land surfaces from interferometric and polarimetric radar. *Radio Science 35*, 1 (2000), 141–177.

[82] Tsang, L, Kong, JA, and Shin, RT. Theory of microwave remote sensing. *Wiley series in remote sensing* (1985).

[83] Tsang, Leung, and Kong, Jin Au. *Scattering of Electromagnetic Waves, Advanced Topics*. John Wiley & Sons, 2004.

[84] Tsang, Leung, Kong, Jin Au, and Ding, Kung-Hau. Electromagnetic Wave MATLAB Library. `http://www.ee.washington.edu/research/laceo/emwave/`, 2006. [Online; accessed 1-May-2014].

[85] Tsang, Leung, Kong, Jin Au, Ding, Kung-Hau, and Ao, Chi On. *Scattering of Electromagnetic Waves: Numerical Simulations*. John Wiley & Sons, Inc., 2002.

[86] Tsang, Leung, Pan, Jin, Liang, Ding, Li, Zhongxin, Cline, Donald W, and Tan, Yunhua. Modeling active microwave remote sensing of snow using dense media radiative transfer (DMRT) theory with multiple-scattering effects. *Geoscience and Remote Sensing, IEEE Transactions on 45*, 4 (2007), 990–1004.

[87] Ulaby, Fawwaz T, and El-Rayes, MOHAMED A. Microwave dielectric spectrum of vegetation-Part II: Dual-dispersion model. *Geoscience and Remote Sensing, IEEE Transactions on*, 5 (1987), 550–557.

[88] Vallese, F, and Kong, JA. Correlation function studies for snow and ice. *Journal of Applied Physics 52*, 8 (1981), 4921–4925.

[89] Weber Hoen, E, and Zebker, Howard A. Penetration depths inferred from interferometric volume decorrelation observed over the Greenland ice sheet. *Geoscience and Remote Sensing, IEEE Transactions on 38*, 6 (2000), 2571–2583.

[90] Werner, Charles, Wegmüller, Urs, Strozzi, Tazio, Wiesmann, Andreas, and Santoro, Maurizio. PALSAR Multi-Mode Interferometric Processing. In *Proc. 1st Joint PI Symposium of ALOS Data Nodes, Kyoto, Japan* (2007), pp. 19–23.

[91] Williams, M. PolSARproSim Design Document and Algorithm Specification, 2006.

[92] Xiong, Chuan, Shi, Jiancheng, Brogioni, Marco, and Tsang, Leung. Microwave snow backscattering modeling based on two-dimensional snow section image and equivalent grain size. In *Geoscience and Remote Sensing Symposium (IGARSS), 2012 IEEE International* (2012), IEEE, pp. 150–153.

[93] Xiong, Chuan, Shi, Jiancheng, and Lemmetyinem, Juha. Refinement of the x and ku band dual-polarization scatterometer snow water equivalent retrieval algorithm. In *Geoscience and Remote Sensing Symposium (IGARSS), 2014 IEEE International* (2014), IEEE.

[94] Xu, Xiaolan, Tsang, Leung, Chang, Wenmo, and Yueh, Simon. DMRT models of bicontinuous media and QCA multiple-sizes for applications to microwave remote sensing of snowpacks. In *Geoscience and Remote Sensing Symposium (IGARSS), 2014 IEEE International* (2014), IEEE.

[95] Xu, Xiaolan, Tsang, Leung, and Yueh, Simon. Electromagnetic Models of Co/Cross Polarization of Bicontinuous/DMRT in Radar Remote Sensing of Terrestrial Snow at X-and Ku-band for CoReH2O and SCLP Applications. *Selected Topics in Applied Earth Observations and Remote Sensing, IEEE Journal of 5*, 3 (2012), 1024–1032.

[96] Zebker, Howard A, and Villasenor, John. Decorrelation in interferometric radar echoes. *Geoscience and Remote Sensing, IEEE Transactions on 30*, 5 (1992), 950–959.